

# Graph Neural Network Flavour Tagging and Boosted Higgs Measurements at the LHC

Samuel John Van Stroud  
University College London

Submitted to University College London in fulfilment  
of the requirements for the award of the  
degree of **Doctor of Philosophy**

March 19, 2023

## **Declaration**

I, Samuel John Van Stroud confirm that the work presented in this thesis is my own. Where information has been derived from other sources, I confirm that this has been indicated in the thesis.

Samuel Van Stroud

---

# Abstract

This thesis presents investigations into the challenges of, potential improvements to, and the application of  $b$ -jet identification to study the Higgs boson at the ATLAS experiment at the Large Hadron Collider (LHC). A focus is placed on the high transverse momentum regime, which is a critical region in which to study the Standard Model, but within which successful  $b$ -jet identification becomes difficult.

As  $b$ -jet identification relies on the successful reconstruction of charged particle trajectories (tracks), the tracking performance is investigated and potential improvements are assessed. Track reconstruction becomes increasingly difficult at high transverse momentum due to the increased multiplicity and collimation of tracks, and also due to the presence of displaced tracks that may occur as the result of the decay of a long-flying  $b$ -hadron. The investigations revealed that the track quality selections applied during track reconstruction are suboptimal for tracks inside high transverse momentum  $b$ -jets, motivating future studies into the optimisation of these cuts.

To improve  $b$ -tagging performance two novel techniques are employed: the classification of the origin of tracks and the application of graph neural networks. An algorithm has been developed to classify the origin of tracks, which allows a more optimal collection of tracks to be selected for use in other algorithms. A graph neural network (GNN) jet flavour tagger has also been developed. This tagger requires only tracks and jet variables as inputs, making a break from previous algorithms, which relied on the outputs of several other

algorithms. This model is trained to simultaneously predict the jet flavour, track origins, and track-pair compatibility (i.e. vertexing), and demonstrates markedly improvements in  $b$ -tagging performance, both at low and high transverse momenta. The closely related task of c-jet identification also benefits from these methods.

Analysis of high transverse momentum  $H \rightarrow b\bar{b}$  decays, where the Higgs boson is produced in association with a vector boson, was also performed using  $139 \text{ fb}^{-1}$  of 13 TeV proton-proton collision data from Run 2 of the LHC. The analysis is described, with a focus on the detailed modelling studies performed by the author. The analysis measured provided first measurements in this channel of the Higgs boson production in two high transverse momentum regions.

# Impact Statement

This thesis details research in experimental particle physics. The primary contributions are on the improvement of the data analysis algorithms which are used to process proton-proton collisions induced within the ATLAS detector at the Large Hadron Collider (LHC), and the analysis of candidate Higgs boson events.

The primary outcome of the research is an advancement of knowledge about how the Universe works on the most fundamental level, encoded for example in the improved measurement of the fundamental constants for the Standard Model, or in the observation of previously unseen particles or interactions. Although this kind of knowledge doesn't always have an immediate and direct relevance for society, potential applications are impossible to rule out and could have a very large impact further in the future, as has been seen with previous advancements in fundamental science.

The research does find indirect application in the form of associated technological developments that have transferable application within different fields. The cutting-edge techniques developed at CERN for ATLAS and the LHC have found many spin-off applications elsewhere in society, for example the World Wide Web, high-field magnet technology in MRI, touch-screen technology and cloud computing. Fundamental physics, as a proposer of novel and difficult problems, can therefore be seen as a way to generate innovative technologies.

Working in the field also helps to train skilled researchers, which can be redeployed to other areas of society to tackle various problems. In this thesis advanced statistical and data science methods are

deployed. Such methods currently find wide and varied use in many fields. The training of such highly skilled individuals, has a sustained and significant positive economic impact.

Finally, the work carried at ATLAS and the LHC is widely publicised – support of and interest in fundamental physics research helps to generate excitement about science and technology, and educate people about how the Universe works. This in turn attracts people into the area, propagating the benefits described above.

## Acknowledgements

Firstly I give thanks to my supervisor Tim Scanlon for all the guidance and support he has offered over the course of this doctorate. Tim has always been consistent with clear explanations and sound advice throughout the last four years. I would also like to thank everyone I've worked with at ATLAS and at UCL. In particular I have Jonathan Shlomi to thank for the fruitful collaboration on advancements in flavour tagging. I would also like to thank Brian Moser and Hannah Arnold for their patient support during the course of the  $VH$ ,  $H \rightarrow b\bar{b}$  analysis. I'm grateful to everyone I've worked with in the ATLAS Flavour Tagging and Tracking groups, in particular to Gabriel Facini, Valerio Dao, Bingxuan Liu and Francesco Di Bello for their guidance, and Dan Guest for his fastidious merge request reviews. This thesis was made in L<sup>A</sup>T<sub>E</sub>X 2 <sub>$\varepsilon$</sub>  using the “heptesis” class [1].

# Contents

<b>1</b>	<b>Introduction</b>	<b>12</b>
<b>2</b>	<b>Theoretical Framework</b>	<b>14</b>
2.1	The Standard Model . . . . .	14
2.1.1	Quantum Electrodynamics . . . . .	15
2.1.2	Quantum Chromodynamics . . . . .	17
2.1.3	The Electroweak Sector . . . . .	18
2.2	The Higgs Mechanism . . . . .	19
2.2.1	Electroweak Symmetry Breaking . . . . .	20
2.2.2	Fermionic Yukawa Coupling . . . . .	23
2.2.3	Higgs Sector Phenomenology . . . . .	25
<b>3</b>	<b>The Large Hadron Collider and the ATLAS Detector</b>	<b>28</b>
3.1	The Large Hadron Collider . . . . .	29
3.2	Coordinate System & Collider Definitions . . . . .	30
3.2.1	ATLAS Coordinate System . . . . .	31
3.2.2	Track Parameterisation . . . . .	32
3.2.3	Hadron Collider Definitions . . . . .	32
3.3	The ATLAS Detector . . . . .	36
3.3.1	Inner Detector . . . . .	37
3.3.2	Calorimeters . . . . .	40
3.3.3	Muon Spectrometer . . . . .	42
3.3.4	The Trigger . . . . .	43
3.4	Reconstructed Physics Objects . . . . .	44
3.4.1	Tracks . . . . .	44
3.4.2	Vertices . . . . .	48
3.4.3	Jets . . . . .	49
3.4.4	Leptons . . . . .	51

3.4.5	Missing Transverse Momentum . . . . .	53
<b>4</b>	<b>Tracking and Flavour Tagging</b>	<b>54</b>
4.1	Datasets . . . . .	55
4.2	<i>b</i> -tagging Algorithms . . . . .	55
4.2.1	Common Definitions . . . . .	56
4.2.2	Low-level Algorithms . . . . .	56
4.2.3	High-level Algorithms . . . . .	57
4.3	<i>b</i> -hadron Reconstruction . . . . .	58
4.3.1	Decay Topology . . . . .	58
4.3.2	Challenges . . . . .	60
4.4	Investigations into High $p_T$ <i>b</i> -hadron Tracking . . . . .	64
4.4.1	Shared Hits . . . . .	64
4.4.2	Global $\chi^2$ Fitter Outlier Removal . . . . .	64
4.5	Conclusion . . . . .	68
<b>5</b>	<b>Track Classification MVA</b>	<b>69</b>
5.1	Machine Learning Background . . . . .	69
5.1.1	Neural Networks . . . . .	71
5.1.2	Training with Gradient Descent . . . . .	73
5.2	Track Truth Origin Labelling . . . . .	73
5.3	Fake Track Identification Tool . . . . .	74
5.3.1	Model Inputs . . . . .	76
5.3.2	Model Hyperparameters . . . . .	78
5.3.3	Results . . . . .	79
5.4	<i>b</i> -hadron Track Identification . . . . .	80
5.5	Combined Approach . . . . .	80
5.6	Conclusion . . . . .	82
<b>6</b>	<b>Graph Neural Network Flavour Tagger</b>	<b>84</b>
6.1	Motivation . . . . .	84
6.2	Graph Neural Network Theory . . . . .	86
6.3	Experimental Setup . . . . .	88
6.3.1	Datasets . . . . .	88
6.4	Model Architecture . . . . .	89
6.4.1	Model Inputs . . . . .	89

6.4.2	Auxiliary Training Objectives . . . . .	91
6.4.3	Architecture . . . . .	92
6.4.4	Training . . . . .	96
6.5	Results . . . . .	97
6.5.1	<i>b</i> -tagging Performance . . . . .	98
6.5.2	<i>c</i> -tagging Performance . . . . .	100
6.5.3	Ablations . . . . .	103
6.5.4	Inclusion of Low-Level Vertexing Algorithms . . . . .	105
6.5.5	Jet Display Diagrams . . . . .	105
6.5.6	Vertexing Performance . . . . .	107
6.5.7	Track Classification Performance . . . . .	113
6.6	Futher Studies . . . . .	115
6.6.1	Looser Track Selection . . . . .	115
6.6.2	High Level Trigger . . . . .	116
6.6.3	High Luminosity LHC . . . . .	116
6.7	Conclusion . . . . .	119
<b>7</b>	<b>Boosted VHbb Analysis</b>	<b>123</b>
7.1	Analysis Overview . . . . .	124
7.1.1	Data & Simulated Samples . . . . .	126
7.1.2	Object Reconstruction . . . . .	126
7.1.3	Selection Criteria . . . . .	128
7.1.4	Control Regions . . . . .	129
7.1.5	Background Composition . . . . .	129
7.2	Systematic Uncertainties & Background Modelling . . . . .	132
7.2.1	Implementation of Variations . . . . .	133
7.2.2	Sources of Systematic Modelling Uncertainties . . . . .	134
7.2.3	Sources of Experimental Uncertainties . . . . .	136
7.2.4	Vector Boson + Jets Modelling . . . . .	137
7.2.5	Diboson Modelling . . . . .	141
7.2.6	$t\bar{t}$ and single-top Modelling . . . . .	146
7.2.7	Signal Modelling . . . . .	147
7.3	Statistical Treatment . . . . .	148
7.3.1	Likelihood Function . . . . .	148
7.3.2	Background Normalisations . . . . .	151

7.3.3	Asimov Dataset & Expected Results . . . . .	152
7.4	Results . . . . .	152
7.4.1	Post-fit Distributions . . . . .	153
7.4.2	Post-fit Yields . . . . .	153
7.4.3	Observed Signal Strength & Significance . . . . .	153
7.4.4	Impact of Systematics . . . . .	159
7.4.5	STXS Interpretation . . . . .	163
7.5	Conclusion . . . . .	163
8	Conclusion	165
8.1	Summary . . . . .	165
8.2	Future Work . . . . .	166
	<b>Bibliography</b>	<b>168</b>
	<b>List of figures</b>	<b>183</b>
	<b>List of tables</b>	<b>195</b>

# <sup>2</sup> Chapter 1

## <sup>3</sup> Introduction

- <sup>4</sup> This thesis describes various efforts in improving the understanding of the Higgs  
<sup>5</sup> boson and its coupling to heavy flavour quarks, primarily through the improvement  
<sup>6</sup> of the algorithms used to reconstruct and analyse jets. The thesis is structured in  
<sup>7</sup> the following manner:
- <sup>8</sup> Chapter 2 describes the theoretical foundations of the work presented in the rest of  
<sup>9</sup> the thesis.
- <sup>10</sup> Chapter 3 describes the ATLAS detector and the CERN accelerator complex. Details  
<sup>11</sup> of reconstructed physics objects are also provided.
- <sup>12</sup> Chapter 4 provides an overview of the reconstruction of charged particle tracks  
<sup>13</sup> (tracking) and identification of jets containing  $b$ -hadrons ( $b$ -tagging) at ATLAS, and  
<sup>14</sup> studies into the challenges of high transverse momentum  $b$ -tagging.
- <sup>15</sup> Chapter 5 describes the development of an algorithm to predict the origins of tracks.  
<sup>16</sup> The tool is used to improve  $b$ -tagging performance by the identification and removal  
<sup>17</sup> of fake tracks before their input to the  $b$ -tagging algorithms.
- <sup>18</sup> Chapter 6 introduces a novel monolithic approach to  $b$ -tagging using graph neural  
<sup>19</sup> networks and auxiliary training objectives.
- <sup>20</sup> Chapter 7 describes the measurement of the associated production of a Higgs boson  
<sup>21</sup> decaying into a pair of  $b$ -quarks at high transverse momentum.
- <sup>22</sup> Chapter 8 contains some concluding remarks.

<sup>23</sup> The author's contribution to the work presented in this thesis is as follows.

<sup>24</sup> **Tracking:** The author was an active member of the Cluster and Tracking in Dense  
<sup>25</sup> Environments group throughout their PhD, starting with their qualification task  
<sup>26</sup> on the understanding of tracking performance at high transverse momentum. The  
<sup>27</sup> author played a key role in software r22 validation studies for the tracking group,  
<sup>28</sup> including the validation of the quasi-stable particle interaction simulation and the  
<sup>29</sup> radiation damage Monte-Carlo simulation. The author helped design and improve  
<sup>30</sup> several tracking software frameworks, and contributed to heavy flavour tracking  
<sup>31</sup> efficiency studies in dense environments. The author developed a tool to identify  
<sup>32</sup> and reject fake-tracks, which is being investigated for use in the upcoming tracking  
<sup>33</sup> paper.

<sup>34</sup> ***b*-tagging:** The author has been an active member of the Flavour Tagging group  
<sup>35</sup> since September 2014. The author played a key role in investigating the performance  
<sup>36</sup> of the low level taggers at high transverse momentum and led studies into the  
<sup>37</sup> labelling and classification of track origins. Based on work by Jonathan Shlomi [2],  
<sup>38</sup> the author helped develop a new flavour tagging algorithm which offers a large  
<sup>39</sup> performance improvement with respect to the current state of the art. The author  
<sup>40</sup> was the primary editor of a public note associated with this work [3], which will  
<sup>41</sup> also be further developed in an upcoming paper. The author also contributed to  
<sup>42</sup> the proliferation of the new algorithm to the trigger, High Luminosity LHC, and  
<sup>43</sup>  $X \rightarrow bb$  use cases. The author also played a key role in software r22 validation  
<sup>44</sup> studies for the Flavour Tagging group, including the validation of the quasi-stable  
<sup>45</sup> particle interaction simulation. The author maintains and contributes to various  
<sup>46</sup> software frameworks used in the Flavour Tagging group, including as lead developer  
<sup>47</sup> of three packages, to create training datasets, pre-process samples for algorithm  
<sup>48</sup> studies and a framework for training graph neural networks, and contributes to group  
<sup>49</sup> documentation.

<sup>50</sup> **Higgs:** The author was an active member of the Boosted VHbb analysis group. The  
<sup>51</sup> author performed various studies deriving systematic uncertainties for the  $V+jets$   
<sup>52</sup> and diboson backgrounds. The author also produced and maintained samples, ran fit  
<sup>53</sup> studies and cross checks, and gave the diboson unblinding approval talk to the Higgs  
<sup>54</sup> group. The author also contributed to the development of the analysis software.

55 **Chapter 2**

56 **Theoretical Framework**

57 The Standard Model (SM) of particle physics is the theory describing all known  
58 elementary particles and their interactions via three of the four fundamental forces.

59 Developed by merging the successful theories of quantum mechanics and relativity  
60 in the second half of the 20th century, the SM's position today at the centre of our  
61 understanding of the nature of the Universe is firmly established by an unparalleled  
62 level of agreement between the model predictions and experimental results [4, 5].

63 The SM has predicted the discovery of the top and bottom quarks [6–8], the  $W$   
64 and  $Z$  bosons [9], and the tau neutrino [10]. The last missing piece of the SM to be  
65 discovered was the Higgs boson, first theorised in the 1960s [11–13], and eventually  
66 observed at the LHC in 2012 [14, 15]. After its discovery, much ongoing work has  
67 been carried out performing detailed measurements of its mass and interactions with  
68 other particles.

69 In this chapter, an overview of the SM is given in Section 2.1, and a more detailed  
70 discussion of the Higgs sector and Higgs phenomenology is provided in Section 2.2.

71 **2.1 The Standard Model**

72 The SM is formulated in the language of Quantum Field Theory (QFT). In this  
73 framework, particles are localised excitations of corresponding quantum fields, which  
74 are operator-valued distributions across spacetime.

75 Central to QFT is the Lagrangian density which describes the kinematics and  
 76 dynamics of a field. Observations of conserved quantities are linked, via Noether's  
 77 theorem, to symmetries which are expressed by the Lagrangian. Alongside Global  
 78 Poincaré symmetry, the SM Lagrangian observes a local non-Abelian  $SU(3)_C \otimes$   
 79  $SU(2)_L \otimes U(1)_Y$  gauge symmetry. Gauge symmetries leave observable properties of  
 80 the system unchanged when the corresponding gauge transformations are applied  
 81 to the fields. The full Lagrangian of the SM can be broken up into distinct terms  
 82 corresponding to the different sectors, as in Eq. (2.1). An overview of each sector is  
 83 given in the following chapters.

$$\mathcal{L}_{\text{SM}} = \mathcal{L}_{\text{EW}} + \mathcal{L}_{\text{QCD}} + \mathcal{L}_{\text{Higgs}} + \mathcal{L}_{\text{Yukawa}} \quad (2.1)$$

84 The SM provides a mathematical description of how three of the four fundamental  
 85 forces interact with the matter content of the Universe. The particle content of the  
 86 SM consists of spin-1/2 fermions, listed in Table 2.1, and integral spin bosons listed  
 in Table 2.2.

<b>Generation</b>	Leptons			Quarks		
	<b>Flavour</b>	<b>Mass [MeV]</b>	<b>Charge [e]</b>	<b>Flavour</b>	<b>Mass [MeV]</b>	<b>Charge [e]</b>
First	$e$	0.511	-1	$u$	2.16	$2/3$
	$\nu_e$	$< 1.1 \times 10^{-6}$	0	$d$	4.67	$-1/3$
Second	$\mu$	105.7	-1	$c$	$1.27 \times 10^3$	$2/3$
	$\nu_\mu$	$< 0.19$	0	$s$	93.4	$-1/3$
Third	$\tau$	1776.9	-1	$t$	$173 \times 10^3$	$2/3$
	$\nu_\tau$	$< 18.2$	0	$b$	$4.18 \times 10^3$	$-1/3$

**Table 2.1:** The fermions of the SM [16]. Three generations of particles are present. Also present (unlisted) are the antiparticles, which are identical to the particles up to a reversed charge sign.

87

### 88 2.1.1 Quantum Electrodynamics

89 Quantum electrodynamics (QED) is the relativistic quantum theory which describes  
 90 the interactions between the photon and charged matter. Consider a Dirac spinor  
 91 field  $\psi = \psi(x)$  and its adjoint  $\bar{\psi} = \psi^\dagger \gamma^0$ , where  $\psi^\dagger$  denotes the Hermitian conjugate

Name	Symbol	Mass [GeV]	Charge [ $e$ ]	Spin
Photon	$\gamma$	$< 1 \times 10^{-27}$	$< 1 \times 10^{-46}$	1
Charged Weak boson	$W^\pm$	$80.377 \pm 0.012$	$\pm 1$	1
Neutral Weak boson	$Z$	$91.1876 \pm 0.0021$	0	1
Gluon	$g$	0	0	1
Higgs	$H$	$125.25 \pm 0.17$	0	0

**Table 2.2:** The bosons of the SM [16]. The photon, weak bosons and gluons are gauge bosons arising from gauge symmetries, and carry the four fundamental forces of the SM. The recently discovered Higgs boson is the only fundamental scalar particle in the SM.

of  $\psi$ . The field  $\psi$  describes a fermionic spin-1/2 particle, for example an electron. The Dirac Lagrangian density is

$$\mathcal{L}_{\text{Dirac}} = \bar{\psi}(i\cancel{\partial} - m)\psi, \quad (2.2)$$

where  $\cancel{\partial} = \gamma^\mu \partial_\mu$  denotes the contraction with the Dirac gamma matrices  $\gamma^\mu$  (summation over up-down pairs of indices is assumed). Application of the Euler-Lagrange equation on Eq. (2.2) yields the Dirac equation

$$(i\cancel{\partial} - m)\psi = 0. \quad (2.3)$$

Suppose some fundamental symmetry that requires invariance under a local  $U(1)$  gauge transformation

$$\psi \rightarrow \psi' = \psi e^{-iq\alpha(x)}, \quad (2.4)$$

where  $\alpha$  varies over every spacetime point  $x$ . Under this transformation, the Dirac equation transforms as

$$(i\cancel{\partial} - m)\psi e^{-iq\alpha(x)} + q\cancel{\partial}\alpha(x)\psi e^{-iq\alpha(x)} = 0. \quad (2.5)$$

For the Dirac equation to remain invariant under the transformation in Eq. (2.4), a new field  $A_\mu$  which transforms as  $A_\mu \rightarrow A'_\mu = A_\mu + \partial_\mu\alpha(x)$  must be added. The transformed interaction term

$$-q\cancel{A}\psi \rightarrow -q\cancel{A}\psi e^{-iq\alpha(x)} - q\cancel{\partial}\alpha(x)\psi e^{-iq\alpha(x)} \quad (2.6)$$

104 will then cancel the asymmetric term in Eq. (2.5) as required. The  $U(1)$  invariant  
105 Lagrangain can therefore be constructed by adding an interaction between the  $\psi$   
106 and  $A_\mu$  fields to Eq. (2.2). For completeness, the kinetic term for the the new field  
107  $A_\mu$  is also added in terms of  $F_{\mu\nu} = \partial_\mu A_\nu - \partial_\nu A_\mu$ , which is trivially invariant under  
108 the transformation in Eq. (2.4). The interaction term is typically absorbed into the  
109 covariant derivative  $D_\mu = \partial_\mu + iqA_\mu$ , thus named as it transforms in the same way as  
110 the field  $\psi$ . Collecting these modifications to Eq. (2.2) yields the QED Lagrangain

$$\mathcal{L}_{\text{QED}} = -\frac{1}{4}F_{\mu\nu}F^{\mu\nu} + \bar{\psi}(iD^\mu - m)\psi. \quad (2.7)$$

111 The quadratic term  $A_\mu A^\mu$  is not invariant and therefore the the field  $A_\mu$  must be  
112 massless. Requiring invariance under local  $U(1)$  gauge transformations necessitated  
113 the addition of a new field  $A_\mu$ , interpreted as the photon field, which interacts with  
114 charged matter. In the SM, the QED Lagrangian is absorbed into the electroweak  
115 sector, discussed in Section 2.1.3.

### 116 2.1.2 Quantum Chromodynamics

117 Quantum Chromodynamics (QCD) is the study of quarks, gluons and their interac-  
118 tions. Quarks and gluons carry colour charge, which comes in three kinds, called  
119 red, green and blue. While the  $U(1)$  symmetry group in Section 2.1.1 was Abelian,  
120 the QCD Lagrangian is specified by requiring invariance under transformations from  
121 the non-Abelian  $SU(3)$  group, making it a Yang-Mills theory [17] which requires the  
122 addition of self-interacting gauge fields. The infinitesimal  $SU(3)$  group generators  
123 are given by  $T_a = \lambda_a/2$ , where  $\lambda_a$  are the eight Gell-Mann matrices. These span the  
124 space of infinitesimal group transformations and do not commute with each other,  
125 instead satisfying the commutation relation

$$[T_a, T_b] = if_{abc}T_c, \quad (2.8)$$

126 where  $f_{abc}$  are the group's structure constants. Consider the six quark fields  $q_k = q_k(x)$ .  
127 Each flavour of quark  $q_k$  transforms in the fundamental triplet representation, in  
128 which each component of the triplet corresponds to the colour quantum number  
129 for red, green and blue colour charged respectively.  $G_{\mu\nu}^a$  are the eight gluon field

<sup>130</sup> strength tensors, one for each generator  $T_a$ , defined as

$$G_{\mu\nu}^a = \partial_\mu A_\nu - \partial_\nu A_\mu - g_s f^{abc} A_\mu^b A_\nu^c, \quad (2.9)$$

<sup>131</sup> where  $A_\mu^a$  are the gluon fields and  $g_s$  is the strong coupling constant. The covariant  
<sup>132</sup> derivative is written as

$$D_\mu = \partial_\mu + ig_s T_a A_\mu^a. \quad (2.10)$$

<sup>133</sup> The full QCD Lagrangian is then given by

$$\mathcal{L}_{\text{QCD}} = -\frac{1}{4} G_{\mu\nu}^a G_a^{\mu\nu} + q_k (i \not{D} - m_k) q_k. \quad (2.11)$$

<sup>134</sup> Cubic and quartic terms of the gauge fields  $A_\mu^a$  appear in the Lagrangian, leading to  
<sup>135</sup> the gluon's self interaction.

<sup>136</sup> The QCD coupling constant  $g_s$  varies, or “runs”, with energy. At lower energy scales  
<sup>137</sup> (and corresponding larger distance scales) the interaction is strong. This leads to  
<sup>138</sup> quark confinement, whereby an attempt to isolate individual colour-charged quarks  
<sup>139</sup> requires so much energy that additional quark-antiquark pairs are produced. At  
<sup>140</sup> higher energy scales (and corresponding smaller distance scales), asymptotic freedom  
<sup>141</sup> occurs as the interactions become weaker, allowing perturbative calculations to be  
<sup>142</sup> performed. Hadrons are bound states of quarks. They are invariant under  $SU(3)$   
<sup>143</sup> gauge transformations (i.e. are colour-charge neutral, or *colourless*).

### <sup>144</sup> 2.1.3 The Electroweak Sector

<sup>145</sup> The weak and electromagnetic forces are unified in the Glashow-Weinberg-Salam  
<sup>146</sup> (GWS) model of electroweak interaction [18–20]. The Lagrangian is specified by  
<sup>147</sup> requiring invariance under the symmetry group  $SU(2)_L \otimes U(1)_Y$ , as motivated by a  
<sup>148</sup> large amount of experimental data. Here,  $SU(2)_L$  is referred to as weak isospin and  
<sup>149</sup>  $U(1)_Y$  as weak hypercharge.

150 The generators of  $SU(2)_L$  are  $T_a = \sigma_a/2$ , where  $\sigma_a$  are the three Pauli spin matrices  
151 which satisfy the commutation relation

$$[T_a, T_b] = i\varepsilon_{abc}T_c. \quad (2.12)$$

152 The generator of  $U(1)_Y$  is  $Y = 1/2$ . Each generator corresponds to a gauge field,  
153 which, after symmetry breaking (discussed in Section 2.2), give rise to the massive  
154 vector bosons,  $W^\pm$  and  $Z$ , and the massless photon. The massive vector bosons  
155 are the carriers of the weak force. Due to the mass of the force carriers, the weak  
156 force has a short range and so it appears weak even though its intrinsic strength is  
157 comparable to that of QED.

158 The charge operator  $Q$  can be written as a combination of the third  $SU(2)_L$  generator  
159 and the  $U(1)_Y$  generator as in

$$Q = T_3 + Y. \quad (2.13)$$

160 The weak force violates parity conservation [21–23], i.e. invariance under parity  
161 transformations (mirror reflections). Only left handed fermions participate in the  
162 weak interaction. Since there is no other force through which neutrinos interact with  
163 other particles, there are no right handed neutrinos in the Standard Model.

## 164 2.2 The Higgs Mechanism

165 The Brout-Englert-Higgs mechanism (henceforth just the “Higgs mechanism”) is the  
166 process through which the fundamental particles of the SM acquire mass [11–13].  
167 Experimentally it was known that the weak force had a low effective strength, which  
168 was suggestive of a massive mediating gauge particle. However, directly adding  
169 mass to the weak gauge bosons violates the non-Abelian symmetry of the SM.  
170 Instead, the gauge bosons gain mass through the interaction with a scalar Higgs  
171 field which results from the spontaneous breakdown of symmetry as discussed in  
172 Section 2.2.1. Similarly, the Higgs mechanism gives mass to the fermions, as discussed  
173 in Section 2.2.2. Section 2.2.3 described some basic phenomenology of the Higgs  
174 particle relevant to hadron colliders.

### <sup>175</sup> 2.2.1 Electroweak Symmetry Breaking

<sup>176</sup> Spontaneous symmetry breaking (SSB) is a key part of the Higgs mechanism. It  
<sup>177</sup> is the transition of a physical system from a state of manifest symmetry to a state  
<sup>178</sup> of hidden, or *broken*, symmetry. In particular, this applies to physical systems  
<sup>179</sup> where the Lagrangian observes some symmetry, but the lowest energy vacuum states  
<sup>180</sup> do not exhibit that same symmetry. In other words, the symmetry is broken for  
<sup>181</sup> perturbations around the vacuum state.

<sup>182</sup> Consider the case in which the gauge fields from the local  $SU(2)_L \otimes U(1)_Y$  symmetry  
<sup>183</sup> group (discussed in Section 2.1.3) are coupled to a complex scalar field  $\phi = \phi(x)$ ,  
<sup>184</sup> transforms as a weak isospin doublet. Omitting the kinetic term of the gauge fields,  
<sup>185</sup> and writing  $\phi^2 \equiv \phi^\dagger \phi$ , the Lagrangain is

$$\mathcal{L}_{\text{Higgs}} = (D_\mu \phi)^\dagger (D^\mu \phi) - [\mu^2 \phi^2 + \lambda \phi^4], \quad (2.14)$$

<sup>186</sup> where the covariant derivative is given by

$$D_\mu = \partial_\mu + igA_\mu^a T^a + ig'B_\mu, \quad (2.15)$$

<sup>187</sup> and  $T^a$  are the generators of  $SU(2)$ . The potential term  $V(\phi)$  is made up of a  
<sup>188</sup> quadratic and quartic term in the scalar field  $\phi$ , which each contain an arbitrary  
<sup>189</sup> parameter, respectively  $\lambda$  and  $\mu$ . The quartic term gives the field self-interaction, and  
<sup>190</sup> cannot be negative as this would lead to a potential that was unbounded from below.  
<sup>191</sup> The quadratic term can be positive or negative. In the case where the quadratic term  
<sup>192</sup> is positive, it is interpreted as a mass term for the scalar field. By choosing  $\mu^2 < 0$   
<sup>193</sup> the field becomes unphysical due to its negative mass. The shape of the potential in  
<sup>194</sup> this case is shown in Fig. 2.1. Note that in the case of the Standard Model, the scalar  
<sup>195</sup> field  $\phi$  is a complex doublet, and so the corresponding potential is 5-dimensional.  
<sup>196</sup> In order to obtain a physical interpretation of the Lagrangain in Eq. (2.14) for the  
<sup>197</sup> case where  $\mu^2 < 0$ , the field  $\phi$  is expanded around the vacuum state. The vacuum  
<sup>198</sup> expectation value (VEV) is the expected value of the field  $\phi$  which minimises the  
<sup>199</sup> potential  $V(\phi)$  (equivalently the expected value of the field operator  $\phi$  when the  
<sup>200</sup> system is in a vacuum state,  $|\langle \phi \rangle_0|^2 \equiv |\langle 0 | \phi | 0 \rangle|^2 \equiv \phi_0^2$ ). Minimising the potential

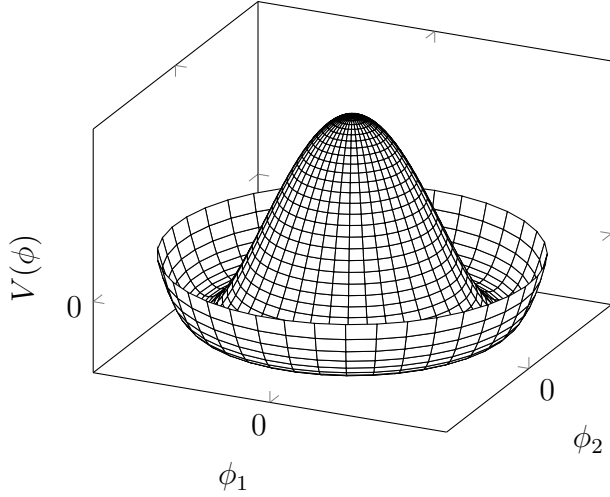


**Figure 2.1:** The Higgs potential  $V(\phi)$  of the complex scalar field singlet  $\phi = \phi_1 + i\phi_2$ , with a choice of  $\mu^2 < 0$  leading to a continuous degeneracy in the true vacuum states. A false vacuum is present at the origin.

201 gives a VEV of

$$\phi_0^2 = -\mu^2/\lambda = v^2. \quad (2.16)$$

202 Due to the shape of the potential in Fig. 2.1, there is a degeneracy in the direction  
203 that the complex doublet  $\phi$  points. As all the different vacuum states minimise  
204 the potential and therefore yield identical physics, one can arbitrarily choose the  
205 state to lie along the second component of the doublet. Application of Eq. (2.13)  
206 shows this choice is manifestly invariant under the charge operator. This allows  
207 the identification of the unbroken subgroup  $U(1)_Q$ , under which the ground state is  
208 invariant. The generator of  $U(1)_Q$  is the charge operator  $Q$ .

209 Adding the particle content back to the theory by expanding the field around the  
210 vacuum state, and making a transformation to the unitary gauge to remove unphysical  
211 Nambu-Goldstone modes (which arise in the context of global symmetries [24, 25]),  
212 yields

$$\phi = \frac{1}{\sqrt{2}} \begin{bmatrix} 0 \\ v + H \end{bmatrix}, \quad (2.17)$$

where  $H$  is a real scalar field, the *true vacuum* Higgs field. Substituting this into Eq. (2.14) and identifying physical fields from the quadratic terms of linear combinations of unphysical fields, one can write the physical fields  $W_\mu^\pm$ ,  $Z_\mu$  and  $A_\mu$  in terms of the original fields  $A_\mu^a$  and  $B_\mu$ . This gives

$$W_\mu^\pm = \frac{1}{\sqrt{2}}(A_\mu^1 \mp iA_\mu^2) \quad \begin{bmatrix} A_\mu \\ Z_\mu \end{bmatrix} = \begin{bmatrix} \cos \theta_W & \sin \theta_W \\ -\sin \theta_W & \cos \theta_W \end{bmatrix} \begin{bmatrix} B_\mu \\ A_\mu^3 \end{bmatrix}. \quad (2.18)$$

where  $\theta_W$  is the weak mixing angle defined by

$$\cos \theta_W = \frac{g}{\sqrt{g^2 + g'^2}}. \quad (2.19)$$

The corresponding masses of the now massive vector bosons can be read off as

$$m_W = \frac{1}{2}gv \quad m_Z = \frac{m_W}{\cos \theta_W}, \quad (2.20)$$

while the photon remains massless. The Higgs mass is  $m_H = v\sqrt{\lambda} = \mu$ .

This is the Higgs mechanism. It maintains the renormalisability and unitarity of the SM whilst allowing the weak vector bosons to acquire mass. In summary, an unphysical complex scalar field  $\phi$  with a nonzero VEV leads to spontaneous symmetry breaking. Due to the non-Abelian symmetry breaking, would-be massless Nambu-Goldstone modes, which arise after expansion around the true vacuum state, are cancelled out by making a local gauge transformation to the unitary gauge, and instead are absorbed by the vector bosons, allowing them to acquire mass.

This sector of the SM contains four fundamental parameters that must be determined from experiment. These can be specified by the Lagrangian parameters  $g$ ,  $g'$ ,  $v$  and  $\lambda$  or the physically measurable parameters  $m_Z$ ,  $\sin \theta_W$ ,  $m_H$  and  $e$ . In the local neighbourhood around the true vacuum, the macroscopic symmetry of the system is not realised, and therefore the physical particles do not obey the original symmetry. However, information about the symmetry is retained through some additional constraints on the parameters of the theory. Prior to symmetry breaking, the potential contained two terms and two constants. After symmetry breaking there are three terms but still only two constants that relate these terms. This is the vestige of the original symmetry.

237 Spontaneous symmetry breaking has modified the original symmetry group of the SM  
238  $SU(2)_L \times U(1)_Y \rightarrow SU(3)_C \otimes U(1)_Q$ . Three broken generators from the symmetry  
239 group  $SU(2)_L \times U(1)_Y$  have been absorbed into the definition of the physical weak  
240 vector bosons, giving them mass. The same methodology can be used to generate  
241 the fermion masses, as shown in the next section.

### 242 2.2.2 Fermionic Yukawa Coupling

243 Adding the masses of the fermions by hand breaks the gauge invariance of the  
244 theory. Instead, we can use a Yukawa coupling between the fermion fields and the  
245 Higgs field in order to generate mass terms after spontaneous electroweak symmetry  
246 breakdown [19]. In this way, the fermion masses are determined by both the respective  
247 couplings to the Higgs field and the VEV of the Higgs field itself, which sets the  
248 basic mass scale of the theory.

249 The Higgs field  $\phi$  transforms as an  $SU(2)$  doublet with  $Y = 1/2$ , as does the left-  
250 handed fermion field  $\psi_L$ . The right-handed fermion field  $\psi_R$  transforms as an  $SU(2)$   
251 singlet.

### 252 Charged Lepton Masses

253 The renormalisable and gauge invariant coupling between a fermionic field  $\psi$  and a  
254 scalar Higgs field  $\phi$  can be written as

$$\mathcal{L}_{\text{Yukawa}} = -g_f(\bar{\psi}_L \phi \psi_R + \bar{\psi}_R \phi^\dagger \psi_L). \quad (2.21)$$

255 where  $\psi_L = (\nu_L, e_L)$  and  $\psi_R = e_R$  for the first generation leptons. After spontaneous  
256 symmetry breaking (see Section 2.2.1), the scalar Higgs field in unitary gauge  
257 Eq. (2.17) consists of a VEV and the true vacuum Higgs field  $H$ . Substituting this  
258 in to Eq. (2.21) yields

$$\mathcal{L}_{\text{Yukawa}} = -\frac{v g_e}{\sqrt{2}} \bar{e} e - \frac{g_e}{\sqrt{2}} \bar{e} H e, \quad (2.22)$$

259 using  $\bar{e} e = (\bar{e}_L + \bar{e}_R)(e_L + e_R) = \bar{e}_L e_R + \bar{e}_R e_L$ . The VEV component of  $\phi$  provides  
260 the first term in Eq. (2.22) which is quadratic in the electron field, and can therefore

261 be identified as the electron mass term. An interaction term between the electron  
 262 field  $e$  and the true vacuum Higgs field  $H$  is also present. Mass is generated for the  
 263 other charged lepton generations in the same way.

264 **Quark Masses**

265 The down-type quarks acquire their mass analogous to the leptons, with  $\psi_L = (u_L, d_L)$   
 266 and  $\psi_R = d_R$  for the first quark generation. Mass is generated for the up-type quarks  
 267 using the conjugate field to  $\phi$  which transforms under  $SU(2)$  as a doublet with  
 268  $Y = -1/2$ . The conjugate field  $\tilde{\phi}$  is constructed as

$$\tilde{\phi} = i\sigma_2 \phi^\dagger = \begin{bmatrix} 0 & 1 \\ -1 & 0 \end{bmatrix} \begin{bmatrix} \phi_1^\dagger \\ \phi_2^\dagger \end{bmatrix} = \frac{1}{\sqrt{2}} \begin{bmatrix} v + H \\ 0 \end{bmatrix}, \quad (2.23)$$

269 and transforms in the same way as  $\phi$ . This field can be used to write an additional  
 270 Yukawa coupling which provides mass for the up-type quarks in a similar way as  
 271 before.

$$\mathcal{L}_{\text{Yukawa}}^{\text{up}} = -g_q (\bar{\psi}_L \tilde{\phi} \psi_R + \bar{\psi}_R \tilde{\phi}^\dagger \psi_L) \quad (2.24)$$

272 Considering the first generation of up-type quarks with  $\psi_L = (u_L, d_L)$  and  $\psi_R = u_R$ ,  
 273 substitution into Eq. (2.24) yields

$$\mathcal{L}_{\text{Yukawa}}^{\text{up}} = -\frac{vg_u}{\sqrt{2}} \bar{u}u - \frac{g_u}{\sqrt{2}} \bar{u}Hu. \quad (2.25)$$

274 The Yukawa terms mix quarks of different generations. Physical particles are detected  
 275 in their mass eigenstates  $q$ , which diagonalise the mass matrix, but interact via the  
 276 weak interaction according to their weak eigenstates  $\tilde{q}$ , which are superpositions  
 277 of the mass eigenstates. This feature of the weak sector leads to mixing between  
 278 different generations of quarks. Quark mixing can be expressed using the Cabibbo-  
 279 Kobayashi-Maskawa (CKM) matrix, which specifies the strength of flavour-changing  
 280 weak currents. The entries in the matrix are enumerated as

$$\begin{bmatrix} \tilde{d} \\ \tilde{s} \\ \tilde{b} \end{bmatrix} = \begin{bmatrix} V_{ud} & V_{us} & V_{ub} \\ V_{cd} & V_{cs} & V_{cb} \\ V_{td} & V_{ts} & V_{tb} \end{bmatrix} \begin{bmatrix} d \\ s \\ b \end{bmatrix}, \quad (2.26)$$

281 where the size of the elements  $|V_{pq}|^2$  measures the probability of a transition between  
282 states  $p$  and  $q$ .

### 283 2.2.3 Higgs Sector Phenomenology

284 As previously discussed in this chapter, the Higgs field plays a key role in the SM  
285 by giving mass to fundamental particles. The strength of the coupling between  
286 the Higgs field and another particle is proportional to that particle's mass. This  
287 fact dictates which production mechanisms and decay modes are dominant at the  
288 LHC. The cross sections for different production mechanisms at a centre of mass  
289 energy  $\sqrt{s} = 13 \text{ TeV}$  are shown as a function of the Higgs mass  $m_H$  in Fig. 2.2. At  
290 leading order in QCD, Higgs boson production occurs mainly through four modes,  
291 shown in Fig. 2.3. The dominant production mode is gluon-gluon fusion ( $pp \rightarrow H$ ),  
292 which is predominantly mediated by a virtual top quark loop. Vector boson fusion  
293 ( $pp \rightarrow qqH$ ) is the second most likely production mechanism, in which a pair of  
294  $W$  or  $Z$  bosons fuse to produce a Higgs after being radiated by two quarks. Next  
295 most common is the associated production of a Higgs boson and a vector boson  
296 ( $pp \rightarrow VH$ ), in which a pair of quarks fuse to produce a single  $W$  or  $Z$  boson which  
297 radiates a Higgs. The final of the four leading production modes is top quark fusion,  
298 in which two gluons each radiate a quark-antiquark pair, and a quark from each pair  
299 fuses to produce a Higgs boson.

300 Although gluon-gluon fusion is the dominant production mode, for hadronic decays  
301 of the Higgs boson the associated production with a vector boson has the advantage  
302 of leading to a more distinct signature due to the likelihood of the vector bosons  
303 decaying leptons. Leptons provide a clean signals to detect and trigger on.

304 Since the Higgs boson couples proportional to mass, decays to heavier particles are  
305 favoured. The branching ratios of different Higgs boson decay modes are shown  
306 as a function of  $m_H$  in Fig. 2.4. Approximately 58% of the time the Higgs boson  
307 decays to a pair of  $b$ -quarks, the dominant decay mode. The next most likely decay  
308 mode is to a pair of  $W$  bosons, which occurs approximately 20% of the time. After  
309 the  $b$ -quark, the next heaviest fermions are the tau lepton and the  $c$ -quark, decays  
310 to pairs of these particles happen approximately an order of magnitude less often.  
311 Decays to pairs of vector bosons are via a virtual off shell Higgs boson only. While  
312 the  $H \rightarrow \gamma\gamma$  and  $H \rightarrow ZZ$  branching ratios are small compared with fermionic decay

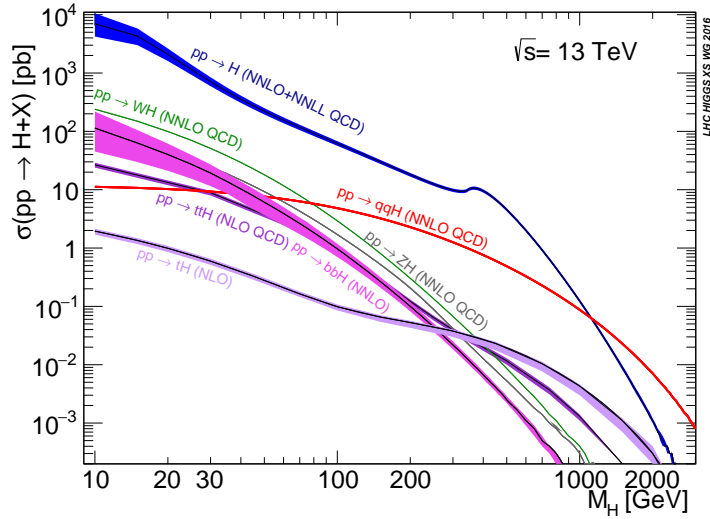


**Figure 2.2:** Higgs boson production cross sections as a function of Higgs mass ( $m_H$ ) at  $\sqrt{s} = 13 \text{ TeV}$  [26]. Uncertainties are shown in the shaded bands. At  $m_H = 125 \text{ GeV}$ , Higgs boson production is dominated by gluon-gluon fusion, vector boson fusion, associated production with vector bosons, and top quark fusion.

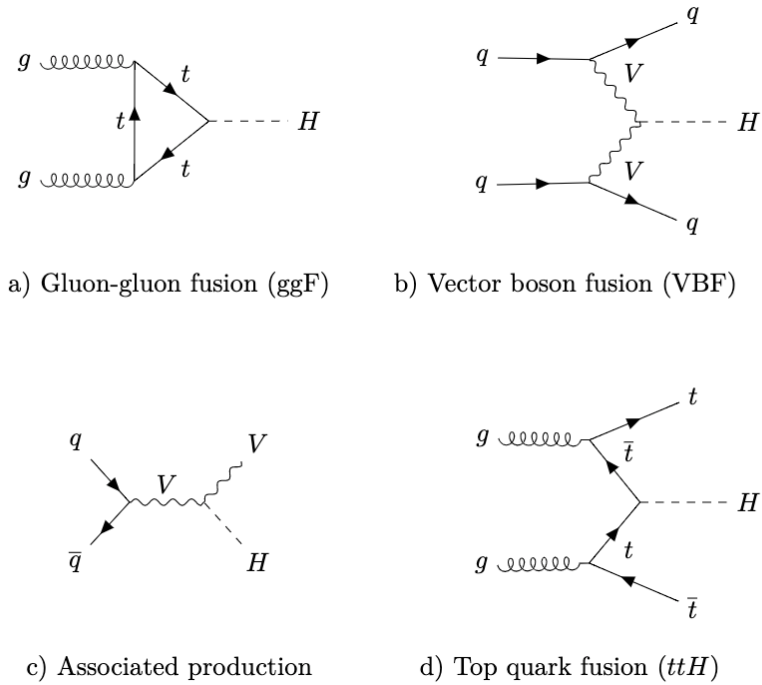


**Figure 2.3:** Diagrams for the four main Higgs boson production modes at the LHC for a Higgs mass  $m_H = 125 \text{ GeV}$  at a centre of mass energy  $\sqrt{s} = 13 \text{ TeV}$ .

<sup>313</sup> modes (around 0.2% for  $H \rightarrow \gamma\gamma$ ), these decay channels were instrumental in the  
<sup>314</sup> initial discovery of the Higgs due to the low level of background processes which  
<sup>315</sup> mimic the final state [14, 15].

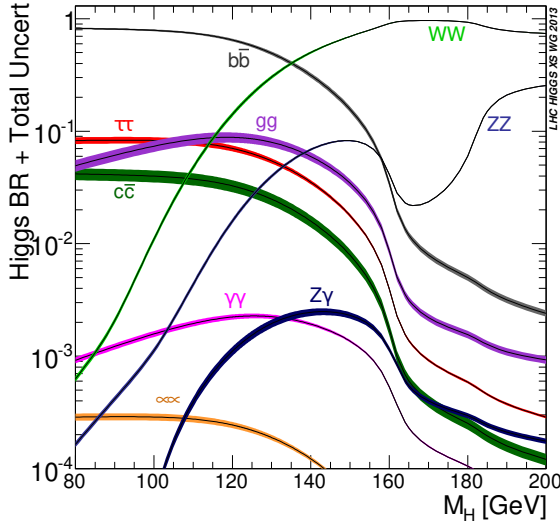


**Figure 2.4:** Higgs boson branching ratios as a function of Higgs mass ( $m_H$ ) at  $\sqrt{s} = 13$  TeV [26]. Uncertainties are shown in the shaded bands. At  $m_H = 125$  GeV, the Higgs predominantly decays to a pair of  $b$ -quarks, around 58% of the time. The leading subdominant decay mode is to a pair of  $W$  bosons.

<sup>316</sup> This thesis presents a measurement of the Higgs bosons production rate using events  
<sup>317</sup> with a Higgs boson produced in association with vector boson and decaying to a pair  
<sup>318</sup> of  $b$ -quarks, i.e.  $pp \rightarrow VH(b\bar{b})$ . The  $H \rightarrow b\bar{b}$  decay mode directly probes the Higgs  
<sup>319</sup> coupling to fermions, and more specifically to the bottom quark. This coupling was  
<sup>320</sup> first observed in 2018 [27, 28]. Ongoing work measuring the coupling strengths, in  
<sup>321</sup> particular in the high energy regime, is the focus of the analysis presented in this  
<sup>322</sup> thesis in Chapter 7.

323 Chapter 3

324 The Large Hadron Collider and the  
325 ATLAS Detector

326 Since the completion of its construction in 2008, the Large Hadron Collider (LHC) [29]  
327 at CERN has extended the frontiers of particle physics through significant increases  
328 in centre of mass energy and luminosity compared with previous collider experiments.  
329 The LHC accelerates bunches of protons around a 27 km ring until they are travelling  
330 just  $3\text{ m s}^{-1}$  slower than the speed of light, at which point they are made to  
331 collide. The proton bunches travel round the ring 11,000 times per second in two  
332 concentric beams, which are guided by superconducting magnets cooled using liquid  
333 helium to  $-271.3^\circ\text{C}$  (1.9 K). The beams travel in opposite directions around the  
334 ring and are crossed at four locations so that collisions between protons can take  
335 place. Around these collision points four specialised detectors, ALICE [30], CMS [31],  
336 LHCb [32] and ATLAS [33], are located to capture information about the products  
337 of the collisions.

338 In this chapter, a brief overview of the LHC and the accelerator complex at CERN  
339 is given in Section 3.1. The coordinate system used at the ATLAS detector and  
340 other common definitions are introduced in Section 3.2. An overview of the different  
341 detector systems is provided in Section 3.3, and finally descriptions of various  
342 commonly used reconstructed objects is given in Section 3.4.

### <sup>343</sup> 3.1 The Large Hadron Collider

<sup>344</sup> The LHC is operated in multi-year *runs* during which beams of protons are circulated  
<sup>345</sup> and collided. Between runs there are periods of shutdown while the accelerator and  
<sup>346</sup> detector machinery is maintained and upgraded. Run 1 began in 2010 when the LHC  
<sup>347</sup> collided proton bunches, each containing more than  $10^{11}$  particles, 20 million times  
<sup>348</sup> per second, providing 7 TeV proton-proton collisions at instantaneous luminosities  
<sup>349</sup> of up to  $2.1 \times 10^{32} \text{ cm}^{-2} \text{ s}^{-1}$ . The centre-of-mass energy was increased to 8 TeV  
<sup>350</sup> in 2012. Over the course of Run 1,  $26.4 \text{ fb}^{-1}$  of usable integrated luminosity was  
<sup>351</sup> recorded. Run 2, which spanned 2015–2018, further increased the the proton-proton  
<sup>352</sup> collision energy to 13 TeV. During Run 2 the bunch spacing was reduced, leading  
<sup>353</sup> to a collision rate of 40 MHz. Over the course of Run 2 a total usable integrated  
<sup>354</sup> luminosity of  $139 \text{ fb}^{-1}$  was recorded. 2022 marked the beginning of Run 3 which,  
<sup>355</sup> with a higher center of mass energy and peak luminosity, is expected to culminate in  
<sup>356</sup> an approximate tripling of the dataset size. A summary of key information about  
<sup>357</sup> each run is listed in Table 3.1.

Period	Year	$\sqrt{s}$ [TeV]	$\langle \mu \rangle$	Bunch spacing [ns]	Luminosity [ $\text{cm}^{-2} \text{ s}^{-1}$ ]
Run 1	2010–2012	7–8	18	50–150	$8 \times 10^{33}$
Run 2	2015–2018	13	34	25	$1\text{--}2 \times 10^{34}$
Run 3	2022–2025	13.6	50	25	$2 \times 10^{34}$

**Table 3.1:** Overview of the different LHC runs [34,35]. The average number of interactions per bunch-crossing is denoted as  $\langle \mu \rangle$  (see Section 3.2.3), and is here averaged over the entire run. The luminosity is the peak instantaneous luminosity. Numbers for Run 3 are preliminary and are only provided to give an indication of expected performance.

<sup>358</sup> An overview of the accelerator complex at CERN is shown in Fig. 3.1. The LHC is  
<sup>359</sup> at the final stage of a chain of accelerators which incrementally step-up the energy  
<sup>360</sup> of incoming protons. The first accelerator is Linac2 (which has been replaced by  
<sup>361</sup> Linac4 in 2020), a linear accelerator which accelerates negative hydrogen ions to an  
<sup>362</sup> energy of 160 MeV. Upon leaving Linac4, the ions are stripped of both electrons  
<sup>363</sup> and the resulting protons are fed into the Proton Synchrotron Booster (PSB), which  
<sup>364</sup> increases the energy of the protons to 2 GeV. The protons leaving the PSB are passed  
<sup>365</sup> to the Proton Synchrotron (PS), which increases the energy to 26 GeV, and then  
<sup>366</sup> from the PS to the Super Proton Synchrotron (SPS) which further increases the

367 energy to 450 GeV. Finally, the proton beams are injected in the LHC where they  
 368 are accelerated to their final energy of 6.5 TeV (for Run 2).

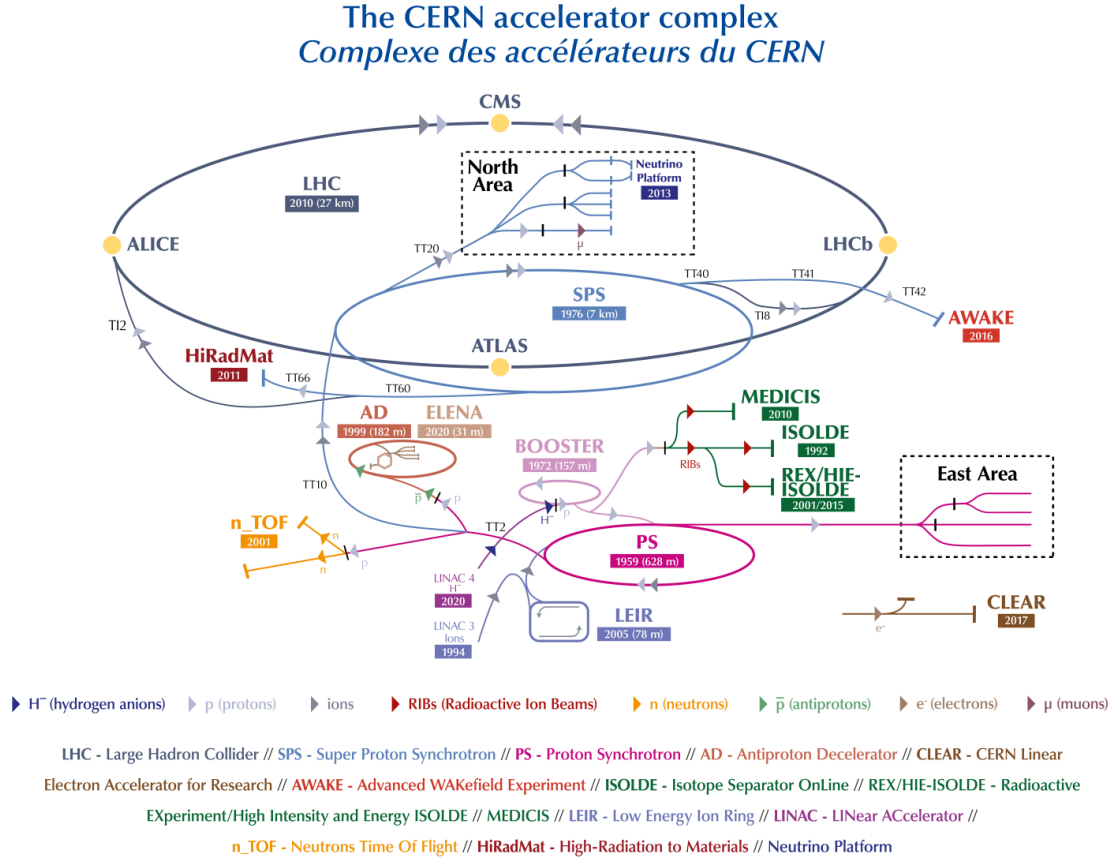


**Figure 3.1:** An overview of the CERN accelerator complex [36]. The LHC is fed by a series of accelerators starting with Linac2 (or Linac4 from 2020). Next are the Proton Synchrotron Booster, the Proton Synchrotron, and finally the Super Proton Synchrotron which injects protons into the LHC.

## 369 3.2 Coordinate System & Collider Definitions

370 In Section 3.2.1, the coordinate system used at ATLAS is introduced. The parame-  
 371 terisation used for specifying the trajectory of charged particle tracks is described in  
 372 Section 3.2.2, and definitions for some frequently occurring concepts and quantities  
 373 is provided in Section 3.2.3.

### <sup>374</sup> 3.2.1 ATLAS Coordinate System

<sup>375</sup> The origin of the coordinate system used by ATLAS is the nominal interaction point  
<sup>376</sup> in the centre of the detector. As shown in Fig. 3.2, the  $z$ -axis points along the  
<sup>377</sup> direction of the beam pipe, while the  $x$ -axis points from the interaction point to the  
<sup>378</sup> centre of the LHC ring, and the  $y$ -axis points upwards. The transverse plane lies  
<sup>379</sup> in  $x$ - $y$  while the longitudinal plane lies along the  $z$ -axis. A cylindrical coordinate  
<sup>380</sup> system with coordinates  $(r, \phi)$  is used in the transverse plane, where  $r$  is the radius  
<sup>381</sup> from the origin and  $\phi$  is the azimuthal angle around the  $z$ -axis.

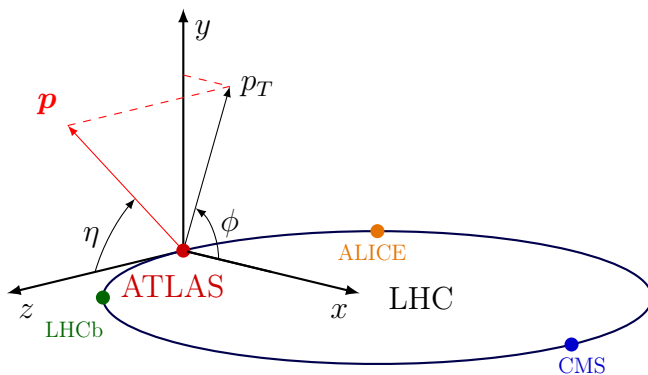


**Figure 3.2:** The coordinate system used at the ATLAS detector, showing the locations of the four main experiments located at various points around the LHC. The 3-vector momentum  $\mathbf{p} = (p_x, p_y, p_z)$  is shown by the red arrow. Reproduced from Ref. [37].

<sup>382</sup> The polar angle  $\theta$  is commonly specified in terms of the pseudorapidity  $\eta$ , defined as

$$\eta = -\ln \left[ \tan \left( \frac{\theta}{2} \right) \right]. \quad (3.1)$$

<sup>383</sup> The pseudorapidity is a convenient quantity to work with as differences in  $\eta$  are  
<sup>384</sup> invariant under Lorentz boosts.

<sup>385</sup> The transverse momentum  $p_T$  of an object is the sum in quadrature of the momenta  
<sup>386</sup> in the transverse plane

$$p_T = \sqrt{p_x^2 + p_y^2}. \quad (3.2)$$

387 Angular distance between two objects is measured in units of  $\Delta R$  and is defined as

$$\Delta R = \sqrt{(\Delta\eta)^2 + (\Delta\phi)^2}, \quad (3.3)$$

388 where  $\Delta\eta$  and  $\Delta\phi$  are the differences in pseudorapidity and azimuthal angle between  
389 the two objects.

### 390 3.2.2 Track Parameterisation

391 The trajectories of charged particle tracks are parameterised as a helix which is fully  
392 specified using five parameters:  $(d_0, z_0, \phi, \theta, q/p)$ . The transverse and longitudinal  
393 impact parameters (IP)  $d_0$  and  $z_0$  specify the closest approach of the trajectory of a  
394 particle to an given origin, where the hard scatter primary vertex (see Section 3.4.2)  
395 is used in this thesis.  $\phi$  and  $\theta$  are the azimuthal and polar angles respectively, and  
396  $q/p$  is the measured charge on the track<sup>1</sup> divided by the scalar 3-momentum. Fig. 3.3  
397 shows each of these parameters diagrammatically.

398 Impact parameter significances are defined as the IP divided by its corresponding  
399 uncertainty,  $s(d_0) = d_0/\sigma(d_0)$  and  $s(z_0) = z_0/\sigma(z_0)$ . When used in flavour tagging  
400 (see Chapter 4), track IP significances are lifetime signed according to the track's  
401 direction with respect to the jet axis and the primary vertex [39]. The signed IP  
402 significances is positive if the track crosses the jet axis in front of the primary vertex  
403 and negative if the crossing is behind the primary vertex.

### 404 3.2.3 Hadron Collider Definitions

#### 405 Cross Section

406 The cross section  $\sigma$  is closely related to the probability of an interaction between  
407 two colliding particles, and is analogous to an effective cross-sectional area of the  
408 particles. The cross section of a process depends on the transition matrix element  
409 and a phase space integral. At hadron colliders such as the LHC, the proton-proton

---

<sup>1</sup>Reconstructed charged particles are assumed to have a charge of  $\pm 1$ .

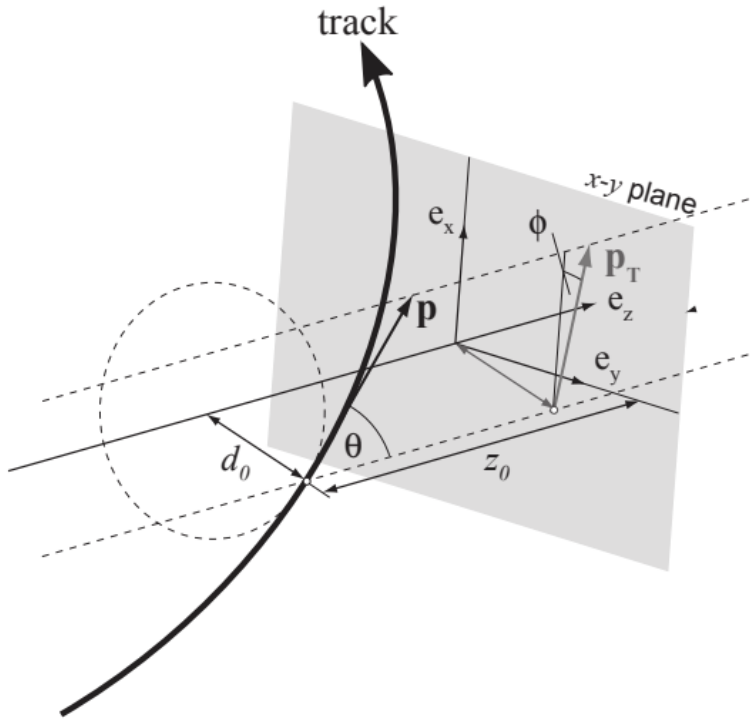


**Figure 3.3:** The track parameterisation used at the ATLAS detector. Five coordinates ( $d_0, z_0, \phi, \theta, q/p$ ) are specified, defined at the track's point of closest approach to the nominal interaction point at the origin of the coordinate system. The figure shows the three-momentum  $\mathbf{p}$  and the transverse momentum  $p_T$  (defined in Eq. (3.2)). The basis vectors  $e_x, e_y$  and  $e_z$  are also shown. Reproduced from Ref. [38].

<sup>410</sup> cross section can be factorised as

$$\sigma(pp \rightarrow X) \approx \text{PDFs} \cdot \text{partonic cross section.} \quad (3.4)$$

<sup>411</sup> The partonic cross section can be calculated at high energies such as those found at  
<sup>412</sup> the LHC, while the parton distribution functions (PDFs) have to be extracted from  
<sup>413</sup> experimental results.

#### <sup>414</sup> Luminosity

<sup>415</sup> The total number of proton-proton collisions  $N$  is related to the total  $pp$  cross  $\sigma$   
<sup>416</sup> section by the integrated luminosity  $L$ , as in

$$N = \sigma L = \sigma \int \mathcal{L} dt. \quad (3.5)$$

<sup>417</sup> The instantaneous luminosity  $\mathcal{L}$  relates the cross section to the number of collisions  
<sup>418</sup> per unit time. For two colliding bunched proton beams, it is defined as

$$\mathcal{L} = \frac{1}{\sigma} \frac{dN}{dt} = \frac{fn_1 n_2}{4\pi \sigma_x \sigma_y}, \quad (3.6)$$

<sup>419</sup> where  $n_1$  and  $n_2$  are the number of protons in the colliding bunches,  $f$  is the bunch  
<sup>420</sup> crossing frequency, and  $\sigma_x$  and  $\sigma_y$  are the rms width of the beam in the horizontal  
<sup>421</sup> and vertical directions.

<sup>422</sup> The total luminosity recorded over the course of Run 2 is shown in Fig. 3.4. In  
<sup>423</sup> total,  $139 \text{ fb}^{-1}$  of usable physics data was collected over the three-year run. The  
<sup>424</sup> uncertainty on the total integrated luminosity is 1.7% [40].

#### <sup>425</sup> Pile-up

<sup>426</sup> At the centre of the ATLAS detector, bunches of more than  $10^{11}$  protons are collided.  
<sup>427</sup> Each bunch-crossing is called an *event*. There is generally one hard proton-proton  
<sup>428</sup> scatter per event. Additional interactions are typically relatively soft ( $low-p_T$ ) and  
<sup>429</sup> are known as *pile-up*. Pile-up from interactions within the same bunch-crossing is  
<sup>430</sup> known as *in-time* pile-up while residual signatures from previous bunch-crossings  
<sup>431</sup> is known as *out-of-time* pile-up. The number of pile-up interactions is denoted  $\mu$ ,

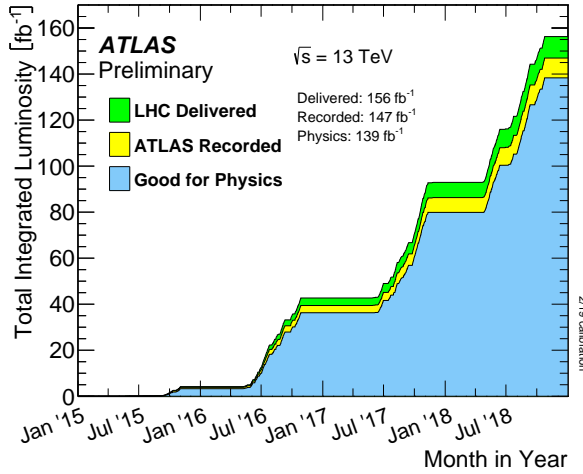


**Figure 3.4:** Delivered, recorded, and usable integrated luminosity as a function of time over the course of Run 2 [35]. A total of  $139 \text{ fb}^{-1}$  of collision data is labelled as good for physics, meaning all sub-detector systems were operating nominally.

432 which is often given as a time-averaged value  $\langle \mu \rangle$ . Histograms showing the number of pile-up interactions over the course of Run 2 are shown in Fig. 3.5.

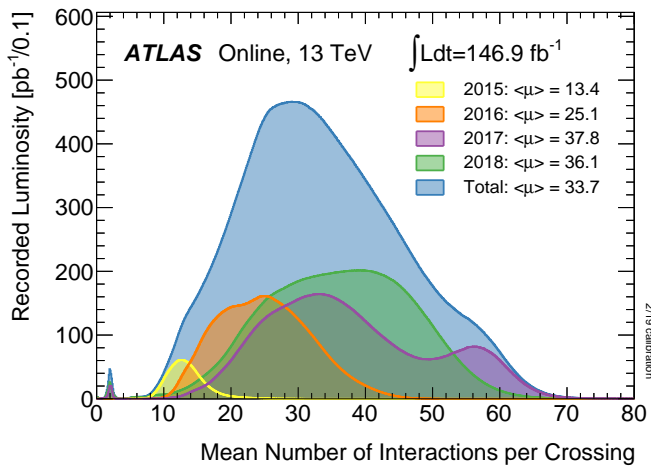


**Figure 3.5:** Average pile-up profiles measured by ATLAS during Run 2 [35].

### <sup>434</sup> 3.3 The ATLAS Detector

<sup>435</sup> The ATLAS<sup>2</sup> detector is made up of several specialised sub-detectors which are  
<sup>436</sup> arranged concentrically around the nominal interaction point at the centre of the  
<sup>437</sup> detector, as shown in Fig. 3.6. The detector is designed to cover nearly the entire solid  
<sup>438</sup> angle around the collision point. In this section a brief overview of each sub-detector  
<sup>439</sup> is given, in order of increasing radial distance from the point of collision. The inner  
<sup>440</sup> tracking detector is described in Section 3.3.1, the electromagnetic and hadronic  
<sup>441</sup> calorimeters in Section 3.3.2, the muon spectrometer in Section 3.3.3, and finally the  
<sup>442</sup> trigger is described in Section 3.3.4. More complete information on the detector can  
<sup>443</sup> be found in Ref. [33], while an overview of physics performance is given in [41].

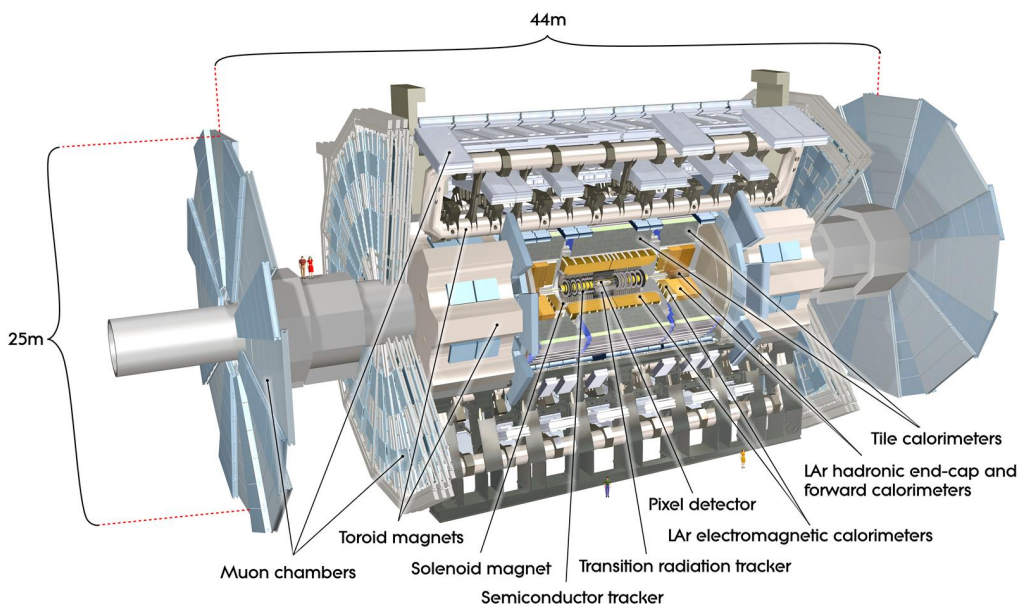


**Figure 3.6:** A 3D model of the entire ATLAS detector [42]. Cutouts to the centre of the detector reveal the different subdetectors which are arranged in concentric layers around the nominal interaction point.

<sup>2</sup>A Toroidal LHC ApparatuS.

### <sup>444</sup> 3.3.1 Inner Detector

<sup>445</sup> The inner-detector system (ID) provides high-resolution charged particle trajectory  
<sup>446</sup> tracking in the range  $|\eta| < 2.5$ . The ID is immersed in a 2 T axial magnetic field,  
<sup>447</sup> produced by a superconducting solenoidal magnet, which enables the measurement  
<sup>448</sup> of particle momentum and charge. After Run 3, the ID will be replaced by the  
<sup>449</sup> ITk [43, 44].

<sup>450</sup> The inner detector is made up of several sub-systems, shown in Figs. 3.7 and 3.8. The  
<sup>451</sup> high-granularity silicon pixel detector covers the innermost region and typically pro-  
<sup>452</sup> vides four spacepoint measurements per track. It is followed by the silicon microstrip  
<sup>453</sup> tracker (SCT), which usually provides a further four spacepoint measurements (8  
<sup>454</sup> hits) per track. These silicon detectors are complemented by the Transition Radiation  
<sup>455</sup> Tracker (TRT), which enables radially extended track reconstruction up to  $|\eta| = 2.0$   
<sup>456</sup> and typically provides 33 (38) additional hits in the barrel (endcap).

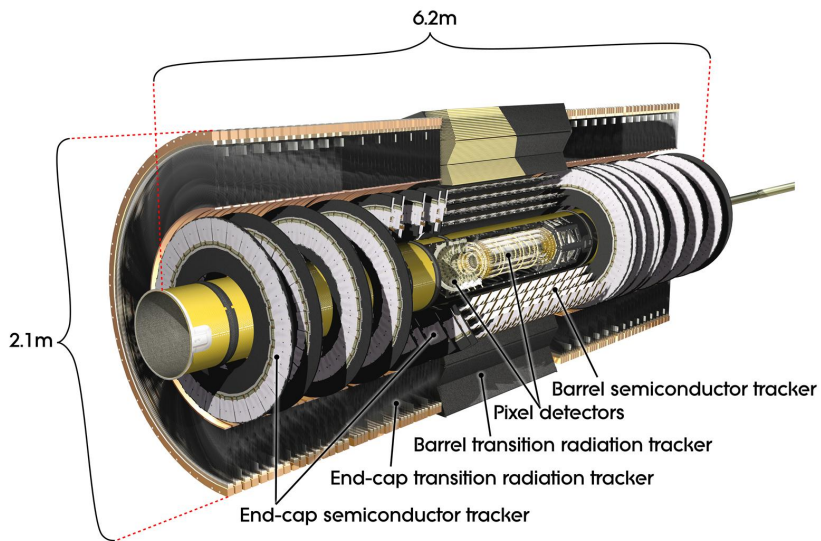


**Figure 3.7:** A 3D model of the ATLAS ID showing the pixel, SCT and TRT subdetectors [45].

<sup>457</sup> The target inverse momentum resolution for the combined ID measurement is  
<sup>458</sup> parameterised as a function of the track transverse momentum and polar angle [41].

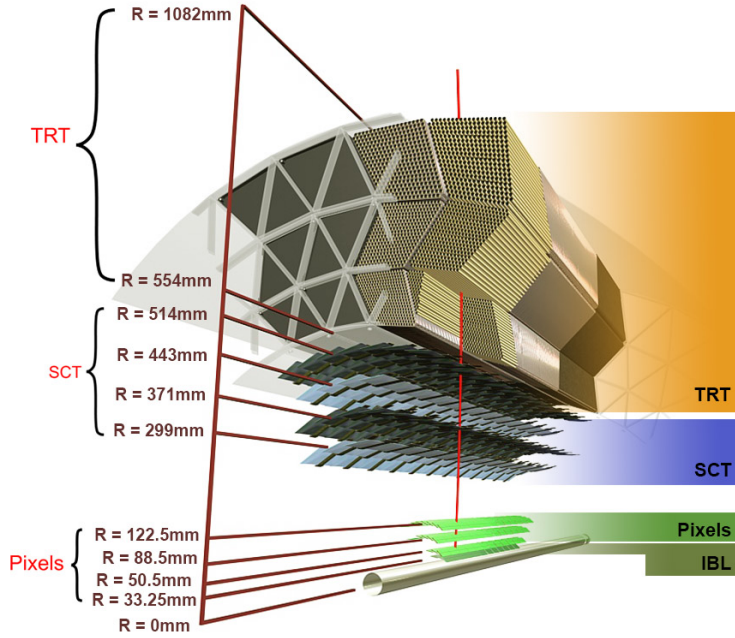


**Figure 3.8:** A cross-sectional view of the ATLAS ID, with the radii of the different barrel layers shown [38].

<sup>459</sup> The parameterisation is given by

$$\sigma(1/p_T) = 0.36 \oplus \frac{13}{p_T \sin \theta} \text{ TeV}^{-1}, \quad (3.7)$$

<sup>460</sup> where  $\oplus$  denotes a sum in quadrature. For low- $p_T$  tracks (e.g.  $p_T \approx 500 \text{ MeV}$ ) in the  
<sup>461</sup> central region this corresponds to a relative error of approximately 0.01%. Meanwhile  
<sup>462</sup> for high- $p_T$  tracks (e.g.  $p_T \approx 100 \text{ GeV}$ ) in the central region this corresponds to  
<sup>463</sup> a relative error of approximately 4%. The momentum resolution generally good  
<sup>464</sup> enough to correctly identify the sign of the charge on particles up to the highest  
<sup>465</sup> energies expected at the LHC. The transverse impact parameter resolution  $\sigma(d_0)$  is  
<sup>466</sup> parameterised similarly as

$$\sigma(d_0) = 11 \oplus \frac{115}{p_T \sin \theta} \mu\text{m}. \quad (3.8)$$

<sup>467</sup> Typical uncertainties for the transverse IP resolution are 230  $\mu\text{m}$  and 11  $\mu\text{m}$  for low  
<sup>468</sup> and high- $p_T$  tracks in the central region, respectively.

#### <sup>469</sup> Pixel Detector

<sup>470</sup> The silicon pixel detector is comprised of four cylindrical barrels at increasing radii  
<sup>471</sup> from the beamline, and four disks on each side. The innermost barrel layer is the  
<sup>472</sup> insertable B-layer (IBL), shown in Fig. 3.9. The IBL was installed before Run 2 [46,47]  
<sup>473</sup> and lies approximately just 33 mm from the beam axis. The second-to-innermost layer  
<sup>474</sup> is often referred to as the B-layer. The specification of the pixel detector determines  
<sup>475</sup> the impact parameter resolution and the ability to reconstruct primary and secondary  
<sup>476</sup> vertices. The detector is required to have a high granularity (i.e. resolution) to  
<sup>477</sup> maintain the low occupancy required to resolve nearby particles. Individual pixels  
<sup>478</sup> are 50  $\mu\text{m}$  in the transverse direction  $R\phi$  and 400  $\mu\text{m}$  in the longitudinal  $z$  direction  
<sup>479</sup> (250  $\mu\text{m}$  for the IBL). Cluster positions have a resolution of approximately 10  $\mu\text{m}$  in  
<sup>480</sup>  $R\phi$  and 100  $\mu\text{m}$  in  $z$ .

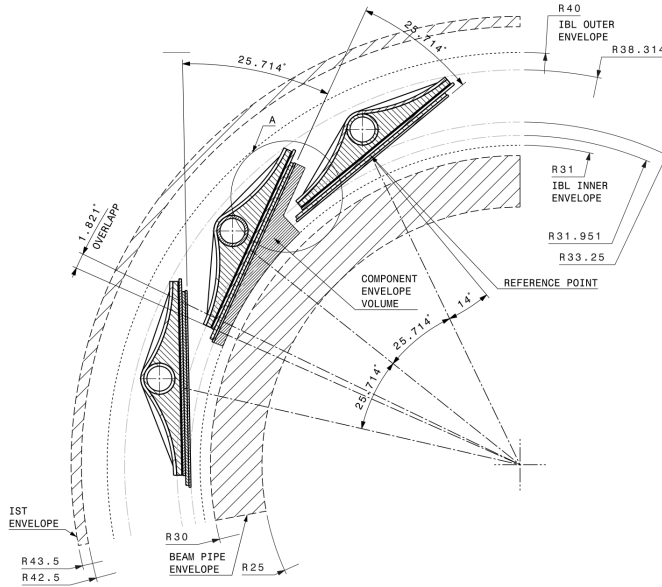


**Figure 3.9:** A schematic cross-sectional view of the ATLAS IBL [46].

#### <sup>481</sup> Semi-Conductor Tracker (SCT)

<sup>482</sup> The SCT is made up of four concentric barrel layers in the central region, and nine  
<sup>483</sup> disks in each end-cap. Each layer is itself made of a pair of silicon microstrip layers,  
<sup>484</sup> with a small stereo angle (20 mrad) between the two layers enabling the  $z$ -coordinate

485 to be measured from a pair of strip measurements. The SCT typically provides four  
486 precision spacepoint measurements (eight strip measurements) per track in the barrel  
487 region. These have intrinsic uncertainties of  $17\text{ }\mu\text{m}$  in the transverse direction  $R\phi$ , and  
488  $580\text{ }\mu\text{m}$  in the longitudinal direction  $z$  [48]. The measurements provide a contribution  
489 to the measurement of charged particle momentum and impact parameter.

490 **Transition Radiation Tracker (TRT)**

491 The TRT is a straw-tube tracker which complements the higher-resolution silicon-  
492 based tracks by offering a larger number of hits per track (typically more than 30)  
493 and a long lever arm, which aids the accurate measurement of particle momentum.  
494 It is made up of approximately 300 000 drift tubes with a diameter of 4 mm which  
495 are filled with an argon/xenon gas mixture. The walls of each tube are electrically  
496 charged, and a thin conducting wire runs along the center. When a charged particle  
497 traverses a tube, it ionises the gas and the resulting liberated electrons drift along  
498 the electric field to the wire, where an associated charge is registered. In the barrel  
499 the straws run parallel to the  $z$ -axis and therefore the TRT only provides tracking  
500 information in  $R\phi$ . Straws are arranged radially in the end-caps. The resulting  
501 two-dimensional spacepoints have a resolution of approximately  $120\text{ }\mu\text{m}$ . The spaces  
502 between the straws are filled with a polymer which encourages the emission of  
503 transition radiation, aiding electron identification.

504 **3.3.2 Calorimeters**

505 The calorimeter system measures the energy of incident particles over the range  
506  $|\eta| < 4.9$ . There are two main sub-systems: the electromagnetic calorimeter (ECal),  
507 which focuses on the measurement of electrons and photons, and the hadronic  
508 calorimeter (HCal), which measures the energy of hadrons. A schematic view of the  
509 calorimeter system is shown in Fig. 3.10. Upon entering the calorimeter, incident  
510 particles will interact with the detector material to produce a shower of secondary  
511 particles with reduced energies. The charge deposited in this process is measured to  
512 reconstruct the energy of the initial incident particle. The two calorimeter sub-systems  
513 must provide strong containment of showering particles to prevent punch-through of  
514 EM and hadronic particles to the HCal and muon systems respectively.

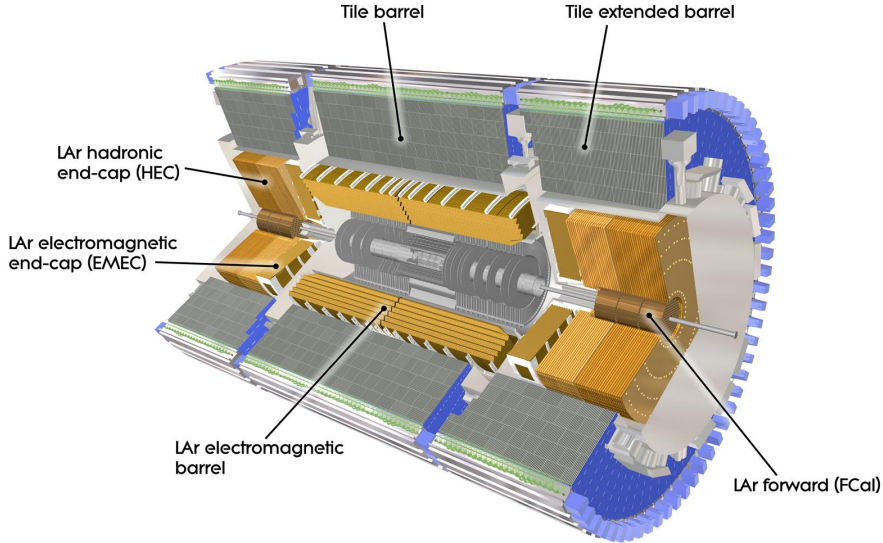


**Figure 3.10:** The ATLAS calorimeters [49]. The ECal uses LAr-based detectors, while the HCal uses mainly scintillating tile detectors. In the forward region the HCal also includes the LAr hadronic endcaps.

### 515 Liquid Argon (LAr) Electromagnetic Calorimeter

516 The more granular lead/liquid-argon ECal covers the region  $|\eta| < 3.2$  and is split  
 517 into barrel (covering  $|\eta| < 1.475$ ) and end-cap (covering  $1.375 < |\eta| < 3.2$ ) regions.  
 518 EM calorimetry works by encouraging electrons and photons to interact with electric-  
 519 ically charged particles in detector material via bremsstrahlung ( $e \rightarrow e\gamma$ ) and pair  
 520 production ( $\gamma \rightarrow e^+e^-$ ). The EM calorimeter uses lead absorber plates to initiate  
 521 EM showers, resulting in secondary particles which ionise the surrounding liquid  
 522 argon. The charge is collected on copper electrodes and read out. The accordion  
 523 geometry of the ECal allows for a full coverage in  $\phi$  without any azimuthal cracks.

524 The energy resolution of the LAr calorimeter is made up of a sampling and a constant  
 525 term, which are summed in quadrature to produce the overall energy resolution. The  
 526 sampling term contributes approximately  $10\%/\sqrt{E}$ , while the constant term adds an  
 527 additional 0.7%. Photons with moderate transverse energy  $E_T \approx 50 \text{ GeV}$  have an  
 528 overall energy resolution of at most 1.6% over most of the pseudorapidity range. At  
 529 lower  $E_T \approx 10 \text{ GeV}$ , the resolution is degraded to approximately 5%. The resolution  
 530 measurements are obtained from test beam data [41].

**531** **Hadronic Tile Calorimeter**

**532** In the central barrel region with  $|\eta| < 1.7$ , the HCal uses a tile calorimeter with  
**533** steel as an absorbing material, and scintillating tiles as the active material. Two  
**534** copper/liquid-argon calorimeter end-caps are also used. Incident hadrons interact  
**535** via the strong and electromagnetic forces with the absorber material, mainly loosing  
**536** energy due to multiple inelastic nuclear collisions. The active material captures the  
**537** resulting electrons and photons to measure the energy of the incident hadron.

**538** The hadronic energy resolution of the HCal is parameterised as a function of the  
**539** hadron's transverse energy

$$\sigma(E_T)/E_T = 50\%/\sqrt{E_T} \oplus 3\%, \quad (3.9)$$

**540** corresponding to a energy resolution of 11% (6.5%) for a hadron with  $E_T$  of approxi-  
**541** mately 10 GeV (50 GeV) [50].

**542** **3.3.3 Muon Spectrometer**

**543** Due to their higher mass, muons easily pass unimpeded through the ID and calorime-  
**544** ters and therefore require specialised detectors for their measurement. The Muon  
**545** Spectrometer (MS) is made up of dedicated tracking and triggering hardware, as  
**546** shown in Fig. 3.11. The precision tracking system uses three layers of monitored drift  
**547** tubes with a barrel region covering  $|\eta| < 1.2$  and end-caps covering  $1 < |\eta| < 2.7$ .  
**548** The inner layers of the end-caps use cathode strip chambers to better cope with the  
**549** high occupancy in the forward region. The trigger system is comprised of resistive  
**550** plate chambers in the barrel region covering  $|\eta| < 1.0$  and thin gap chambers in  
**551** the end-cap regions covering  $1 < |\eta| < 2.4$ . A set of three superconducting air-core  
**552** toroidal magnets, each made up of eight coils, is used in each of the barrel and  
**553** end-caps to deflect the muons as they pass through the MS, allowing their momentum  
**554** and charge to be measured from the direction and magnitude of curvature. The  
**555** toroidal magnets generate a field which is largely orthogonal to the muon trajec-  
**556** tories which allows for maximum deflection. The transverse momentum resolution  
**557** (measured for combined ID and muon tracks, see Section 3.4.4) has been measured

558 to be approximately 1.7% in the central region for low- $p_T$  muons, increasing to 4% for high- $p_T$  muons in the forward regions [51].

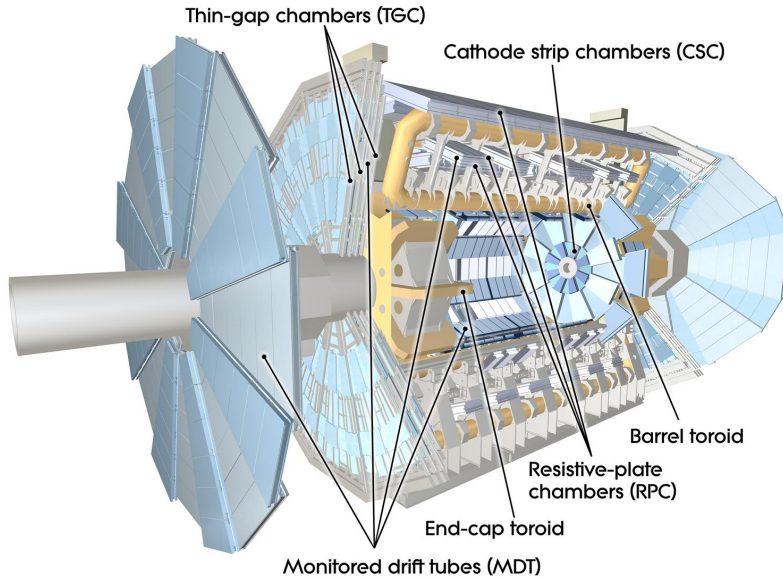


**Figure 3.11:** The ATLAS muon spectrometer [52].

559

### 560 3.3.4 The Trigger

561 The 25 ns bunch spacing used over the course of Run 2 corresponds to a bunch-  
 562 crossing or event rate of 40 MHz (see Table 3.1). If the full information for the  
 563 detector was written out for each event, this would correspond to the generation  
 564 of 60 TB of data each second. This is more than can be feasibly read out from the  
 565 hardware, processed and stored, requiring the use of a trigger system which quickly  
 566 makes a decision about whether or not an event is potentially interesting and should  
 567 be kept for further analysis. The trigger system is comprised of two levels which  
 568 aim to identify various signatures, such as electrons, muons, taus, photons, and jets  
 569 (including  $b$ -jets), as well as events with large total or missing transverse energy. The  
 570 hardware-based Level-1 (L1) trigger uses coarse information from the calorimeters  
 571 and MS to accept events at an average rate of 100 kHz approximately 2.5  $\mu$ s after the  
 572 event. After the L1 trigger, the software-based High Level Trigger (HLT) makes use  
 573 of 40 000 CPU cores to make a final selection on surviving events in approximately a  
 574 few hundred milliseconds. The final event read-out rate is approximately 1.2 kHz,

575 corresponding to  $1.2 \text{ GB s}^{-1}$  of permanent data storage. More information is provided  
576 in [53].

## 577 3.4 Reconstructed Physics Objects

578 Event reconstruction is the process of analysing the output from the detector to  
579 determine the type and properties of particles present in an event. The reconstructed  
580 event provides information about the underlying physics process that led to these  
581 observable final state particles. Events passing the trigger selection (described in  
582 Section 3.3.4) undergo offline reconstruction, which makes use of the full information  
583 from the detector. Reconstruction and analysis of events relies on the extensive  
584 ATLAS software stack, see Ref. [54] for more information.

585 Several different reconstructed objects are used for physics analyses. Objects relevant  
586 to this thesis are described below.

### 587 3.4.1 Tracks

588 The reconstructed trajectories of charged particles are referred to as *tracks*. Tracks  
589 are reconstructed from the energy depositions (called *hits*) left by the particles as  
590 they traverse the inner detector. Tracks are used in the reconstruction of other  
591 objects, including vertices and jets, so their accurate reconstruction is a critical  
592 task. A comprehensive introduction to ATLAS tracking is available in Ref. [55],  
593 while specific optimisations for dense environments are detailed in Refs. [56, 57]. An  
594 overview of track reconstruction is given below.

### 595 Space-point Formation (Clustering)

596 When a charged particle traverses a silicon layer, charge can be collected in more  
597 than one pixel or strip. This is due to the incident angle of the particles with respect  
598 to the sensor, and also the drift of electrons between sensors caused by the magnetic  
599 field. Clusters (also called *hits* or *space-points*) are formed by clustering neighbouring  
600 pixels or strips and estimating locations of space-points using the shape and energy  
601 distribution of the clusters.

**602 Track Finding**

603 Space-points are used to build track seeds. These are groups of three hits which  
604 are geometrically compatible with being part of a track segment. A combinatorial  
605 Kalman filter (KF) is used to build track candidates by extending track seeds. The  
606 filter can create multiple track candidates per seed, with bifurcations along the track  
607 occurring when more than one compatible space-point exists on a given layer. In  
608 this way, the KF creates an excess of *track candidates*, which are only required to  
609 satisfy basic quality requirements. Track candidates are allowed to reuse or *share*  
610 hits freely (a single hit may be used by multiple track candidates). Typically, the  
611 presence of shared hits is a predictor of a bad track due to the high granularity of  
612 the ATLAS tracking detectors. At this stage, there can also be a large number of  
613 incorrect hits assigned to otherwise good tracks, and additionally large numbers of  
614 *fake* tracks, which are comprised of a majority of wrong hits and do not correspond  
615 to the trajectory of any one physical particle (fake tracks are defined as those where  
616 the majority of associated hits do not originate from one single truth particle, see  
617 Eq. (5.5)). The low quality of tracks at this stage necessitates an ambiguity solving  
618 step, in which candidates are cleaned, and the highest quality track are selected.

**619 Ambiguity Solving**

620 Ambiguity solving was introduced as part of the ATLAS New Tracking effort [55],  
621 which was intended to improve track reconstruction performance in dense envi-  
622 ronments. In the ambiguity solver, track candidates are processed individually in  
623 descending order of a track score. The track score quantifies the likelihood of the  
624 track corresponding to the trajectory of a real particle. Scoring uses a number of  
625 variables, including the number and positions of hits (preferring hits in more precise  
626 regions of the detector), the transverse momentum of the track and the track fit  
627 quality. The track fit quality describes the quality of the track as the  $\chi^2$  divided  
628 by the number degrees of freedom on the track. A preference for high transverse  
629 momentum tracks promotes the successful reconstruction of the more physically  
630 interesting energetic particles, and suppresses the large number of wrong hits assigned  
631 to low momentum tracks. The ambiguity solver also penalises tracks with missing  
632 hits on the innermost detector layers.

During the processing of a track candidate, the track is cleaned (whereby problematic hits are removed), and, if the resulting track satisfies the quality selection criteria, a high precision fit of the track parameters using the surviving hits is performed. The high precision fit makes full use of all available information, and uses an updated position and uncertainty estimate for each cluster obtained from a Neural Network (NN) [58]. If the track has reached this stage without being rejected by passing various quality requirements, it is re-scored and returned to the list of track candidates. If the same track is then processed again without requiring modification, it is added to the final track collection. Track candidates that fall below certain quality threshold are rejected. This selection does allow for the possibility of a track having small number of shared hits, as detailed in Table 3.2.

Parameter	Selection
$p_T$	$> 500 \text{ MeV}$
$ \eta $	$< 2.5$
$ d_0 $	$< 3.5 \text{ mm}$
$ z_0 \sin \theta $	$< 5 \text{ mm}$
Silicon hits	$\geq 8$
Shared silicon hits	$< 2$
Silicon holes	$< 3$
Pixel holes	$< 2$

**Table 3.2:** Quality selections applied to tracks, where  $d_0$  is the transverse IP of the track,  $z_0$  is the longitudinal IP with respect to the PV and  $\theta$  is the track polar angle (see Section 3.2.2 for the IP definitions). Silicon hits are hits on the pixel and SCT layers. Shared hits are hits used on multiple tracks which have not been classified as split by the cluster-splitting neural networks [57]. A hole is a missing hit, where one is expected, on a layer between two other hits on a track.

#### 644 Neural Network Cluster Splitting

As part of track cleaning, shared hits are classified by a NN to determine if they are compatible with the characteristic features of a merged cluster [56, 58]. A merged cluster is one made up of a combination of energy deposits from more than one particle, which have become merged due to the closeness of the associated particles and the limited resolution of the detector. It is common for clusters to become

merged in dense environments, as discussed in Section 4.3. If the cluster is predicted to be merged it is labelled as being freely shareable, or *split*. Hits not compatible with the merged hypothesis can still be shared by a limited number of tracks, but come with a penalty for the track which may hinder its acceptance into the final track collection.

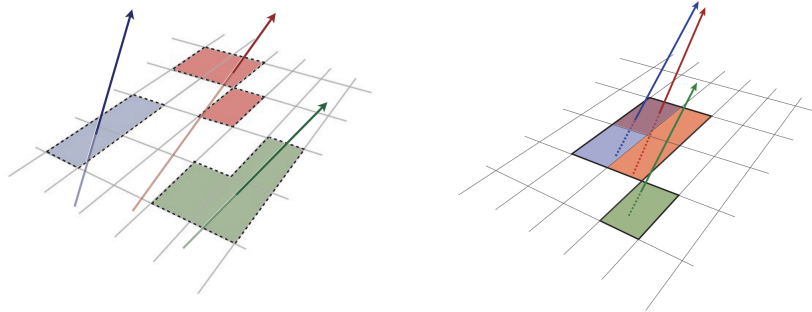


**Figure 3.12:** Particles (left) which have enough separation will leave charge depositions which are resolved into separate clusters. Sufficiently close particles (right) can lead to merged clusters. Their combined energy deposits are reconstructed as a single merged cluster [57].

654

## 655 Pseudotracking

Pseudotracking uses Monte Carlo truth information to group together all the hits left by each truth particle. Each collection of hits which, as a unit, satisfies basic quality requirements is directly used in a full resolution track fit. If the track fit is successful, a “pseudotrack” track is created and stored. If the track fit fails, or the collection of hits does not pass the basic quality requirements (for example because of a lack of hits) then the particle is said to be un-reconstructable. In this way, pseudotracking performance represents the ideal reconstruction performance given the ATLAS detector, with perfect hit-to-track association and track reconstruction efficiency. The approach was introduced in Ref. [59] as a way to obtain a fast approximation of tracking reconstruction for simulated data, however the technique has become a useful tool for studying tracking performance in general [56].

### 667 3.4.2 Vertices

668 Groups of reconstructed tracks can be examined to determine whether the particles  
669 originated from a common spatial point of origin. This occurs when proton-proton  
670 collisions take place (primary vertices), when a particle decays or radiates, and also  
671 as a result of interaction with the detector material (secondary vertices). Vertex  
672 reconstruction is made up of two stages. First, vertex finding takes place, which  
673 is the process of grouping tracks into compatible vertices. Second, vertex fitting  
674 combines information from compatible tracks to reconstruct the physical properties  
675 of the vertex, such as mass and position.

#### 676 Primary Vertices

677 Each proton-proton interaction happens at a *primary vertex* (PV). Primary vertices  
678 are iteratively reconstructed with tracks using the iterative vertex finder (IVF) [60].  
679 The *hard scatter vertex* of an event is chosen as the primary vertex whose associated  
680 tracks have the largest sum of transverse momentum squared,  $\Sigma(p_T^2)$ .

#### 681 Secondary Vertices

682 Secondary vertices (SV) occur when a particle radiates or decays at a sufficient  
683 distance from the primary vertex to be resolved from the primary vertex (see  
684 Section 4.3.1). Two widely used secondary vertexing tools are used within ATLAS:  
685 SV1 and JetFitter [61, 62]. Each attempts to reconstruct secondary vertices inside a  
686 jet using the tracks associated to that jet (see Section 3.4.3 for more information  
687 about track association). SV1 by design attempts to reconstruct only a single  
688 inclusive vertex per jet. This inclusive vertex groups all  $b$ -hadron decay products,  
689 including tracks from the  $b$ -hadron decay itself and tracks from  $b \rightarrow c$  decays. The  
690 second tool, JetFitter attempts to resolve each displaced vertex inside the jet, such  
691 that secondary vertices from  $b$ -hadron decays are reconstructed separately to tertiary  
692 vertices from  $b \rightarrow c$  decay chains.

### 693 3.4.3 Jets

694 Jets are an aggregate reconstructed object corresponding to a collection of collimated  
 695 stable particles which results from the presence of a quark or gluon. Jets are built  
 696 by clustering constituent objects (e.g. tracks or calorimeter clusters) using a jet  
 697 finding algorithm, for example the anti- $k_t$  algorithm [63], which is implemented in  
 698 FASTJET [64].

699 Objects can be associated to jets in one of two ways. The first is via a geometrical  
 700 matching in  $\Delta R$  (see) The second is via a ghost association [65], where the object is  
 701 assigned a negligible momentum and re-clustered into the jet after its formation.

702 Jets from pile-up interactions are suppressed using the Jet Vertex Tagger (JVT)  
 703 algorithm, which uses the transverse momenta of tracks to identify jets from pile-up  
 704 interactions [56].

### 705 EMTopo Jets

706 EMTopo jets are reconstructed from noise-suppressed topological clusters (topoclus-  
 707 ters) of calorimeter energy depositions [66]. The clustering uses the energy significance  
 708 of each cell, defined as

$$S_{\text{cell}} = \frac{E_{\text{cell}}}{\sigma_{\text{noise, cell}}}, \quad (3.10)$$

709 where  $E_{\text{cell}}$  is the energy measured in a given calorimeter cell, and  $\sigma_{\text{noise, cell}}$  is the  
 710 expected level of noise on the cell (e.g. from pile-up interactions). Topoclusters are  
 711 formed from a seed cell with a large  $S_{\text{cell}}$ , and expanded by iteratively adding neigh-  
 712 bouring cells with a sufficiently large energy significance. Collections of topoclusters  
 713 are then clustered into a jet using the anti- $k_t$  algorithm with a radius parameter of  
 714 0.4 (small- $R$  jets) or 1.0 (large- $R$  jets). More information, including information on  
 715 the calibration of the topocluster jet energy scale, is available in Ref. [66].

### 716 Particle Flow Jets

717 Particle-flow (PFlow) jets are reconstructed from particle-flow objects [67] using  
 718 the anti- $k_t$  algorithm with a radius parameter of 0.4. Particle-flow objects integrate

719 information from both the ID and the calorimeters, improving the energy resolution  
720 at high transverse momenta and reducing pile-up contamination. The PFlow jet  
721 energy scale is calibrated according to Ref. [68].

722 **Large- $R$  Jets**

723 Large- $R$  jets have a radius parameter  $R = 1.0$  and are built by clustering topological  
724 calorimeter clusters using the anti- $k_t$  algorithm [69]. The large radius parameter  
725 is especially useful for containing the decay products of a boosted Higgs boson, as  
726 discussed in Chapter 7. Due to their large size, large- $R$  jets benefit from a grooming  
727 procedure called trimming which remove soft contaminants inside the jet [70, 71].  
728 Trimming aims to remove jet constituents from pile-up and the underlying event,  
729 which helps to improve the jet mass resolution and its robustness to varying levels  
730 of pile-up. The jet mass is computed using a combination of information from the  
731 calorimeters and ID, and a calibration to data is applied [72].

732 **Track-jets**

733 Track-jets are built by clustering tracks using the anti- $k_t$  clustering algorithm. They  
734 are associated to large- $R$  jets as sub-jets and used to identify large- $R$  jets containing  
735  $b$ -hadrons. The radius parameter is allowed to vary with transverse momentum such  
736 that a broader cone (up to  $R = 0.4$ ) is used for low- $p_T$  track-jets and a narrower  
737 cone (down to  $R = 0.02$ ) for high- $p_T$  track-jets [73, 74]. The narrower cone is better  
738 suited to clustering highly collimated jet constituents at high- $p_T$ .

739 **Jet Flavour Labels**

740 Jet flavour labels are assigned to small- $R$  jets according to the presence of a truth  
741 hadron within  $\Delta R(\text{hadron}, \text{jet}) < 0.3$  of the jet axis. If a  $b$ -hadron is found the jet is  
742 labelled a  $b$ -jet. In the absence of a  $b$ -hadron, if a  $c$ -hadron is found the jet is called  
743 a  $c$ -jet. If no  $b$ - or  $c$ -hadrons are found, but a  $\tau$  is found in the jet, it is labelled as a  
744  $\tau$ -jet, else it is labelled as a light-jet.

745 PFlow jets are used to train the algorithms discussed in Chapter 5 and Chapter 6.

## 746 Jet Track Association

747 Tracks are associated to small- $R$  jets using a  $\Delta R$  association cone, the width of which  
 748 decreases as a function of jet  $p_T$ , with a maximum cone size of  $\Delta R \approx 0.45$  for jets  
 749 with  $p_T = 20$  GeV and minimum cone size of  $\Delta R \approx 0.25$  for jets with  $p_T > 200$  GeV.  
 750 If a track is within the association cones of more than one jet, it is assigned to the  
 751 jet which has a smaller  $\Delta R(\text{track}, \text{jet})$ .

## 752 3.4.4 Leptons

753 Electrons and muons leave characteristic signatures that are picked up in the ECal  
 754 and MS respectively. The reconstruction of both types of charged lepton is briefly  
 755 outlined below.

### 756 Electrons

757 A diagrammatic view of electron reconstruction is shown in Fig. 3.13. Electrons  
 758 candidates are reconstructed by matching PV-compatible<sup>3</sup> inner detector tracks  
 759 to topological calorimeter clusters. The track-cluster matching criteria takes into  
 760 account the significant energy loss of the electron due to bremsstrahlung. If a match  
 761 is found, a refit of the track is performed using the Gaussian Sum Filter (GSF) [75],  
 762 which better handles trajectory reconstruction in the presence of bremsstrahlung.  
 763 Various identification criteria are then applied to the candidates using a likelihood-  
 764 based (LH) method to improve purity. These include requirements on the track  
 765 quality and cluster matching, the shape of electromagnetic shower in the ECal,  
 766 leakage into the HCal, and the amount of transition radiation detected in the TRT.  
 767 Isolation criteria with respect to other nearby ID tracks and calorimeter clusters may  
 768 also be applied. A full description can be obtained from Ref. [76].

### 769 Muons

770 Muon reconstruction makes use of the dedicated MS (see Section 3.3.3), the tracks  
 771 from the ID, and the presence of characteristic signatures in the calorimeters. Muon

---

<sup>3</sup>The ID track associated with the electron is required to satisfy  $d_0/s(d_0) < 5$  and  $z_0 \sin \theta < 0.5$  mm.

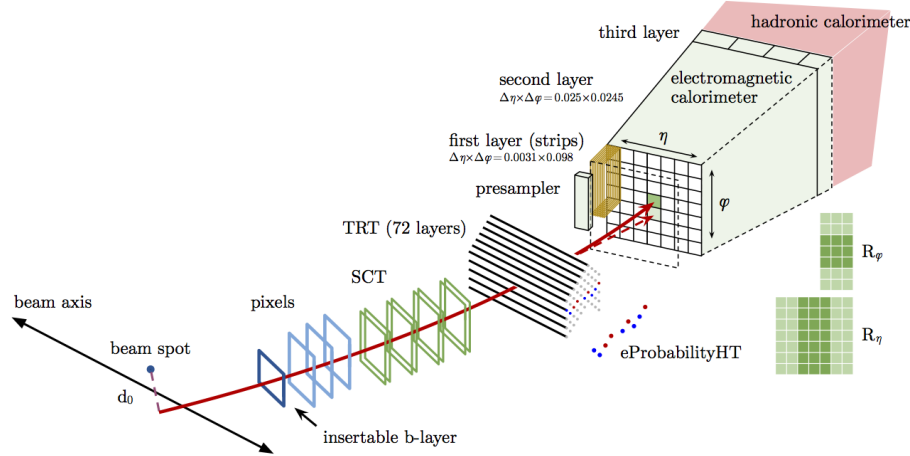


**Figure 3.13:** A sketch of electron reconstruction using the ATLAS detector [76]. Electron reconstruction makes use of the entire ID and the calorimeters.

772 tracks (i.e. a track reconstructed in the MS) are reconstructed by connecting straight-  
 773 line track segments, which are identified via a Hough transform, and combined into  
 774 a approximately parabolic trajectory. Finally, a global  $\chi^2$  fit is performed, taking  
 775 into account possible interactions between the muon and the detector material. A  
 776 reconstructed muon is called *combined* if it can be matched successfully to an to  
 777 an ID track. Combined muons undergo a further fit with the combined ID and MS  
 778 hits, with the energy loss due to the traversal of the calorimeters being taking into  
 779 account.

780 After reconstruction, candidate undergo an identification processes which helps to  
 781 efficiently identify prompt muons whilst rejecting background signals (e.g. non-  
 782 prompt muons from pion and kaon decays, the punch-through of a hadron from the  
 783 calorimeter, or the semi-leptonic decay of a heavy flavour hadron). Combined muon  
 784 identification takes into account discrepancies in the  $p_T$  and charge measurements  
 785 in the MS and ID, and the  $\chi^2$  of the combined track fit. Selections on the number  
 786 of hits in the ID and MS are also applied. At the medium identification working  
 787 point, approximately 96% of prompt muons with  $20 \text{ GeV} < p_T < 100 \text{ GeV}$  are  
 788 successfully identified. On top of the identification requirements, a number of  
 789 isolation requirements can also be applied to further suppress background signals.

790 More information on muon reconstruction, identification and isolation can be found  
 791 in Ref. [77].

### 792 3.4.5 Missing Transverse Momentum

793 An imbalance in the final state transverse momentum can occur as a result of  
794 incomplete measurement of the final state particles. In particular, neutrinos are  
795 not measured by the detector and contribute to the missing transverse momentum  
796  $\mathbf{E}_T^{\text{miss}}$ . Incomplete detector acceptance and inaccuracies in the reconstruction of the  
797 final state can also contribute to the missing transverse momentum of an event. In  
798 order to calculate the missing transverse momentum, the negative vector sum of  
799 the momentum of all photons, leptons and small- $R$  jets with  $p_T > 20 \text{ GeV}$  is taken.  
800 The momenta of tracks associated to the primary vertex are also taken into account.  
801 The magnitude of  $\mathbf{E}_T^{\text{miss}}$  is written  $E_T^{\text{miss}}$ . More information about missing transverse  
802 momentum reconstruction is provided in [78].

803

# Chapter 4

804

## Tracking and Flavour Tagging

805 Many ATLAS analyses rely on flavour tagging, which is the identification of jets  
806 containing heavy-flavour hadrons ( $b$ -hadrons and  $c$ -hadrons) as opposed to those  
807 containing only light-flavour hadrons or gluons. In particular,  $b$ -tagging is the  
808 identification of jets originating only from  $b$ -hadrons (i.e.  $b$ -jets).

809 Flavour tagging is a critical component of the physics programme of the ATLAS  
810 experiment. It is of crucial importance for the study of the Standard Model (SM)  
811 Higgs boson and the top quark, which decay preferentially to  $b$ -quarks [79, 80], and  
812 additionally for several Beyond the Standard Model (BSM) resonances that readily  
813 decay to heavy flavour quarks [81].

814 This chapter is structured as follows. In Section 4.1 an introduction to the datasets  
815 used in this thesis is given. The various  $b$ -jet identification algorithms (also called  
816 *taggers*) used in ATLAS are described in Section 4.2. These work by identifying  
817 the unique signatures of  $b$ -jets, which are outlined in Section 4.3. Ultimately,  
818 the tagging algorithms use input information about the reconstructed jet and its  
819 associated tracks. Successful  $b$ -tagging relies therefore on the efficient and accurate  
820 reconstruction of tracks, and especially those tracks corresponding to the products of  
821  $b$ -hadron decays. A summary of the challenges facing tracking and  $b$ -tagging at high  
822 transverse momentum is provided in Section 4.3.2. Some preliminary investigations  
823 into improving tracking in the high- $p_T$  regime are investigated in Section 4.4. In  
824 Section 4.5 the conclusions of this chapter are given.

## 825 4.1 Datasets

826 This thesis makes extensive use of two simulated datasets which are described in this  
 827 section. The datasets are made up of simulated SM  $t\bar{t}$  and BSM  $Z'$  events initiated by  
 828 proton-proton collisions at a center of mass energy  $\sqrt{s} = 13$  TeV. The  $Z'$  sample is  
 829 constructed in such a manner that it has a relatively flat jet  $p_T$  spectrum up to 5 TeV  
 830 and decays democratically to equal numbers of  $b$ -,  $c$ - and light-jets. The generation  
 831 of the simulated event samples includes the effect of multiple  $pp$  interactions per  
 832 bunch crossing with an average pile-up of  $\langle \mu \rangle = 40$ , which includes the effect on the  
 833 detector response due to interactions from bunch crossings before or after the one  
 834 containing the hard interaction.

835 The  $t\bar{t}$  events are generated using the POWHEGBox v2 generator [82–85] at next-  
 836 to-leading order with the NNPDF3.0NLO [86] set of parton distribution functions  
 837 (PDFs). The  $h_{\text{damp}}$  parameter<sup>1</sup> is set to 1.5 times the mass of the top-quark ( $m_{\text{top}}$ ) [87],  
 838 with  $m_{\text{top}} = 172.5$  GeV. The events are interfaced to PYTHIA 8.230 [88] to model the  
 839 parton shower, hadronisation, and underlying event, with parameters set according  
 840 to the A14 tune [89] and using the NNPDF2.3LO set of PDFs [90].  $Z'$  events are  
 841 generated with PYTHIA 8.2.12 with the same tune and PDF set. The decays of  $b$ -  
 842 and  $c$ -hadrons are performed by EVTGEN v1.6.0 [91]. Particles are passed through  
 843 the ATLAS detector simulation [92] based on GEANT4 [93].

844 Jets are required to have a pseudorapidity  $|\eta| < 2.5$  and  $p_T > 20$  GeV. Additionally,  
 845 a standard selection using the JVT tagger (see Section 3.4.3) at the tight working  
 846 point is applied to jets with  $p_T < 60$  GeV and  $|\eta| < 2.4$  in order to suppress pile-up  
 847 contamination [94].

## 848 4.2 $b$ -tagging Algorithms

849 In this section some common definition used in flavour tagging are given in Sec-  
 850 tion 4.2.1, followed by a description of the various  $b$ -tagging algorithms used in  
 851 ATLAS in Sections 4.2.2 and 4.2.3.

---

<sup>1</sup>The  $h_{\text{damp}}$  parameter is a resummation damping factor and one of the parameters that controls the matching of POWHEG matrix elements to the parton shower and thus effectively regulates the high- $p_T$  radiation against which the  $t\bar{t}$  system recoils.

### 852 4.2.1 Common Definitions

853 Each flavour tagging algorithm outputs a discriminant value that can be used to  
 854 select jets of the signal flavour. The efficiency of a flavour tagging algorithm is  
 855 defined as the fraction of signal jets which are correctly identified by the tagger.  
 856 Given  $N^{\text{signal}}$  signal jets,  $N_{\text{tagger}}^{\text{signal}}$  of which have passed the algorithm's selection and  
 857  $N_{\text{untagger}}^{\text{signal}}$  of which have not, the efficiency is given by

$$\varepsilon = \frac{N_{\text{tagged}}^{\text{signal}}}{N_{\text{tagged}}^{\text{signal}} + N_{\text{untagged}}^{\text{signal}}}. \quad (4.1)$$

858 Meanwhile the *fake rate* is defined as the efficiency for a background class to be  
 859 selected, i.e.

$$\text{fake rate} = \frac{N_{\text{tagged}}^{\text{background}}}{N_{\text{tagged}}^{\text{background}} + N_{\text{untagged}}^{\text{background}}}. \quad (4.2)$$

860 The *rejection power* of the model is quantified for a given background as the reciprocal  
 861 of the fake rate, i.e.

$$\text{rejection power} = \frac{1}{\text{fake rate}}. \quad (4.3)$$

862 A *fixed-cut working point* (WP) defines the corresponding selection applied to the  
 863 tagging discriminant in order to achieve a given efficiency on the inclusive  $t\bar{t}$  sample.

### 864 4.2.2 Low-level Algorithms

865 The low-level algorithms are the first step in the  $b$ -tagging process. They take inputs  
 866 information about the jet and its associated tracks and reconstruct distinct features  
 867 of the experimental signature of heavy flavour jets. The low-level algorithms are a  
 868 combination of manually optimised reconstruction algorithms, for example SV1 and

869 JetFitter which reconstruct displaced decay vertices (see Section 3.4.2) and IPxD  
 870 which discriminates based on track IPs, and trained machine learning models such  
 871 as RNNIP and DIPS which use IP and hit information from a variable number of  
 872 tracks [95, 96].

### 873 4.2.3 High-level Algorithms

874 The high-level algorithms combine the outputs of the independently optimised low-  
 875 level algorithms using a multivariate approach to produce a discriminant value for  
 876 each jet. For example the MV2c10 algorithm, used in the analysis described in  
 877 Chapter 7, consists of a boosted decision tree which combines the outputs of IPxD,  
 878 SV1 and JetFitter [61, 97, 98]. The working point is tuned to achieve an average  $b$ -jet  
 879 efficiency of 70% on simulated  $t\bar{t}$  events. At this efficiency working point, rejection  
 880 factors for  $c$ -jets and light-jets are approximately 9 and 304 respectively.

881 The current ATLAS flavour tagger, DL1r [98], is part of a series of taggers that  
 882 use a deep neural network to combine the outputs of the low-level algorithms. The  
 883 low-level algorithms used by the different high-level taggers DL1, DL1r and DL1d is  
 884 shown in Fig. 4.1.

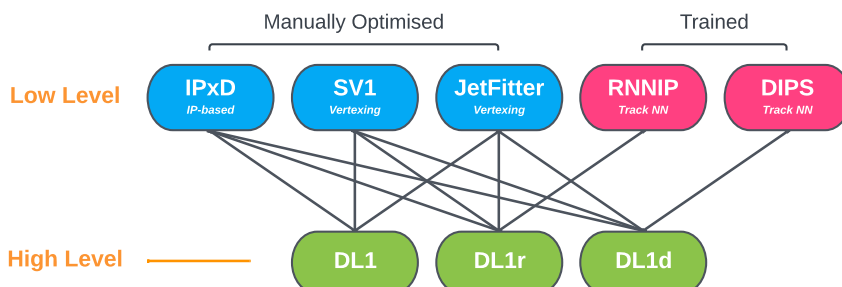


**Figure 4.1:** An overview of different high and low level level taggers used in ATLAS. The low level taggers are IPxD, SV1 and JetFitter, and RNNIP and DIPS [61, 62, 95, 96]. The outputs of these taggers are fed into the high-level taggers DL1, DL1r and DL1d [98, 99].

## 885 4.3 $b$ -hadron Reconstruction

886 This section outlines the typical detector signature of a  $b$ -hadron in Section 4.3.1  
 887 and discusses some associated reconstruction difficulties in Section 4.3.2.

### 888 4.3.1 Decay Topology

889  $b$ -hadrons are quasi-stable bound states of a bottom quark and one or more lighter  
 890 quarks. Collectively, these are the  $B$ -mesons (e.g.  $B^+ = u\bar{b}$ ,  $B^0 = d\bar{b}$ ) and baryons  
 891 (e.g.  $\Lambda_b^0 = udb$ ). After a  $b$ -quark is produced as the result of a proton-proton collision,  
 892 they quickly hadronise. The hadronisation process is hard – around 70-80% of  
 893 the  $b$ -quark’s momentum is passed to the  $b$ -hadron, with the rest being radiated  
 894 as prompt hadronisation or fragmentation particles. See Ref. [100] for a more in  
 895 depth discussion on hadronisation and the closely related process of fragmentation.  
 896 Henceforth the combined hadronisation and fragmentation products will be referred  
 897 to collectively as fragmentation.

898  $b$ -hadrons are interesting objects of study due to their relatively long proper lifetimes  
 899  $\tau \approx 1.5$  ps [101]. This lifetime corresponds to a proper decay length  $c\tau \approx 450$   $\mu\text{m}$ . In  
 900 the rest frame of the detector, the typical  $b$ -hadron travels a distance

$$d = \gamma\beta c\tau \approx \gamma c\tau \quad (4.4)$$

901 before decaying, where in the high energy limit  $\gamma = E_b/m_b$  and  $\beta = v/c = 1$ .

902 For a 50 GeV  $b$ -hadron, this gives  $d \approx 4.5$  mm, which is displaced enough to be  
 903 resolved from the primary vertex. Meanwhile for a 1 TeV  $b$ -hadron,  $d \approx 90$  mm –  
 904 well beyond the radius of the first pixel layer (the IBL) which is situated at a radius  
 905 of approximately 33 mm from the center of the detector (the distance varies due  
 906 to the interleaved structure) Fig. 4.2 shows how the mean decay radius varies as a  
 907 function of  $b$ -hadron  $p_T$ . This significant displacement is characteristic of  $b$ -jets and  
 908 makes it possible to reconstruct secondary vertices (SV) at the  $b$ -hadron decay point.

909  $b$ -hadrons decay weakly to on average four or five collimated stable particles [102].  
 910 These particles, along with any other fragmentation particles, are reconstructed in  
 911 the detector as a jet. A  $b$ -jet has several characteristic features which differentiate it

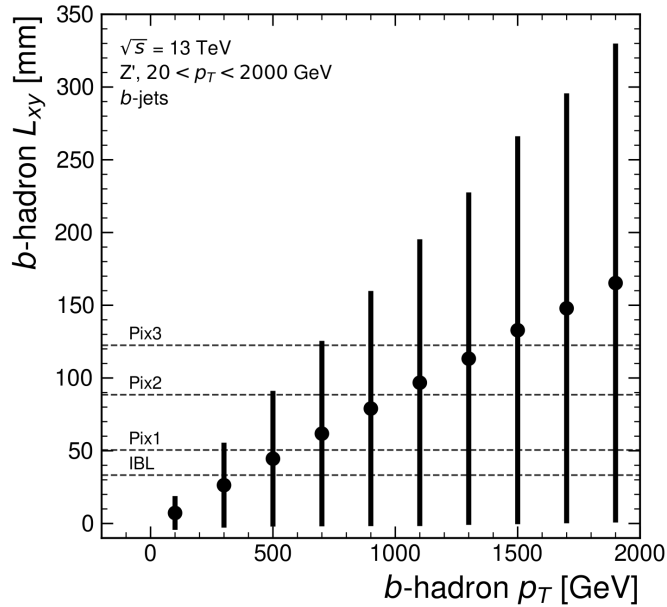


**Figure 4.2:** The truth  $b$ -hadron decay radius  $L_{xy}$  as a function of truth transverse momentum  $p_T$  for reconstructed  $b$ -jets in  $Z'$  events. Error bars show the standard deviation. The pixel layers are shown in dashed horizontal lines.

from light-jets. The primary feature is the presence of a high mass secondary vertex that is significantly displaced from the primary vertex. Reconstruction of these vertices from tracks with common points of spatial origin is a common approach used in the identification of  $b$ -jets.

Additional signatures of  $b$ -hadrons are as follows. Associated tracks and SVs can have a large transverse impact parameter  $d_0$  as a result of the  $b$ -hadron displacement (as shown in Fig. 4.3). Since it is common for the  $b$ -hadron to decay to a  $c$ -hadron with non-negligible lifetime, tertiary vertices can be found within  $b$ -jets resulting from  $b \rightarrow c$  decay chains. Additionally, as the  $b$ - or  $c$ -hadron decays semileptonically in approximately 40% of cases [16], the presence of a reconstructed electron or muon inside a jet gives information about the jet flavour.

These signatures are primarily identified using tracks associated to jets, or using reconstructed electrons or muons, which also rely on tracks as discussed in Section 3.4.4. As such, efficient and accurate track reconstruction is essential for high performance flavour tagging.

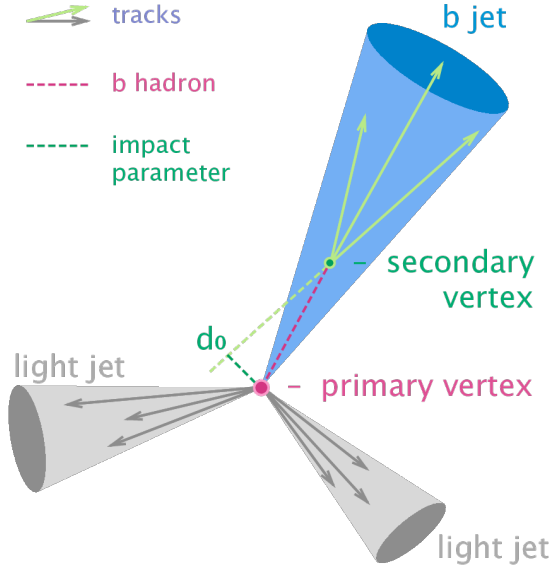


**Figure 4.3:** Diagram of a typical  $b$ -jet (blue) which has been produced in an event alongside two light jets (grey) [103]. The  $b$ -hadron has travelled a significant distance (pink dashed line) from the primary interaction point (pink dot) before its decay. The large transverse impact parameter  $d_0$  is a characteristic property of the trajectories of  $b$ -hadron decay products.

### 4.3.2 Challenges

As discussed, a necessary requirement for successful  $b$ -tagging is the efficient and accurate reconstruction of the charged particle trajectories in the jet. For high  $p_T$  jets ( $p_T > 200$  GeV) this task becomes difficult due to a combination of effects. As the  $b$ -jet energy increases, the multiplicity of the fragmentation products inside the jet increases, while the multiplicity of the products of the weak decay is unaffected. The “signal” tracks (those from the weak decay of the  $b$ -hadron) therefore become significantly outnumbered. Both fragmentation and  $b$ -hadron weak decay products also become increasingly collimated as their inherited transverse momentum increases. This is compounded by the increased decay length of  $b$ -hadrons (and  $c$ -hadrons) at high- $p_T$ , which means that the decay products have less of an opportunity to diverge before reaching the first tracking layers of the detector (shown in Fig. 4.4). If the weak decay of the  $b$ -hadron takes place close enough to a detector layer, or if the particles are otherwise sufficiently collimated, charge deposits left by nearby particles may not be resolved individually, instead being reconstructed as merged clusters [57].

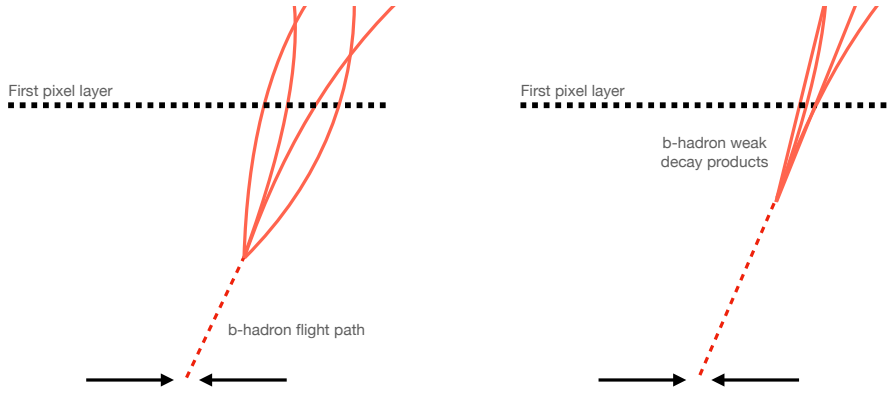


**Figure 4.4:** At lower  $p_T$  (left) the decay length of the  $b$ -hadron is on average reduced, and the decay tracks are less collimated. At higher  $p_T$  (right) the  $b$ -hadron decay length increases and the resulting decay tracks are more collimated and have less distance over which to diverge before reaching detector elements. As a result, the ID may be unable to resolve charged depositions from different particles, resulting merged clusters.

As discussed in Section 3.4.1, merged clusters are generally rare, and so shared hits generally predict bad tracks and are correspondingly penalised during track reconstruction. However, in the core of high  $p_T$   $b$ -jets the density of particles is high enough that the probability of cluster merging increases dramatically. Successful reconstruction of such tracks requires the presence of shared hits to be effectively dealt with but in the standard reconstruction the presence of these can end up impairing the successfully reconstruction of the track. Furthermore, decays may also take place inside the tracking detectors themselves, which at best leads to missing measurements on the most sensitive detector layers, and at worst can lead to wrong inner layer hits being added to displaced tracks, since the reconstruction process penalises tracks without inner layer hits.

The above effects create two related, but distinct problems for  $b$ -tagging. The first part is a drop in track reconstruction efficiency. The presence of shared and missing hits reduces a track's score in the ambiguity solver meaning that higher ranking, but potentially worse, track candidates are processed first and take ownership of the hits. This can make it difficult for otherwise reasonable  $b$ -hadron decay tracks to meet the ambiguity solver's stringent track quality requirements, leading to their rejection at this stage and an overall decrease in the  $b$ -hadron decay track reconstruction

efficiency. As shown in Fig. 4.5, this can result in a large drop in reconstruction efficiency for  $b$ -hadron decay products of up to 50% for at  $p_T = 2 \text{ TeV}$ .

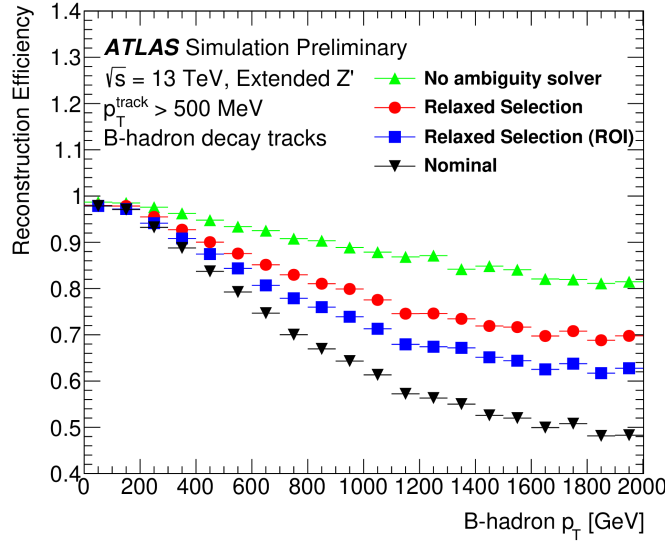


**Figure 4.5:**  $b$ -hadron decay track reconstruction efficiency as a function of truth  $b$ -hadron  $p_T$  [104]. Nominal track reconstruction is shown in black, while the track reconstruction efficiency for track candidates (i.e. the pre-ambiguity solver efficiency) is shown in green. For high- $p_T$   $b$ -hadrons, the ambiguity solver is overly aggressive in its removal of  $b$ -hadron decay tracks. Suggestions for the improvement of the track reconstruction efficiency in this regime by the loosening of cuts in the ambiguity solver are shown in blue and red.

The second part of the problem is that, due to the high multiplicity of clusters available for assignment in the vicinity of the typical high- $p_T$   $b$ -hadron decay track, and also given the strong positive bias of the ambiguity solver towards those tracks with pixel measurements in each layer (especially the innermost IBL measurement), many  $b$ -hadron decay tracks are assigned incorrect inner layer hits. This is only a problem for those decay products which were produced within the pixel detector as a result of a significantly displaced  $b$ -hadron decay, and so do not have a correct hit available for assignment. Fig. 4.6 shows the number of hits as a function of the reconstructed track  $p_T$  for fragmentation tracks and tracks from the weak decay of the  $b$ -hadron. The baseline tracks represent the standard reconstruction setup, while the pseudotracks represent the ideal tracking setup as outlined in Section 3.4.1. Hit multiplicities on the pseudotracks decrease at high  $p_T$  due to the flight of the  $b$ -hadron before its decay. The baseline tracks have more hits than the pseudotracks,

975 indicating that they are being incorrectly assigned additional hits on the inner layers  
 976 of the detector.

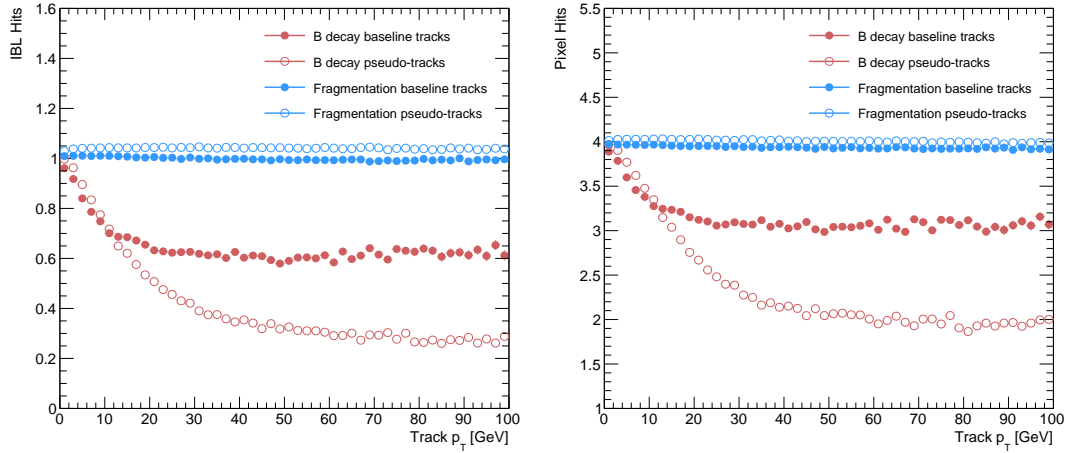


**Figure 4.6:** Hit multiplicities on the IBL (left) and the pixel layers (right) as a function of the  $p_T$  of the reconstructed track for tracks in jets in a  $Z'$  sample at  $\sqrt{s} = 13$  TeV. Tracks from the weak decay of the  $b$ -hadron are shown in red, while fragmentation tracks (which are prompt) are in blue. Baseline tracks are those produced in the standard reconstruction described in Section 3.4.1, while pseudotrack represent the ideal performance of the ATLAS detector and are described in Section 3.4.1.

977 These incorrect hits may skew the parameters of the track, which can in turn lower  
 978 the performance of the downstream  $b$ -tagging algorithms. In particular,  $b$ -tagging  
 979 algorithms rely heavily on the transverse impact parameter significance  $s(d_0)$  of the  
 980 track (see Section 3.2.2). The quality of this measurement is expected to be adversely  
 981 affected by wrong inner-layer hits on the track. Furthermore, multiple tracks sharing  
 982 an incorrect hit can lead to the creation of spurious secondary vertices, which can  
 983 cause further problems for the  $b$ -tagging algorithms.

984 The combination of the effects described makes reconstructing tracks in the core  
 985 of high  $p_T$   $b$ -jets particularly challenging. The reduced reconstruction efficiency of  
 986  $b$ -hadron decay tracks and incorrectly assigned hits is thought to be the primary  
 987 cause of the observed drop in  $b$ -tagging efficiency at high energies, however further  
 988 study is required to determine which effect may dominate.

## 989 4.4 Investigations into High $p_T$ $b$ -hadron Tracking

990 In Section 4.4.1 pseudotracks, a key tool for studying the ideal tracking performance  
991 of the ATLAS detector, are used to study the shared hit requirements on tracks in  
992 the dense cores of high- $p_T$   $b$ -jets. Section 4.4.2 details a study which investigated  
993 modifying the global track fitter to improve reconstruction performance in this  
994 regime.

### 995 4.4.1 Shared Hits

996 The ambiguity solver is not run for pseudotracks. However, if the standard track  
997 collection is produced alongside the pseudotracks, then cluster splitting neural  
998 networks will be run for the standard tracks, and the resulting classification of  
999 clusters will be propagated to hits on pseudotracks. This quirk allows one to study  
1000 the inefficiencies of the cluster splitting process, and relatedly to determine whether  
1001 shared hit cuts in the ambiguity solver are too loose or too tight. The fraction of hits  
1002 that are shared for the IBL and the B-layer is shown in Fig. 4.7. The shared hits on  
1003 pseudotracks represent correctly assigned hits from merged clusters that were not  
1004 able to be classified as split by the cluster splitting neural networks. As such, these  
1005 represent the number of shared hits the ambiguity solver should aim to allow given  
1006 the current performance of the cluster splitting algorithm. For shared hits on the IBL  
1007 for particles produced before the IBL, the baseline selection appears to be successful  
1008 in disallowing excessive numbers of shared hits. However, the ambiguity solver fails to  
1009 limit shared hits for those particles produced after the IBL, reflecting the previously  
1010 discussed problem of displaced tracks picking up incorrect hits. Meanwhile, it is clear  
1011 that for the B-layer, the ambiguity solver is being overly aggressive in its rejection of  
1012 shared hits.

### 1013 4.4.2 Global $\chi^2$ Fitter Outlier Removal

1014 This section documents ongoing studies into improving hit-to-track assignment by  
1015 using the Global  $\chi^2$  Fitter (GX2F) to identify and prevent incorrect hits from being  
1016 assigned to tracks during the track fit. This is in contrast to a previously investigated  
1017 approach [105] which attempted to identify and remove incorrect hits after the

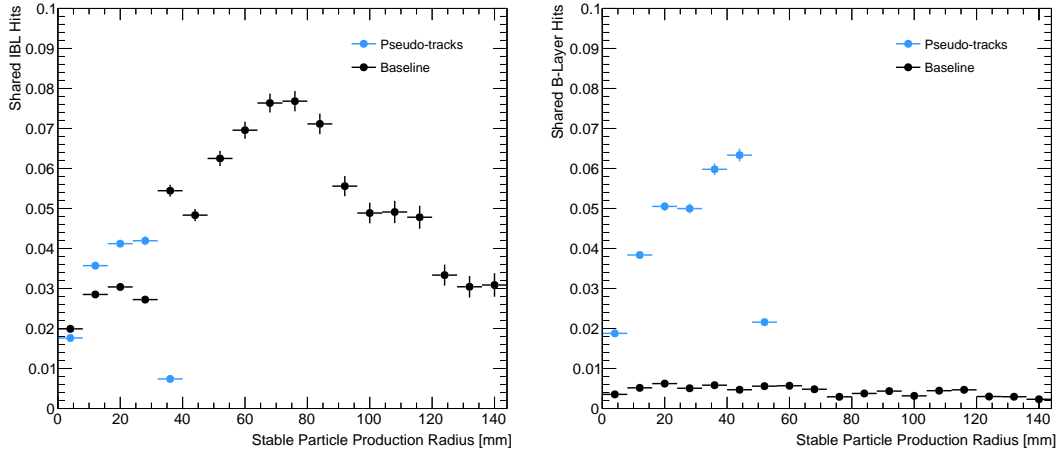


**Figure 4.7:** The fraction of IBL (left) and B-layer (right) hits which are shared on  $b$ -hadron decay tracks as a function of the production radius of the  $b$ -hadron decay product for tracks in jets in a  $Z'$  sample at  $\sqrt{s} = 13$  TeV. Pseudotrack represent the ideal performance given the ATLAS detector, see Section 3.4.1.

reconstruction of the track. As part of the track fit, an outlier removal procedure is run, in which suspicious hits are identified and removed.

The GX2F code, as a relatively low-level component of track reconstruction, has not undergone significant modification for several years, and was originally only optimised in the context of prompt, isolated tracks. During this time, a new tracking sub-detector, the IBL, was installed. The motivation for looking at the GX2F is that these changes may require re-optimisation of the GX2F code, and in particular the outlier removal procedures. Further motivation for this approach comes from the low rate of labelled outliers in baseline tracking, in contrast to the relatively higher rate of tracks with an incorrect IBL hit.

## Implementation

The outlier removal procedure for the pixel detector is described in this section. The hits on the track are looped over in order of increasing radial distance to the beam pipe. For each hit, errors  $\sigma(m_i)$  on the measurement of the transverse and longitudinal coordinates are calculated. These errors are dependent on the sub-detector which recorded the measurement (some sub-detectors are more precise than others). Additionally, a residual displacement  $r_i = m_i - x_i$  between the predicted

1035 position of the track  $x_i$  (inclusive of the current measurement), and the position of  
1036 the hit itself,  $m_i$ , is calculated. The pull  $p_i$  on the track state due to the current  
1037 measurement is calculated according to

$$p_i = \frac{m_i - x_i}{\sqrt{\sigma(m_i)^2 - \sigma(x_i)^2}} \quad (4.5)$$

1038 This pull is computed for the transverse and longitudinal coordinates of the mea-  
1039 surement, and the maximum of the two is selected and checked to see if it exceeds  
1040 a certain selection threshold. If it does, the hit will be removed if the track also  
1041 exceeds a threshold on the total  $\chi^2/n$ , where  $n$  is the number of degrees of freedom  
1042 on the track. The results of varying the outlier selection and  $\chi^2/n$  thresholds are  
1043 described below.

#### 1044 Selection Optimisation

1045 A systematic variation of the outlier selection and  $\chi^2/n$  thresholds has been carried  
1046 out. Both thresholds were reduced in fixed step sizes of 0.25 for the outlier selection  
1047 threshold and 1 for the  $\chi^2/n$  threshold. The results for the best performing selections  
1048 are discussed below. The value of the outlier selection threshold was reduced from 4  
1049 down to 1.75, a change which affects the silicon layers (the TRT has separate outlier  
1050 removal logic). Furthermore, a specific cut for the IBL was introduced, and after  
1051 optimisation is set to 1.25. The second threshold on the track  $\chi^2/n$  was also reduced  
1052 from 7 to 4. Finally, instead of taking the maximum of the pulls in the longitudinal  
1053 and transverse directions, a quadrature sum is taken of these two values and used.  
1054 This variation is labelled “Mod GX2F” and was found to improve performance.

1055 The results are shown in Fig. 4.8 and demonstrate a reduction in wrong hit assignment  
1056 whilst also improving slightly the rate at which good hits are assigned to tracks. For  
1057 a 1 TeV track, the rate to assign good hits to the track increases by approximately  
1058 10%, while the rate to assign incorrect hits decreases by approximately 16%. The  
1059 improvements are also observed when looking inclusively in all tracks, which avoids  
1060 the need for a specific  $b$ -jet region-of-interest selection.

1061 An improvement, though modest, of all track parameter resolutions and pulls is  
1062 observed. The improvement for the transverse impact parameter pull is shown in

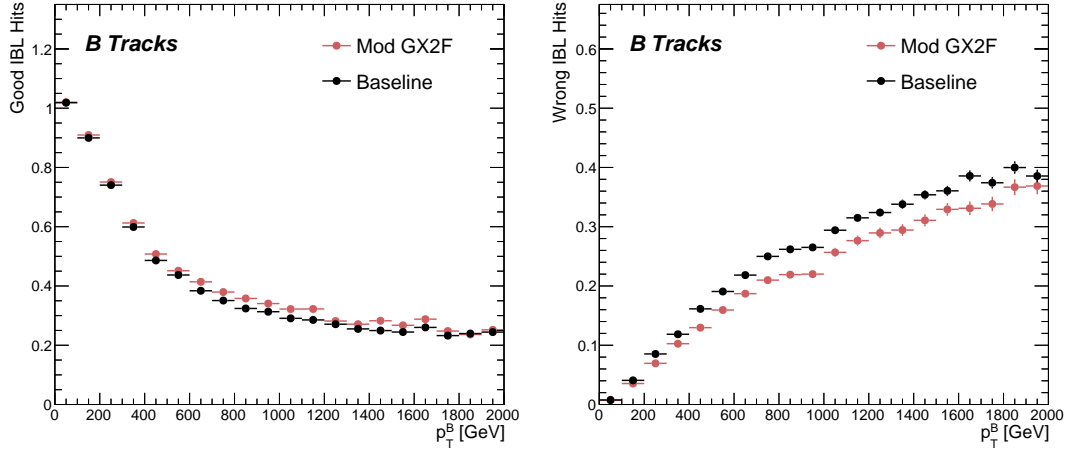


**Figure 4.8:** The average number of good (left) and wrong (right) IBL hits as a function of  $b$ -hadron  $p_T$  for tracks using baseline tracking (black) and the modified version of the outlier removal procedure (red).

1063 Fig. 4.9. The results demonstrate an improvement in hit assignment, unchanged  
 1064 reconstruction efficiency, and modest improvement in track parameter resolutions  
 1065 and pulls. In addition, the truth match probability of tracks is unchanged, suggesting  
 1066 that there is no increase in fake track rates. The changes are expected to have a  
 1067 negligible impact on computational resources.

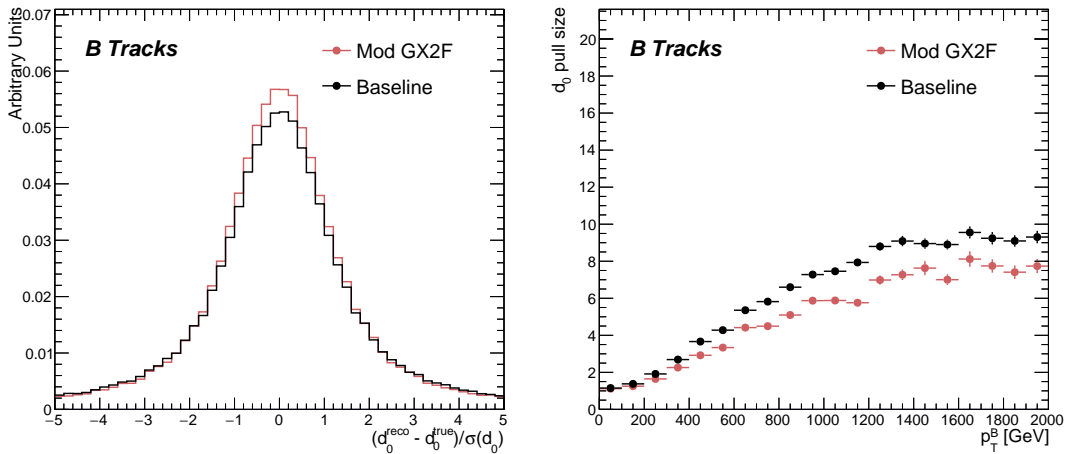


**Figure 4.9:** (left)  $b$ -hadron decay track  $d_0$  pulls ( $d_0/s(d_0)$ ) for baseline and modified GX2F tracks. (right) The absolute value of the  $d_0$  pull as a function of the truth  $b$ -hadron transverse momentum.

## 1068 4.5 Conclusion

1069 In this section, the difficulties facing efficient and accurate track reconstruction,  
1070 and hence performant  $b$ -tagging, have been outlined. The ambiguity solver, which  
1071 attempts to clean or reject tracks which have an excessive number of shared hits,  
1072 is shown to be overly aggressive in the removal of  $b$ -hadron decay product track  
1073 candidates. The ambiguity solving process relies on a complicated pre-defined  
1074 selection which has not been optimised for high transverse momentum  $b$ -hadron  
1075 track reconstruction. These conclusions have motivated further ongoing studies into  
1076 the improvement of the track reconstruction in dense environments and the high- $p_T$   
1077 regime, such as those in Ref. [104].

1078 An optimisation of the outlier removal process in the global  $\chi^2$  fitter was carried out.  
1079 The results of the optimisation show that more aggressive removal of outlier hits can  
1080 lead to fewer wrong hits being assigned to tracks, and improvements in the pulls of  
1081 the track parameters.

## 1082 Future Work

1083 The studies were carried out in Release 21 of the ATLAS software, and need to be  
1084 reproduced using the newer Release 22 to confirm the results against other changes  
1085 in the baseline tracking configuration. It is also necessary to study the impact of  
1086 the improved outlier removal on the downstream  $b$ -tagging algorithms. Thanks to  
1087 the all-in-one flavour tagging approach described in Chapter 6, this will in future be  
1088 easier to study.

1089 As there are some known data-MC discrepancies, fine tuned optimisation such as the  
1090 work presented here presents an opportunity to over-optimize the tracking algorithms  
1091 on MC. As such, further studies validating the improved outlier removal procedure  
1092 on data are required.

1093 **Chapter 5**

1094 **Track Classification MVA**

1095 This chapter details work on implementing a multivariate algorithm (MVA) to predict  
1096 the truth origin of reconstructed tracks. An introduction to formalisms of machine  
1097 learning is given in Section 5.1. In Section 5.2, the truth origin label is defined,  
1098 and in Section 5.3 these labels are used to train a machine learning model that can  
1099 effectively discriminate between good and fake tracks. Several studies motivated this  
1100 work by demonstrating that at high  $p_T$ ,  $b$ -tagging performance was degraded by the  
1101 presence of large numbers of poorly reconstructed or fake tracks. If an algorithm  
1102 could be trained to detect fake tracks, these could be removed before their input to  
1103 the  $b$ -tagging algorithms with the aim of improving performance. In addition, other  
1104 groups that are sensitive to the presence of fake tracks would also benefit from this  
1105 work.

1106 **5.1 Machine Learning Background**

1107 Over the past few decades, machine learning (ML) techniques have become increas-  
1108 ingly popular in High Energy Physics experiments due the increased volumes of  
1109 high-dimensional data and improvements in the techniques used (in particular deep  
1110 learning). Machine learning is the process by which a computer program uses data  
1111 to learn suitable parameters for a predictive model. This is opposed to explicitly  
1112 providing instructions on how to perform a task. A subfield known as *supervised*  
1113 *learning* is used in this work, and consists of exposing a model to a large number of  
1114 labelled examples in order to extract relationships between the input data and their

1115 labels. These relationships are often complex, and explicitly programmed rules can  
1116 fail to fully capture the relationships between inputs and outputs.

1117 In the simplest case, a set of  $m$  labelled training examples  $S = \{(x_1, y_1), \dots, (x_m, y_m)\}$   
1118 is collected. Each element  $(x_i, y_i)$  consists of a input vector  $x_i \in \mathbb{R}^{\text{input}}$ , and the  
1119 corresponding label  $y_i$ . In classification problems, these labels are integer *class labels*  
1120  $y_i \in \{0, \dots, N - 1\}$ , where  $N$  is the number of classes, which specify which of a  
1121 pre-determined set of categorical classes the training example belongs to. The rest  
1122 of the discussion in this chapter is limited to binary classification problems ( $N = 2$ ).  
1123 The two classes are often referred to as signal ( $y_i = 1$ ) and background ( $y_i = 0$ ),  
1124 which need to be separated. Collecting sufficient and suitable data is one of the  
1125 primary challenges of machine learning, as such data is not always readily available.  
1126 Fortunately, sophisticated tools to simulate particle collisions have already been  
1127 developed by the scientific community [106, 107]. These tools play a key role in  
1128 generating a suitably large amount of labelled data which is used to train algorithms.  
1129 More detail on the input datasets is given in Section 4.1.

1130 After obtaining suitable training data, the next step is to define a model. Given an  
1131 input domain  $\mathbb{R}^{\text{input}}$  and an output domain  $(0, 1)$ , the model  $f_\theta : \mathbb{R}^{\text{input}} \rightarrow (0, 1)$  is a  
1132 parameterised functional mapping from input space to output space. Given an input  
1133 example  $x_i$  and a set of parameters  $\theta$ , the model outputs a prediction  $\hat{y}_i \in (0, 1)$  for  
1134 the true label  $y_i$ , as in

$$f_\theta(x_i) = \hat{y}_i. \quad (5.1)$$

1135 The output  $\hat{y}_i$  is in the interval  $(0, 1)$  so as to be interpreted as the probability that  
1136 the input example  $x_i$  belongs to the signal class. The parameters  $\theta$  of the model are  
1137 randomly initialised, and the model is designed to be expressive enough to correctly  
1138 map the inputs  $x_i$  to the outputs  $y_i$  given a reasonable optimisation of the parameters.  
1139 To perform this optimisation, the model is then trained, which amounts to showing  
1140 the model a series of labelled training examples and modifying the parameters of the  
1141 model based on its ability to correctly predict the labels.

### 5.1.1 Neural Networks

Neural networks (NNs) are a common choice for the machine learning model  $f$  since they have the ability to approximate any function [108] and are easy to train via backpropagation [109].

#### Artificial Neurons

The basic functional component of a NN is the *artificial neuron* or node, which is loosely inspired by a mathematical model of a biological neuron [110, 111]. A diagram of an artificial neuron is shown in Fig. 5.1. Each neuron is defined by its parameters or *weights*  $\theta$  and a choice of activation function. Each neuron takes a fixed number of inputs and computes the dot product of the input and weight vectors  $x^T\theta$  and additionally adds a constant bias term  $\theta_0$ . This term plays the role of a trainable constant value that is independent of the inputs.

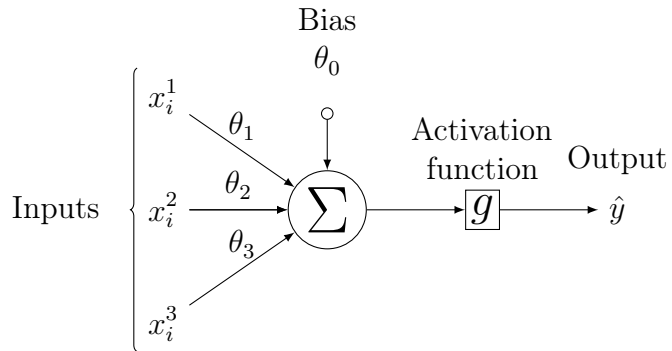


**Figure 5.1:** A diagram displaying the logical flow of a single neuron with three inputs  $x_i^j$ . Each input is multiplied by a weight  $\theta_j$ , and the resulting values are summed. A bias term  $\theta_0$  is added, and the result  $z$  is passed to an activation function. Each neuron can be thought of as a logistic regression model.

The output of the dot product and bias term  $z$  is fed into an activation function  $g(z)$ . The activation function has several uses, most notably acting as a source of non-linearity and bounding the output of the neuron. Some common activation functions (sigmod, tanh, ReLU and SiLU) [112, 113] are shown in Fig. 5.2. The choice of activation function can have implications for the performance and convergence of the network, since the gradient of  $g(z)$  is used to compute the weight updates during

1160 training. This is also why input data is typically normalised to have zero mean and  
1161 unity variance [114].

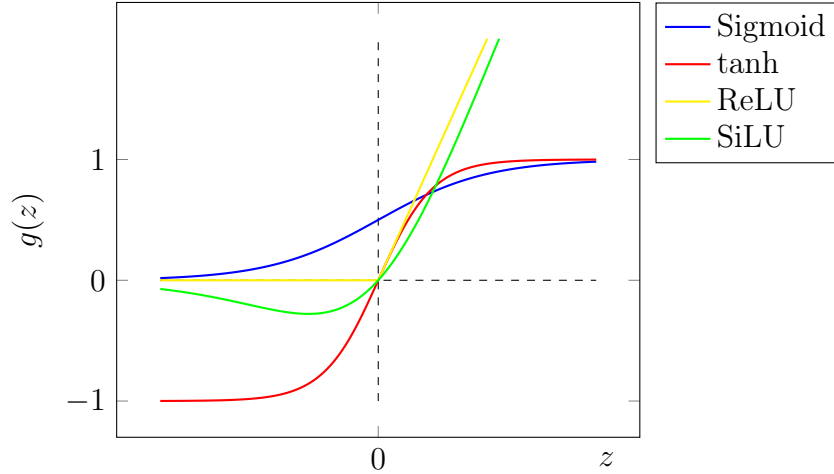


**Figure 5.2:** The output of several common choices for the activation function  $g(z)$  of an artificial neuron. The input  $z$  is the output of the dot product between the activation and the weights, plus a bias term.

1162 **Networks**

1163 Several neurons are linked together in layers to form a neural network. The inputs  
1164 are propagated layer-by-layer through the network until reaching the final output  
1165 layer. The number of layers and neurons per layer are important hyperparameters  
1166 (those parameters which are not optimised as part of the training process) which  
1167 influence the performance of the model. In the case of binary classification, the final  
1168 output layer generally consists of a single neuron with a sigmoid activation

$$g(z) = \frac{1}{1 + e^{-z}}, \quad (5.2)$$

1169 where  $z$  is the output from the dot product of the inputs and the weights, plus the  
1170 bias term. This value is bounded between zero and one allowing the final output to  
1171 be interpreted as the probability that the input sample belongs to the signal class.  
1172 NNs have the crucial property of being differentiable functions, which facilitates the  
1173 training process described in the next section.

### 1174 5.1.2 Training with Gradient Descent

1175 A training algorithm is used to optimise the weights and biases of a NN after  
1176 exposure to the training data. The training algorithm works by minimising a loss  
1177 function  $L$ , which quantifies the error in the model's predictions. NNs are commonly  
1178 trained using backpropagation in combination with a variant of the stochastic gradient  
1179 descent algorithm to iteratively update the model parameters. In binary classification  
1180 problems, the binary cross entropy given in Eq. (5.3) loss if often used.

$$L(x_i, \theta) = y_i \ln[f_\theta(x_i)] + (1 - y_i) \ln[1 - f_\theta(x_i)] \quad (5.3)$$

1181 Since the model  $f$  is differentiable, a correction for each parameter  $\theta_i$  can be computed  
1182 by taking the partial derivative of  $L$  with respect to the parameter. Updated  
1183 parameters  $\theta'_i$  are calculated by updating the original parameter in the direction  
1184 which reduces the loss.

$$\theta'_i = \theta_i - \alpha \frac{\partial L}{\partial \theta_i} \quad (5.4)$$

1185 The hyperparameter  $\alpha$  is known as the *learning rate* and dictates the size of the  
1186 step taken in the direction of the slope. The errors for each parameter are efficiently  
1187 calculated using the backpropagation algorithm [109]. The process of updating  
1188 weights is repeated until the weights are judged to have converged, which means the  
1189 network is trained. In practice, small batches of the input data are shown to the  
1190 network at a time. For each batch the average loss is calculated and the network's  
1191 weights are updated. There are many extensions and variations of the gradient  
1192 descent algorithm. This work uses the Adam optimiser which adds momentum to  
1193 the weight updates (dampening oscillations) and an adaptive per-parameter learning  
1194 rate [115].

## 1195 5.2 Track Truth Origin Labelling

1196 Crucial to supervised learning techniques are the ground truth class labels which the  
1197 machine learning model is trained to predict. A set of track truth labels which a  
1198 high degree of granularity have been implemented in the ATLAS software stack, and  
1199 are listed in Table 5.1. The labelling scheme has been designed to be useful beyond

the classification of good and fake tracks. The origins are determined by analysing the simulated record to determine the physical process that led to the creation of the truth (i.e. simulated) particle which is associated with each reconstructed track. Tracks are associated with truth particles by selecting the particle with the highest *truth-matching probability* (TMP), defined in Eq. (5.5). For a given truth particle, the TMP is a weighted sum of the number of hits on a reconstructed track which are matched to the truth particle  $N^{\text{match}}$ , divided the total number of hits on the track  $N^{\text{total}}$ . The weights are subdetector-dependent and are designed to account for the varying importance of the different ID subdetectors (based upon their precision) in the reconstruction of a track.

$$\text{TMP} = \frac{10N_{\text{Pix}}^{\text{match}} + 5N_{\text{SCT}}^{\text{match}} + N_{\text{TRT}}^{\text{match}}}{10N_{\text{Pix}}^{\text{total}} + 5N_{\text{SCT}}^{\text{total}} + N_{\text{TRT}}^{\text{total}}} \quad (5.5)$$

For the fake track classification tool, the track truth origins in Table 5.1 are used to construct a binary label by assigning all fake tracks to the background category, and all other tracks as signal. The fake track classifier is then trained to distinguish between these two categories of tracks. Fake tracks are defined using the TMP, with a  $\text{TMP} < 0.75$ <sup>1</sup> giving a track the label of fake. Fake tracks are made up of combinatorial fakes, which are tracks which do not correspond to the trajectory of any truth particle, and poorly reconstructed tracks, which may somewhat resemble the trajectory of a truth particle but due to the presence of some wrong hits on the track will not accurately reproduce the true trajectory. In such cases the fake track can still be identified as having an origin: it is for example possible to have a fake track which is from the decay of a  $b$ -hadron.

### 5.3 Fake Track Identification Tool

The rate of fake tracks increases at high transverse momentum as shown in Fig. 5.3 due to the difficulties in track reconstruction outlined in Section 4.3.2. The performance of  $b$ -tagging algorithms is reduced as a direct result of the presence of these tracks as

---

<sup>1</sup>An alternative definition of a fake track as one with  $\text{TMP} < 0.5$  is also in use within ATLAS, but 0.75 was used for this study.

Truth Origin	Description
Pile-up	From a $pp$ collision other than the primary interaction
Fake	Created from the hits of multiple particles
Primary	Does not originate from any secondary decay
fromB	From the decay of a $b$ -hadron
fromBC	From a $c$ -hadron decay which itself is from the decay of a $b$ -hadron
fromC	From the decay of a $c$ -hadron which is not from the decay of a $b$ -hadron
OtherSecondary	From other secondary interactions and decays

**Table 5.1:** Truth origins which are used to categorise the physical process that led to the production of a track. Tracks are matched to charged particles using the truth-matching probability [57]. A truth-matching probability of less than 0.75 indicates that reconstructed track parameters are likely to be mismeasured and may not correspond to the trajectory of a single charged particle. The “OtherSecondary” origin includes tracks from photon conversions,  $K_S^0$  and  $\Lambda^0$  decays, and hadronic interactions.

1225 shown for SV1 (see Section 3.4.2) in Fig. 5.4, where the efficiency to mistag a light-jet  
 1226 decreases by up to 35% at a  $b$ -jet efficiency of 35% if such tracks are removed.

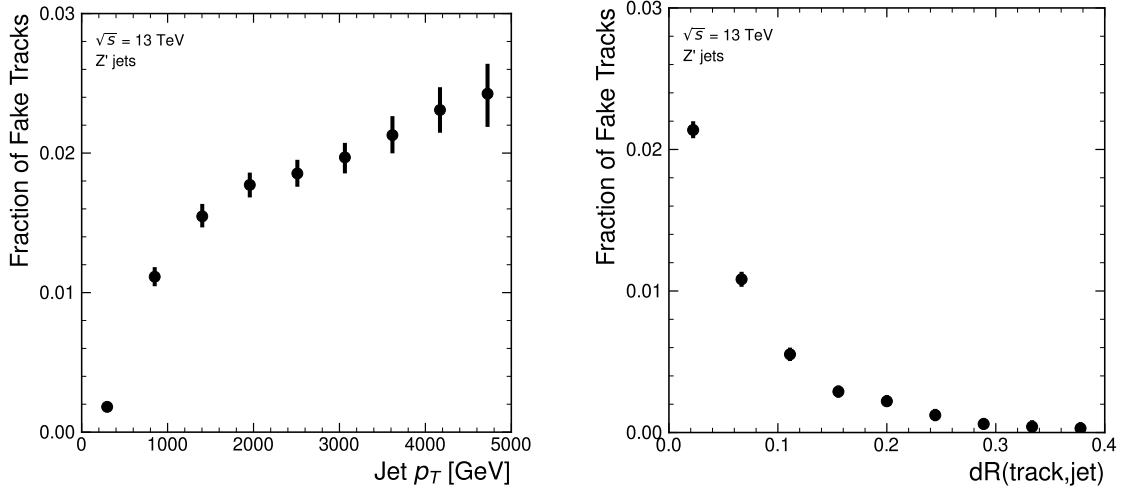


**Figure 5.3:** Rate of fake tracks as a function of jet transverse momentum (left) and  $\Delta R(\text{track},\text{jet})$  (right) for jets in the  $Z'$  sample. The rate of fake tracks increases significantly as a function of  $p_T$ , and also increases as the distance to the jet axis decreases.

1227 To identify and remove fake tracks, a NN classification tool was trained with all  
 1228 non-fake tracks as the signal class and fake tracks as the background class. Inputs to  
 1229 the model are described in Section 5.3.1, while fake track removal performance is

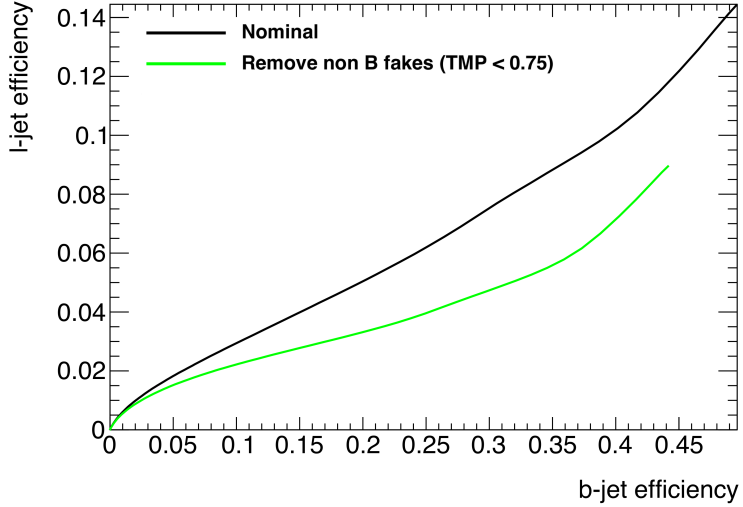


**Figure 5.4:** The light-jet efficiency of the low level tagger SV1 for jets in the  $Z'$  sample with  $250 < p_T < 5000$  GeV, as a function of  $b$ -jet efficiency. The nominal tracking setup (black) is shown alongside the case where fake tracks which are not from the decay of a  $b$ -hadron are removed. The light-jet efficiency is decreased, demonstrating that the presence of fake tracks is detrimental to the algorithm performance.

1230 given in Section 5.3.3. Both models are trained and evaluated using jets from the  $t\bar{t}$   
 1231 and  $Z'$  samples described in Section 4.1

### 1232 5.3.1 Model Inputs

1233 The fake track MVA is given two jet variables and 20 tracking related variables  
 1234 for each track fed into the network. The jet transverse momentum and signed  
 1235 pseudorapidity constitute the jet-level inputs, with the track-level inputs listed in  
 1236 Table 5.2.

1237 The track parameters and hit pattern are key indicators of whether or not a track  
 1238 is fake. The FracRank variable is the ordered index of the tracks that pass the  
 1239 ambiguity solver's selection divided by the total number of successfully reconstructed  
 1240 tracks in the event. The ambiguity solver processes track candidates iteratively  
 1241 in order of an internal score (see Section 3.4.1), and the order in which tracks are  
 1242 accepted is preserved. Since tracks with shared hits have lower scores, tracks which  
 1243 do not require the removal of shared hits are likely to be processed and accepted

Jet Input	Description
$p_T$	Jet transverse momentum
$\eta$	Signed jet pseudorapidity
Track Input	Description
$p_T$	Track transverse momentum
$\Delta R$	Angular distance between the track and jet
$d_0$	Closest distance from the track to the PV in the longitudinal plane
$z_0$	Closest distance from the track to the PV in the transverse plane
nIBLHits	Number of IBL hits
nPixHits	Number of pixel hits
nSCTHits	Number of SCT hits
nTRTHits	Number of TRT hits
nBLHits	Number of B-layer hits
nIBLShared	Number of shared IBL hits
nIBLSplit	Number of split IBL hits
nPixShared	Number of shared pixel hits
nPixSplit	Number of split pixel hits
nSCTShared	Number of shared SCT hits
$r_{\text{first}}$	Radius of first hit
nDOF	Number of degrees of freedom on the track
FracRank	Ambiguity solver ordering variable

**Table 5.2:** Input features to the fake track classification NN. Basic jet kinematics, along with information about the reconstructed track parameters and constituent hits are used. Shared hits, are hits used on multiple tracks which have not been classified as split by the cluster-splitting neural networks [57], while split hits are hits used by multiple tracks which have been identified as merged, and therefore split.

1244 earlier on, whereas tracks with shared hits will be processed later and potentially  
1245 have their shared hits removed. Hence the FracRank variable gives an indication  
1246 of the track quality and how likely it is that hits would have been removed (tracks  
1247 processed later on are more likely to have hits removed).

1248 Track selection follows the loose selection described in Ref. [96] and outlined in  
1249 Table 3.2, which was found to improve the performance compared to previous tighter  
1250 selections, whilst ensuring good resolution of the track’s parameters and a low fake  
1251 rate [57]. Inputs are scaled to have a central value of zero and a variance of unity  
1252 before training and evaluation.

### 1253 5.3.2 Model Hyperparameters

1254 Due to the imbalance between the two classes (with fake tracks being relatively  
1255 uncommon), a weight was added to the loss function for the background class to  
1256 balance their relative weights. The NN was made up of two hidden layers with  
1257 220 nodes per layer. The ReLU activation function was used in conjunction with  
1258 the Adam optimiser with a learning rate of  $1e-3$ . Optimisation of the networks  
1259 architecture was carried out to ensure optimal performance with a relatively small  
1260 number of learnable parameters – 54,000. The model was trained using 40 million  
1261 tracks with a further 4 million tracks each used for validation and testing. A full list  
1262 of the model hyperparameters is given in Table 5.3.

Hyperparameter	Value
Batch size	2048
Activation	ReLU
Optimiser	Adam
Initial learning rate	$1e-3$
Training epochs	20
Training tracks	40m
Validation tracks	4m
Testing tracks	4m

**Table 5.3:** Hyperparameter for the track classification model

### 5.3.3 Results

In order to evaluate the fake track classification tool, a orthogonal test sample of 4 million tracks in jets in the combined  $t\bar{t}$  and  $Z'$  samples was used. The continuous scalar output from the NN model is interpreted as the probability that a given track is a signal track (i.e. not fake). Fig. 5.5 shows the performance of the fake track classification MVA. The signal and background classes are well separated in the output of the tool. Also shown is a receiver operating characteristic (ROC) curve, which plots the rate of true positives against the rate of false positives over a scan of cut points on the NN output ranging from zero to one. The area under the curve (AUC) gives a summary of the aggregate classification power of the model. The fake track classification tool achieves an AUC of 0.935 for all tracks, which is indicative of a well-performing model. Considering only tracks from  $b$ -hadron decays, this value drops slightly to 0.928.

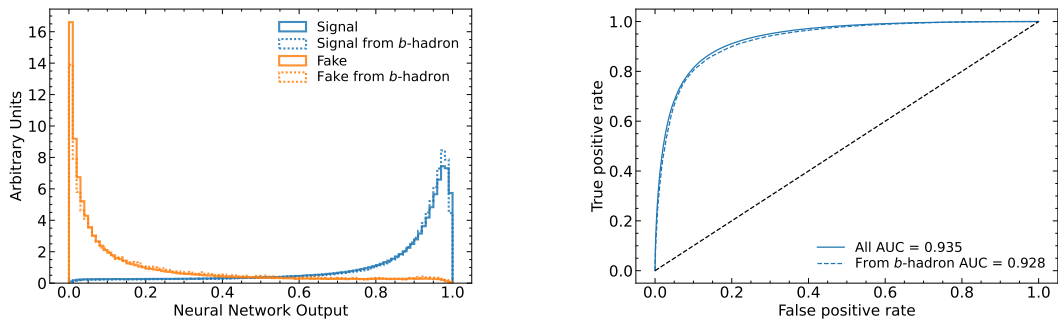


**Figure 5.5:** (left) Normalised histograms of the fake track classification model output separated for signal and fake tracks, and further separated by those tracks which are from the decay of a  $b$ -hadron. (right) The ROC curve for all tracks (solid line) and tracks from the decay of a  $b$ -hadron (dashed line). The plots show tracks in the combined  $t\bar{t}$  and  $Z'$  testing sample. The model is able to successfully discriminate between signal and fake tracks, and shows a very similar performance when looking specifically at tracks from the decay of a  $b$ -hadron.

Signal and fake track efficiencies at two different NN output cut points are shown in Table 5.4. The results demonstrate that the tool is effective in retaining 98.8% of signal tracks, while correctly identifying (and therefore enabling the removal of) 45.6% of fake tracks. Table 5.4 also shows that a significant amount of tracks which are labelled as both fake and from the decay of a  $b$ -hadron are also removed. This can

1281 happen because fake tracks with  $\text{TMP} < 0.75$  are still matched to a truth particle,  
1282 which can be the decay product of a  $b$ -hadron.

MVA Output Cut	Signal Track Efficiency		Fake Track Efficiency	
	All	From $b$	All	From $b$
0.06	98.8%	98.9%	45.6%	39.8%
0.12	97.3%	97.5%	59.4%	53.6%

**Table 5.4:** Good and fake track selection efficiencies for the combined  $t\bar{t}$  and  $Z'$  samples. Two working points are defined, cutting on the NN output at 0.06 and 0.12.

## 1283 5.4 $b$ -hadron Track Identification

1284 After initial tests and investigation, it was found that fake tracks which were the  
1285 result of  $b$ -hadron decays actually aided  $b$ -tagging performance, as demonstrated in  
1286 Fig. 5.7. The application of a single tool which removed all fake tracks was therefore  
1287 not optimal. A second tool was therefore trained in the same manner as the first,  
1288 this one was designed to distinguish between those tracks which were from the decay  
1289 of a  $b$ -hadron (FromB and FromBC in Table 5.1) and those which were not (all other  
1290 truth origins). Fake tracks which were from the decay of a  $b$ -hadron were included in  
1291 the signal class. The  $b$ -hadron decay track MVA was trained using the same setup  
1292 as described above, with the same tracks, input variables, and training procedure.  
1293 The performance of the model to separate  $b$ -hadron decay tracks from other tracks  
1294 is shown in Fig. 5.6. Using a selection WP of 0.1, the model can retain 98.5% of  
1295  $b$ -hadron tracks and reject 46.2% of tracks not from the decay of a  $b$ -hadron. In  
1296 Section 5.5, this model is used in conjunction with the fake track identification MVA  
1297 to identify and remove fake tracks which are not from the decay of a  $b$ -hadron.

## 1298 5.5 Combined Approach

1299 A 2-dimensional cut was then used to only reject those tracks that had a high  
1300 probability of being fake, and also a low probability of being a  $b$ -hadron decay track.  
1301 The results of the combined approach are provided in Table 5.5, which shows that

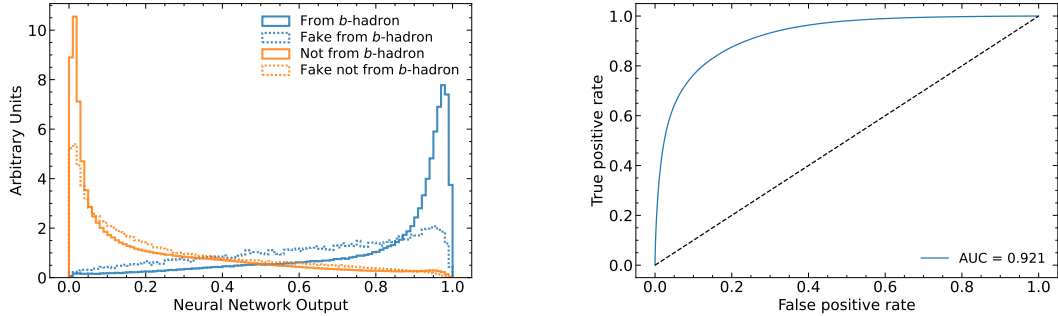


**Figure 5.6:** (left) Normalised histogram of the  $b$ -hadron track identification model output separated for tracks from the decay of a  $b$ -hadron and tracks from other sources. The two groups are further separated into those tracks which are fake. (right) The ROC curve for all tracks (solid line). The plots show tracks in the combined  $t\bar{t}$  and  $Z'$  testing sample.

1302 for the working point “A”, 98.6% of  $b$ -hadron decay tracks (both good and fake) are  
 1303 retained, while 50.7% of fake tracks which are not from  $b$ -hadron decays are rejected.

WP	Fake MVA Cut	$b$ -hadron Decay MVA Cut	Retained $b$ -hadron Tracks	Fake non- $b$ -hadron Tracks Rejected
A	0.5	0.4	98.6%	50.7%
B	0.6	0.5	97.5%	62.0%

**Table 5.5:** Cut values for the fake and  $b$ -hadron decay track MVAs for the two defined working points. Working point “B” cuts more aggressively on the MVA outputs than WP “A”, removing more fake tracks but resulting in an increased loss of signal tracks (which here are all  $b$ -hadron decay tracks).

1304 The light-jet efficiency of SV1 is successfully reduced when using the combined tools  
 1305 to remove fake tracks that are not from a  $b$ -hadron decay, as shown in Fig. 5.7. At a  
 1306  $b$ -jet efficiency of 70%, the light-jet mistag rate for jets with  $250 < p_T < 400$  GeV  
 1307 is reduced from 0.054 to 0.044, a relative improvement of approximately 20%. For  
 1308 jets with  $400 < p_T < 1000$  GeV the mistage rate drops from 0.1 to 0.08 for a similar  
 1309 relative improvement of 20%. The performance of the fake track removal approach  
 1310 was also tested for the other low level vertexing algorithm – JetFitter. A similar level  
 1311 of improvement in the light-jet mistag rate was observed with a reduction of up to a  
 1312 20% reduction for both low- and high- $p_T$  jets in the  $Z'$  sample achieved. Together,  
 1313 these results demonstrate that by identifying and removing fake tracks which are not

the result of the weak decay of a  $b$ -hadron, the performance of the low level tagging algorithms can be improved by an amount which is comparable to the improvement that would be observed if the tracks were selected at truth level1.

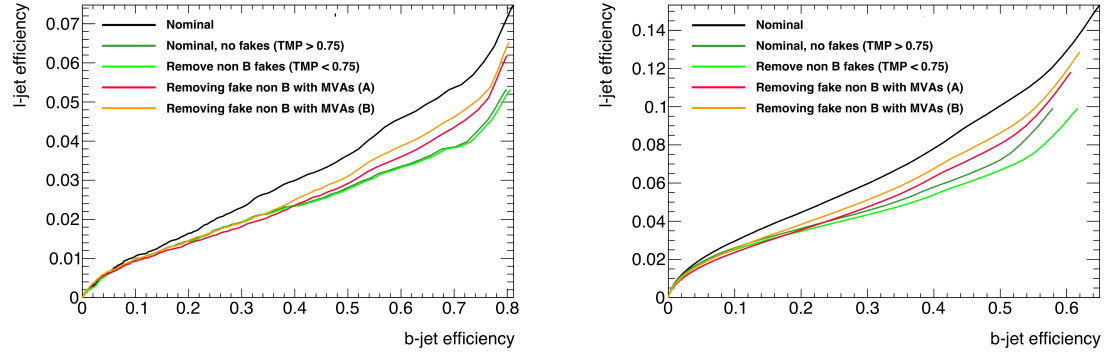


**Figure 5.7:** The effect of applying the fake track identification algorithm together with the  $b$ -hadron decay track identification on the jet tagging performance of SV1 for jets in the  $Z'$  sample with  $250 \text{ GeV} < p_T < 400 \text{ GeV}$  (left) and  $400 \text{ GeV} < p_T < 1 \text{ TeV}$  (right). The nominal SV1 light-jet rejection (black) is compared to two working points of fake track removal, labelled “A” (red) and “B” (orange), which represent two different 2D working points of the track classification tools. Removal of fake tracks based on truth information is shown by the green curves.

## 5.6 Conclusion

Fake tracks, which are prevalent in the core of high  $p_T$  jets, have an adverse impact on  $b$ -tagging performance. A ML tool to identify fake tracks has been developed, which can be used to limit the number of fake tracks being input to the  $b$ -tagging algorithms. An advantage of the approach is that the continuous output of the model allows for the tuning of good and fake track identification efficiencies. Since it was found that  $b$ -hadron decay tracks can also be poorly reconstructed and thus marked as fake, it was deemed necessary also to train a second algorithm to detect  $b$ -hadron decay tracks so that the removal of these tracks could be avoided. Removing fake and non- $b$  decay tracks in this way was found to improve the light-jet mistagging rate of SV1 and JetFitter by up to 20% at high transverse momentum. The improvement achieved using the classification tools was in general comparable with that achieved when using the truth information to remove the fake tracks not from the decay of a  $b$ -hadron.

## 1331 Future Work

1332 While removing tracks prior to their input to the low level tagging algorithms is  
1333 shown here to be beneficial, a more performant alternative might be to keep these  
1334 tracks but label them as being fake (for example using the output of the classification  
1335 tool), and allow the tagging algorithms to take this into consideration. This is not  
1336 straightforward with manually optimised taggers such as SV1 and JetFitter, but is  
1337 possible with more advanced taggers as described in Chapter 6.

1338 Tools which identify the origin of a given track have other potential uses. One  
1339 application is to isolate a relatively pure sample of fake tracks which can be used  
1340 to estimate the fake track rate in data, which would be useful for estimating the  
1341 uncertainty on fake track modelling. Another application is to use the  $b$ -hadron  
1342 track identification tool to improve the track-to-jet association. Both applications  
1343 are currently under investigation.

1344 The approach here works on a track-by-track basis, but a more sophisticated approach  
1345 would consider the correlations between the tracks inside a jet. Also left for future  
1346 work is to simultaneously train a single tool which discriminates between all the  
1347 truth origins listed in Table 5.1. Such a tool would be useful as a general purpose  
1348 multiclass classifier. An algorithm which takes both these aspects into consideration  
1349 is discussed in Chapter 6.

<sub>1350</sub> **Chapter 6**

<sub>1351</sub> **Graph Neural Network Flavour  
Tagger**

<sub>1353</sub> This chapter introduces GN1, a novel ML-based flavour tagging algorithm based on  
<sub>1354</sub> graph neural networks (GNNs). In Section 6.1, an overview of the approach used  
<sub>1355</sub> for GN1 is given. An introduction to the theory of GNNs is provided in Section 6.2.  
<sub>1356</sub> Details of the experimental setup are provided in Section 6.3, while the architecture  
<sub>1357</sub> of GN1 is specified in Section 6.4.3. In Section 6.4.4, the training procedure is  
<sub>1358</sub> described, and in Section 6.5 the results are shown.

<sub>1359</sub> **6.1 Motivation**

<sub>1360</sub> GN1 is a monolithic approach to flavour tagging as illustrated in Fig. 6.1. As opposed  
<sub>1361</sub> to the existing approach to flavour tagging described in Chapter 4, which relies  
<sub>1362</sub> on a two tiered approach requiring the use of both low- and high-level algorithms,  
<sub>1363</sub> GN1 takes as inputs information directly from an unordered variable number of  
<sub>1364</sub> tracks as input, and predicts the jet flavour without requiring outputs from the  
<sub>1365</sub> intermediate low-level algorithms. In addition to predicting the flavour of the jet, the  
<sub>1366</sub> model predicts which physical processes produced the various tracks, and groups the  
<sub>1367</sub> tracks into vertices. These auxiliary training objectives provide valuable additional  
<sub>1368</sub> information about the contents of the jet and enhance the performance of the primary  
<sub>1369</sub> flavour prediction task. The use of GNNs offers a natural way to classify jets with

1370 variable numbers of unordered associated tracks (see Section 6.2), while allowing for  
1371 the inclusion of auxiliary training objectives [2, 116].

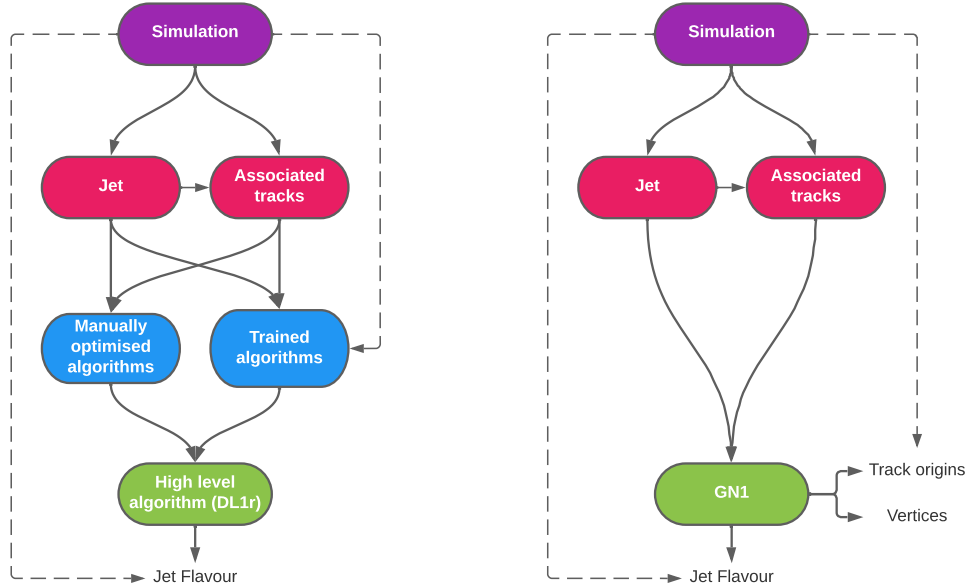


**Figure 6.1:** Comparison of the existing flavour tagging scheme (left) and GN1 (right). The existing approach utilises low-level algorithms (shown in blue), the outputs of which are fed into a high-level algorithm (DL1r). Instead of being used to guide the design of the manually optimised algorithms, additional truth information from the simulation is now being used as auxiliary training targets for GN1. The solid lines represent reconstructed information, whereas the dashed lines represent truth information [3].

1372 The current flavour tagging algorithms utilise a two-tired approach, with five low  
1373 level algorithms feeding intermediate features into the high-level tagger DL1r, which  
1374 outputs variables which discriminate between the different jet flavours. In contrast  
1375 GN1 consists of only a single neural network, which takes the tracks as inputs along  
1376 with some kinematic information about the jet. As a result, it does not depend on  
1377 the outputs of any other flavour tagging algorithm. A simple training of the model  
1378 fully optimises its parameters, representing a significant simplification with respect to  
1379 the optimisation procedure for DL1r. This is particularly important when optimising  
1380 the tagger for new regions of phase space (e.g.  $c$ -tagging or high- $p_T$   $b$ -tagging), or  
1381 when the detector is upgraded or the charged particle reconstruction or selection  
1382 algorithms are re-optimised.

1383 GN1 is trained to learn about the internal structure of the jet through the use of two  
 1384 auxiliary training objectives: the prediction of the underlying physics process from  
 1385 which each track originated, and the grouping of tracks originating from a common  
 1386 spatial position (i.e. a common vertex). These auxiliary objectives are meant to  
 1387 guide the neural network towards a more complete understanding of the underlying  
 1388 physics inside the jet, thereby removing the need for the low-level algorithms, which  
 1389 previously contained information about the underlying physics in their design. The  
 1390 training targets for the primary and auxiliary objectives are extracted from truth  
 1391 information, as opposed to reconstructed quantities available in both collision data  
 1392 and simulation.

1393 In this chapter, the following advantages of the GN1 approach will be demonstrated:

- 1394 1. GN1 boasts improved performance with respect to the current ATLAS flavour  
 1395 tagging algorithms, with significantly larger background rejection rates for a  
 1396 given signal efficiency. Alternatively the rejection rates can be kept fixed for a  
 1397 substantial increase in signal efficiency, in particular at high- $p_T$ .
- 1398 2. The same network architecture can be easily optimised for a wider variety of  
 1399 use cases (e.g.  $c$ -jet tagging and high- $p_T$  jet tagging) since there are no low-level  
 1400 algorithms to retune.
- 1401 3. There are fewer algorithms to maintain.
- 1402 4. Alongside the network's prediction of the jet flavour, the auxiliary vertex and  
 1403 track origin predictions provide more information on why a jet was (mis)tagged  
 1404 or not. This information can also have uses in other applications, for instance  
 1405 to explicitly reconstruct displaced decay vertices or to remove fake tracks.<sup>1</sup>

## 1406 6.2 Graph Neural Network Theory

1407 Graph neural networks are a more sophisticated neural network model (see Sec-  
 1408 tion 5.1.1) that are designed to operate on graph structured data. A brief introduction  
 1409 to GNNs is provided in this section following the formalism in Ref. [117].

---

<sup>1</sup>A fake track is defined in this chapter as a track with a truth-matching probability less than 0.5, where the truth-matching probability is defined in Ref. [57].

1410 A graph  $\mathcal{G}$  consists of a set of  $N^n$  nodes  $\mathcal{N} = \{h_i\}_{i=1:N^n}$ , a set of  $N^e$  edges  $\mathcal{E} =$   
1411  $\{e_i\}_{i=1:N^e}$ , and a global representation  $u$ . Each node represents an individual object,  
1412 and edges are directed connections between two nodes, called the *sender* and *receiver*  
1413 nodes. The connectivity of the graph therefore encodes information about the  
1414 relationships between objects that exist in the graph.

1415 A single graph network layer consists of three separate update functions  $\phi^e$ ,  $\phi^h$  and  
1416  $\phi^u$  one for each of the nodes, edges, and global graph representation, and similarly  
1417 three aggregation functions  $\rho^{e \rightarrow h}$ ,  $\rho^{e \rightarrow u}$  and  $\rho^{h \rightarrow u}$ . The aggregation functions combine  
1418 information across different edges or nodes for input into the update functions,  
1419 which produce new representations for the nodes, edges and global objects based on  
1420 the information in the previous layer and the aggregated information. The update  
1421 functions are typically each implemented as a dense feedforward neural network (as  
1422 described in Section 5.1.1). The edges  $e_i$  are updated by a edge network  $\phi^e$  as in

$$e'_i = \phi^e(e_i, h_s, h_r, u), \quad (6.1)$$

1423 where  $h_s$  and  $h_r$  are the sender and receiver nodes respectively. The nodes are  
1424 updated with a node network  $\phi^h$  as in

$$h'_i = \phi^h(\bar{e}'_i, h_i, u), \quad (6.2)$$

1425 where  $\bar{e}'_i = \rho^{e \rightarrow h}(E'_i)$ , and  $E'_i$  is the set of sender nodes for receiver node  $h_i$ .  $\rho^{e \rightarrow h}$  is  
1426 referred to as the edge aggregation function. The global representation is updated  
1427 using the global network  $\phi^u$  as in

$$u' = \phi^u(\bar{e}', \bar{h}', u), \quad (6.3)$$

1428 where  $\bar{e}'$  is the aggregation  $\rho^{e \rightarrow u}$  over all updated edges  $e'_i$  and  $\bar{h}'$  is the aggregation  
1429  $\rho^{h \rightarrow u}$  over all updated nodes  $h'_i$ .

1430 The graph network layer performs a graph convolution, in an analogous way to a  
1431 convolutional neural network operating on a grid of pixels. The above description  
1432 is general, and not all concrete implementations of GNNs need to implement every  
1433 aspect. For example, the global graph representation need not be present, and  
1434 it is also possible that no dedicated edge features are present. In such cases the  
1435 corresponding update and aggregation functions are not needed. Fig. 6.2 shows two

1436 possible graph network update layers. The layer used in the GN1 model is specified  
1437 in more detail in Section 6.4.3.

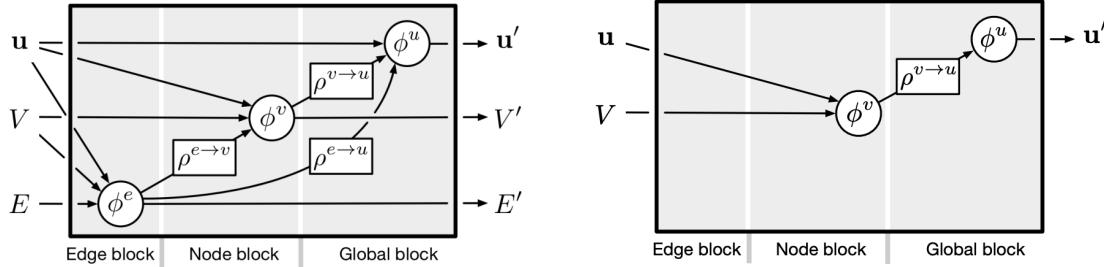


**Figure 6.2:** The flow of information through a graph neural network layer for (left) a full implementation of the layer and (right) a deep sets model [118]. Reproduced from Ref. [117].

### 1438 6.3 Experimental Setup

#### 1439 6.3.1 Datasets

1440 The datasets used to train the GN1 tagger are the same as described in Section 4.1.  
1441 The training dataset contains 30 million jets, 60% of which are  $t\bar{t}$  jets and 40% of  
1442 which are  $Z'$  jets. In order to evaluate the performance of the model during training,  
1443 a statistically independent validation set of 500k jets from both the  $t\bar{t}$  and  $Z'$  samples  
1444 are used. For the testing of the model and the creation of the performance plots,  
1445 a further 1 million independent testing jets from each of the  $t\bar{t}$  and  $Z'$  samples are  
1446 used. Before being fed into the model, the track- and jet-level inputs are normalised  
1447 to have a mean of zero and a variance of unity. The jet flavour labels are assigned  
1448 as described in Section 3.4.3. Truth labelled  $b$ -,  $c$ - and light-jets are kinematically  
1449 re-sampled in  $p_T$  and  $\eta$  to ensure identical distributions in these variables.

## 1450 6.4 Model Architecture

### 1451 6.4.1 Model Inputs

1452 As inputs, GN1 is fed two kinematic jet variables and an unordered set of up to 40  
1453 tracks which have been associated to the jet. If more than 40 tracks are associated  
1454 to a given jet, only the first 40 tracks with the largest transverse IP significance  $s(d_0)$   
1455 (see Section 3.2.2) are fed into the model as inputs. Each track is characterised by 21  
1456 variables as detailed in Table 6.1. The kinematic jet variables are the jet transverse  
1457 momentum and signed pseudorapidity. For each track, variables containing the  
1458 track parameters and uncertainties, and detailed information on the hit content are  
1459 provided as inputs to the model.

1460 Dependence of the model on the absolute value of the azimuthal jet angle  $\phi$  is  
1461 explicitly removed by providing only the azimuthal angle of tracks relative to the jet  
1462 axis. The track pseudorapidity is also provided relative to the jet axis.

1463 Since heavy flavour hadrons can decay semileptonically approximately 40% of the time,  
1464 the presence of a reconstructed lepton in the jet carries discriminating information  
1465 about the jet flavour. To exploit this, a variant of GN1 called GN1Lep is trained in  
1466 addition to the baseline model. The GN1Lep variant is identical to the baseline model,  
1467 except for the inclusion an additional track-level input, leptonID, which indicates  
1468 if the track was used in the reconstruction of an electron, a muon or neither. The  
1469 variable is signed by the charge of the reconstructed lepton. The leptons used in the  
1470 definition of the leptonID variable are required to satisfy basic quality requirements.  
1471 The muons are required to be combined [119], and the electrons are required to pass  
1472 the *VeryLoose* likelihood-based identification working point [120].

1473 The selections applied to the tracks, outlined in Table 3.2, is the same as that used  
1474 for the fake track classification MVA described in Chapter 5. However, Section 6.6.1  
1475 demonstrates that further relaxation of the track selection requirements may be  
1476 warranted.

Jet Input	Description
$p_T$	Jet transverse momentum
$\eta$	Signed jet pseudorapidity
Track Input	Description
$q/p$	Track charge divided by momentum
$d\eta$	Pseudorapidity of the track, relative to the jet $\eta$
$d\phi$	Azimuthal angle of the track, relative to the jet $\phi$
$d_0$	Closest distance from the track to the PV in the longitudinal plane
$z_0 \sin \theta$	Closest distance from the track to the PV in the transverse plane
$\sigma(q/p)$	Uncertainty on $q/p$
$\sigma(\theta)$	Uncertainty on track polar angle $\theta$
$\sigma(\phi)$	Uncertainty on track azimuthal angle $\phi$
$s(d_0)$	Lifetime signed transverse IP significance
$s(z_0)$	Lifetime signed longitudinal IP significance
nPixHits	Number of pixel hits
nSCTHits	Number of SCT hits
nIBLHits	Number of IBL hits
nBLHits	Number of B-layer hits
nIBLShared	Number of shared IBL hits
nIBLSplit	Number of split IBL hits
nPixShared	Number of shared pixel hits
nPixSplit	Number of split pixel hits
nSCTShared	Number of shared SCT hits
nPixHoles	Number of pixel holes
nSCTHoles	Number of SCT holes
leptonID	Indicates if track was used to reconstruct an electron or muon

**Table 6.1:** Input features to the GN1 model. Basic jet kinematics, along with information about the reconstructed track parameters and constituent hits are used. Shared hits, are hits used on multiple tracks which have not been classified as split by the cluster-splitting neural networks [57], while split hits are hits used on multiple tracks which have been identified as merged. A hole is a missing hit, where one is expected, on a layer between two other hits on a track. The track leptonID is an additional input to the GN1Lep model [3].

## 6.4.2 Auxiliary Training Objectives

In addition to the jet flavour classification, two auxiliary training objectives are defined. The first auxiliary objective is the prediction of the physical process that gave rise to each track within the jet (i.e. the track origin), while the second is the prediction of track-pair vertex compatibility. Each auxiliary training objective comes with a training target which, similar to the jet flavour label, is a truth labels derived from the simulation. The presence of the auxiliary training objectives improves the jet classification performance as demonstrated in Section 6.5.3.

For the track origin prediction objective, each track is labelled with one of the exclusive categories defined in Table 5.1 of Section 5.2 after analysing the particle interaction (or lack thereof) which led to its formation. Since the presence of different track origins is strongly related to the flavour of the jet, training GN1 to recognise the origin of the tracks provides an additional handle on the classification of the jet flavour. This task may also aid the jet flavour prediction by acting as a form of supervised attention [121] - in detecting tracks from heavy flavour decays the model may learn to pay more attention to these tracks.

The vertexing auxiliary objective makes use of the fact that displaced decays of  $b$ - and  $c$ -hadrons lead to secondary and tertiary vertices inside the jet, as described in Section 4.3.1. The presence of displaced secondary vertices is not a completely clean signal of a heavy flavour jet, as displaced secondary vertices can also occur in light-jets as a result of material interactions, conversions, and long-lived particle decays (e.g.  $K_S^0$  and  $\Lambda^0$ ). For this objective, GN1 predicts a binary label for each pair of tracks in the jet. The label has a value of 1 if the truth particles associated with the two tracks in the pair originated from the same spatial point, and 0 otherwise. To derive the corresponding truth labels for training, truth production vertices within 0.1 mm are merged. Track-pairs where one or both of the tracks in the pair have an origin label of either Pile-up or Fake are assigned a label of 0. Using the pairwise predictions from the model, groups of tracks that have common compatibility can be formed, resulting in the identification of vertices. Two existing low-level tagging algorithms, SV1 and JetFitter (introduced in Section 3.4.2), are currently used to find and reconstruct vertices inside jets and are used as inputs to the existing jet flavour tagger DL1r. The addition of this auxiliary training objective removes the need for inputs from a dedicated secondary vertexing algorithm.

1510 Both of the auxiliary training objectives described here can be considered as “stepping  
1511 stones” on the way to classifying the flavour of the jet. By requiring the model to  
1512 predict the truth origin of each track and the vertex compatibility of each track-pair,  
1513 the model is guided to learn representations of the jet which are connected to the  
1514 underlying physics and therefore relevant for classifying the jet flavour.

1515 **6.4.3 Architecture**

1516 A coarse optimisation of the network architecture hyperparameters (for example  
1517 number of layers and number of neurons per layer) has been carried out in order  
1518 to maximise the flavour tagging performance, but it is likely that further dedicated  
1519 optimisation studies could lead to further performance improvements.

1520 The model architecture builds on a previous implementation of a GNN-based jet  
1521 tagger [116]. The previous approach was comprised of two separate graph neural  
1522 networks with the auxiliary tasks being performed at an intermediate stage after the  
1523 first and before the second. This two stage approach was found to be unnecessary and  
1524 as such GN1 simplifies the architecture into a single graph neural network with the  
1525 auxiliary tasks being performed at the end, alongside the primary jet classification  
1526 task. GN1 makes use of a more sophisticated graph neural network layer [122],  
1527 which is described in more detail below. The changes significantly improved tagging  
1528 performance and also led to a significant reduction in training time.

1529 As inputs, the model takes information about the jet and a number of associated  
1530 tracks, as detailed in Section 6.4.1. The jet variables are concatenated with the  
1531 variables for each track as shown in Fig. 6.3. The combined jet-track input vectors  
1532 are then fed into a per-track initialisation network with three hidden layers, each  
1533 containing 64 neurons, and an output layer with a size of 64, as shown in Fig. 6.4. The  
1534 track initialisation network is similar to a deep sets model [118], but does not include  
1535 a reduction operation (mean or summation) over the output track representations.  
1536 The initialisation network allows for initial per-track input processing without the  
1537 associated parameter count cost of the graph convolutional layers described below.

1538 The outputs of the track initialisation network are used to populate the nodes of a  
1539 fully connected graph, such that each node in the graph neighbours every other node.  
1540 Each node  $h_i$  in the graph corresponds to a single track in the jet, and is characterised

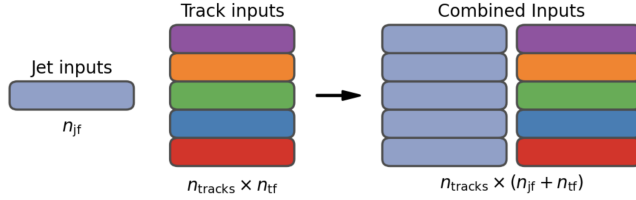


**Figure 6.3:** The inputs to GN1 are the two jet features ( $n_{jf} = 2$ ), and an array of  $n_{tracks}$ , where each track is described by 21 track features ( $n_{tf} = 21$ ). The jet features are copied for each of the tracks, and the combined jet-track vectors of length 23 form the inputs of GN1 [3].

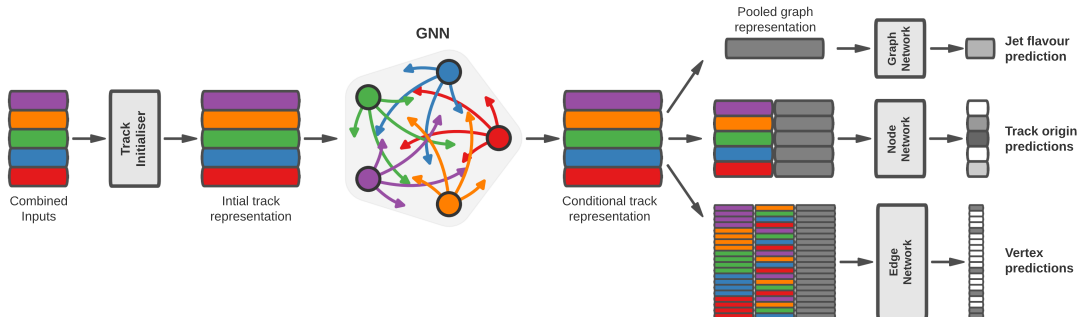


**Figure 6.4:** The network architecture of GN1. Inputs are fed into a per-track initialisation network, which outputs an initial latent representation of each track. These representations are then used to populate the node features of a fully connected graph network. After the graph network, the resulting node representations are used to predict the jet flavour, the track origins, and the track-pair vertex compatibility [3].

1541 by a feature vector, also called a representation. The per-track output representations  
 1542 from the initialisation networks are used as the initial feature vectors of each node  
 1543 in the graph. In each layer of the graph network, output node representations  $h'_i$   
 1544 are computed by aggregating the features of  $h_i$  and neighbouring nodes  $\mathcal{N}_i$  using  
 1545 a multi-head attention mechanism ( $n = 2$ ) as described in Ref. [122, 123]. First,  
 1546 the feature vectors of receiver and sender nodes are fed into two fully connected  
 1547 linear layers  $\mathbf{W}_r$  and  $\mathbf{W}_s$ , to produce an updated representation for each sender and  
 1548 receiver node  $\mathbf{W}_r h_i$  and  $\mathbf{W}_s h_j$ . These updated feature vectors are used to compute  
 1549 edge scores  $e(h_i, h_j)$  for each node pair, as in

$$e(h_i, h_j) = \mathbf{a} \cdot \theta [\mathbf{W}_r h_i + \mathbf{W}_s h_j], \quad (6.4)$$

1550 where,  $\theta$  is a non-linear activation function, and  $\mathbf{a}$  is a learned vector. These edge  
 1551 scores are then used to calculate attention weights  $a_{ij}$  for each pair of nodes using  
 1552 the softmax function over the edge scores

$$a_{ij} = \text{softmax}_j [e(h_i, h_j)]. \quad (6.5)$$

1553 Finally, the updated representations for the receiver nodes  $h'_i$  are computed by taking  
 1554 the weighted sum over each updated node representation  $\mathbf{W}_r h_i$ , with weights  $a_{ij}$

$$h'_i = \sigma \left[ \sum_{j \in \mathcal{N}_i} a_{ij} \cdot \mathbf{W}_r h_j \right]. \quad (6.6)$$

1555 The set of operations described above constitute a single graph network layer. Three  
 1556 such layers are stacked to construct the graph network, representing a balance  
 1557 between achieving good performance in a reasonable time and avoiding overtraining  
 1558 due to inflation of the parameter count of the model. The final output from the graph  
 1559 neural network is a set of per-node (i.e. per-track) feature vectors that are conditional  
 1560 representations of each track given the other tracks in the jet. In order to perform

the jet flavour prediction, a flattened global representation of the jet is needed. To produce this, the output track representations are combined using a weighted sum, where the weights are learned during training and therefore act as a form of attention over the different tracks. The flattened outputs from the sum are then fed into a fully connected feedforward neural network with four layers and three outputs, one for each jet flavour. Two other separate fully connected feedforward neural networks are then also used to independently perform the auxiliary classification objectives of GN1. A summary of the different classification networks used for the various training objectives is shown in Table 6.2.

Network	Hidden layers	Output size	Label
Node classification network	128, 64, 32	7	Track origin
Edge classification network	128, 64, 32	1	Track-pair compatibility
Graph classification network	128, 64, 32, 16	3	Jet flavour

**Table 6.2:** A summary of GN1’s different classification networks used for the various training objectives, adapted from Ref. [3]. The hidden layers column contains a list specifying the number of neurons in each layer. ReLU activation is used through the network [112].

The node classification network predicts the track truth origin as defined in Table 5.1. This network takes as inputs the features from a single output node from the graph network and the global representation of the jet. The node network has three hidden layers containing 128, 64 and 32 neurons respectively, and an output size of seven, corresponding to the seven different truth origins defined in Table 5.1.

The edge classification network is used to predict whether the tracks in the track-pair belong to a common vertex. This network takes as inputs the concatenated representations from each pair of tracks and the global jet representation. Similar to the node network, the edge network has three hidden layers containing 128, 64 and 32 neurons respectively, and a single output, which is used to perform binary classification of the track-pair compatibility. The output predictions for the two auxiliary networks are used for the auxiliary training objectives discussed in Section 6.4.2.

Finally, the graph classification network is used to predict the jet flavour. This network takes only the global jet representation as input. The graph classification

1585 network is comprised of four fully connected hidden layers with 128, 64, 32 and 16  
1586 neurons respectively, and has three outputs corresponding to the  $b$ -,  $c$ - and light-  
1587 jet classes. To obtain probability outputs for each task, the outputs from each  
1588 classification network are passed through a softmax function.

1589 **6.4.4 Training**

1590 The full GN1 training procedure minimises the total loss function  $L_{\text{total}}$ , defined as

$$L_{\text{total}} = L_{\text{jet}} + \alpha L_{\text{vertex}} + \beta L_{\text{track}}. \quad (6.7)$$

1591 This loss is composed of three terms:  $L_{\text{jet}}$ , the categorical cross entropy loss over the  
1592 different jet flavours;  $L_{\text{vertex}}$ , the binary track-pair compatibility cross entropy loss;  
1593 and  $L_{\text{track}}$ , the categorical cross entropy loss for the track origin prediction.  $L_{\text{vertex}}$  is  
1594 computed via a weighted average over all intra-jet track-pairs in the batch, and  $L_{\text{track}}$   
1595 is computed by a weighted average over all tracks in the batch, where the weights  
1596 are described below.

1597 The different losses converge to different values during training, reflecting differences  
1598 in the relative difficulty of the various training objectives. The values of  $L_{\text{vertex}}$  and  
1599  $L_{\text{track}}$  are weighted by  $\alpha = 1.5$  and  $\beta = 0.5$  respectively to ensure they converge to  
1600 similar values, giving them an equal weighting towards  $L_{\text{total}}$ . The values of  $\alpha$  and  
1601  $\beta$  are chosen to ensure that  $L_{\text{jet}}$  converges to a larger value than either  $L_{\text{vertex}}$  and  
1602  $L_{\text{track}}$ , which reflects the primary importance of the jet classification objective. It  
1603 was found that in practice the overall performance of the model was not sensitive  
1604 to modest changes in the loss weights  $\alpha$  and  $\beta$ . Pre-training using  $L_{\text{total}}$  (i.e. on  
1605 all tasks) and fine tuning on only the jet classification task also did not improve  
1606 performance versus the standard setup, indicating that the auxiliary tasks are not  
1607 in direct competition with the jet classification task. As there was a large variation  
1608 in the relative abundance of tracks of the different origins, the contribution of each  
1609 origin to  $L_{\text{track}}$  was weighted by the inverse of the frequency of their occurrence. In  
1610 vertexing loss  $L_{\text{vertex}}$ , the class weight for track-pairs where both tracks are from  
1611 either a  $b$ - or  $c$ -hadron was increased by a factor of two as compared with other

1612 track-pairs, to encourage the network to focus on correctly classifying heavy flavour  
1613 vertices.

1614 GN1 can be trained with either the node or edge networks (and their corresponding  
1615 auxiliary tasks), or both, removed, as discussed in Section 6.5.3. In such cases,  
1616 the corresponding losses  $L_{\text{vertex}}$  and  $L_{\text{track}}$  are also removed from the calculation  
1617 of the overall loss  $L_{\text{total}}$ . The performance of the resulting models provides a  
1618 useful indication of the benefit of including the auxiliary tasks to the primary jet  
1619 classification objective.

1620 GN1 was trained for 100 epochs on 4 NVIDIA V100 GPUs. Each epoch takes  
1621 approximately 25 mins to complete over the training sample of 30 million jets. The  
1622 Adam optimiser [124] with an initial learning rate of  $1e-3$ , and a batch size of 4000  
1623 jets (spread across the 4 GPUs) was used. Typically the validation loss, calculated  
1624 on 500k jets, became stable after around 60 epochs. The epoch that minimized the  
1625 validation loss was used for evaluation. GN1 has been integrated into the ATLAS  
1626 software [54] using ONNX [125]. The test sample jet flavour predictions scores are  
1627 computed using the ATLAS software stack as a verification of this process.

## 1628 6.5 Results

1629 The GN1 tagger is evaluated both as a  $b$ -tagging and  $c$ -tagging algorithm in Sec-  
1630 tion 6.5.1 and Section 6.5.2 respectively. Evaluation is performed separately on  
1631 jets in the  $t\bar{t}$  sample with  $20 < p_T < 250 \text{ GeV}$  and jets in the  $Z'$  sample with  
1632  $250 < p_T < 5000 \text{ GeV}$ . The performance of the model is compared to the DL1r  
1633 tagger [98, 99], which has been retrained on 75 million jets from the same samples as  
1634 GN1. The input RNNIP tagger [95] to DL1r has not been retrained. As discussed,  
1635 each tagger predicts the probability that a jet belongs to the  $b$ -,  $c$ - and light-classes.  
1636 To use the model for  $b$ -tagging, these probabilities are combined into a single score  
1637  $D_b$ , which is defined as

$$D_b = \log \frac{p_b}{(1 - f_c)p_l + f_c p_c}, \quad (6.8)$$

where  $f_c$  is a free parameter that determines the relative weight of  $p_c$  to  $p_l$  in the score  $D_b$ , controlling the trade-off between  $c$ - and light-jet rejection performance. The choice of  $f_c$  is arbitrary, and is optimised based upon the desired light- vs  $c$ -jet rejection performance. This parameter is set to a value of  $f_c = 0.018$  for the DL1r model, obtained through an optimisation procedure described in Ref. [98]. Based on a similar optimisation procedure, a value of  $f_c = 0.05$  is used for the GN1 models.

A comparison of the  $b$ -tagging discriminant  $D_b$  between DL1r and GN1 is shown in Fig. 6.5. The shapes of the  $D_b$  distributions are generally similar for  $b$ -,  $c$ - and light-jets between both models, however, GN1 shifts the  $b$ -jet distribution to higher values of  $D_b$  in the regions with the greatest discrimination. The GN1  $c$ -jet distribution is also shifted to lower values of  $D_b$  when compared with DL1r, enhancing the separation and indicating that GN1 is improving  $c$ -jet rejection when compared with DL1r.

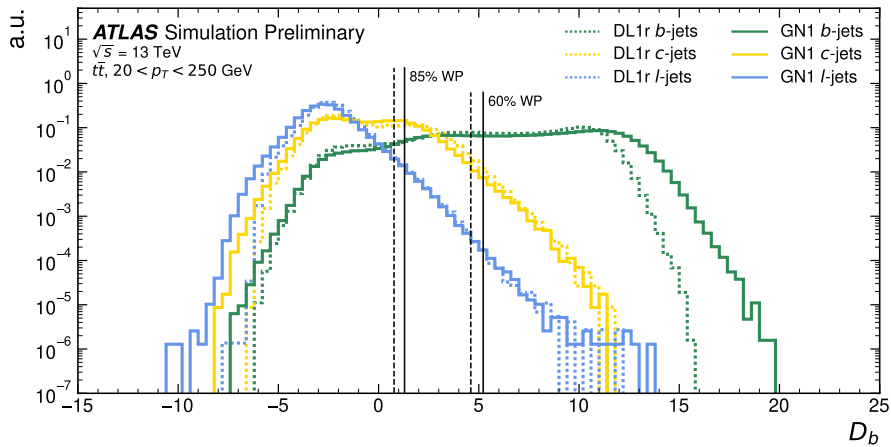


**Figure 6.5:** Comparison between the DL1r and GN1  $b$ -tagging discriminant  $D_b$  for jets in the  $t\bar{t}$  sample. The 85% WP and the 60% WP are marked by the solid (dashed) lines for GN1 (DL1r), representing respectively the loosest and tightest WPs typically used by analyses. A value of  $f_c = 0.018$  is used in the calculation of  $D_b$  for DL1r and  $f_c = 0.05$  is used for GN1. The distributions of the different jet flavours have been normalised to unity area [3].

### 6.5.1 $b$ -tagging Performance

The performance of  $b$ -tagging algorithms is quantified by their ability to reject  $c$ - and light-jets for a given  $b$ -jet selection efficiency WP. In order to compare the  $b$ -tagging performance of the different taggers for the  $b$ -jet tagging efficiencies in the range

1654 typically used by analyses, the corresponding  $c$ - and light-jet rejection rates are  
1655 displayed in Figs. 6.6 and 6.7 for jets in the  $t\bar{t}$  and  $Z'$  samples respectively. Four  
1656 standard WPs are defined with  $b$ -jet tagging efficiencies of 60%, 70%, 77% and 85%  
1657 respectively. These WPs are commonly used by physics analyses depending on their  
1658 specific signal and background requirements. The WPs are defined based on jets in  
1659 the  $t\bar{t}$  sample only. Due to the much higher jet  $p_T$  range in the  $Z'$  sample, and the  
1660 increased difficulty in tagging jets at high- $p_T$  (see Chapter 4), the corresponding  $b$ -jet  
1661 tagging efficiencies for jets in the  $Z'$  sample are lower than the corresponding WPs  
1662 calculated in the  $t\bar{t}$  sample. For instance the WP cut value computed to provide a  
1663 70%  $b$ -jet tagging efficiency on the  $t\bar{t}$  sample results in a  $b$ -jet tagging efficiency of  
1664 just  $\sim 30\%$  on the  $Z'$  sample. In order to account for this, the range of  $b$ -jet tagging  
1665 efficiencies displayed for plots showing the performance for jets in the  $Z'$  sample (for  
1666 example Fig. 6.7) is chosen to span the lower efficiencies achieved in the  $Z'$  sample  
1667 at high- $p_T$ .

1668 For jets in the  $t\bar{t}$  sample with  $20 < p_T < 250 \text{ GeV}$ , GN1 demonstrates considerably  
1669 better  $c$ - and light-jet rejection when compared with DL1r across the full range of  
1670  $b$ -jet tagging efficiencies studied. The relative improvement is strongly dependent  
1671 on the  $b$ -jet tagging efficiency under study. The largest improvements are found at  
1672 lower  $b$ -jet tagging efficiencies. At a  $b$ -jet tagging efficiency of 70%, the  $c$ -jet rejection  
1673 improves by a factor of  $\sim 2.1$  while the light-jet rejection improves by a factor of  $\sim 1.8$   
1674 with respect to DL1r. For high- $p_T$  jets in the  $Z'$  sample with  $250 < p_T < 5000 \text{ GeV}$ ,  
1675 GN1 also brings a significant performance improvement with respect to DL1r across  
1676 the range of  $b$ -jet tagging efficiencies studied. Again, the largest relative improvement  
1677 in performance comes at the lower  $b$ -jet tagging efficiencies. At a  $b$ -jet efficiency of  
1678 30%, GN1 improves the  $c$ -jet rejection with respect to DL1r by a factor of  $\sim 2.8$  and  
1679 the light-jet rejection by a factor of  $\sim 6$ . The performance comparison at lower  $b$ -jet  
1680 tagging efficiencies is made more difficult due to the increased statistical uncertainties  
1681 which result from the high rejection of background.

1682 The GN1Lep variant of GN1 demonstrates further improved performance with respect  
1683 to the baseline model. This demonstrates the additional jet flavour discrimination  
1684 power provided by the leptonID track input. For jets in the  $t\bar{t}$  sample, the relative  $c$ -  
1685 jet rejection improvement with respect to GN1 at the 70%  $b$ -jet WP is approximately  
1686 25%. The improvement in light-jet rejection also increases by 40% at the same WP.  
1687 For jets in the  $Z'$  sample, the relative  $c$ -jet rejection (light-jet rejection) performance

1688 with respect to GN1 improves by approximately 10% (25%) at a  $b$ -jet tagging  
1689 efficiency of 30%.

1690 In general, the performance of all the taggers is strongly dependent on jet  $p_T$ , due  
1691 to the increased multiplicity and collimation of tracks, and the displaced decays  
1692 that result from within the heavy flavour jets (see Chapter 4). Together, they  
1693 contribute to a reduced reconstruction efficiency for heavy flavour tracks, and a  
1694 general degradation in quality of tracks inside the core of a jet, which in turn reduces  
1695 the jet tagging performance. In order to study how the tagging performance changes  
1696 as a function of the jet  $p_T$ , the  $b$ -jet tagging efficiency as a function of  $p_T$  for a fixed  
1697 light-jet rejection of 100 in each bin is shown in Fig. 6.8. For jets in the  $t\bar{t}$  sample,  
1698 at a fixed light-jet rejection of 100, GN1 improves the  $b$ -jet tagging efficiency by  
1699 approximately 4% across all the jet  $p_T$  bins. Meanwhile, GN1Lep again demonstrates  
1700 improved performance with respect to GN1, in particular at lower  $p_T$ . The relative  
1701 increase in the  $b$ -jet tagging efficiency increases from 4% to 8% with respect to DL1r.  
1702 For jets in the  $Z'$  sample, GN1 again outperforms DL1r across the entire jet  $p_T$  range  
1703 studied. The largest relative improvement in performance is found at the highest  
1704 transverse momenta of jet  $p_T > 2 \text{ TeV}$ , and corresponds to an approximate factor of  
1705 2 improvement in efficiency with respect to DL1r.

1706 The performance of the model was also evaluated as a function of the average  
1707 number of pile-up interactions in the event. No significant dependence of the tagging  
1708 performance was observed.

### 1709 6.5.2 $c$ -tagging Performance

1710 As discussed previously, GN1 does not rely on any inputs from manually optimised  
1711 low-level tagging algorithms. Since these algorithms were originally designed and  
1712 tuned with the aim of  $b$ -tagging, and not  $c$ -tagging, the low level tagging algorithms  
1713 may perform suboptimally for  $c$ -tagging purposes. The tagging of  $c$ -jets therefore  
1714 presents a compelling use case for GN1. As each of the models is trained with three  
1715 output classes, using it as a  $c$ -tagging algorithm is trivially analogous to the approach  
1716 used for  $b$ -tagging. The model output probabilities are combined into a single score  
1717  $D_c$ , which is defined similarly to Eq. (6.8) as

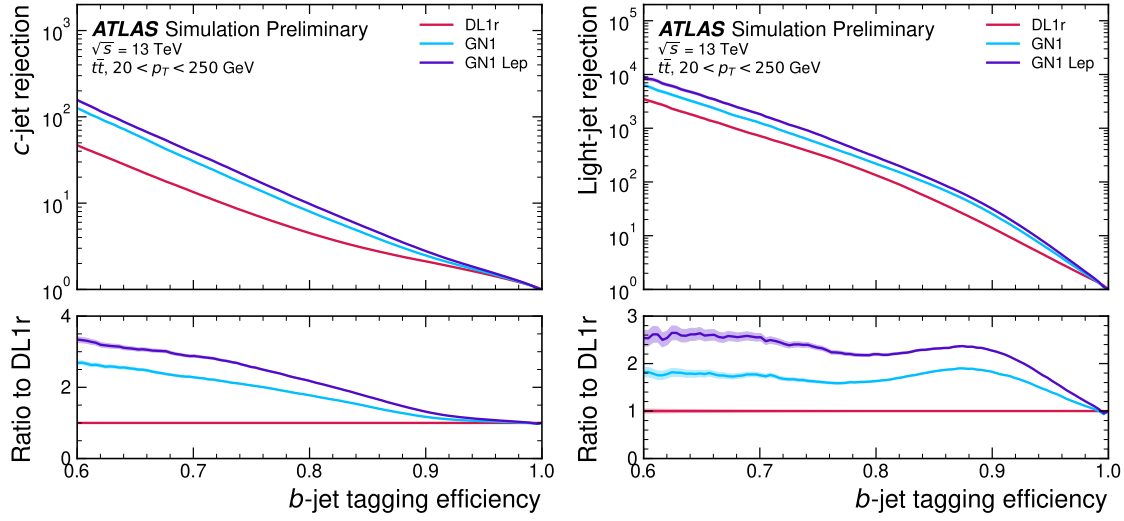


**Figure 6.6:** The  $c$ -jet (left) and light-jet (right) rejections as a function of the  $b$ -jet tagging efficiency for jets in the  $t\bar{t}$  sample with  $20 < p_T < 250 \text{ GeV}$ . The ratio with respect to the performance of the DL1r algorithm is shown in the bottom panels. A value of  $f_c = 0.018$  is used in the calculation of  $D_b$  for DL1r and  $f_c = 0.05$  is used for GN1 and GN1Lep. Binomial error bands are denoted by the shaded regions. The  $x$ -axis range is chosen to display the  $b$ -jet tagging efficiencies usually probed in these regions of phase space [3].

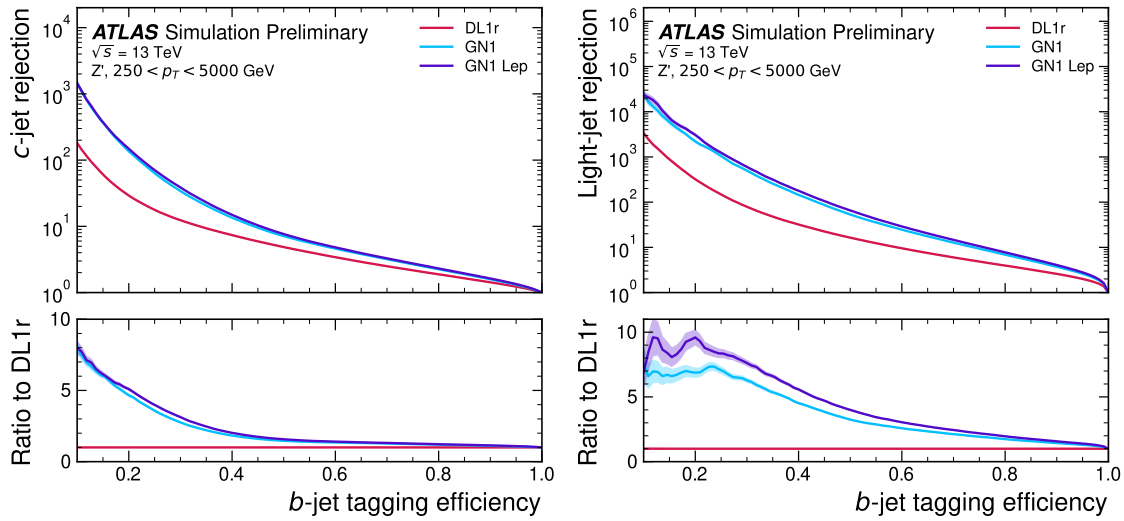


**Figure 6.7:** The  $c$ -jet (left) and light-jet (right) rejections as a function of the  $b$ -jet tagging efficiency for jets in the  $Z'$  sample with  $250 < p_T < 5000 \text{ GeV}$ . The ratio with respect to the performance of the DL1r algorithm is shown in the bottom panels. A value of  $f_c = 0.018$  is used in the calculation of  $D_b$  for DL1r and  $f_c = 0.05$  is used for GN1 and GN1Lep. Binomial error bands are denoted by the shaded regions. The  $x$ -axis range is chosen to display the  $b$ -jet tagging efficiencies usually probed in these regions of phase space [3].

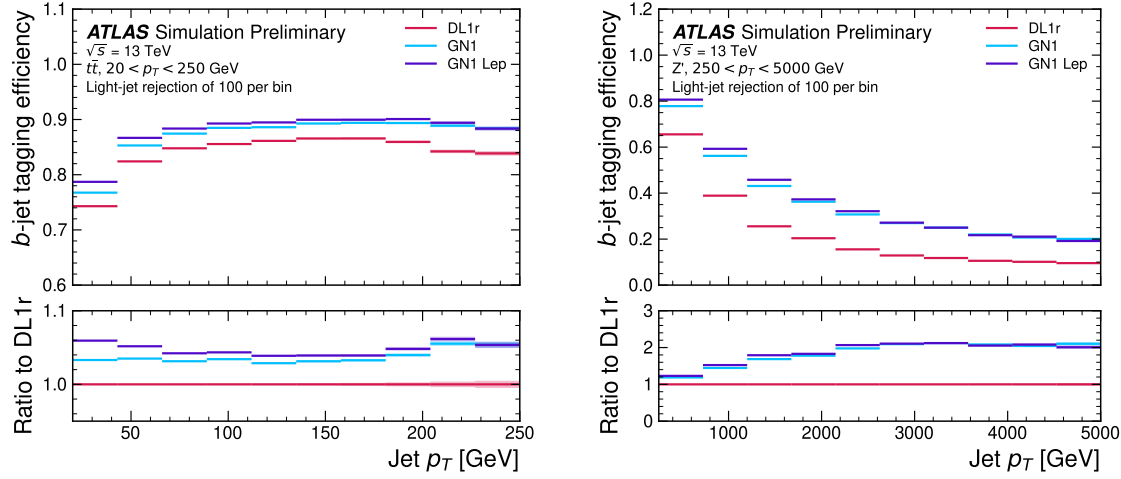


**Figure 6.8:** The  $b$ -jet tagging efficiency for jets in the  $t\bar{t}$  sample (left) and jets in the  $Z'$  sample (right) as a function of jet  $p_T$  with a fixed light-jet rejection of 100 in each bin. A value of  $f_c = 0.018$  is used in the calculation of  $D_b$  for DL1r and  $f_c = 0.05$  is used for GN1 and GN1Lep. GN1 demonstrates improved performance with respect to DL1r across the  $p_T$  range shown. Binomial error bands are denoted by the shaded regions [3].

$$D_c = \log \frac{p_c}{(1 - f_b)p_l + f_b p_b}. \quad (6.9)$$

A value of  $f_b = 0.2$  is used for all models, based on the same optimisation procedure that was used for the  $b$ -tagging use case. Similar to Section 6.5.1, the different taggers are compared to one another by scanning through a range of  $c$ -jet tagging efficiencies and plotting the corresponding  $b$ - and light-jet rejection rates, and the WPs are defined using jets in the  $t\bar{t}$  sample. Standard  $c$ -jet tagging efficiency WPs used by physics analyses are significantly lower than the  $b$ -tagging WPs in order to maintain reasonable  $b$ - and light-jet rejection rates. This is reflected in the range of  $c$ -jet tagging efficiencies used in  $c$ -tagging plots such as Figs. 6.9 and 6.10. Fig. 6.9 displays the  $c$ -tagging performance of the models on the jets in the  $t\bar{t}$  sample. GN1 is shown to perform significantly better than DL1r. Similar to the  $b$ -tagging case, the  $b$ - and light-jet rejection improve most at lower  $c$ -jet tagging efficiencies, with the  $c$ -jet rejection (light-jet rejection) improving by a factor 2 (1.6) with respect to DL1r at a  $c$ -jet tagging efficiency of 25%. GN1Lep again outperforms GN1, though the improvements are more modest than observed for the  $b$ -tagging use case,

1732 with both the  $b$ -jet rejection (light-jet rejection) improving with respect to GN1  
1733 by approximately 10% (20%) at the 25%  $c$ -jet WP. Fig. 6.10 shows the  $c$ -tagging  
1734 performance on the jets in the  $Z'$  sample with  $250 < p_T < 5000$  GeV. Both GN1 and  
1735 GN1Lep perform similarly, improving the  $b$ -jet rejection by 60% and the light-jet  
1736 rejection by a factor of 2 at the 25%  $c$ -jet WP.

### 1737 6.5.3 Ablations

1738 Ablation studies (the removal of certain components of a model in order to study  
1739 the impact of that component) are carried out to determine the importance of the  
1740 auxiliary training objectives of GN1 to the overall performance. The “GN1 No  
1741 Aux” variant retains the primary jet classification objective, but removes both track  
1742 classification and vertexing auxiliary objectives and correspondingly only minimises  
1743 the jet classification loss. The “GN1 TC” variant includes the track classification  
1744 objective but not the vertexing objective. Finally, the “GN1 Vert” includes the  
1745 vertexing objective, but not the track classification objective.

1746 For jets in both the  $t\bar{t}$  and  $Z'$  samples, a general trend is observed that the models  
1747 trained without one or both of the auxiliary objectives results in significantly reduced  
1748  $c$ - and light-jet rejection when compared with the baseline GN1 model, as shown  
1749 in Figs. 6.11 and 6.12. For jets in the  $t\bar{t}$  sample, the performance of GN1 No Aux  
1750 is similar to DL1r, while GN1 TC and GN1 Vert perform similarly to each other.  
1751 For jets in the  $Z'$  sample, the GN1 No Aux model shows a clear improvement in  $c$ -  
1752 and light-jet rejection when compared with DL1r at lower  $b$ -jet tagging efficiencies.  
1753 Similar to jets in the  $t\bar{t}$  sample, GN1 TC and GN1 Vert perform similarly, and bring  
1754 large gains in background rejection when compared with GN1 No Aux, but the  
1755 combination of both auxiliary objectives yields the best performance.

1756 It is notable that the GN1 No Aux model matches or exceeds the performance of  
1757 DL1r without the need for inputs from the low-level algorithms. This indicates that  
1758 the performance improvements enabled by the improved neural network architecture  
1759 used in GN1 appear to be able to compensate for the removal of the low-level  
1760 algorithm inputs. The GN1 TC and GN1 Vert variants each similarly outperform  
1761 DL1r, demonstrating that both contribute to the overall high performance of the  
1762 baseline model. The overall best performing model is the full version of GN1 trained

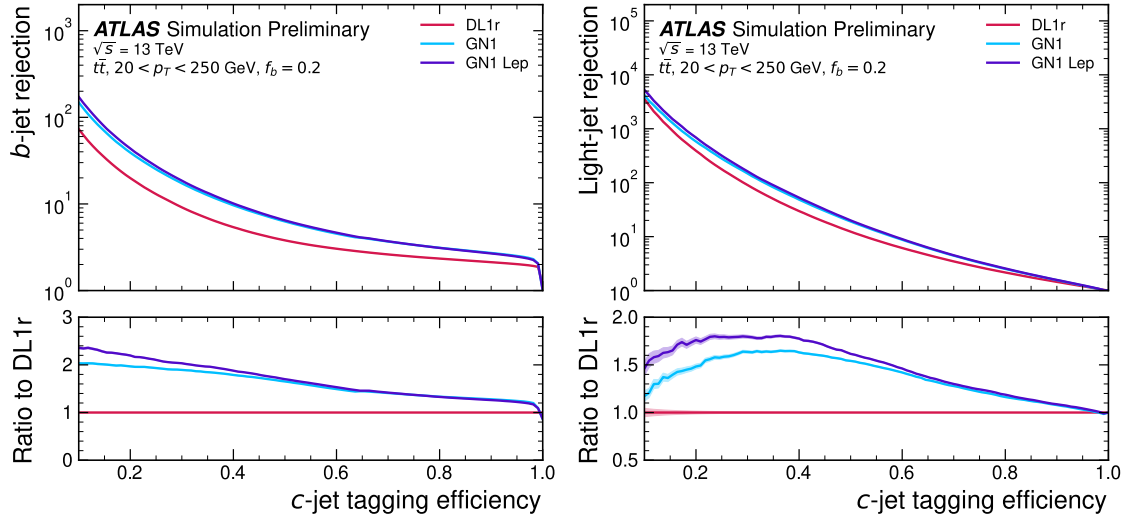


**Figure 6.9:** The  $b$ -jet (left) and light-jet (right) rejections as a function of the  $c$ -jet tagging efficiency for  $t\bar{t}$  jets with  $20 < p_T < 250$  GeV. The ratio to the performance of the DL1r algorithm is shown in the bottom panels. Binomial error bands are denoted by the shaded regions. The  $x$ -axis range is chosen to display the  $c$ -jet tagging efficiencies usually probed in these regions of phase space [3].

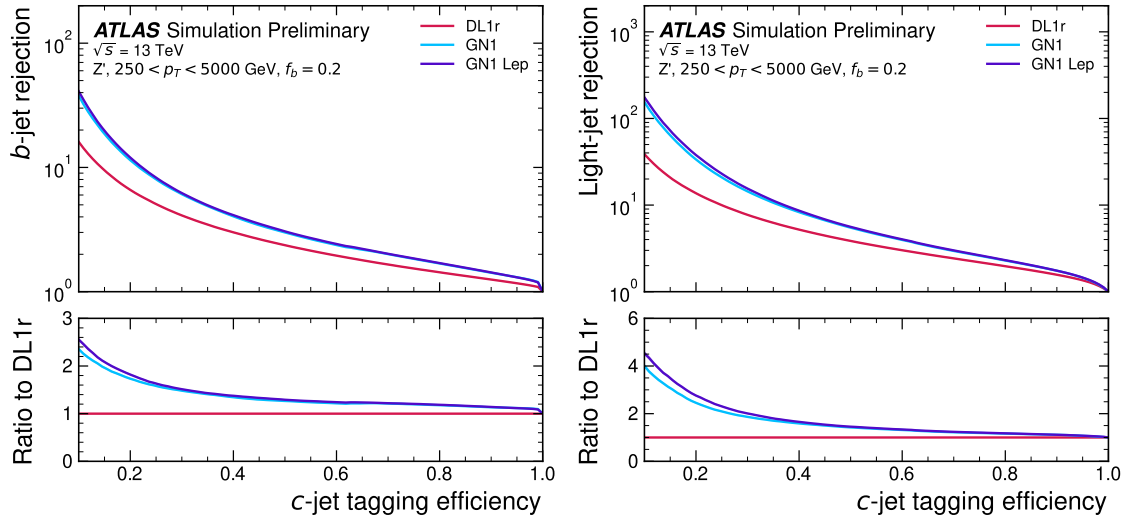


**Figure 6.10:** The  $b$ -jet (left) and light-jet (right) rejections as a function of the  $c$ -jet tagging efficiency for  $Z'$  jets with  $250 < p_T < 5000$  GeV. The ratio to the performance of the DL1r algorithm is shown in the bottom panels. Binomial error bands are denoted by the shaded regions. The  $x$ -axis range is chosen to display the  $c$ -jet tagging efficiencies usually probed in these regions of phase space [3].

1763 with both auxiliary objective, demonstrating that the two auxiliary objectives are  
1764 complementary.

1765 **6.5.4 Inclusion of Low-Level Vertexing Algorithms**

1766 As already mentioned, GN1 does not include any inputs from the low-level tagging  
1767 algorithms, including the vertexing algorithms SV1 and JetFitter [61]. Since these  
1768 algorithms are known to play a key role in contributing to the performance of DL1r,  
1769 it was studied whether their inclusion in GN1 could result in further performance  
1770 improvements. In a dedicated training of GN1, the SV1 and JetFitter tagger outputs  
1771 were added to the GN1 jet classification network as an input, similar to how they  
1772 are used in DL1r. These outputs include information on the reconstructed vertices,  
1773 including the number of vertices, and the properties of the reconstructed vertices.  
1774 In addition, if track was used in the reconstruction of a vertex, a corresponding  
1775 index to the vertex was included as a track-level inputs to GN1. These indices were  
1776 also used to construct an input feature for the edge classification network used to  
1777 identify vertices, which was given a value of one if the track-pair were from a common  
1778 reconstructed SV1 or JetFitter vertex, and zero otherwise. The jet classification  
1779 performance of this GN1 model was not significantly different to the baseline model,  
1780 and in some cases the performance was slightly reduced. It was therefore concluded  
1781 that GN1 does not benefit from the inclusion of information from SV1 and JetFitter,  
1782 indicating that the model is able to reconstruct the relevant information provided  
1783 by these low-level algorithms. The study also demonstrates that the model can  
1784 function as a highly performant standalone tagger that does not require (beyond  
1785 retraining) any manual optimisation to achieve good performance in a wide range  
1786 of phase spaces. A dedicated look at the vertexing performance of GN1 with some  
1787 comparisons to SV1 and JetFitter is found in Section 6.5.6

1788 **6.5.5 Jet Display Diagrams**

1789 The auxiliary training objectives of GN1 allow for improved model interpretability,  
1790 which is especially important for a monolithic approach as the low level taggers,  
1791 which provide useful physical insight, are no longer present. Figs. 6.13 and 6.14  
1792 provide example comparisons of the true origin and vertexing information compared

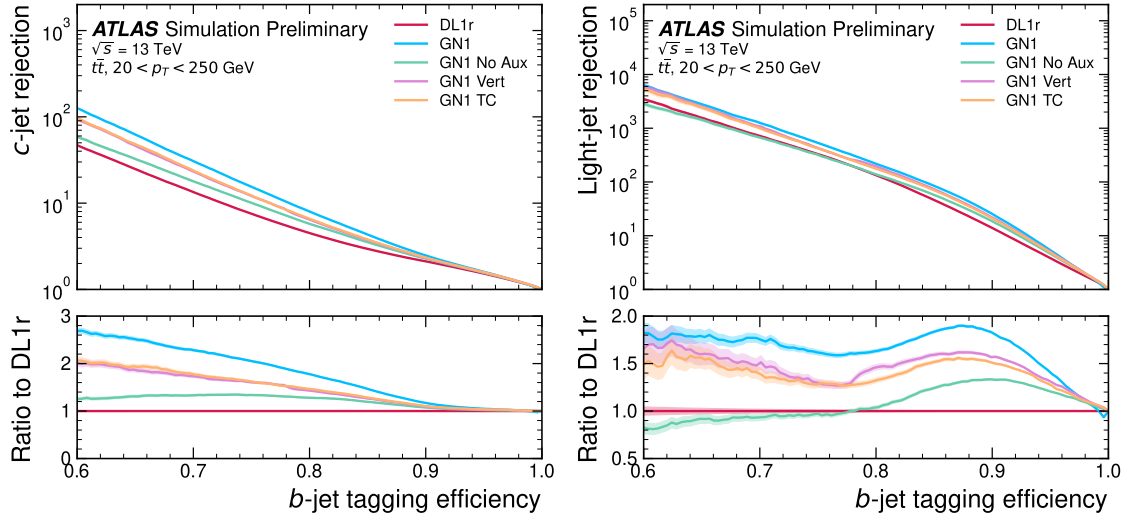


**Figure 6.11:** The  $c$ -jet (left) and light-jet (right) rejections as a function of the  $b$ -jet tagging efficiency for  $t\bar{t}$  jets with  $20 < p_T < 250$  GeV, for the nominal GN1, in addition to configurations where no (GN1 No Aux), only the track classification (GN1 TC) or only the vertexing (GN1 Vert) auxiliary objectives are deployed. The ratio to the performance of the DL1r algorithm is shown in the bottom panels. A value of  $f_c = 0.018$  is used in the calculation of  $D_b$  for DL1r and  $f_c = 0.05$  is used for GN1 [3].

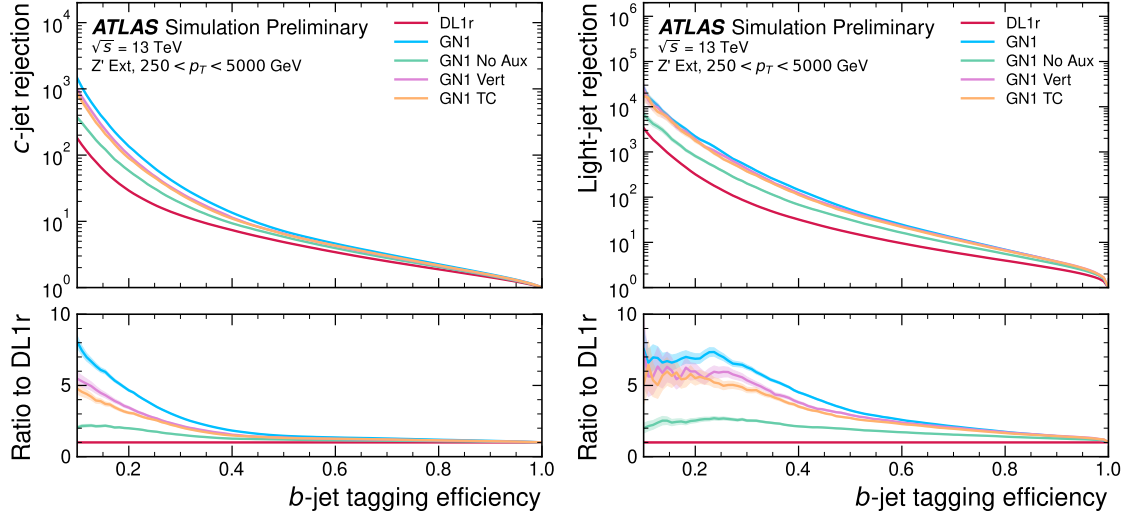


**Figure 6.12:** The  $c$ -jet (left) and light-jet (right) rejections as a function of the  $b$ -jet tagging efficiency for  $Z'$  jets with  $250 < p_T < 5000$  GeV, for the nominal GN1, in addition to configurations where no (GN1 No Aux), only the track classification (GN1 TC) or only the vertexing (GN1 Vert) auxiliary objectives are deployed. The ratio to the performance of the DL1r algorithm is shown in the bottom panels. A value of  $f_c = 0.018$  is used in the calculation of  $D_b$  for DL1r and  $f_c = 0.05$  is used for GN1 [3].

1793 with the predicted values from GN1, SV1 and JetFitter. Such comparisons can be  
 1794 used to provide an indication that GN1 reconstructs the correct representation of the  
 1795 jet structure, and may also help to identify limitations of the model. In the figures,  
 1796 the tracks in the jet are indexed twice on each of the  $x$ - and  $y$ -axes, and tracks are  
 1797 grouped into vertices along with other tracks as indicated by common markings in  
 1798 the relevant rows and columns.

1799 In Fig. 6.13, GN1 correctly groups the three primary tracks as having come from the  
 1800 primary vertex. The  $b$ -hadron and  $b \rightarrow c$ -hadron decay vertices are also correctly  
 1801 predicted, and the origin of the tracks in each is correct. There is a single OtherSec-  
 1802 ondary track which GN1 incorrectly predicts as having come from pile-up. Meanwhile  
 1803 SV1 (by design) merges the two heavy flavour decay vertices, but incorrectly includes  
 1804 a track from the primary vertex. JetFitter reconstructs two vertices, one which is a  
 1805 combination of two tracks from different truth vertices and two other single track  
 1806 vertices in each of the heavy flavour vertices. GN1 also predicts the flavour of the jet  
 1807 with a high degree of certainty.

1808 Similarly Fig. 6.13 shows that GN1 is also able to relatively accurately predict the  
 1809 origin and vertex information of tracks inside a jet. The pile-up tracks and primary  
 1810 vertex tracks are correctly identified, and the heavy flavour decay tracks are also  
 1811 correctly identified with the exception of one of the  $b$ -hadron decay tracks. Again,  
 1812 SV1 merges the two heavy flavour decay vertices along with a track from pile-up,  
 1813 while JetFitter shows signs of being underconstrained by reconstructing two single  
 1814 track vertices, one with a pile-up track and one with a track from a  $b \rightarrow c$ -hadron  
 1815 decay. While these examples do not give a complete picture of the performance of  
 1816 GN1, they do show provide a powerful way to visualise and diagnose the behaviour  
 1817 of GN1.

### 1818 6.5.6 Vertexing Performance

1819 From the track-pair vertex prediction, tracks can be partitioned into compatible  
 1820 groups representing vertices through the use of a deterministically clustering algorithm  
 1821 (see Ref. [116]). As such, GN1 can perform vertex “finding”, but not vertex “fitting”,  
 1822 i.e. the reconstruction of a vertex’s properties, which currently still requires the  
 1823 use of a dedicated vertex fitter. In order to study the performance of the different  
 1824 vertexing tools, the truth vertex label of the tracks are used.

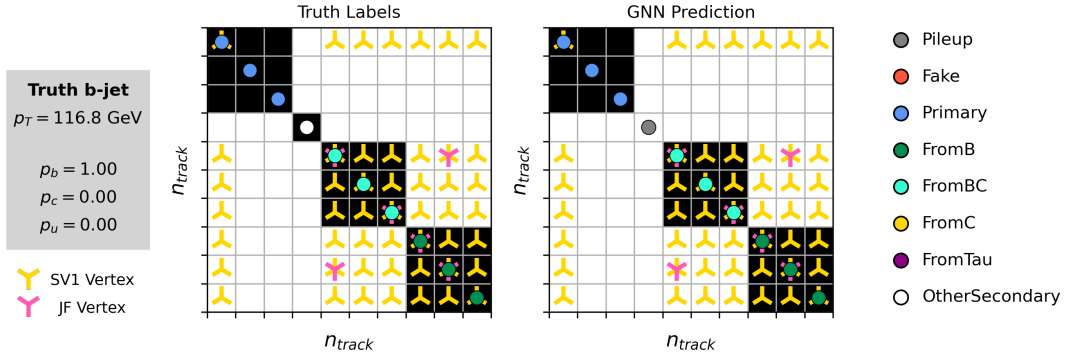


**Figure 6.13:** A schematic showing the truth track origin and vertex information (left) compared with the predictions from GN1 (right). The diagrams show the truth (left) and predicted (right) structure of a  $b$ -jet. The true and predicted origins of the tracks is shown by the coloured circles along the diagonal. The shaded black boxes show the groupings of tracks into different vertices. Vertices reconstructed by SV1 and JetFitter are also marked. Class probabilities  $p_b$ ,  $p_c$  and  $p_u$  are rounded to three significant figures. GN1 improves over SV1 and JetFitter by successfully determining the origins and vertex compatibility of all the tracks in the jet with the exception of the truth OtherSecondary track, which is misidentified as pile-up.

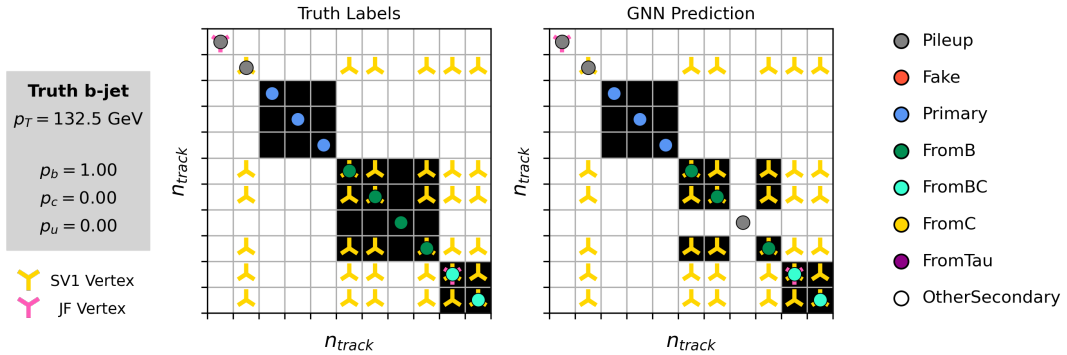


**Figure 6.14:** A schematic showing the truth track origin and vertex information (left) compared with the predictions from GN1 (right). The diagrams show the truth (left) and predicted (right) structure of a  $b$ -jet. The true and predicted origins of the tracks is shown by the coloured circles along the diagonal. The shaded black boxes show the groupings of tracks into different vertices. Vertices reconstructed by SV1 and JetFitter are also marked. Class probabilities  $p_b$ ,  $p_c$  and  $p_u$  are rounded to three significant figures. GN1 improves over SV1 and JetFitter by successfully determining the origins and vertex compatibility of all but one tracks in the jet.

1825 There are several caveats to a comparison of the vertexing tools which are a result  
1826 of the different approaches they take to vertexing. SV1 and JetFitter are designed  
1827 to only find secondary vertices in the jet, whereas GN1 is also trained to determine  
1828 which tracks in the jet belong to the primary vertex. To account for this the GN1  
1829 vertex with the largest number of predicted primary tracks is excluded from the  
1830 vertex finding efficiency calculation. While JetFitter and GN1 aim to resolve each  
1831 displaced vertex inside the jet, such that secondary vertices from  $b$ -hadron decays  
1832 are found separately to tertiary vertices from  $b \rightarrow c$  decay chains, SV1 by design  
1833 attempts to find a single inclusive vertex per jet. This inclusive vertex groups tracks  
1834 from the  $b$ -hadron decay itself (FromB) and tracks from  $b \rightarrow c$  decays (FromBC). In  
1835 order to fairly compare the performance of the different tools, both the exclusive and  
1836 inclusive vertex finding efficiencies are studied. For the exclusive vertex finding case  
1837 JetFitter and GN1 can be directly compared, while a comparison with SV1 is not  
1838 possible due to the aforementioned design constraints. The inclusive vertex finding  
1839 performance of all three tools can be compared using the procedure outlined below.

1840 The starting point for the secondary vertex finding efficiency in both the exclusive and  
1841 inclusive cases is to select truth HF secondary vertices, defined as those containing  
1842 only inclusive  $b$ -hadron decays. For exclusive HF vertex finding, these truth secondary  
1843 HF vertices can be used directly as the denominator for the efficiency calculation.  
1844 Meanwhile for the inclusive efficiency all such truth HF secondary vertices in the jet  
1845 are merged into a single inclusive target vertex. Correspondingly, for the inclusive  
1846 HF vertex finding case, the vertices found by JetFitter are merged into a single  
1847 vertex, and the vertices found by GN1 which contain at least one predicted  $b$ -hadron  
1848 decay track, are also merged. SV1 does not require any vertex merging. Only jets  
1849 containing a single  $b$ -hadron at truth level are considered.

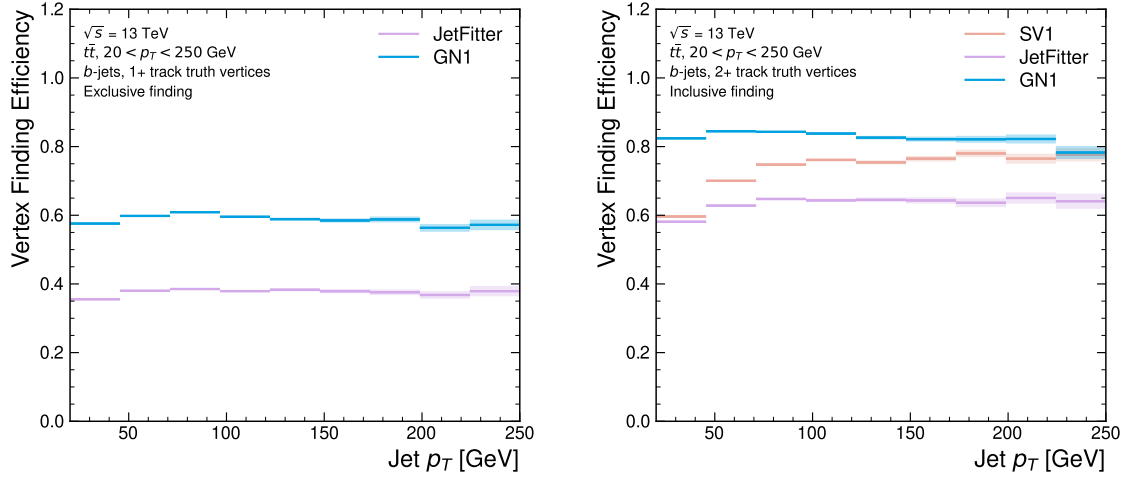
1850 Next, vertices in the jet found by the different vertexing tools are compared with  
1851 the target truth vertices. The number of correctly and incorrectly assigned tracks is  
1852 computed. In order to call a vertex efficient, it is required to contain at least 65% of  
1853 the tracks in the corresponding truth vertex, and to have a purity of at least 50%.  
1854 Single track vertices are required to have a purity of 100%. Additionally, for GN1  
1855 only, at least one track in the vertex is required to have a predicted heavy flavour  
1856 origin.

1857 Vertex finding efficiencies for  $b$ -jets in the  $t\bar{t}$  sample are displayed as a function of  
1858  $p_T$  separately for the inclusive and exclusive approaches in Fig. 6.15. For  $b$ -jets in

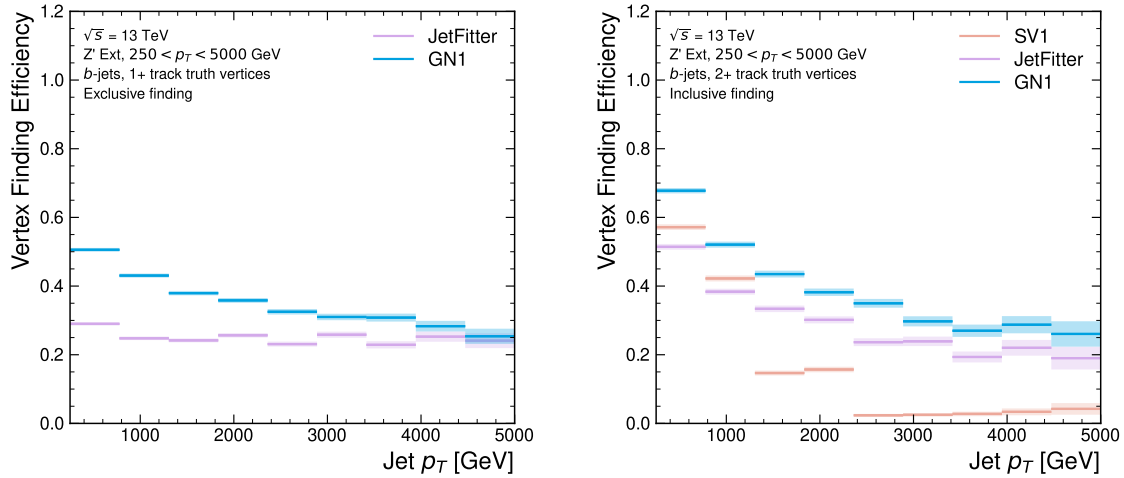
the  $t\bar{t}$  sample with  $20 < p_T < 250$  GeV, the exclusive vertex finding efficiency of JetFitter and GN1 is relatively flat as a function of  $p_T$ . For the truth secondary vertices in this  $p_T$  region, JetFitter efficiently finds approximately 40% and GN1 finds approximately 55%. When finding vertices inclusively the vertex finding efficiency is generally higher. An increased dependence on  $p_T$  is also visible for JetFitter and SV1. As the jet  $p_T$  increases from 20 GeV to 100 GeV, the efficiency of JetFitter increases from 60% to 65%. In the same range, the efficiency of SV1 increases from 60% to 75%. GN1 displays less dependence on  $p_T$  than JetFitter and SV1, finding upwards of 80% of vertices in  $b$ -jets in this  $p_T$  region. For  $b$ -jets with  $p_T > 100$  GeV, JetFitter finds approximately 65% of vertices, SV1 finds approximately 75% of vertices, and GN1 finds approximately 80% of vertices.

Fig. 6.16 compares the exclusive and inclusive HF vertex finding efficiencies for  $b$ -jets in the  $Z'$  sample. The inclusive vertex finding efficiency drops steeply with increasing  $p_T$  up until  $p_T = 3$  TeV. GN1 outperforms SV1 and JetFitter across the  $p_T$  spectrum. In the first bin, the efficiency of GN1 is 65%, while the efficiencies of SV1 and JetFitter are around 55%. The efficiency of SV1 drops rapidly to almost zero above 3 TeV, while JetFitter and GN1 retain approximately 20% and 30% efficiency respectively. For the exclusive HF vertex finding efficiency, JetFitter finds 35% of vertices in the first bin, dropping to 20% of vertices above 2 TeV. GN1 finds 55% of vertices in the first bin, dropping to 30% above 2 TeV.

While Figs. 6.15 and 6.16 indicate that GN1 is able to successfully find displaced heavy flavour vertices in  $b$ -jets, it is also important to consider the vertexing performance inside light-jets. Light-jets may also contain real displaced vertices due to long lived secondary particles and material interactions. These tracks have a truth origin of OtherSecondary in the truth labelling scheme enumerated in see Table 5.1. The efficiency to reconstruct vertices comprised of OtherSecondary tracks can be computed in an analogous way to the heavy flavour vertexing efficiency, which is described above. Figs. 6.17 and 6.18 show the efficiency to reconstruct displaced OtherSecondary vertices in light-jets as a function of  $p_T$  for jets in the  $t\bar{t}$  sample and jets in the  $Z'$  sample respectively. The figures demonstrate that GN1 is able to more effectively find such vertices in light-jets as compared with SV1 and JetFitter. Since the properties of the displaced vertices in light-jets are likely to be significantly different to heavy flavour vertices found in heavy flavour jets, the improved reconstruction of such vertices may help to differentiate between different flavour of jet.



**Figure 6.15:** Heavy flavour vertex finding efficiency as a function of jet  $p_T$  for  $b$ -jets in the  $t\bar{t}$  sample using the exclusive (left) and inclusive (right) vertex finding approaches. The exclusive vertexing approach includes single track vertices while the inclusive approach requires vertices to contain at least two tracks. Efficient vertex finding requires the recall of at least 65% of the tracks in the truth vertex, and allows no more than 50% of the tracks to be included incorrectly. Binomial error bands are denoted by the shaded regions.



**Figure 6.16:** Heavy flavour vertex finding efficiency as a function of jet  $p_T$  for  $b$ -jets in the  $Z'$  sample using the exclusive (left) and inclusive (right) vertex finding approaches. The exclusive vertexing approach includes single track vertices while the inclusive approach requires vertices to contain at least two tracks. Efficient vertex finding requires the recall of at least 65% of the tracks in the truth vertex, and allows no more than 50% of the tracks to be included incorrectly. Binomial error bands are denoted by the shaded regions.

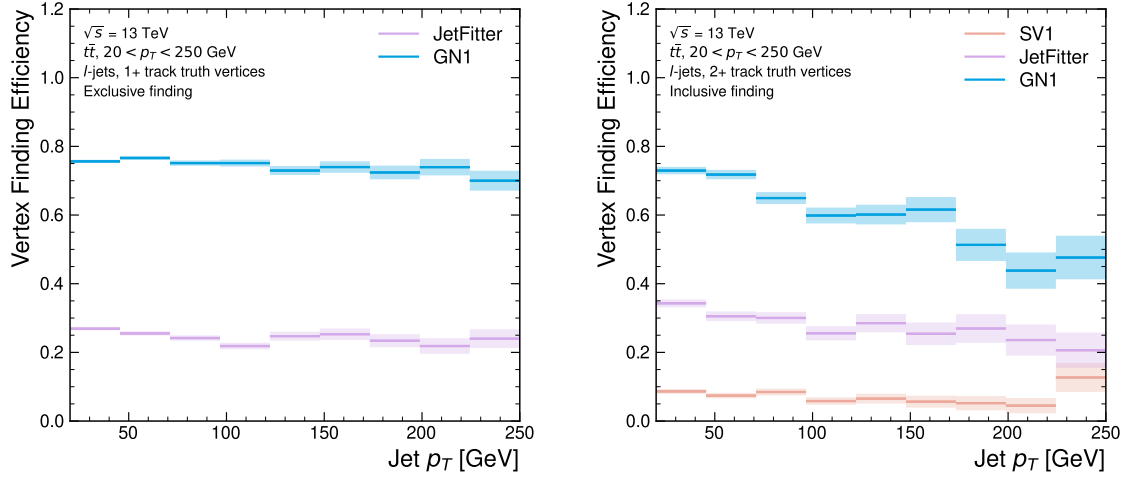


**Figure 6.17:** Vertex finding efficiency for other secondary decays as a function of jet  $p_T$  for light-jets in the  $t\bar{t}$  sample using the exclusive (left) and inclusive (right) vertex finding approaches. The exclusive vertexing approach includes single track vertices while the inclusive approach requires vertices to contain at least two tracks. Efficient vertex finding requires the recall of at least 65% of the tracks in the truth vertex, and allows no more than 50% of the tracks to be included incorrectly. Binomial error bands are denoted by the shaded regions.

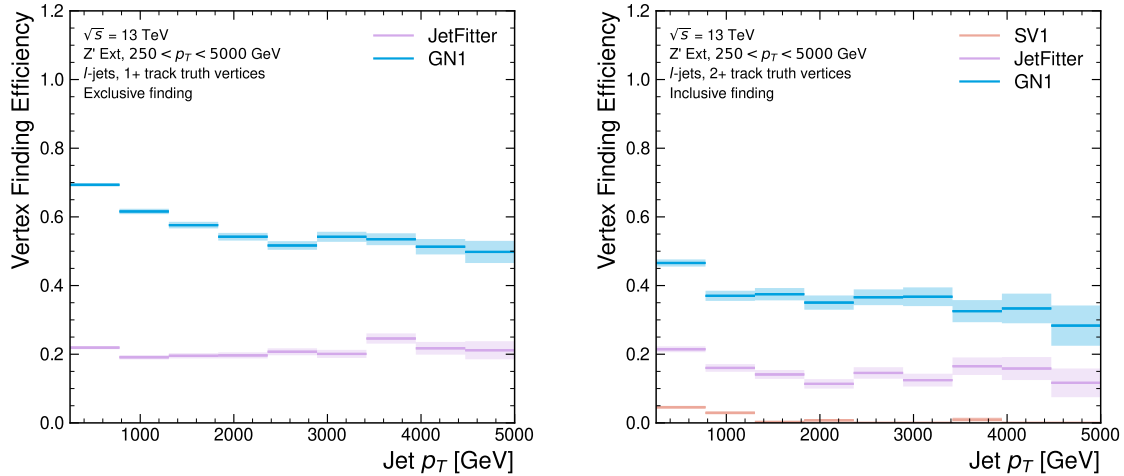


**Figure 6.18:** Vertex finding efficiency as a function of jet  $p_T$  for light-jets in the  $Z'$  sample using the exclusive (left) and inclusive (right) vertex finding approaches. The exclusive vertexing approach includes single track vertices while the inclusive approach requires vertices to contain at least two tracks. Efficient vertex finding requires the recall of at least 65% of the tracks in the truth vertex, and allows no more than 50% of the tracks to be included incorrectly. Binomial error bands are denoted by the shaded regions.

1893 Collectively, the results in this section demonstrate that GN1 is able to accurately  
1894 group tracks by their spatial origin in both  $b$ -jets and light-jets. The purity of the  
1895 found vertices was also investigated and was found to be comparable or better than  
1896 that of SV1 and JetFitter.

### 1897 6.5.7 Track Classification Performance

1898 One of the two auxiliary training objectives used by GN1 is to predict the truth origin  
1899 of each track associated to the jet. Since the equivalent information is not provided  
1900 by any of the existing flavour tagging tools, a benchmark model used to predict the  
1901 truth origin of each track is trained based on a standard multi-class feed-forward  
1902 classification network. The benchmark model is trained on the same tracks used for  
1903 the baseline GN1 training. The model uses precisely the same concatenated track-  
1904 and-jet inputs as used by GN1, but processes only a single track at a time, meaning  
1905 it cannot take into account the correlations between tracks when determining the  
1906 track origin. The model is made up of five densely connected linear layers with 200  
1907 neurons in each layer. The performance of the model was found to be unsensitive to  
1908 changes in the network structure.

1909 To measure the track classification performance, the area under the curve (AUC) of  
1910 the receiver operating characteristic (ROC) curve is computed for each origin class,  
1911 using a one-versus-all classification approach<sup>2</sup>. The AUCs for the different truth  
1912 origins are averaged using both an unweighted and a weighted mean. The unweighted  
1913 mean treats the performance of each class equally, while the weighted mean uses  
1914 as a weight the relative abundance of tracks of each class. The same approach is  
1915 used to compute the precision, recall and F1 scores<sup>3</sup>. Table 6.3 demonstrates clearly  
1916 that GN1 outperforms the MLP both at  $20 < p_T < 250$  GeV for jets in the  $t\bar{t}$  sample  
1917 and at  $250 < p_T < 5000$  GeV for jets in the  $Z'$  sample. For example, GN1 can reject  
1918 65% of fake tracks in jets in the  $t\bar{t}$  sample, while retaining more than 99% of good  
1919 tracks (i.e. those tracks which are not fake). The GN1 model has two advantages  
1920 over the MLP which can explain the performance improvement. Firstly, the graph

---

<sup>2</sup>One class is taken to be signal and the rest are taken as background, subsequently a binary classification approach is used.

<sup>3</sup>The precision is the fraction of selected tracks from the signal class. The recall, similar to the efficiency, is the fraction of tracks from the signal class which are selected. The F1 score is the harmonic mean of the precision and recall.

1921 neural network architecture enables the sharing of information between tracks. This  
1922 is likely to be beneficial since the origins of different tracks within a jet are correlated.  
1923 Secondly, the jet classification and vertexing objectives may be complementary to the  
1924 track classification objective, and so the track classification performance is improved  
1925 by the combined training of complementary objectives.

		AUC		Precision		Recall		F1	
		Mean		Weighted		Mean		Weighted	
		MLP	GN1	MLP	GN1	MLP	GN1	MLP	GN1
$t\bar{t}$	MLP	0.87	<b>0.92</b>	0.39	<b>0.51</b>	0.51	<b>0.64</b>	0.36	0.62
	GN1	<b>0.95</b>	<b>0.95</b>	<b>0.71</b>	<b>0.82</b>	<b>0.56</b>	<b>0.70</b>	<b>0.51</b>	<b>0.74</b>
$Z'$	MLP	0.90	0.94	0.36	0.84	0.47	0.72	0.31	0.76
	GN1	<b>0.94</b>	<b>0.96</b>	<b>0.48</b>	<b>0.88</b>	<b>0.60</b>	<b>0.79</b>	<b>0.48</b>	<b>0.82</b>

**Table 6.3:** The area under the ROC curves (AUC) for the track classification from GN1, compared to a standard multilayer perceptron (MLP) trained on a per-track basis. The unweighted mean AUC over the origin classes and weighted mean AUC (using as a weight the fraction of tracks from the given origin) is provided. GN1, which uses an architecture that allows track origins to be classified in a conditional manner as discussed in Section 6.4.3, outperforms the MLP model for both  $t\bar{t}$  and  $Z'$  jets.

1926 Fig. 6.19 shows the track origin classification ROC curves for the different track  
1927 origins for jets in both the  $t\bar{t}$  and  $Z'$  samples. In order to improve visual readability  
1928 of the plot, the curves for the heavy flavour truth origins (FromB, FromBC and  
1929 FromC) have been combined (weighted by their relative abundance), as have the  
1930 Primary and OtherSecondary origins. In jets in both the  $t\bar{t}$  and  $Z'$  samples, the AUC  
1931 of all the different origin groups exceeds 0.9, representing strong overall classification  
1932 performance. In both samples fake tracks are the easiest to classify, followed by  
1933 pile-up tracks. The FromC tracks which are  $c$ -hadron decay products, are the hardest  
1934 to classify, possibly due to their similarity to both fragmentation tracks and  $b$ -hadron  
1935 decay tracks, depending on the  $c$ -hadron species in question.

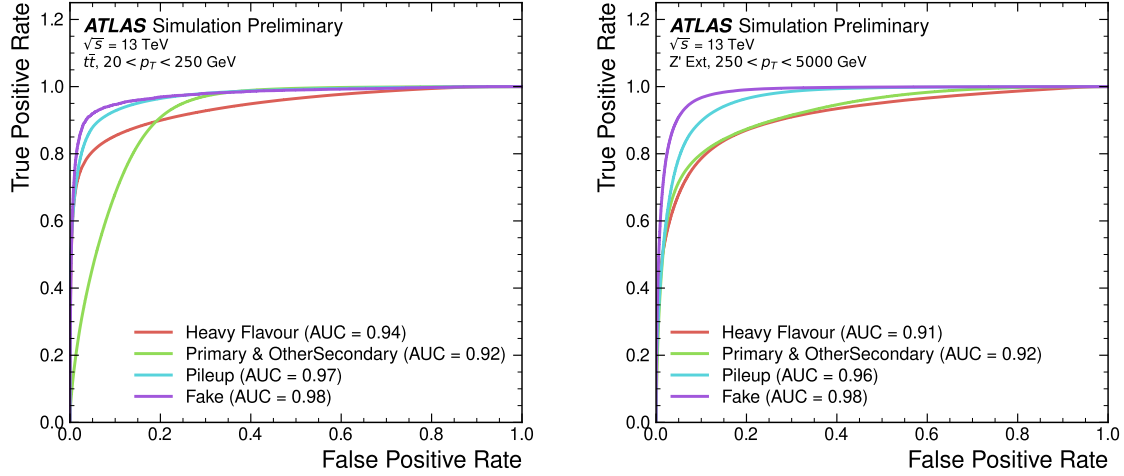


**Figure 6.19:** ROC curves for the different groups of truth origin labels defined in Table 5.1 for jets in the  $t\bar{t}$  sample (left) and jets in the  $Z'$  sample (right). The FromB, FromBC and FromC labels have been combined, weighted by their relative abundance, into the Heavy Flavour category, and the Primary and OtherSecondary labels have similarly been combined into a single category. The mean weighted area under the ROC curves (AUC) is similar for both samples [3].

## 1936 6.6 Futher Studies

### 1937 6.6.1 Looser Track Selection

1938 The track selections used to produce the main results are listed in Table 3.2. This  
 1939 includes a selection on the number of shared silicon modules used to reconstruct the  
 1940 track  $N_{\text{shared}}^{\text{Si}}$ . This value is calculated as

$$N_{\text{shared}}^{\text{Si}} = N_{\text{shared}}^{\text{Pix}} + N_{\text{shared}}^{\text{SCT}} / 2 \quad (6.10)$$

1941 where  $N_{\text{shared}}^{\text{Pix}}$  is the number of shared pixel hits and  $N_{\text{shared}}^{\text{SCT}}$  is the number of shared  
 1942 SCT modules on a track. The nominal selection used elsewhere in this thesis is  
 1943  $N_{\text{shared}}^{\text{Si}} < 2$ . As the rate of shared hits is significantly higher for  $b$ -hadron decay  
 1944 tracks than for other tracks, especially at high- $p_T$ , this selection rejects a significant  
 1945 proportion of these tracks.

1946 Figs. 6.20 and 6.21 show the result of training the GN1 tagger with the full relaxation  
 1947 of this selection, i.e. allowing tracks with any number of shared hits. The shared hit

1948 requirements applied by the ambiguity solver as part of track reconstruction (see  
1949 Section 3.4.1) are still applied. In addition, the maximum allowed value of  $d_0$  is  
1950 increased from 3.5 mm to 5.0 mm. The results show that optimisation of the input  
1951 track selection can lead to significant improvements in performance over the default  
1952 selection. For the jets in the  $t\bar{t}$  sample shown in Fig. 6.20, the effect of loosening  
1953 the track selection is limited. This is expected due to the lower prevalence of shared  
1954 hits at lower transverse momenta. However for jets in the  $Z'$  sample as shown in  
1955 Fig. 6.21, the  $c$ -jet rejection improves with respect to the baseline GN1 model by  
1956 35%, while the light-jet rejection improves by 40% at the 20%  $b$ -jet WP. Relative  
1957 improvements of a similar magnitude are also observed for GN1Lep.

### 1958 6.6.2 High Level Trigger

1959 The implementation of GN1 described in this chapter has been re-used in several  
1960 other contexts, demonstrating its flexibility to easily provide good jet flavour tagging  
1961 performance with minimal overhead. The model has been implemented as a  $b$ -jet  
1962 tagger in the High Level Trigger (HLT) (see Section 3.3.4). The inputs to the model  
1963 are the running on precision tracks<sup>4</sup> and jet level quantities reconstructed after  
1964 primary vertex reconstruction has been performed. Fig. 6.22 shows the performance  
1965 of GN1 versus a comparable DL1d model [99], and two versions of DIPS [96], with  
1966 EMTopo and PFlow jets (see Section 3.4.3) based on a low-precision region-of-interest  
1967 based tracking pass, which is optimised for speed. The trigger implementation of  
1968 GN1 improves upon the light-jet rejection of DL1d by 50% at the 60%  $b$ -jet WP for  
1969 jets in the  $t\bar{t}$  sample with  $20 < p_T < 250$  GeV.

### 1970 6.6.3 High Luminosity LHC

1971 The model also demonstrates strong performance for the High Luminosity LHC (HL-  
1972 LHC) using the proposed ITk inner tracking detector, as documented in Ref. [127].  
1973 Figs. 6.23 and 6.24 are reproduced from Ref. [127]. The results show that GN1  
1974 outperforms other existing flavour tagging algorithms when trained on an entirely  
1975 different detector geometry, the ITk (see Section 3.3.1). When compared with

---

<sup>4</sup>Precision tracking refers to tracks reconstructed in the trigger using the same reconstruction algorithms as for the offline event reconstruction.

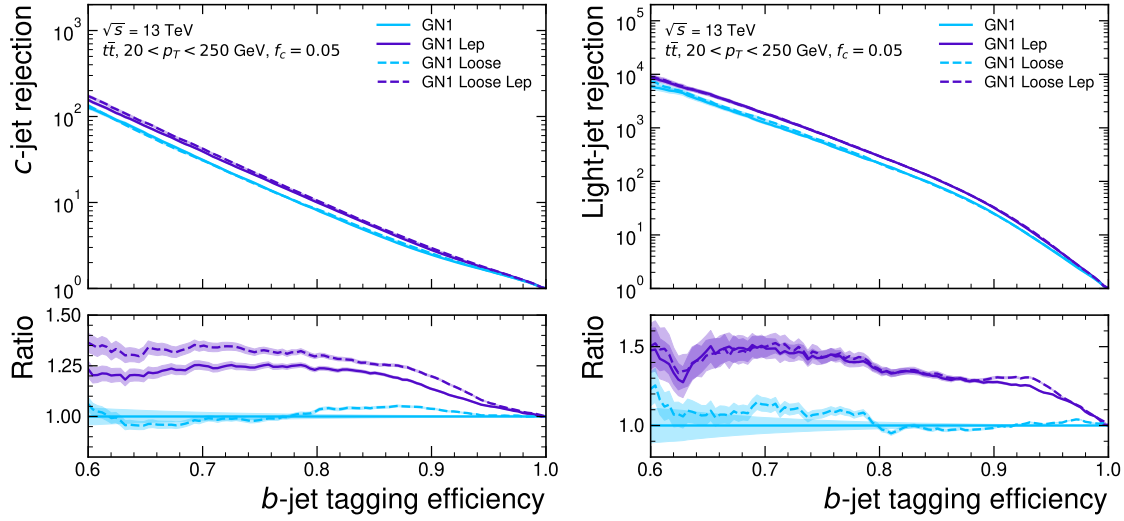


**Figure 6.20:** The  $c$ -jet (left) and light-jet (right) rejections as a function of the  $b$ -jet tagging efficiency for  $t\bar{t}$  jets with  $20 < p_T < 250$  GeV, for the looser track selection trainings of GN1. The ratio to the performance of the baseline GN1 model is shown in the bottom panels. A value of  $f_c = 0.05$  is used for all models. Binomial error bands are denoted by the shaded regions.

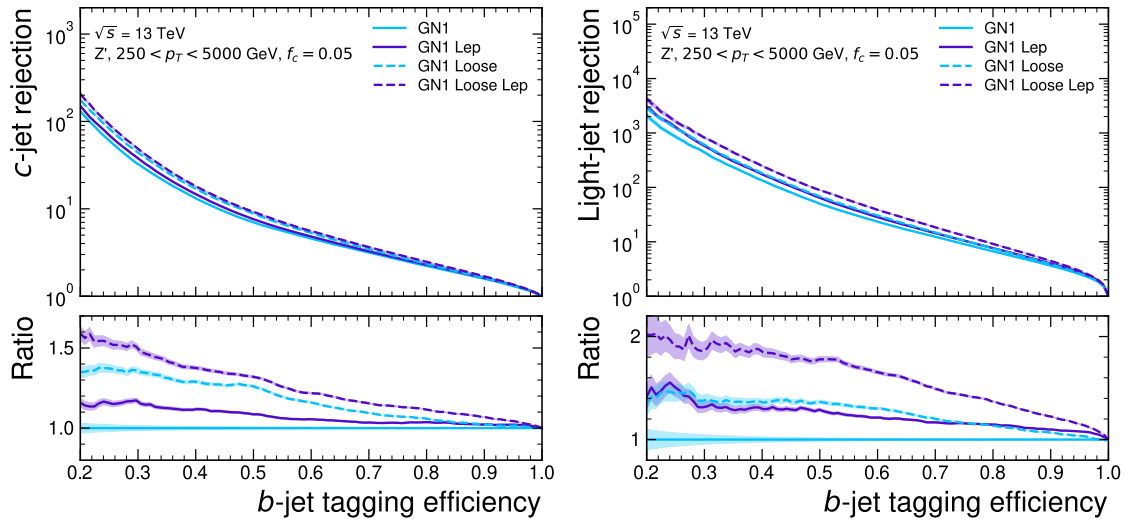


**Figure 6.21:** The  $c$ -jet (left) and light-jet (right) rejections as a function of the  $b$ -jet tagging efficiency for  $Z'$  jets with  $250 < p_T < 5000$  GeV, for the looser track selection trainings of GN1. The ratio to the performance of the baseline GN1 model is shown in the bottom panels. A value of  $f_c = 0.05$  is used for all models. Binomial error bands are denoted by the shaded regions.

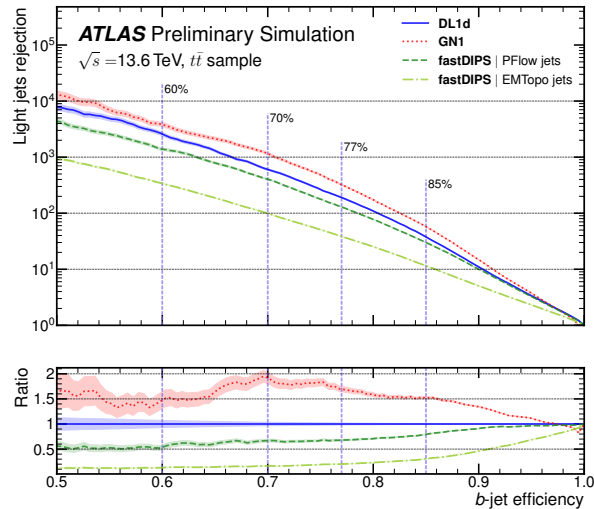


**Figure 6.22:** The HLT light-jet rejection as a function of the  $b$ -jet efficiency jets in the  $t\bar{t}$  sample with  $20 < p_T < 250 \text{ GeV}$  for events with a centre of mass energy  $\sqrt{s} = 13.6 \text{ TeV}$  [126]. The ratio to the performance of the DL1d algorithm [99] is shown in the bottom panels. Binomial error bands are denoted by the shaded regions. The purple vertical dashed lines represent the most common working points used for  $b$ -tagging.

1976 DL1d [99], GN1 improves on the  $c$ -jet rejection (light-jet rejection) by a factor of  $\sim 2$   
1977 ( $\sim 2.5$ ) for jets in the  $t\bar{t}$  sample at the 60%  $b$ -jet WP. Significant improvements in  
1978 rejections are also observed for jets in the  $Z'$  sample.

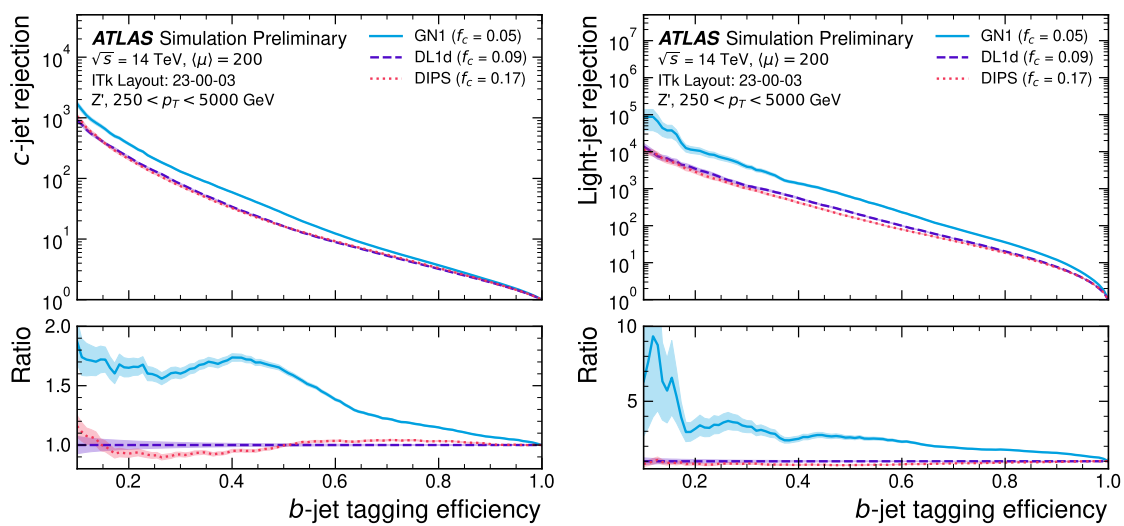
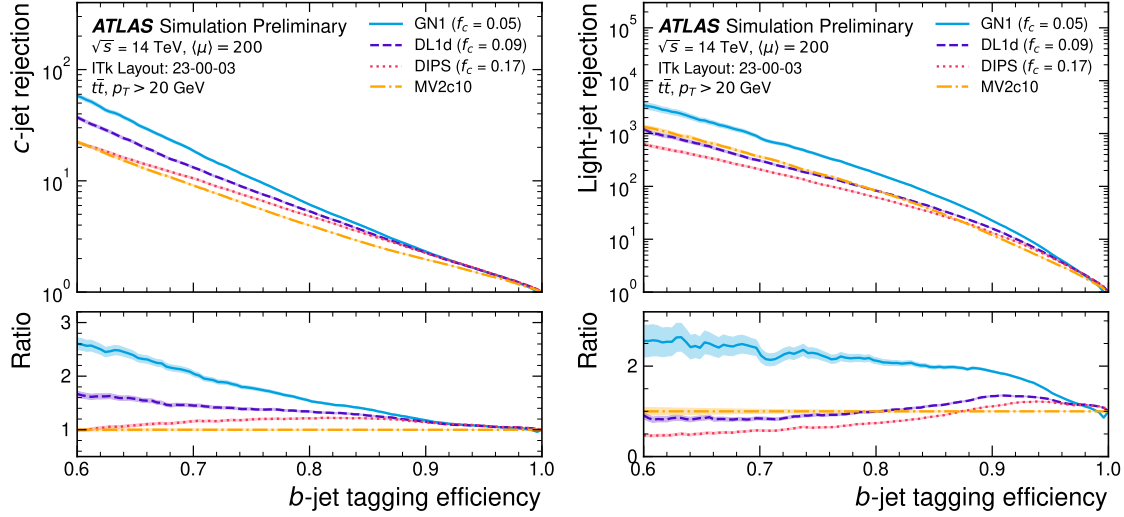
## 1979 6.7 Conclusion

1980 In this chapter a novel jet tagger, GN1, is presented. The model has a graph neural  
1981 network architecture and is trained with auxiliary training objectives, which are  
1982 shown to improve the performance of the basic model. GN1 significantly improves  
1983 flavour tagging performance with respect to DL1r, the current default ATLAS flavour  
1984 tagging algorithm, when compared in simulated collisions. GN1 improves  $c$ - and  
1985 light-jet rejection for jets in the  $t\bar{t}$  sample with  $20 < p_T < 250$  GeV by factors of  
1986  $\sim 2.1$  and  $\sim 1.8$  respectively at a  $b$ -jet tagging efficiency of 70% when compared with  
1987 DL1r. For jets in the  $Z'$  sample with  $250 < p_T < 5000$  GeV, GN1 improves the  
1988  $c$ -jet rejection by a factor of  $\sim 2.8$  and light-jet rejection by a factor of  $\sim 6$  for a  
1989 comparative  $b$ -jet efficiency of 30%.

1990 Previous multivariate flavour tagging algorithms relied on inputs from low-level  
1991 tagging algorithms, whereas GN1 needs no such inputs, making it more flexible.  
1992 It can be easily fully optimised via a retraining for specific flavour tagging use  
1993 cases, as demonstrated with  $c$ -tagging and high- $p_T$   $b$ -tagging, without the need for  
1994 time-consuming retuning of the low-level tagging algorithms. The model is also  
1995 simpler to maintain and study due to the reduction in the number of constituent  
1996 components.

1997 GN1 demonstrates improved track classification performance when compared with a  
1998 simple per-track MLP. The model is also able to perform vertex finding, and preliminary  
1999 studies suggest it outperforms previous manually optimised approaches. The  
2000 auxiliary track classification and vertex finding objectives are shown to significantly  
2001 contribute to the performance in the jet classification objective, and, along with the  
2002 more advanced graph neural network architecture, are directly responsible for the  
2003 improvement over DL1r.

2004 GN1 has also been shown to perform well for  $b$ -tagging in the High Level Trigger,  
2005 and in the projected environment for the upgraded High Luminosity LHC. The



2006 performance of the model at high- $p_T$  can be improved by loosening the input track  
2007 selection, which increases the number of  $b$ -hadron decay tracks that are inputted to  
2008 the model.

2009 Preliminary validation of the model demonstrates that the level of discrepancy  
2010 between different Monte Carlo event generators is similar to that seen for previous  
2011 ATLAS ML based taggers such as DL1r, suggesting that the model has not learnt  
2012 additional information that is specific to a single event generator. Initial comparisons  
2013 between simulated events and data also show similar levels of agreement as for  
2014 previous taggers [128].

2015 **Future Work**

2016 Further improvements in the  $b$ - and  $c$ -tagging performance are likely possible with  
2017 a more thorough optimisation of the model architecture, and the integration of  
2018 additional information from other parts of the ATLAS detector. The addition of  
2019 other auxiliary training objectives, such as the prediction of the truth  $b$ -hadron decay  
2020 radius and transverse momentum and the truth type of input tracks may also yield  
2021 additional performance gains.

2022 Although the results demonstrate a significant performance improvement at high- $p_T$ ,  
2023 it is also possible that additional studies on further loosening the selection could yield  
2024 further improved results. For example the selections on the number of number of  
2025 holes and the longitudinal impact parameter could be further relaxed. The maximum  
2026 number of tracks provided as input to the model could also be increased from the  
2027 default value of 40. In order to validate the change from the default tracking setup,  
2028 studies investigating the modelling uncertainties of the additional tracks need to be  
2029 carried out.

2030 Given that GN1 exploits the input information in a more sophisticated way than  
2031 DL1r, further studies are needed to confirm that the performance gain observed in  
2032 these simulated samples is also observed in experimental data. Additional future  
2033 work includes the full calibration of the model so it can be used by physics analyses.

2034 The flexible nature of the model means it can also be readily applied to other related  
2035 problems outside of standard  $b$ - and  $c$ -tagging applications, as demonstrated in  
2036 Section 6.6. Additional applications for the architecture include  $X \rightarrow bb$  and  $X \rightarrow cc$

2037 tagging. The model could also be repurposed as a pile-up jet or  $\tau$  tagger, or general  
2038 primary and secondary vertexing tool. Using a vertex fitting algorithm to compare  
2039 the reconstructed vertex quantities with those from SV1 and JetFitter is left for  
2040 future work.

2041 Chapter 7

2042 Boosted VHbb Analysis

2043 The Higgs boson, first observed by ATLAS and CMS at the LHC in 2012 [14, 15],  
2044 is predicted by the standard model to decay primarily to a pair of  $b$ -quarks, with  
2045 a branching fraction of  $0.582 \pm 0.007$  for  $m_H = 125$  GeV [26]. Observation of this  
2046 decay mode was reported by ATLAS [79] and CMS [28] in 2018, establishing the  
2047 first direct evidence for the Yukawa coupling of the Higgs boson to down-type quarks  
2048 (see Section 2.2.2). The  $H \rightarrow b\bar{b}$  process is also important for constraining the total  
2049 decay width of the Higgs [129].

2050 Whilst the dominant Higgs production mechanism at the LHC is gluon-gluon fusion  
2051 as outlined in Section 2.2.3, this mechanism has an overwhelming QCD multijet  
2052 background and so overall sensitivity to the Higgs is low. The QCD multijet  
2053 background refers to events containing one or more strongly produced jets which  
2054 are not the decay product of heavy resonances, for example  $g \rightarrow q\bar{q}$ . The gluon-  
2055 gluon fusion channel contains to leading order only jets in the final state, and  
2056 therefore it is extremely difficult to distinguish signal events from the overwhelming  
2057 multijet background. The  $H \rightarrow b\bar{b}$  observation therefore searched for Higgs bosons  
2058 produced in association with a vector boson  $V$  (where  $V$  can be a  $W$  or  $Z$  boson)  
2059 which subsequently decays leptonically. The leptonic final states allow for leptonic  
2060 triggering whilst at the same time significantly reducing the multijet background.

2061 Two full Run 2 dataset analyses were carried out as a follow-up to the  $H \rightarrow b\bar{b}$   
2062 observation [79]. Similar to the observation, both measured the associated production  
2063 of a Higgs with a vector boson, with the Higgs boson decaying to a pair of  $b$ -quarks.  
2064 The first analysis [130] was focussed on the resolved phase-space, where the Higgs-jet  
2065 candidate is reconstructed as two distinct jets with radius parameter  $R = 0.4$ . The

2066 second analysis [131] was focussed on the boosted phase-space, where the Higgs-jet  
2067 candidate has a sufficiently large transverse momenta such that it can be reconstructed  
2068 as a single jet with a radius parameter of  $R = 1.0$ . This chapter will focus on the  
2069 latter analysis. The analysis is outlined in Section 7.1. Modelling studies performed  
2070 are detailed in Section 7.2, and the results of the analysis are presented in Section 7.4.  
2071 This analysis has been published in Ref. [131]. Figures and tables from Ref. [131]  
2072 are reproduced here.

## 2073 7.1 Analysis Overview

2074 The boosted  $VH$ ,  $H \rightarrow b\bar{b}$  analysis is focused on the high transverse momentum  
2075 regime, which has the benefit of being more sensitive to physics beyond the Standard  
2076 Model [132], but the disadvantage of being more challenging due to the increased  
2077 difficulty in the accurate reconstruction of high transverse momentum physics objects  
2078 (discussed in Chapter 4). In order to focus on the high- $p_T$  regime, the reconstructed  
2079 vector boson  $p_T^V$  is required to be  $p_T^V > 250$  GeV (see Section 7.1.2). Events are  
2080 also split into two  $p_T^V$  bins with the first bin covering  $250 \text{ GeV} < p_T^V < 400 \text{ GeV}$  and  
2081 the second covering  $p_T^V > 400 \text{ GeV}$ , which allows the analysis to benefit from the  
2082 improved signal-to-background in the high- $p_T$  regime.

2083 The previous ATLAS analysis in Ref. [79] was primarily sensitive to vector bosons  
2084 with a more modest  $p_T^V$  boost in the region of 100–300 GeV. In this regime, the  
2085 Higgs candidate was reconstructed using a pair of jets with radius parameter of  
2086  $R = 0.4$ , called small- $R$  jets. However in the high- $p_T$  regime, the decay products  
2087 of the Higgs boson become increasingly collimated and the small- $R$  jets may  
2088 not be individually resolved. In order to enhance the reconstruction of the Higgs  
2089 boson candidate, this analysis uses a large- $R$  jet with radius parameter  $R = 1.0$  to  
2090 reconstruct the Higgs boson candidate (see Section 3.4.3). The Higgs candidate is  
2091 required to have exactly two ghost-assciated (see Section 3.4.3) and  $b$ -tagged variable-  
2092 radius track-jets. The candidate large- $R$  jet is reconstructed using jet substructure  
2093 techniques, in particular it is trimmed by removing soft and wide-angle components,  
2094 which helps to remove particles from the underlying event and pile-up collisions [133].  
2095 Refer to Section 3.4.3 for more details on jet reconstruction.

On top of the binning in  $p_T^V$ , selected events are further categorised into the 0-, 1- and 2-lepton channels depending on the number of charged leptons (electrons and muons) present in the reconstructed final state (also referred to as the 0L, 1L, and 2L channels respectively). The 0-lepton channel targets the  $ZH \rightarrow \nu\nu b\bar{b}$  process, the 1-lepton channel targets  $WH \rightarrow \ell\nu b\bar{b}$ , and the 2-lepton channel targets  $ZH \rightarrow \ell\ell b\bar{b}$ , where  $\ell$  is an electron or muon and  $\nu$  is a neutrino. Each channel has a dedicated set of selections which are listed in more detail in Section 7.1.3. Events in the 0- and 1-lepton channels are further split depending on the number of additional small- $R$  jets not matched to the Higgs-jet candidate. The high-purity signal region (HP SR) has zero such jets, while the low-purity signal region (LP SR) has one or more, and therefore absorbs a larger number of background  $t\bar{t}$  events. Maintaining a high purity signal region is important for the extraction of the signal yield. The 0- and 1-lepton channels also make use of a dedicated  $t\bar{t}$  control region for jets with one or more additional  $b$ -tagged small- $R$  jets, described described in Section 7.1.4. A complete overview of the different analysis regions is given in Table 7.1.

Channel	Analysis Regions					
	$250 < p_T^V < 400 \text{ GeV}$			$p_T^V \geq 400 \text{ GeV}$		
	0 add. $b$ -track-jets		$\geq 1$ add. $b$ -track-jets	0 add. $b$ -track-jets		$\geq 1$ add. $b$ -track-jets
	0 add. small- $R$ jets	$\geq 1$ add. small- $R$ jets		0 add. small- $R$ jets	$\geq 1$ add. small- $R$ jets	
0-lepton	HP SR	LP SR	CR	HP SR	LP SR	CR
1-lepton	HP SR	LP SR	CR	HP SR	LP SR	CR
2-lepton	SR			SR		

**Table 7.1:** Summary of the definitions of the different analysis regions . Signal enriched regions are marked with the label SR. There are regions with relatively large signal purity (HP SR) and with low purity (LP SR). Background enriched regions are marked with the label CR. The shorthand “add” stands for additional small- $R$  jets, i.e. number of small- $R$  jets not matched to the Higgs-jet candidate. The medium and high  $p_T^V$  regions are referred to as  $Mp_T^V$  and  $Hp_T^V$ , respectively [131].

The signal  $VH, H \rightarrow b\bar{b}$  yields is extracted from a profile likelihood fit to the large- $R$  jet mass over several signal and control analysis regions, which are described in Sections 7.1.3 and 7.1.4. The diboson background  $VZ, Z \rightarrow b\bar{b}$  yield is simultaneously extracted from the fit, and provides a cross check on the signal extraction. The fit

2115 model (described henceforth only as ‘‘the fit’’) is described in more detail in described  
2116 in Section 7.3.

### 2117 7.1.1 Data & Simulated Samples

2118 Data from centre-of-mass energy  $\sqrt{s} = 13$  TeV proton-proton collisions at the LHC  
2119 recorded over the course of Run 2 (between 2015 and 2018) were used for the analysis.  
2120 The resulting dataset corresponds to a total integrated luminosity of  $139 \text{ fb}^{-1}$  (see  
2121 Fig. 3.4).

2122 An overview of the MC simulated samples used in the analysis is given in Table 7.2.  
2123 These samples are used to model the signal and background processes relevant to the  
2124 analysis, with the exception of the multijet background which is modelled using a  
2125 data-driven technique. Data and simulated events are reconstructed using the same  
2126 algorithms, and a reweighting is applied to the simulated events in order to match  
2127 the pile-up distribution observed in the data.

### 2128 7.1.2 Object Reconstruction

2129 The presence of neutrinos in the  $WH \rightarrow \ell\nu b\bar{b}$  and  $ZH \rightarrow \ell\ell b\bar{b}$  signatures can be  
2130 inferred from a momentum imbalance in the transverse plane Section 3.4.5. The  
2131 vector boson transverse momentum  $p_T^V$  is reconstructed as the missing transverse  
2132 energy  $E_T^{\text{miss}}$  in the 0-lepton channel, as the magnitude of the summed  $\mathbf{E}_T^{\text{miss}}$  and  
2133 charged-lepton momentum in the 1-lepton channel, and as the transverse momentum  
2134 of the 2-lepton system in the 2-lepton channel (see Section 3.4.5).

2135 Electrons and muons are reconstructed as outlined in Section 3.4.4, and following the  
2136 approach described in Ref. [79]. Leptons are required to satisfy the selections listed  
2137 in Table 7.3. *Baseline* electrons are required to pass the likelihood-based method  
2138 described in Section 3.4.4, and *Signal* electron additionally are required to satisfy  
2139 a tighter likelihood identification selection. *Baseline* muons are required to pass  
2140 the ‘loose’ identification described in Ref. [77], while *signal* muons are required to  
2141 pass the ‘medium’ identification working point. All signal leptons are required to  
2142 additionally satisfy a  $p_T > 27$  GeV selection criteria, except for muons in the 1-lepton  
2143 channel where a cut of 25 GeV is used. The number of baseline leptons is used to

Process	ME generator	ME PDF	PS and Hadronisation	UE model tune	Cross-section order
Signal ( $m_H = 125$ GeV and $b\bar{b}$ branching fraction set to 58%)					
$qg \rightarrow W H \rightarrow \ell\nu b\bar{b}$	POWHEG-Box v2 [134] + GoSam [136] + MiNLO [137, 138]	NNPDF3.0NLO <sup>(*)</sup> [86]	PyTHIA 8.212 [88]	AZNLO	NNLO(QCD) + NLO(EW) [139–145]
$qq \rightarrow ZH \rightarrow \nu\nu b\bar{b}/\ell\ell b\bar{b}$	POWHEG-Box v2 + GoSam + MiNLO	NNPDF3.0NLO <sup>(*)</sup>	PyTHIA 8.212	AZNLO	NNLO(QCD) <sup>(†)</sup> + NLO(EW)
$gg \rightarrow ZH \rightarrow \nu\nu b\bar{b}/\ell\ell b\bar{b}$	POWHEG-Box v2	NNPDF3.0NLO <sup>(*)</sup>	PyTHIA 8.212	AZNLO	NLO+ NLL [146–150]
Top quark ( $m_t = 172.5$ GeV)					
$t\bar{t}$	POWHEG-Box v2 [134, 151]	NNPDF3.0NLO	PyTHIA 8.230	A14 [89]	NNLO+NNLL [152]
$s$ -channel	POWHEG-Box v2 [134, 153]	NNPDF3.0NLO	PyTHIA 8.230	A14	NLO [154]
$t$ -channel	POWHEG-Box v2 [134, 153]	NNPDF3.0NLO	PyTHIA 8.230	A14	NLO [155]
$Wt$	POWHEG-Box v2 [134, 156]	NNPDF3.0NLO	PyTHIA 8.230	A14	Approximate NNLO [157]
Vector boson + jets					
$W \rightarrow \ell\nu$	SHERPA 2.2.1 [158–161]	NNPDF3.0NNLO	SHERPA 2.2.1 [162, 163]	Default	NNLO [164]
$Z/\gamma^* \rightarrow \ell\ell$	SHERPA 2.2.1	NNPDF3.0NNLO	SHERPA 2.2.1	Default	NNLO
$Z \rightarrow \nu\nu$	SHERPA 2.2.1	NNPDF3.0NNLO	SHERPA 2.2.1	Default	NNLO
Diboson					
$qq \rightarrow WW$	SHERPA 2.2.1	NNPDF3.0NNLO	SHERPA 2.2.1	Default	NLO
$qq \rightarrow WZ$	SHERPA 2.2.1	NNPDF3.0NNLO	SHERPA 2.2.1	Default	NLO
$qq \rightarrow ZZ$	SHERPA 2.2.1	NNPDF3.0NNLO	SHERPA 2.2.1	Default	NLO
$gg \rightarrow VV$	SHERPA 2.2.2	NNPDF3.0NNLO	SHERPA 2.2.2	Default	NLO

**Table 7.2:** Signal and background processes with the corresponding generators used for the nominal samples [131]. If not specified, the order of the cross-section calculation refers to the expansion in the strong coupling constant ( $\alpha_s$ ). <sup>(\*)</sup> The events were generated using the first PDF in the NNPDF3.0NLO set and subsequently reweighted to the PDF4LHC15NLO set [165] using the internal algorithm in POWHEG-BOX v2. <sup>(†)</sup> The NNLO(QCD)+NLO(EW) cross-section calculation for the  $pp \rightarrow ZH$  process already includes the  $gg \rightarrow ZH$  contribution. The  $qg \rightarrow ZH$  process is normalised using the cross-section for the  $pp \rightarrow ZH$  process, after subtracting the  $gg \rightarrow ZH$  contribution. An additional scale factor is applied to the  $qg \rightarrow VH$  processes as a function of the transverse momentum of the vector boson, to account for electroweak (EW) corrections at NLO. This makes use of the  $VH$  differential cross-section computed with HAWK [166, 167].

2144 categorise the event into the 0-, 1- or 2-lepton channels. The 1- and 2-lepton channels  
2145 additionally require one signal lepton to be present.

Variable	Electrons	Muons
$p_T$	$> 7 \text{ GeV}$	
$ \eta $	$< 2.47$	$< 2.7$
$s(d_0)$	$< 5$	$< 3$
$ z_0 \sin(\theta) $	$< 0.5 \text{ mm}$	

**Table 7.3:** Selections applied to baseline and signal electrons and muons.

2146 The analysis makes use of large- $R$  and variable-radius small- $R$  track-jets, which  
2147 are described in Section 3.4.3. The large- $R$  jets are used to reconstruct the Higgs  
2148 boson candidate, while the small- $R$  jets are used for  $b$ -tagging and for selection of  
2149 the analysis region. The track-jets matched to the Higgs candidate are  $b$ -tagged  
2150 using the MV2c10  $b$ -tagging algorithm (see Chapter 4). The efficiency of the tagging  
2151 algorithm is calibrated to events in data [168–170]. The jet tagging strategy relies  
2152 on extensive studies into track-jet  $b$ -tagging in boosted topologies [171, 172].

### 2153 7.1.3 Selection Criteria

2154 An extensive list of selection cuts are applied to each event in order to reject  
2155 background events whilst retaining as many signal events as possible. A full list of  
2156 selection cuts applied to the different analysis regions is given in Table 7.4, while  
2157 some key selections are listed below.

2158 All channels require events with at least one large- $R$  jet with  $p_T > 250 \text{ GeV}$   
2159 and  $|\eta| < 2.0$ . The vector boson transverse momentum is also required to satisfy  
2160  $p_T^V > 250 \text{ GeV}$ . The Higgs candidate is chosen as the highest  $p_T$  large- $R$  jet satisfying  
2161 these requirements. As mentioned, the candidate large- $R$  jet is required to have  
2162 two ghost-assciated and  $b$ -tagged variable-radius track-jets. These track-jets are  
2163 required to have at least two constituent tracks with  $p_T > 500 \text{ MeV}$  and  $|\eta| < 2.5$ .  
2164 The track-jets themselves must satisfy  $p_T > 10 \text{ GeV}$  and  $|\eta| < 2.5$ .

2165 In the 0-lepton channel, trigger selections are applied using an  $E_T^{\text{miss}}$  trigger with a  
2166 luminosity-dependent threshold between 70–110 GeV. In the 1-lepton electron sub-  
2167 channel a combination of single electron triggers is used with minimum  $p_T$  thresholds  
2168 between 24–26 GeV. In the muon sub-channel the same  $E_T^{\text{miss}}$  trigger as the 0-lepton  
2169 channel is used. Since muons are not used for the  $E_T^{\text{miss}}$  trigger calculations, this  
2170 is in effect a  $p_T$  requirement on the muon-neutrino system, which in the analysis  
2171 phase space is more efficient than a single-muon trigger. The 2-lepton channel uses  
2172 the same triggering strategy as the 1-lepton channel. In all channels, the trigger  
2173 selections applied are fully efficient for events selected using the full requirements in  
2174 Table 7.4.

2175 The combined selections in Table 7.4 result in a signal efficiency ranging from 6–16%  
2176 for the  $WH$  and  $ZH$  processes depending on the channel and  $p_T^V$  bin.

### 2177 7.1.4 Control Regions

2178 The  $t\bar{t}$  process presents a major background in the 0- and 1-lepton channels. In these  
2179 events, the Higgs candidate is often reconstructed from a correctly tagged  $b$ -jet from  
2180 the top decay  $t \rightarrow Wb$ , and an incorrectly tagged  $c$ - or light-jet from the subsequent  
2181 decay of the  $W$ , as shown in Fig. 7.1.

2182 The top quark predominately decays to a  $W$  and a  $b$ -quark. Hence, the second top  
2183 quark from the  $t\bar{t}$  pair is also likely to result in a second tagged  $b$ -tagged track-jet  
2184 outside of the large- $R$  Higgs candidate. To ensure sufficient  $t\bar{t}$  rejection, 0- and  
2185 1-lepton channel signal regions are defined using a veto on events with  $b$ -tagged  
2186 track-jets outside the Higgs-jet candidate. These events are used to construct a  
2187 control region (CR) which is enriched in  $t\bar{t}$  events. The CR is used to constrain the  
2188 normalisation of the  $t\bar{t}$  background in the fit.

### 2189 7.1.5 Background Composition

2190 After the selections described in Section 7.1.3 the number of background events  
2191 mimicking the  $VH$ ,  $H \rightarrow b\bar{b}$  signal is greatly reduced. However, the number of  
2192 background events still greatly outnumbers that of signal events. The background  
2193 processes are channel dependent. In the 0-lepton channel the dominant sources of

Selection	0 lepton channel	1 lepton channel	2 leptons channel	
Trigger	$E_T^{\text{miss}}$	$E_T^{\text{miss}}$	$e$ sub-channel	$\mu$ sub-channel
Leptons	0 baseline leptons	1 signal lepton	$E_T^{\text{miss}}$	Single electron
		$p_T > 27 \text{ GeV}$	$p_T > 25 \text{ GeV}$	$E_T^{\text{miss}}$
		no second baseline lepton		
				2 baseline leptons among which $\geq 1$ signal lepton, $p_T > 27 \text{ GeV}$
				both leptons of the same flavour -
				opposite sign muons
$E_T^{\text{miss}}$	$> 250 \text{ GeV}$	$> 50 \text{ GeV}$	-	-
$p_T^V$			$p_T^V > 250 \text{ GeV}$	-
Large- $R$ jets		at least one large- $R$ jet, $p_T > 250 \text{ GeV},  \eta  < 2.0$		
Track-jets		at least two track-jets, $p_T > 10 \text{ GeV},  \eta  < 2.5$ , matched to the leading large- $R$ jet		
$b$ -tagged jets		leading two track-jets matched to the leading large- $R$ must be $b$ -tagged (MV2c10, 70%)		
$m_J$			$> 50 \text{ GeV}$	
$\min[\Delta\phi(\mathbf{E}_T^{\text{miss}}, \text{small-}R \text{ jets})]$	$> 30^\circ$		-	
$\Delta\phi(\mathbf{E}_T^{\text{miss}}, H_{\text{cand}})$	$> 120^\circ$		-	
$\Delta\phi(\mathbf{E}_T^{\text{miss}}, \mathbf{E}_{T, \text{trk}}^{\text{miss}})$	$< 90^\circ$		-	
$\Delta y(V, H_{\text{cand}})$	-		$ \Delta y(V, H_{\text{cand}})  < 1.4$	
$m_{\ell\ell}$	-			$66 \text{ GeV} < m_{\ell\ell} < 116 \text{ GeV}$
Lepton $p_T$ imbalance	-			$(p_T^{\ell_1} - p_T^{\ell_2})/p_T^Z < 0.8$

**Table 7.4:** Event selection requirements for the boosted  $VH$ ,  $H \rightarrow b\bar{b}$  analysis channels and sub-channels [131]. Various channel dependent selections are used to maximise the signal efficiency and reduce the number of background events in each analysis region. The  $\min[\Delta\phi(\mathbf{E}_T^{\text{miss}}, \text{small-}R \text{ jets})]$  selection is used to remove jets when the missing transverse momentum  $\mathbf{E}_T^{\text{miss}}$  is pointing in the direction of the Higgs candidate, and the  $\Delta\phi(\mathbf{E}_T^{\text{miss}}, \mathbf{E}_{T, \text{trk}}^{\text{miss}})$  is used to reject events where the calorimeter missing transverse momentum  $\mathbf{E}_T^{\text{miss}}$  is not pointing in the direction of the track-based missing transverse momentum  $\mathbf{E}_{T, \text{trk}}^{\text{miss}}$ . The  $\Delta y(V, H_{\text{cand}})$  quantifies the rapidity difference between the reconstructed vector boson and Higgs candidate.

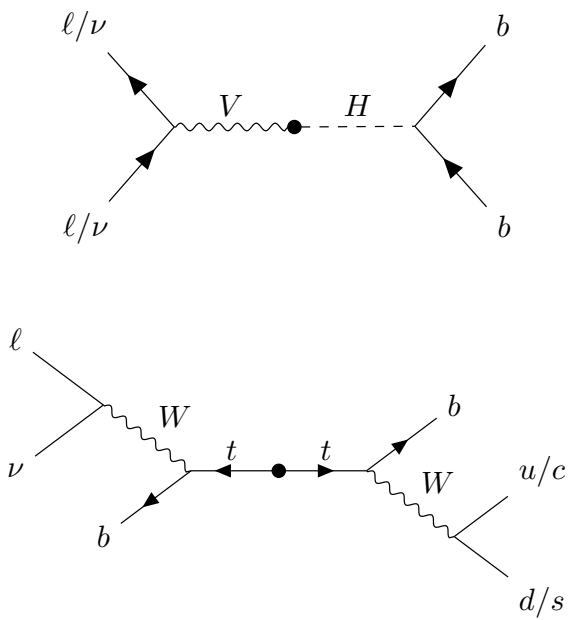


**Figure 7.1:** Diagrams of the signal process (top) and  $t\bar{t}$  background (bottom). Object to the right of centre are reconstructed within the large- $R$  jet. For the  $t\bar{t}$  background, the large- $R$  jet contains a mis-tagged  $c$ -jet or (less often) a mis-tagged light-jet. The contribution in the 0-lepton channel results from hadronically decaying  $\tau$  lepton, or a electron or muon which is out of the analysis acceptance.

2194 backgrounds are  $Z + \text{jets}$  ( $Z \rightarrow \nu\nu$ ) and  $t\bar{t}$ , with  $W + \text{jets}$  and diboson events being  
2195 subdominant. In the event of  $W \rightarrow \tau\nu$ , and subsequent hadronic decay of the  $\tau$  or  
2196 lack of successful reconstruction/selection of the leptonic decay products,  $W + \text{jets}$   
2197 can also contribute to the 0-lepton channel.  $t\bar{t}$  and  $W + \text{jets}$  (with a leptonic decay  
2198 of the  $W$  as in  $W \rightarrow \ell\nu$ ) are dominant in the 1-lepton channel, while single-top is  
2199 subdominant. In the 2-lepton channel,  $Z + \text{jets}$  ( $Z \rightarrow \ell\ell$ ) is again dominant followed  
2200 by  $Z Z$  diboson events.

2201 The diboson background  $VV$  consists primarily of  $WZ$  and  $ZZ$  events in which the  
2202  $Z$  decays to a pair of  $b$ -quarks. This process very closely matches the signal, with  
2203 a resonant peak occurring at  $m_Z = 91$  GeV and so is considered as an irreducible  
2204 background ( $V+b$ -jets is also irreducible).

2205 The  $t\bar{t}V$ ,  $t\bar{t}H$  and multijet backgrounds are negligible in the analysis phase space  
2206 after the selections have been applied, with the exception of the 1-lepton electron  
2207 sub-channel, in which multijet background is not negligible. The multijet background  
2208 is made up of events where the isolated leptonic signature has been mimicked by  
2209 either a jet or a muon or electron from a semi-leptonic heavy flavour decay, where  
2210 the lepton has escaped the jet.

2211 The contributions from the different backgrounds are modelled using Monte Carlo  
2212 event generators and the uncertainties associated with these samples are studied in  
2213 Section 7.2. The multijet background is modelled using a data-driven technique.

## 2214 7.2 Systematic Uncertainties & Background 2215 Modelling

2216 Systemic uncertainties are extensively employed to give the fit model enough flexibility  
2217 to account for inaccuracies in the various inputs. Two main types of systematic  
2218 uncertainty are considered: experimental and modelling. Experimental uncertainties  
2219 arise due to the imperfect reconstruction algorithms (in particular the jet recon-  
2220 struction and  $b$ -tagging algorithms), and due to the imperfect modelling of pile-up  
2221 and other effects, as described in Section 7.2.3. Modelling uncertainties arise due  
2222 to the imperfections in the Monte-Carlo simulations used to model the signal and  
2223 background events. In order to observe a certain process, for example  $VH$ ,  $H \rightarrow b\bar{b}$ ,

2224 an increase in the number of observed events with respect to the background-only  
2225 hypothesis is looked for. The excess is often relatively small against the total number  
2226 of background events, and hence accurate modelling of the expected number of  
2227 background and signal events is crucial for successfully performing the analysis.  
2228 Particular care is paid to the uncertainties on the modelling predictions as discussed  
2229 in this section.

2230 Modelling uncertainties are described in detail in the following sections. *Nominal*  
2231 samples are used as a reference to which different variations can be compared.  
2232 The nominal samples are chosen as the best possible representation of the underlying  
2233 physical process. *Alternative* samples are used to understand inaccuracies that may  
2234 be present in the nominal samples. Some aspect of the nominal model is varied, and  
2235 the discrepancy with respect to the nominal model is quantified. The discrepancy is  
2236 used to estimate a systematic uncertainty associated with the model parameter which  
2237 was varied. The alternative samples are sometimes obtained via internal weight  
2238 variations or parameterisation methods, rather than by re-running the simulation.  
2239 This is discussed in more detail in Section 7.2.1.

2240 Modelling studies involving  $c$ - and light-jets is hampered by the low number of events  
2241 available after the analysis selection is applied, due to the high rejection rates of the  
2242  $b$ -tagging algorithm MV2c10. For modelling studies, truth tagging (TT) is therefore  
2243 employed to ensure sufficient numbers of jets are available to calculate uncertainties.  
2244 TT works by computing a 2-dimensional efficiency map using the jet  $p_T$  and  $\eta$ . The  
2245 two leading track-jets associated to the large- $R$  jet are weighted based on their  $p_T$   
2246 and  $\eta$  using the pre-calculated efficiency map, rather than being required to explicitly  
2247 pass the  $b$ -tagging requirement.

### 2248 7.2.1 Implementation of Variations

2249 Modelling variations are implemented in different ways, depending on the associ-  
2250 ated uncertainty. Table 7.5 lists the different sources of uncertainty described in  
2251 Section 7.2.2 and for each lists the implementation. As production of high-stastic  
2252 MC samples is computationally expensive, a technique in state of the art simulation  
2253 packages is to store some sources of variation as internal weights, which can be  
2254 generated alongside the nominal samples, saving computation time. The nominal

Source of Uncertainty	Implementation
Renormalisation scale ( $\mu_R$ )	Internal weights
Factorisation scale ( $\mu_F$ )	Internal weights
PDF set	Internal weights
Parton Shower (PS) models	Alternative samples
Underlying Event (UE) models	Alternative samples
Resummation scale (QSF)	Parameterisation
Merging scale (CKKW)	Parameterisation

**Table 7.5:** Different sources of uncertainty (i.e. variations in the model) considered for the  $V+jets$  background, and the corresponding implementation. For each uncertainty, acceptance and shape uncertainties are derived.

sample then effectively contains information about an ensemble of different samples, corresponding to different model parameters, which are accessible via reweightings. When filling histograms for the variations, bins are incremented by the internal weight of the event associated with the variation in question.

While the inclusion of internal weight variation in MC event generators has decreased simulation times and increased available statistics, there are in SHERPA 2.2.1 currently some sources of systematic uncertainty that are unable to be stored as internal weight variations due to technical limitations. Two examples are the choice of resummation and merging scales. A method to parameterise the systematic variation using one sample, and to then apply this parameterisation to another sample, has been developed by ATLAS [173]. This method was used to derive resummation and merging uncertainties for the nominal SHERPA 2.2.1 sample, using a previous (lower statistic) SHERPA 2.1 alternative sample. The resulting uncertainties were studied and found to be negligible in comparison with systematics from other sources.

## 7.2.2 Sources of Systematic Modelling Uncertainties

This section briefly describes the different sources of uncertainty in the analysis, and how each is implemented. For each source of uncertainty, acceptance and shape uncertainties are derived. Acceptance uncertainties account for the uncertainty in the overall number of events in each channel, and for the migration of events between

2274 different analysis regions. Meanwhile, shape uncertainties account for differences in  
2275 the shapes, but not overall normalisations, of the large- $R$  jet mass.

## 2276 QCD Scales

2277 The  $V + \text{jets}$  matrix element calculations contains infrared and ultraviolet divergences.  
2278 These are handled by introducing arbitrary parameters corresponding to the renor-  
2279 malisation scale ( $\mu_R$ ) and factorisation scale ( $\mu_F$ ). Physical observables are not  
2280 dependent on these parameters when using the infinite perturbation series expansion,  
2281 however at some fixed order in QCD a limited dependence is present. To assess the  
2282 impact of this, both  $\mu_R$  and  $\mu_F$  are independently varied from their nominal values  
2283 by factors of 0.5 and 2 to account for higher order corrections to the calculation of  
2284 the matrix element used to simulate the process.

## 2285 PDF Sets

2286 Parton distribution functions (PDFs) specify the probability of finding a parton with  
2287 a given momentum inside a hadron (in this case, colliding protons). PDFs have  
2288 to be derived from data and are a significant source of uncertainty in analyses of  
2289 hadronic collision data. There are three sources of PDF uncertainties: the statistical  
2290 and systematic errors on the underlying data used to derive the PDFs, the theory  
2291 which is used to describe them (which is based on some fixed order perturbative  
2292 QCD expansion), and finally the procedure which is used to extract the PDFs from  
2293 the data. PDF-related uncertainties were derived following Ref. [165]. This involves  
2294 considering 100 PDF replicas which, when combined, form a central value and  
2295 associated uncertainty, and also in parallel direct changes to the central values of  
2296 PDFs using the MMHT2014 [174] and CT14NLO [175] PDF sets.

## 2297 Event Generator

2298 The choice of parton shower (PS) and underlying event (UE) generators can affect  
2299 the analysis outcome. Changing these models modifies several aspects of the event  
2300 generation at the same time, such as the accuracy of matrix element predictions and

2301 different approaches to parton showering. This change tends to lead to the largest  
2302 discrepancy with respect to the nominal samples.

2303 **Resummation and Merging Scales**

2304 Resummation is a technique used in QCD to help cope with calculations involving  
2305 disparate energy scales, and involves the introduction of an associated resummation  
2306 scale, the choice of which introduces some systematic uncertainty into the model.  
2307 Parton showering models are accurate when simulating low- $p_T$  radiation, however  
2308 inaccuracies start to arrive when simulating hard emissions. To combat this, par-  
2309 ton showering models utilise more precise matrix element calculations above some  
2310 momentum threshold. The choice of threshold, or *merging scale* introduces some  
2311 uncertainty into the final result. Resummation (QSF) and merging (CKKW) scale  
2312 variations are available for a subset of the SHERPA samples. The number of available  
2313 events is significantly lower than the number of events in the nominal sample, and no  
2314 statistically significant discrepancy with respect to the nominal samples is observed.  
2315 The corresponding uncertainties and therefore neglected.

2316 **7.2.3 Sources of Experimental Uncertainties**

2317 The main experimental uncertainties in the analysis are due to the following sources:

- 2318 • The small- $R$  jet energy scale and resolution, which are informed by in situ  
2319 calibration studies and the dependence of the jet energy on the level of pile-  
2320 up [68].
- 2321 • The large- $R$  jet energy and mass scales and resolutions. The scales are calibrated  
2322 as described in Ref. [72], and an uncertainty of 2% and 20% is applied for the  
2323 jet energy and mass resolutions, respectively.
- 2324 •  $b$ -tagging uncertainties, which are computed separately for  $b$ -,  $c$ - and light-flavour  
2325 jets as described in the calibration studies in Refs. [168–170]. An additional  
2326 extrapolation uncertainty is added to account for jets with transverse momenta  
2327 above that which is accessible in the calibration analyses.

- 2328 • Uncertainties associated with the lepton energy and momentum scales, and  
2329 reconstruction and identification efficiencies.
  - 2330 • Uncertainty on the pile-up models which are used in the simulated samples,  
2331 described in Ref. [176].
  - 2332 • Uncertainties associated with the reconstruction of the missing transverse energy  
2333  $E_T^{\text{miss}}$ , which have various sources as described in Ref. [78].
- 2334 The impact of these uncertainties on the analysis can be found in Table 7.16.

### 2335 7.2.4 Vector Boson + Jets Modelling

2336 After event selection, the  $V+jets$  background is a dominant background in all three  
2337 analysis channels as described in Section 7.1.5. The  $V+jets$  samples are split into  
2338 categories depending on the truth flavour of the track-jets which are ghost-associated  
2339 to the large- $R$  jet Higgs candidate. The categories are  $V+bb$ ,  $V+bc$ ,  $V+bl$ ,  $V+cc$ ,  
2340  $V+cl$ ,  $V+ll$ , and  $V+hf$  refers collectively to the categories containing at least one  $b$ -  
2341 or  $c$ -jet.  $V+bb$  is dominant generally accounting for 80% of the events, while  $V+hf$   
2342 accounts for around 90% of the events. The full flavour composition breakdown for  
2343 each channel and analaysis region are given in Tables 7.6, 7.8 and 7.9.

2344 In order to access uncertainties associated with the use of MC generators, variations  
2345 of the simulation are produced using alternative generators or variation of nominal  
2346 generator parameters as described in Section 7.2.1. As described in Section 7.1.1,  
2347 the nominal MC event generator used for  $V+jets$  events is SHERPA 2.2.1, while  
2348 MADGRAPH5\_AMC@NLO+PYTHIA8 (which uses a different parton showering  
2349 model) is used as an alternative generator.

2350 Modelling systematics can have several impacts, including affecting the overall  
2351 normalisation for different processes, the relative acceptances between different  
2352 analysis regions (i.e. migrations between HP and LP SRs, between the SR and CR,  
2353 and between  $p_T^V$  bins), and the shapes of the  $m_J$  distributions. Since the fit model  
2354 fits only the large- $R$  jet mass  $m_J$  to data, all shape uncertainties are estimated with  
2355 respect to this observable. Several sources of uncertainty, summarised in Section 7.2.2,  
2356 have been assessed.

Sample	$Mp_T^V$ HP SR	$Hp_T^V$ HP SR	$Mp_T^V$ LP SR	$Hp_T^V$ LP SR	$Mp_T^V$ CR	$Hp_T^V$ CR
<b>Wbb</b>	$79.3\% \pm 4.4\%$	$75.0\% \pm 8.6\%$	$77.4\% \pm 2.5\%$	$71.7\% \pm 4.5\%$	$68.0\% \pm 7.6\%$	$63.5\% \pm 14.0\%$
<b>Wbc</b>	$6.6\% \pm 0.9\%$	$3.4\% \pm 1.7\%$	$6.2\% \pm 0.5\%$	$5.3\% \pm 0.9\%$	$14.5\% \pm 3.2\%$	$3.4\% \pm 3.2\%$
<b>Wbl</b>	$3.9\% \pm 0.9\%$	$11.4\% \pm 3.5\%$	$4.5\% \pm 0.5\%$	$8.7\% \pm 1.4\%$	$9.8\% \pm 2.2\%$	$9.1\% \pm 3.8\%$
<b>Wcc</b>	$5.1\% \pm 1.7\%$	$6.8\% \pm 2.4\%$	$7.1\% \pm 1.0\%$	$6.3\% \pm 1.4\%$	$4.2\% \pm 2.4\%$	$12.3\% \pm 7.0\%$
<b>Wcl</b>	$2.3\% \pm 1.4\%$	$2.4\% \pm 2.1\%$	$3.4\% \pm 0.7\%$	$5.2\% \pm 1.5\%$	$2.6\% \pm 1.5\%$	$3.4\% \pm 2.1\%$
<b>Wl</b>	$2.9\% \pm 1.0\%$	$0.9\% \pm 1.6\%$	$1.3\% \pm 0.7\%$	$2.8\% \pm 0.7\%$	$0.9\% \pm 0.6\%$	$8.4\% \pm 5.1\%$
Events	<b><math>187.5 \pm 7.7</math></b>	<b><math>38.2 \pm 3.1</math></b>	<b><math>429.5 \pm 10.0</math></b>	<b><math>97.8 \pm 4.2</math></b>	<b><math>33.8 \pm 2.5</math></b>	<b><math>8.3 \pm 1.2</math></b>

**Table 7.6:** 0-lepton  $W+jets$  nominal sample flavour composition and total event yield [177].  $Mp_T^V$  refers to the medium  $p_T^V$  region, and  $Hp_T^V$  refers to the high  $p_T^V$  region (see Table 7.1).

Sample	$Mp_T^V$ HP SR	$Hp_T^V$ HP SR	$Mp_T^V$ LP SR	$Hp_T^V$ LP SR	$Mp_T^V$ CR	$Hp_T^V$ CR
<b>Wbb</b>	$77.2\% \pm 2.6\%$	$72.4\% \pm 4.3\%$	$77.8\% \pm 1.8\%$	$69.3\% \pm 2.5\%$	$64.6\% \pm 4.9\%$	$53.5\% \pm 6.3\%$
<b>Wbc</b>	$7.4\% \pm 0.7\%$	$7.3\% \pm 1.1\%$	$6.6\% \pm 0.4\%$	$6.3\% \pm 0.6\%$	$13.7\% \pm 1.9\%$	$16.4\% \pm 3.7\%$
<b>Wbl</b>	$4.0\% \pm 0.5\%$	$6.7\% \pm 1.1\%$	$5.1\% \pm 0.3\%$	$8.7\% \pm 0.8\%$	$10.3\% \pm 1.7\%$	$14.6\% \pm 3.0\%$
<b>Wcc</b>	$6.2\% \pm 1.1\%$	$5.5\% \pm 1.7\%$	$6.6\% \pm 0.6\%$	$6.4\% \pm 0.7\%$	$4.5\% \pm 1.7\%$	$9.5\% \pm 3.0\%$
<b>Wcl</b>	$3.6\% \pm 0.8\%$	$4.2\% \pm 1.8\%$	$2.8\% \pm 0.5\%$	$6.2\% \pm 0.8\%$	$4.6\% \pm 1.2\%$	$4.4\% \pm 1.5\%$
<b>Wl</b>	$1.5\% \pm 0.5\%$	$3.9\% \pm 1.3\%$	$1.1\% \pm 0.2\%$	$3.1\% \pm 0.5\%$	$2.3\% \pm 1.2\%$	$1.6\% \pm 0.6\%$
Events	<b><math>477.1 \pm 11.7</math></b>	<b><math>147.5 \pm 6.4</math></b>	<b><math>784.7 \pm 12.3</math></b>	<b><math>301.8 \pm 7.2</math></b>	<b><math>68.7 \pm 3.5</math></b>	<b><math>26.9 \pm 2.0</math></b>

**Table 7.7:** 1-lepton  $W+jets$  nominal sample flavour composition and total event yield [177].  $Mp_T^V$  refers to the medium  $p_T^V$  region, and  $Hp_T^V$  refers to the high  $p_T^V$  region (see Table 7.1).

Channel	$Mp_T^V$ HP SR	$Hp_T^V$ HP SR	$Mp_T^V$ LP SR	$Hp_T^V$ LP SR	$Mp_T^V$ CR	$Hp_T^V$ CR
<b>Zbb</b>	84.56%	81.84%	82.37%	76.06%	66.12%	63.18%
<b>Zbc</b>	6.03%	6.98%	5.80%	7.46%	15.04%	14.30%
<b>Zbl</b>	4.06%	6.55%	3.83%	6.59%	12.66%	12.81%
<b>Zcc</b>	3.68%	3.40%	5.82%	3.75%	3.36%	3.38%
<b>Zcl</b>	1.23%	0.44%	1.47%	3.97%	1.82%	4.95%
<b>Zl</b>	0.44%	0.78%	0.70%	2.16%	1.00%	1.38%
Events	$259.91 \pm 4.86$	$66.12 \pm 2.04$	$420.45 \pm 5.73$	$141.97 \pm 2.50$	$43.49 \pm 1.73$	$16.07 \pm 0.83$

**Table 7.8:** 0-lepton  $Z+jets$  nominal sample flavour composition and total event yield [177].  $Mp_T^V$  refers to the medium  $p_T^V$  region, and  $Hp_T^V$  refers to the high  $p_T^V$  region (see Table 7.1).

Channel	$Mp_T^V$	$Hp_T^V$	$p_T^V$ inclusive
<b>Zbb</b>	80.80%	76.95%	79.76%
<b>Zbc</b>	8.10%	6.26%	7.60%
<b>Zbl</b>	4.95%	7.06%	5.52%
<b>Zcc</b>	3.97%	4.46%	4.10%
<b>Zcl</b>	1.61%	3.60%	2.14%
<b>Zll</b>	0.57%	1.68%	0.87%
Events	$115.49 \pm 2.42$	$42.42 \pm 1.27$	$157.92 \pm 2.73$

**Table 7.9:** 2-lepton  $Z+jets$  nominal sample flavour composition and total event yield [177].  $Mp_T^V$  refers to the medium  $p_T^V$  region, and  $Hp_T^V$  refers to the high  $p_T^V$  region (see Table 7.1).

## 2357 Acceptance Uncertainties

2358 Several different types of acceptance uncertainties have been calculated and im-  
 2359 plemented as nuisance parameters in the fit. These account for the uncertainty  
 2360 in the overall number of events in each channel, and for the migration of events  
 2361 between different analysis regions. The acceptance uncertainties relevant to the  
 2362  $V+jets$  processes are summarised below.

- 2363 • **Overall normalisation:** only relevant where normalisation cannot be left  
 2364 unconstrained (or “floating”, i.e. determined as part of the fit). The  $V+hf$   
 2365 component is left floating in the fit, with independent normalisations used for  
 2366  $W+hf$  and  $Z+hf$ . The normalisations are mainly determined by the 1-lepton  
 2367 (for  $W+hf$ ) and 2-lepton (for  $Z+hf$ ) regions respectively and then extrapolated  
 2368 to the 0-lepton channel. The negligible  $V+jets$  backgrounds were constrained to  
 2369 their cross-sections in the fit. were constrained to their cross-sections

- **SR-to-CR relative acceptance:** the uncertainty on the relative number of  $V+jets$  events in the signal and control regions.
- **HP-to-LP relative acceptance:** the uncertainty on the relative number of  $V+jets$  events in the HP and LP SRs.
- **Medium-to-high  $p_T^V$  relative acceptance:** the uncertainty on the relative number of  $V+jets$  events in the medium and high  $p_T^V$  bins.
- **Flavour relative acceptance:** for each flavour  $V+xx$ , where  $xx \in \{bc, bl, cc\}$  the ratio of  $V+xx/V+bb$  events is calculated. This corresponds to the uncertainty on the heavy flavour composition of the  $V+hf$  background.
- **Channel relative acceptance:** the uncertainty on the relative number of  $V+jets$  events between the channels.

The uncertainties arising from the different sources described in Section 7.2.2 are summed in quadrature to give a total uncertainty on each region. A summary of the different acceptance uncertainties that were derived and subsequently applied in the fit are given in Table 7.10. An effort has been made, wherever possible, to harmonise similar uncertainties across different analysis regions and channels.

V+jets Acceptance Uncertainties				
Boson	W		Z	
Channel	0L	1L	0L	2L
Vbb Norm.	30%	-	-	-
SR-to-CR	90% <sup>†</sup>	40% <sup>†</sup>	40%	-
HP-to-LP	18%		18%	-
Medium-to-high $p_T^V$	30%	10%*	10%	
Channel relative acceptance.	20%	-	16%	-
Vbc/Vbb	30%			
Vbl/Vbb	30%			
Vcc/Vbb	20%			
Vcl Norm.	30%			
VI Norm.	30%			

**Table 7.10:**  $V+jets$  acceptance uncertainties [177].  $W+jets$  SR and CR uncertainties marked with a superscript  $\dagger$  are correlated. The 1L  $W+jets$  H/M uncertainty marked by \* is applied as independent and uncorrelated NPs in both HP and LP signal regions.

2386 **Shape Uncertainties**

2387 In order to derive shape uncertainties for a given background or signal process,  
2388 normalised distributions of the reconstructed large- $R$  Higgs candidate jet mass  $m_J$   
2389 are compared for the nominal sample and variations. For each variation, the ratio of  
2390 the variation to nominal is calculated, the up and down variations are symmetrised,  
2391 and an analytic function is used to parameterise the ratio. If different analysis regions  
2392 or channels show the same pattern of variation, a common uncertainty is assigned.

2393 An example of a significant source of uncertainty, arising from choice of factorisation  
2394 scale  $\mu_R$  is shown in Fig. 7.2. The HP SRs in the medium and high  $p_T^V$  bins are  
2395 shown for the 0-lepton channel for the  $W+hf$  and  $Z+hf$  jets. The 0- and 1-lepton  
2396 channels for the  $W+hf$  contribution and the 0- and 2-lepton channels for the  $Z+jets$   
2397 contribution were found to have compatible shapes in  $m_J$  across channels, and so  
2398 were jointly measured. An exponential function  $e^{p_0+p_1x} + p_2$  has been fitted to the  
2399 ratio of the normalised distributions. The magnitude of the variation is  $p_T^V$  dependent,  
2400 and so separate uncertainties are implemented in the fit for each  $p_T^V$  region.

2401 The shape uncertainties for  $\mu_R$  were derived on the SRs but are also applied to the  
2402 CRs, as the low statistics in the CRs make it difficult to derive dedicated shape  
2403 uncertainties. All the shape uncertainties are fully correlated across regions.

2404 A comparison of the  $m_J$  shapes between SHERPA and MADGRAPH is shown in  
2405 Fig. 7.3. The plots are split by process and channel, but merged in SR purity and  $p_T^V$   
2406 bins reflecting similarities between the  $m_J$  shapes and variations across these regions.  
2407 Due to the low statistics available for the alternate MADGRAPH sample, and the  
2408 lack of statistically significant variation between the samples, no additional shape  
2409 uncertainty was added to the fit in this case.

2410 The impacts of variations in the factorisation scale  $\mu_F$  and the choice of PDF set on  
2411  $m_J$  shape were also found to be negligible in comparison with  $\mu_R$  and are hence no  
2412 additional uncertainty was added to the fit.

2413 **7.2.5 Diboson Modelling**

2414 The procedure to derive the uncertainties for the diboson background generally  
2415 follows that of  $V+jets$ .

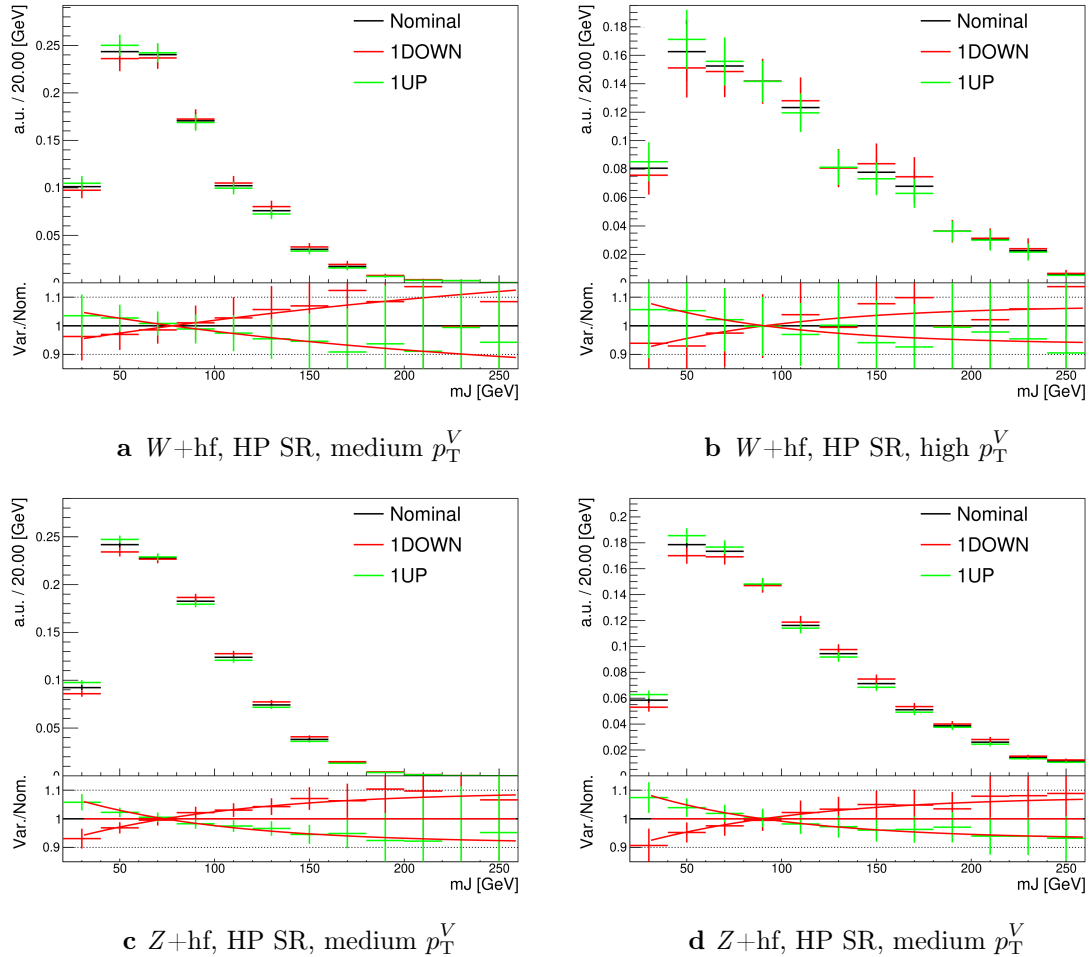


**Figure 7.2:** Leading large- $R$  jet mass for the  $Z$  and  $W+\text{hf}$  processes in the HP SR of the 0-lepton channel [177]. The renormalisation scale  $\mu_r$  has been varied by a factor of 0.5 (1DOWN) and 2 (1UP). An exponential function is fitted to the ratio between the nominal and alternate samples.

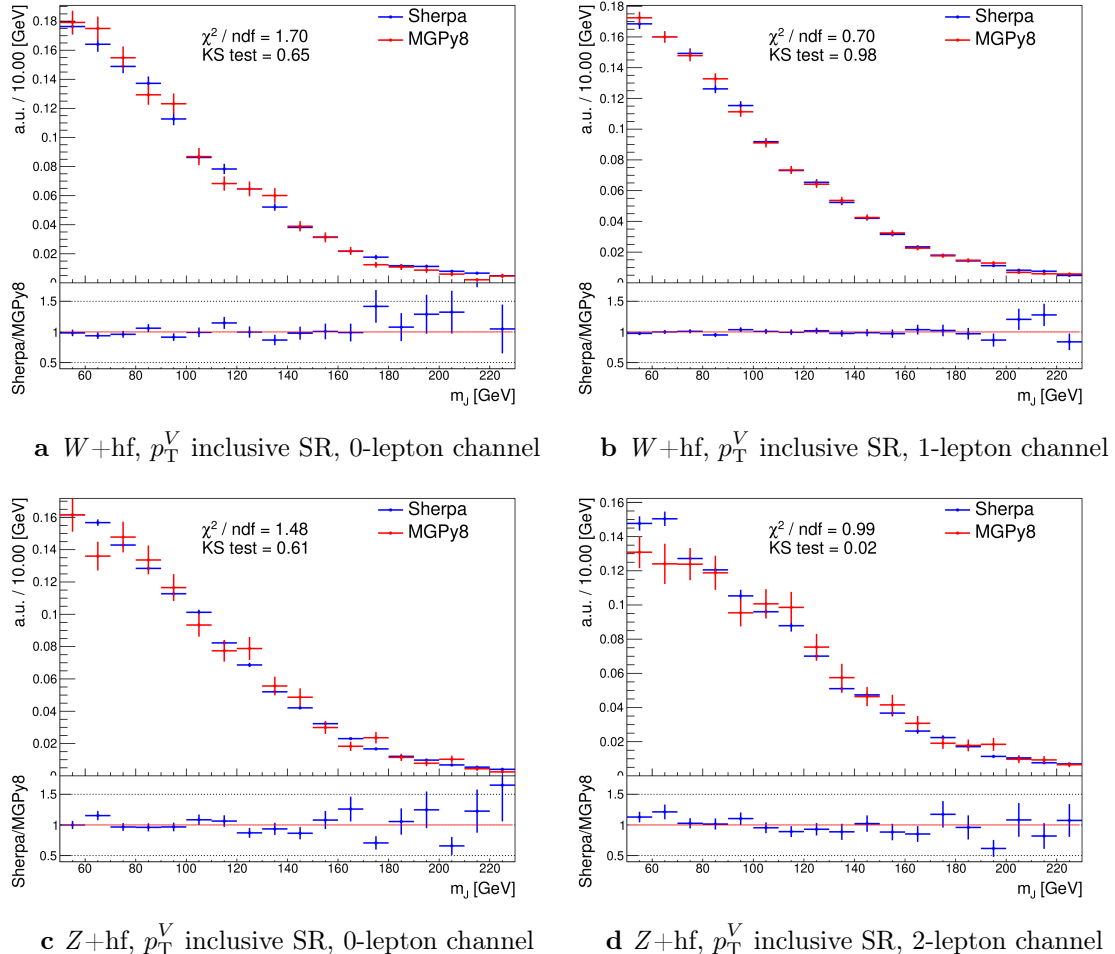


**Figure 7.3:** Leading large- $R$  jet  $m_J$  inclusive in  $p_T^V$  for the  $V + \text{hf}$  process modelled using both the SHERPA (blue) and MADGRAPH (red) samples [177]. The Kolmogorov-Smirnov test and  $\chi^2/ndf$  are shown on the plots.

2416 The nominal diboson samples are generated using SHERPA 2.2.1 (except for  $gg \rightarrow VV$   
2417 which uses SHERPA 2.2.2) with the NNPDF3.0NNLO tune. Alternative samples were  
2418 generated using POWHEG interfaced with PYTHIA8, using the AZNLO shower tune  
2419 with the CTEQ6L1 PDFs [178]. Unlike SHERPA, POWHEG models the off-shell  $Z$   
2420 contribution at NLO.

2421 Acceptance and shape uncertainties are derived in an analogous fashion to  $V+jets$   
2422 as described below.

### 2423 Acceptance Uncertainties

2424 Diboson acceptance uncertainties are summarised in Table 7.11. Variations from  $\mu_R$ ,  
2425  $\mu_F$ , PDF choice and an alternative generator are considered and are combined via  
2426 a sum in quadrature as described in Section 7.2.4. The largest modification to the  
2427 nominal acceptance results from the POWHEG+PYTHIA8 alternate sample. Since  
2428 the diboson contribution to the  $t\bar{t}$  control region is negligible, no SR-to-CR relative  
2429 acceptance uncertainty is necessary.

2430 For the  $WZ$  contribution, uncertainties are derived using the 1-lepton channel  
2431 and applied to all three channels. The 1-lepton channel was used as it has the  
2432 largest amount of available statistics. As far as was possible given the limited  
2433 statistics available in the other channels, compatibility was checked between the  
2434 derived uncertainties and the other channels. An additional 8% channel migration  
2435 uncertainty is applied on the  $WZ$  0-lepton channel. For the  $ZZ$  contribution, the  
2436 normalisation uncertainty is calculated using the 2-lepton channel and applied to all  
2437 three channels. The 0- and 1-lepton channels were found to have a similar HP-to-LP  
2438 relative acceptance uncertainty of 18%. The 1-lepton medium-to-high  $p_T^V$  relative  
2439 acceptance is based off the value obtained from the 2-lepton channel, since the  
2440 1-lepton channel had an insufficient number of events to estimate the uncertainty  
2441 directly. 30% and 18% channel migration uncertainties are applied in the 0- and  
2442 1-lepton channels respectively.

2443 Since the contribution from  $WW$  is negligible, dedicated studies are not performed,  
2444 but a 25% normalisation uncertainty is applied in all the three channels which is  
2445 based on the modelling studies performed for the previous analysis [79].

Diboson Acceptance Uncertainties						
Bosons	WZ			ZZ		
Channel	0L	1L	2L	0L	1L	2L
Normalisation	16%			10%		
HP/LP	18%			18%		
High/Medium	10%			6%	18%	
Channel Extrap.	8%	-	-	30%	18%	-

**Table 7.11:** Diboson acceptance uncertainties [177]. All uncertainties except channel extrapolation uncertainties are fully correlated between  $ZZ$  and  $WZ$  processes and channels.

## 2446 Shape Uncertainties

2447 Diboson shape uncertainties are derived in a similar fashion to  $V+jets$ . Only the  
 2448 uncertainties associated with systematic variation of  $\mu_R$  and the alternate event  
 2449 generator have a non-negligible impact on the  $m_J$  shape. Variation of  $\mu_R$  produces  
 2450 consistent  $m_J$  shape changes across all regions and channels, and hence only a single  
 2451 associated uncertainty is derived, shown in Fig. 7.4. A hyperbolic tangent is fitted  
 2452 to the symmetrised ratio.

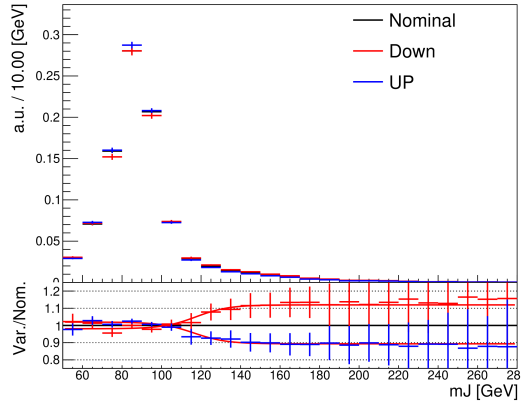


**Figure 7.4:** Leading large- $R$  jet mass distribution for the  $WZ$  and  $ZZ$  processes, inclusive across all signal regions and lepton channels [177]. The renormalisation scale  $\mu_R$  has been varied by a factor of 2 (1up) and 0.5 (1down). The red line shape shows the fitting results of the hyperbolic tangent function.

2453 The comparison between the nominal SHERPA and alternative POWHEG+PYTHIA8  
 2454 samples is shown in Fig. 7.5 for the 0- and 1-lepton channels for both the  $WZ$  and

2455  $ZZ$  processes. For these channels, the shape of  $m_J$  varies in opposite directions  
2456 in the LP and HP signal regions. Shapes are similar between  $p_T^V$  bins, the 0- and  
2457 1-lepton channels and for  $WZ$  and  $ZZ$ . In order to reduce the effects of statistical  
2458 fluctuations on the fit, these regions are merged before deriving the shape uncertainty.  
2459 A third order polynomial is fitted to the ratio, and this function transitions to a  
2460 constant piecewise function in the high mass region to accurately represent the shape.  
2461 Dependence on the event generator was found to be negligible within statistical  
2462 uncertainty in the 2-lepton channel, and so no uncertainty was applied. All diboson  
2463 shape uncertainties are fully correlated in the fit.

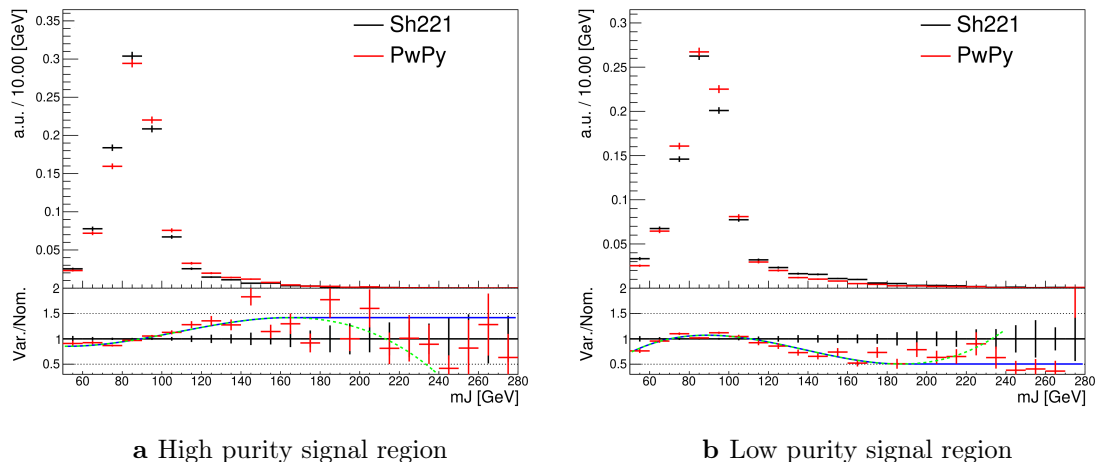


**Figure 7.5:** The comparison of the shapes of the large- $R$  jet mass  $m_J$  between SHERPA (black) and POWHEG+PYTHIA8 (red) samples from  $WZ$  and  $ZZ$  process in high and low purity signal regions, integrated over  $p_T^V$  regions and the 0- and 1-lepton channels [177]. The dashed green line shows the fitted third order polynomial function and the blue lines show the function after a protection is added in the high mass region.

## 2464 7.2.6 $t\bar{t}$ and single-top Modelling

2465 The main features of the systematic uncertainties on the remaining two modelled  
2466 backgrounds,  $t\bar{t}$  and single-top, are described below.

2467 The modelling of the  $t\bar{t}$  background uses a POWHEG+PYTHIA8 nominal sample.  
2468 Two alternate samples were considered: POWHEG+HERWIG7 (providing an alternate  
2469 parton shower model) and MADGRAPH5+PYTHIA8.2 (providing an alternate hard  
2470 scatter model). Effects of initial and final state radiation (ISR and FSR, respectively)

were assessed using internal weight variations in the nominal sample. Acceptance and shape uncertainties were derived for each of the variations. Of the acceptance uncertainties, the largest contribution is due to the matrix element calculation, with the parton showering model being second. The ISR and FSR acceptance uncertainties were found to be subdominant. For the shape uncertainties, only the ISR and parton showering variations have non-negligible impacts on the  $m_J$  shape.

The dominant process contributing to the single-top background is  $Wt$  production, relevant for the 0- and 1-lepton channels. The same nominal and alternative samples are used as for the  $t\bar{t}$  background. Again, ISR and FSR variations are obtained from internal weight variations in the nominal sample. At higher orders in QCD, diagrams contributing to the  $Wt$  production process can also be found in leading-order  $t\bar{t}$  production processes. To account for the arising interference effects, the diagram removal (DR) scheme in Ref. [179] was employed for the nominal sample. The uncertainty on the DR scheme was assessed using an alternate sample using a diagram subtraction (DS) method which removes interference at the generator level. The largest sources of acceptance and shape uncertainties were due to this DS-DR variation.

### 7.2.7 Signal Modelling

The modelling of the systematic uncertainties affecting the signal processes follows the procedure described in Refs. [26, 180, 181]. The  $qq \rightarrow VH$  signal samples are generated with POWHEG BOX v2 + GoSAM at next-to-leading order (NLO) accuracy in QCD. An additional  $gg \rightarrow ZH$  sample is generated using POWHEG Box v2 at leading order (LO) in QCD. In both cases, the generated events are interfaced with PYTHIA 8 for the parton showering modelling. An alternate HERWIG7 sample is used to assess the uncertainty on the parton showering model. Recommended systematic uncertainties on the signal production cross-sections and  $H \rightarrow b\bar{b}$  branching ratio from the LHC Higgs Cross Section Working Group are applied [182, 183]. Acceptance and shape uncertainties arising from missing higher-order QCD and electroweak corrections, PDF uncertainties, renormalisation and factorisation scales, and alternate parton showering model are applied.

## 2501 7.3 Statistical Treatment

2502 A binned global maximum-profile-likelihood fit of the  $m_J$  distribution is performed  
 2503 to extract information on the signal, combining all the analysis regions defined  
 2504 in Table 7.1. The signal strength  $\mu = \sigma/\sigma_{\text{SM}}$  is defined as the ratio between the  
 2505 observed and predicted cross-sections, where  $\mu = 0$  corresponds to the background-  
 2506 only hypothesis and  $\mu = 1$  corresponds to the SM prediction. This is a parameter of  
 2507 interest (POI) which acts to scale the total number of signal events, and is determined  
 2508 during the fit procedure.

2509 The present analysis makes use of two POIs. The first,  $\mu_{VH}^{bb}$ , is the signal strength  
 2510 for the  $VH$ ,  $H \rightarrow b\bar{b}$  process, the primary process under investigation. The diboson  
 2511 production strength  $\mu_{VZ}^{bb}$  for the  $VZ$ ,  $Z \rightarrow b\bar{b}$  process is measured simultaneously and  
 2512 provides a validation of the analysis apparatus used for the primary  $H \rightarrow b\bar{b}$  measure-  
 2513 ment. Alongside the two POIs, the predictive model depends on several parameters  
 2514 which are not the primary target of measurement, and represent the systematic  
 2515 uncertainties discussed previously. These parameters are called nuisance parameters  
 2516 (NPs), collectively referred to as  $\theta$ . Freely floating background normalisations are  
 2517 implemented as NPs and are also extracted during the fitting processes.

### 2518 7.3.1 Likelihood Function

2519 The statistical setup treats each bin as a Poisson counting experiment and is based on  
 2520 the ROOSTATS framework [184]. The combined likelihood over  $N$  bins is constructed  
 2521 as the product of Poisson probabilities in each bin. Considering the simplified case  
 2522 of a single signal strength parameter  $\mu$ , and neglecting sources of systematic or  
 2523 statistical uncertainty, this is given by

$$\mathcal{L}(\mu) = \prod_{i=1}^N \frac{(\mu s_i + b_i)^{n_i}}{n_i!} \exp [-(\mu s_i + b_i)], \quad (7.1)$$

2524 where  $s_i$  ( $b_i$ ) is the expected number of signal (background) events in bin  $i$ , and  $n_i$  is  
 2525 the number of observed data events in bin  $i$ .

2526 **Treatment of Uncertainties**

2527 Systematic uncertainties can modify the predicted signal and background yields  $s_i$   
2528 and  $b_i$ . Each source of systematic uncertainty is taken into account by adding an  
2529 additional NP  $\theta_j$  to the likelihood in the form of a Gaussian cost function. The  
2530 combined effect of the NPs is then

$$\mathcal{L}(\theta) = \prod_{j=1}^{N_\theta} \frac{1}{\sqrt{2\pi}\sigma_j} \exp \left[ \frac{-(\theta_j - \hat{\theta}_j)^2}{2\sigma_j^2} \right], \quad (7.2)$$

2531 where  $N_\theta$  is the number of NPs,  $\theta_j$  is the nominal value of the  $j$ th NP,  $\hat{\theta}_j$  is the fitted  
2532 value, and  $\sigma_j$  is the corresponding associated prior uncertainty on the NP. As the  
2533 fitted value  $\hat{\theta}_j$  deviates from its nominal value, a cost is introduced. The presence of  
2534 NPs modifies the likelihood as

$$\mathcal{L}(\mu) \rightarrow \mathcal{L}(\mu, \theta) = \mathcal{L}(\mu)\mathcal{L}(\theta). \quad (7.3)$$

2535 The predicted signal and background yields are also modified by the presence of the  
2536 NPs with

$$s_i \rightarrow s_i(\theta), \quad b_i \rightarrow b_i(\theta). \quad (7.4)$$

2537 For NPs which are left freely floating in the fit, no corresponding Gaussian constraints  
2538 are added to the likelihood.

2539 The pull of a NP is defined as the difference between the fitted value  $\hat{\theta}_j$  and the  
2540 nominal value  $\theta_j$ , divided by the uncertainty on the NP  $\sigma_j$ . To obtain the uncertainty  
2541 on the pull of a NP, the following procedure is used. The Hessian matrix  $\mathbf{H}$  is  
2542 calculated as

$$\mathbf{H} = \begin{bmatrix} \frac{\partial^2 \mathcal{L}}{\partial \theta_1^2} & \frac{\partial^2 \mathcal{L}}{\partial \theta_1 \partial \theta_2} & \dots & \frac{\partial^2 \mathcal{L}}{\partial \theta_1 \partial \theta_n} \\ \frac{\partial^2 \mathcal{L}}{\partial \theta_2 \partial \theta_1} & \frac{\partial^2 \mathcal{L}}{\partial \theta_2^2} & \dots & \frac{\partial^2 \mathcal{L}}{\partial \theta_2 \partial \theta_n} \\ \vdots & \vdots & \ddots & \vdots \\ \frac{\partial^2 \mathcal{L}}{\partial \theta_n \partial \theta_1} & \frac{\partial^2 \mathcal{L}}{\partial \theta_n \partial \theta_2} & \dots & \frac{\partial^2 \mathcal{L}}{\partial \theta_n^2} \end{bmatrix}. \quad (7.5)$$

2543 Taking the inverse of the Hessian matrix  $\mathbf{H}^{-1}$  yields the covariance matrix, from  
 2544 which the post-fit uncertainties on the different NPs can be extracted. If the post-fit  
 2545 uncertainty is smaller than the nominal uncertainty, additional information about  
 2546 the NP has been extracted by the fit, and NP is said to be *constrained*.

2547 The statistical uncertainty on the simulated events is implemented using a dedicated  
 2548 NP for each bin which can scale the background yield in that bin. Statistical NPs  
 2549 are also implemented using a Gaussian constraint.

## 2550 Smoothing and Pruning

2551 To simplify the fit to reduce and improve its robustness, systematic uncertainties  
 2552 are smoothed and pruned. Smoothing accounts for the large statistical uncertainty  
 2553 present in some samples that can lead to unphysical fluctuations in the shape  
 2554 systematics. The smoothing procedure relies on the assumption that the impact of  
 2555 systematics should be approximately monotonic and correlated between neighbouring  
 2556 bins.

2557 In addition to smoothing, pruning is the process of removing from the fit those  
 2558 systematics which only have a very small effect. This improves the stability of the  
 2559 fit by reducing the number of degrees of freedom. Acceptance uncertainties are  
 2560 pruned in a given region if they have a variation of less than 0.5%, or if the up and  
 2561 down variations have the same sign in that region. Shape uncertainties are pruned  
 2562 in a given region if the deviation in each bin is less than 0.5% in that region. In  
 2563 addition, acceptance and shape uncertainties are neglected in a given region for any  
 2564 background which makes up less than 2% of the total background in a given region.

---

## 2565 Fit Procedure and Statistical Tests

2566 The best-fit value of  $\mu$ , denoted  $\hat{\mu}$ , is obtained via an unconditional maximisation of  
 2567 the likelihood. The likelihood is also used to construct a statistical test which can  
 2568 confirm or reject the background-only hypothesis. The test statistic  $q_\mu$  is constructed  
 2569 from the profile likelihood ratio,

$$q_\mu = -2 \ln \frac{\mathcal{L}(\mu, \hat{\theta}_\mu)}{\mathcal{L}(\hat{\mu}, \hat{\theta})} \quad (7.6)$$

2570 where  $\hat{\mu}$  and  $\hat{\theta}$  are chosen to maximise the likelihood  $\mathcal{L}$ , and the profile value  $\hat{\theta}_\mu$  is  
 2571 obtained from a conditional maximisation of the likelihood for a specific choice of  
 2572  $\mu = 0$  corresponding to the background-only hypothesis.

2573 The test statistic is used to construct a  $p$ -value which is used to probe the background-  
 2574 only hypothesis. The  $p$ -value is typically reported in terms of the significance  $Z$ ,  
 2575 defined as the number of standard deviations for a Gaussian Normal distribution  
 2576 which will produce a one-sided tail integral equal to the  $p$ -value, as in

$$p = \int_Z^\infty \frac{1}{\sqrt{2\pi}} e^{-x^2/2} dx = 1 - \Phi(Z). \quad (7.7)$$

2577 Typically a value of  $Z = 3$  constitutes *evidence* of a processes, while  $Z = 5$  is required  
 2578 for a *discovery*, or observation. Alongside the  $p$ -value, the best-fit value of the signal  
 2579 strength  $\hat{\mu}$  and its corresponding uncertainty are quoted, and compared to their  
 2580 expected values.

### 2581 7.3.2 Background Normalisations

2582 The backgrounds which can be constrained by the fit are left freely floating and  
 2583 the corresponding normalisation factors are extracted. Normalisation factors (NF),  
 2584 represent the value by which the predicted normalisations are scaled, and are im-  
 2585 plemented for the dominant backgrounds ( $t\bar{t}$ ,  $Z+hf$ ,  $W+hf$ ). The NFs are also  
 2586 subdivided into different regions of phase-space for  $t\bar{t}$ , given it is possible to obtain  
 2587 a strong constraint in the individual channels. This also removes the need for an  
 2588 extrapolation uncertainty.

2589 The normalisations and shapes of all other backgrounds, with the exception of the  
2590 multijet background which is estimated using a data driven technique, are initialised  
2591 using the nominal samples and the state-of-the art process normalisations, as outlined  
2592 in Table 7.2.

2593 **7.3.3 Asimov Dataset & Expected Results**

2594 The Asimov dataset is constructed by replacing the data with the sum of the signal  
2595 and background predictions  $n_i = s_i + b_i$ . A fit to this dataset using the nominal  
2596 values of the NPs from the simulation will recover the input values and is useful for  
2597 studying the expected result, in addition to constraints on and correlations between  
2598 the NPs.

2599 Alternatively, a conditional fit to the Asimov dataset can be performed using values  
2600 of the background NPs which are determined from an unconditional fit to data. The  
2601 signal NPs and POIs are fixed at their nominal values from the SM simulation. The  
2602 result of this fit can be used to calculate expected (median) significances given a  
2603 more realistic background model, which can be compared to their observed values,  
2604 as is done in Section 7.4.3.

2605 **7.4 Results**

2606 In the present analysis, the two signal strength parameters  $\mu_{VH}^{bb}$  and  $\mu_{VZ}^{bb}$  are extracted  
2607 from a simultaneous maximisation of the likelihood described in Section 7.3. The  
2608 results of the analysis are summarised in this section. The corresponding post-fit  
2609 background normalisations are listed in Table 7.12. Post-fit  $m_J$  distributions are  
2610 shown in Section 7.4.1. The observed signal strengths are given in Section 7.4.3,  
2611 along with observed and expected significances. Finally in Section 7.4.4 the impact  
2612 of systematic uncertainties on the results is examined.

Process	Normalisation factor
$t\bar{t}$ 0-lepton	$0.88 \pm 0.10$
$t\bar{t}$ 1-lepton	$0.83 \pm 0.09$
$W+\text{hf}$	$1.12 \pm 0.14$
$Z+\text{hf}$	$1.32 \pm 0.16$

**Table 7.12:** Factors applied to the nominal normalisations of the  $t\bar{t}$ ,  $W+\text{hf}$ , and  $Z+\text{hf}$  backgrounds, as obtained from the likelihood fit [131]. The errors represent the combined statistical and systematic uncertainties.

#### 2613 7.4.1 Post-fit Distributions

2614 In addition to the observed significance and signal strength, it is also necessary to  
 2615 study the post-fit  $m_J$  distributions to compare level of the agreement between the  
 2616 simulation (using the best-fit values of the signal strength  $\hat{\mu}$  and the NP  $\hat{\theta}$ ) and the  
 2617 data. The best-fit values  $\hat{\mu}$  and  $\hat{\theta}$  are obtained from an unconditional fit to data over  
 2618 all analysis regions. Post-fit  $m_J$  distributions are given for the signal regions in the  
 2619 0-, 1- and 2-lepton channels in Fig. 7.6. The LP and HP regions are merged for the  
 2620 0- and 1-lepton channels for the sake of simplicity. In general there is a good level of  
 2621 agreement between the simulation and data, indicating the fit model is performing as  
 2622 expected. Fig. 7.7 shows the post-fit plots for the  $t\bar{t}$  control regions. Again, a good  
 2623 level of agreement is observed given the statistical uncertainties on the distributions.

#### 2624 7.4.2 Post-fit Yields

2625 The post-fit yields resulting from the unconditional fit to data are shown in Table 7.13,  
 2626 Table 7.14, and Table 7.15 for the 0-, 1- and 2-lepton channels, respectively.

#### 2627 7.4.3 Observed Signal Strength & Significance

2628 The measured signal strength is computed as the ratio between the measured signal  
 2629 yield to the prediction from the SM. The combined result for all three lepton channels  
 2630 and all analysis regions is given for  $\mu_{VH}^{bb}$  in Eq. (7.8), and for  $\mu_{VZ}^{bb}$  in Eq. (7.9). Both

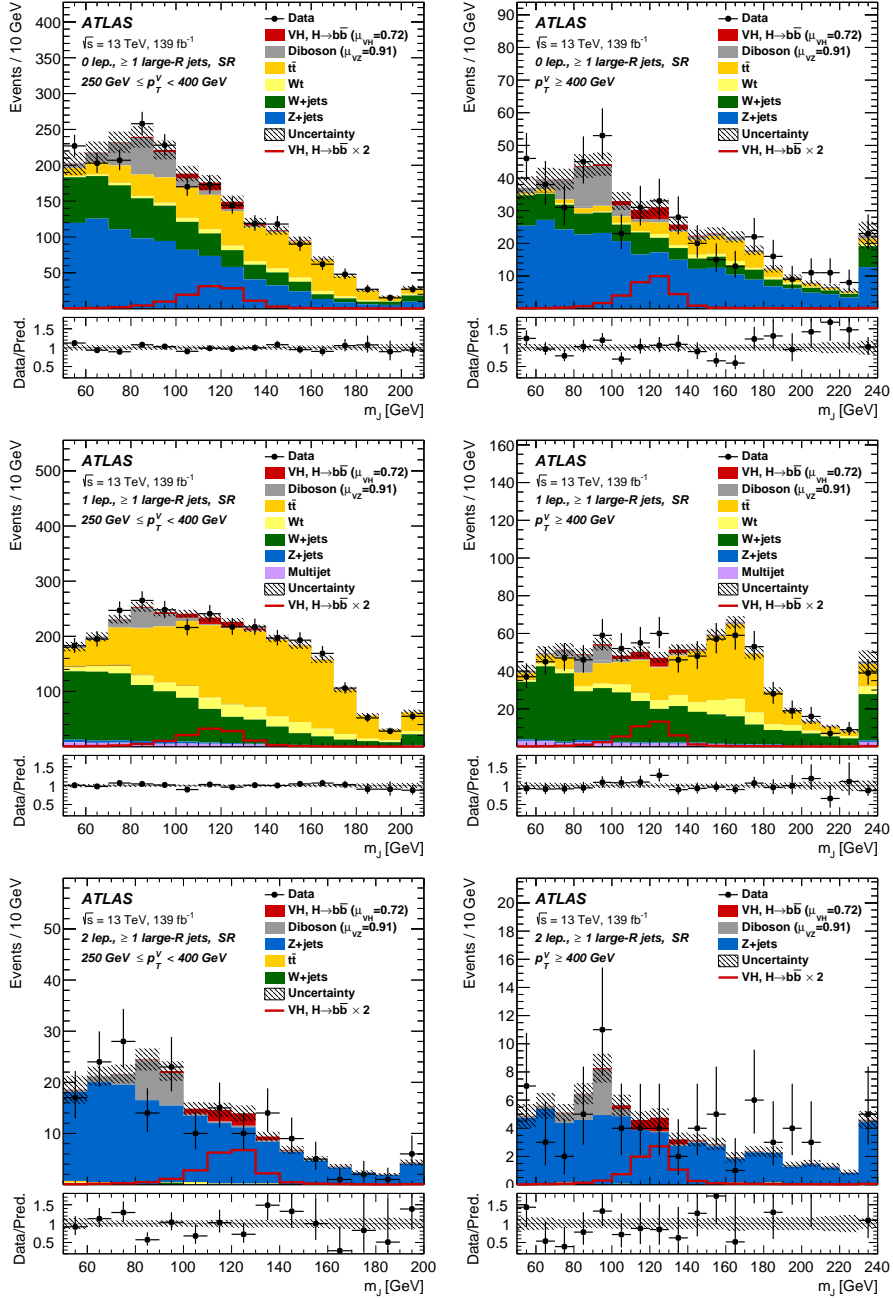


**Figure 7.6:** The  $m_J$  post-fit distributions in (top) the 0-, (middle) 1- and (bottom) 2-lepton SRs for (left)  $250 \text{ GeV} < p_T^V < 400 \text{ GeV}$  and (right)  $p_T^V \geq 400 \text{ GeV}$ . The LP and HP regions are merged for the 0-lepton and 1-lepton channels. The fitted background contributions are shown as filled histograms. The Higgs boson signal ( $m_H = 125 \text{ GeV}$ ) is shown as a filled histogram and is normalised to the signal yield extracted from data ( $\mu_{VH}^{bb} = 0.72$ ), and as an unstacked unfilled histogram, scaled by the SM prediction times a factor of two. The size of the combined on the sum of the fitted signal and background is shown in the hatched band. The highest bin contains the overflow [131].

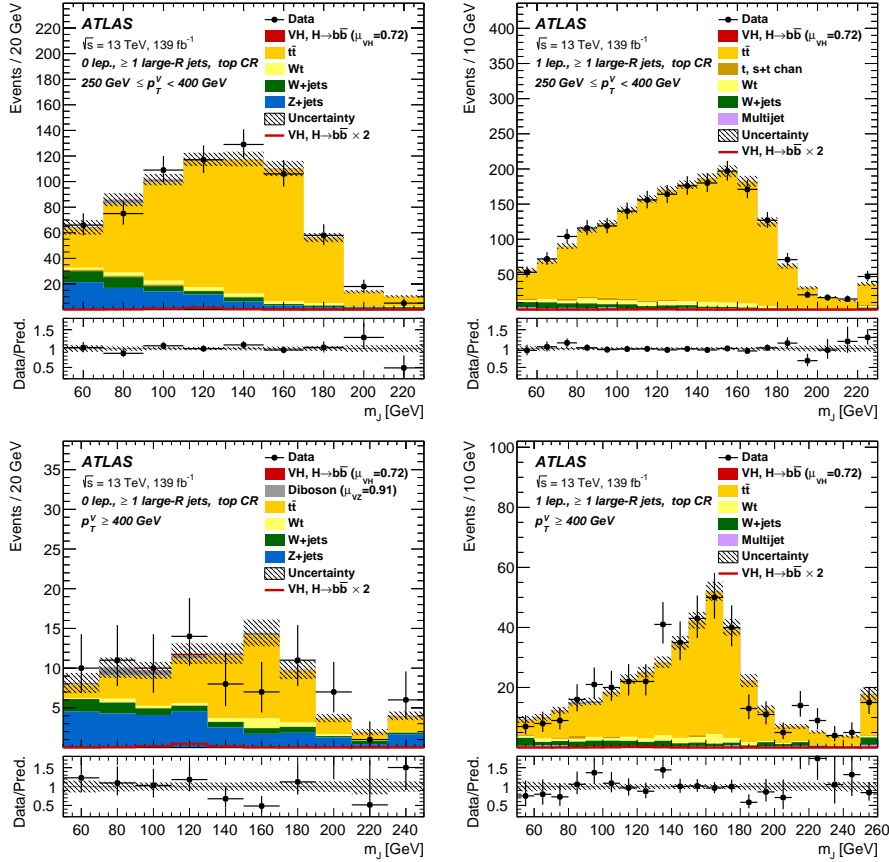


**Figure 7.7:** The  $m_J$  post-fit distributions in the  $t\bar{t}$  control region for (top) the 0-lepton channel and the 1-lepton channel for  $250 \text{ GeV} < p_T^V < 400 \text{ GeV}$  and (bottom) the 0-lepton channel and the 1-lepton channel for  $p_T^V > 400 \text{ GeV}$ . The background contributions after the likelihood fit are shown as filled histograms. The Higgs boson signal ( $m_h = 125 \text{ GeV}$ ) is shown as a filled histogram on top of the fitted backgrounds normalised to the signal yield extracted from data ( $\mu_{VH}^{bb} = 0.72$ ), and unstacked as an unfilled histogram, scaled by the SM prediction times a factor of 2. The size of the combined statistical and systematic uncertainty for the sum of the fitted signal and background is indicated by the hatched band. The highest bin in the distributions contains the overflow [131].

Processes	$250 \text{ GeV} < p_T^V \leq 400 \text{ GeV}$			$p_T^V > 400 \text{ GeV}$		
	HP	LP	CR	HP	LP	CR
Signal	21.93±11.17	18.99±9.76	1.05±0.54	5.69±2.88	5.85±3.01	0.33±0.17
W+t	14.70±5.37	45.55±19.44	17.18±8.09	2.03±0.98	8.93±6.33	3.76±2.49
other t+X	0.79±0.03	3.18±0.66	4.51±1.28	-	0.66±0.03	0.11±0.00
$t\bar{t}$	75.19±13.60	423.85±36.12	539.21±31.39	7.54±1.77	38.20±6.75	44.07±7.43
VZ	77.01±17.09	87.70±19.36	6.16±1.56	17.30±4.10	28.77±6.55	2.79±0.72
WW	-	2.15±0.05	0.24±0.01	0.33±0.02	1.80±0.06	-
Whf	100.78±20.01	331.31±59.54	29.97±21.85	20.19±6.24	59.82±17.91	6.61±5.09
Wcl	5.13±2.31	8.44±3.24	0.46±0.01	0.99±0.69	2.77±1.14	0.19±0.07
Wl	5.61±3.93	4.61±2.45	0.16±0.00	1.41±2.06	2.67±1.67	0.57±0.36
Zhf	318.76±35.27	548.71±61.84	76.97±21.47	86.79±10.63	184.99±21.43	25.76±7.43
Zcl	3.97±1.63	6.74±2.68	0.83±0.02	-	6.36±2.73	0.93±0.41
Zl	1.34±0.67	3.61±2.14	0.42±0.01	1.05±0.63	3.68±2.47	0.29±0.16
Data	623	1493	683	146	330	85
Background	603±25	1466±36	676±25	138±9	339±15	85±7

**Table 7.13:** Post-fit yields in the 0-lepton channel. Combined statistical and systematic uncertainties are shown [177].

Processes	$250 \text{ GeV} < p_T^V \leq 400 \text{ GeV}$			$p_T^V > 400 \text{ GeV}$		
	HP	LP	CR	HP	LP	CR
Signal	24.23±12.34	18.02±9.29	0.88±0.45	7.84±3.96	7.50±3.87	0.39±0.20
W+t	64.35±21.12	159.95±75.14	73.44±29.96	16.40±7.31	53.28±41.74	21.16±15.36
other t+X	1.92±0.48	16.33±0.31	21.89±6.18	0.13±0.01	1.70±0.06	3.95±1.40
$t\bar{t}$	234.76±30.21	1189.51±75.91	1758.08±57.99	50.87±7.34	226.85±23.98	340.61±25.32
VZ	35.94±8.87	56.30±13.98	4.93±1.38	8.63±2.30	20.02±5.29	2.61±0.84
WW	-	6.48±1.63	-	-	4.35±1.32	0.93±0.03
Whf	265.13±27.68	617.81±63.56	59.91±21.90	91.42±11.51	238.81±29.53	26.55±9.84
Wcl	7.33±2.95	13.81±5.65	2.10±0.04	6.23±2.49	10.17±4.09	0.63±0.02
Wl	2.99±1.47	5.66±3.39	0.65±0.01	2.21±1.35	7.67±4.98	0.31±0.01
Zhf	10.16±1.24	24.61±2.46	3.45±0.41	2.12±0.30	6.56±0.79	0.98±0.12
Zcl	0.02±0.00	0.75±0.02	-	-	0.33±0.01	0.02±0.00
Zl	-	0.49±0.01	0.03±0.00	0.30±0.19	0.23±0.01	0.02±0.00
ggWW	-	0.35±0.01	0.27±0.01	0.15±0.02	0.33±0.01	-
MultiJet	17.04±8.87	44.29±22.82	21.78±11.22	7.81±4.50	21.85±12.73	7.86±4.01
Data	668	2161	1946	185	597	410
Background	640±26	2136±44	1947±43	186±11	592±21	406±18

**Table 7.14:** Post-fit yields in the 1-lepton channel. Combined statistical and systematic uncertainties are shown [177].

Processes	$250 \text{ GeV} < p_T^V \leq 400 \text{ GeV}$	$p_T^V > 400 \text{ GeV}$
	SR	SR
Signal	$7.62 \pm 3.88$	$2.79 \pm 1.41$
W+t	$1.28 \pm 0.39$	-
t̄t	$1.64 \pm 0.35$	$0.45 \pm 0.10$
VZ	$19.90 \pm 4.86$	$7.49 \pm 2.05$
Whf	$0.41 \pm 0.07$	$0.07 \pm 0.01$
Zhf	$150.94 \pm 12.72$	$57.15 \pm 5.81$
Zcl	$2.20 \pm 0.91$	$1.80 \pm 0.76$
Zl	$0.94 \pm 0.67$	$1.01 \pm 0.67$
Data	179	73
Background	$177 \pm 12$	$68 \pm 6$

**Table 7.15:** Post-fit yields in the 2-lepton channel. Combined statistical and systematic uncertainties are shown [177].

2631 results include a full breakdown of the systematic and statistical uncertainties.

$$\mu_{VH}^{bb} = 0.72^{+0.39}_{-0.36} = 0.72^{+0.29}_{-0.28}(\text{stat.})^{+0.26}_{-0.22}(\text{syst.}) \quad (7.8)$$

2632

$$\mu_{VZ}^{bb} = 0.91^{+0.29}_{-0.23} = 0.91 \pm 0.15(\text{stat.})^{+0.24}_{-0.17}(\text{syst.}) \quad (7.9)$$

2633 The results for  $\mu_{VH}^{bb}$  and  $\mu_{VZ}^{bb}$  are consistent with the expectation from the SM. The  
 2634  $\mu_{VH}^{bb}$  measurement is dominated by statistical uncertainty, while the  $\mu_{VZ}^{bb}$  measurement  
 2635 is dominated by systematic sources of uncertainty. The measured signal strength  
 2636 for  $\mu_{VZ}^{bb}$  corresponds to an observed significance of 2.1 standard deviations, with an  
 2637 expected (median) significance given the SM prediction of 2.7 standard deviations.  
 2638 The diboson observed (expected) signal strength significance is 5.4 (5.7). These  
 2639 results are summarised in Fig. 7.8, which shows the background-subtracted  $m_J$   
 2640 distribution. A clear signal excess is visible around the Higgs mass of  $m_H = 125 \text{ GeV}$ .

## 2641 Compatability Studies

2642 Alongside the standard 2-POI fit, a (3+1)-POI fit can be performed by splitting  $\mu_{VH}^{bb}$   
 2643 into three separate POIs, one for each channel. A simultaneous fit to the channel  
 2644 specific signal strengths can then be performned, which allows a comparison of the  
 2645 contributions from each channel. Fig. 7.9 compares the best-fit signal strengths.  
 2646 The 0- and 1-lepton channels show a signal strength which is consistent with the

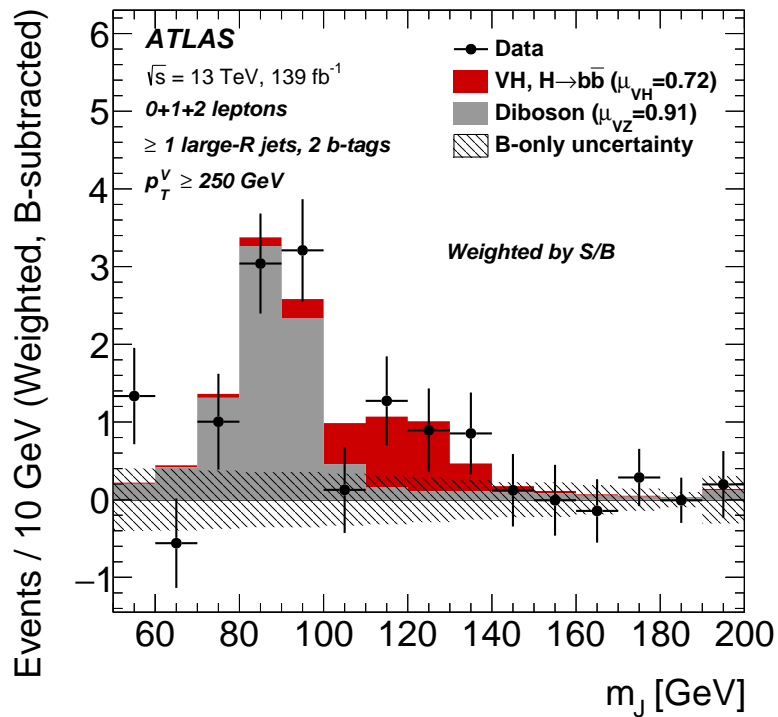


**Figure 7.8:**  $m_J$  distribution in data after subtraction of all backgrounds except for the  $WZ$  and  $ZZ$  diboson processes. The contributions from all lepton channels and signal regions are summed and weighted by their respective values of the ratio of fitted Higgs boson signal and background yields. The expected contribution of the associated  $WH$  and  $ZH$  production of a SM Higgs boson with  $m_H = 125 \text{ GeV}$  is shown scaled by the measured combined signal strength ( $\mu_{VH}^{bb} = 0.72$ ). The diboson contribution is normalised to its best-fit value of  $\mu_{VZ}^{bb} = 0.91$ . The size of the combined statistical and systematic uncertainty is indicated by the hatched band. This error band is computed from a full signal-plus-background fit including all the systematic uncertainties defined in Section 7.2, except for the  $VH/VZ$  experimental and theory uncertainties [131].

2647 SM prediction, while the 2-lepton channel shows a small deviation within the  $1\sigma$   
2648 uncertainty. Overall, good compatibility is observed via a  $\chi^2$  test with a corresponding  
2649  $p$ -value of 49%.

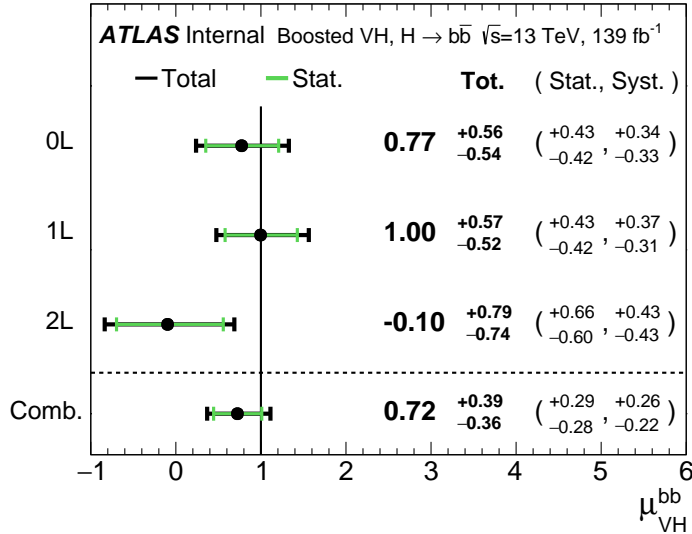


**Figure 7.9:** Signal strength compatibility test between the (3+1)-POI fit (with the three lepton channels splitted) and the default (1+1)-POI fit. The compatibility of the three channels is evaluated via a  $\chi^2$  difference test and results in a  $p$ -value of 49% [131].

#### 2650 7.4.4 Impact of Systematics

2651 The impact of systematic uncertainties on the final fitted value  $\hat{\mu}^{bb}$  can be studied  
2652 using the NP rankings, and the uncertainty breakdown.

2653 Fig. 7.10 shows the NP ranking, which is used to visualise which out of the many  
2654 NPs involved in the fit have the largest impact on the sensitivity to the fitted  
2655 POI. To obtain the ranking, a likelihood scan is performed for each NP  $\theta_j$ . First,  
2656 an unconditional fit is used to determine  $\hat{\theta}_j$ . The NP is then fixed to its post-fit  
2657 value varied by  $\pm 1\sigma$ , the fit is repeated and the best-fit value of the POI,  $\Delta\hat{\mu}_{VH}^{bb}$ , is  
2658 calculated, and used to rank the NPs. Also shown in Fig. 7.10 are the pulls and  
2659 constraints for the highest ranked NPs.

2660 The experimental uncertainty on the signal large- $R$  jet mass resolution (JMR) has  
2661 the largest impact. JMR and jet energy scale (JES) uncertainties also have impacts

for the  $V+jets$  background and for the diboson background. The freely-floating  $Z+hf$  normalisation is the second highest ranked NP, and is heavily constrained by the fit. The  $VZ$  POI  $\mu_{VZ}^{bb}$  is also a significant NP when considering the primary  $\mu_{VH}^{bb}$  measurement.

The NP ranking highlights individual NPs which have a large impact on the POI measurement sensitivity. Complementary information is provided at a higher level by considering the overall impact of different groups of systematics. The groups are constructed from NPs which have similar physical origin. The impact of each group is calculated by running a fit with all the NPs in the given group fixed to their nominal values. The uncertainty on the POI extracted from this fit is subtracted in quadrature from the the uncertainty on the POI from the nominal fit, and the resulting values are provided as the impact for each group. The full breakdown for the observed impact of uncertainties on the  $\mu_{VH}^{bb}$  signal strength is provided in Table 7.16. The total systematic impact is the difference in quadrature between the nominal uncertainty on  $\mu_{VH}^{bb}$  and the combined statistical impact. The “data stat only” group fixes all NPs at their nominal value, while the total statistical impact fixes all NPs except floating normalisations. The floating normalisations group fixes only the NPs associated with normalisation which are left floating in the fit. The uncertainty on  $\mu_{VH}^{bb}$  is dominated by combined statistical effects (0.28), although the combined impact of systematics (0.24) is of a comparable size. The signal largest group is the data stat uncertainty (0.25), demonstrating that the analysis would benefit from an increased integrated luminosity or improved efficiency to select signal events (recall from Section 7.1.3 the signal efficiency is in the range of 10%). Of the experimental systematic sources of uncertainty, the dominant impact is the experimental uncertainties associated with the reconstruction of large- $R$  jets (0.13). Other experimental sources of uncertainty are small in comparison. Modelling uncertainties also have a large contribution to the overall systematic uncertainty. The biggest contribution to the overall uncertainty is the combined statistical uncertainty on the simulated samples (0.09). Out of the backgrounds, the  $W+jets$  and  $Z+jets$  have the highest (0.06) and second-highest (0.05) impact respectively.

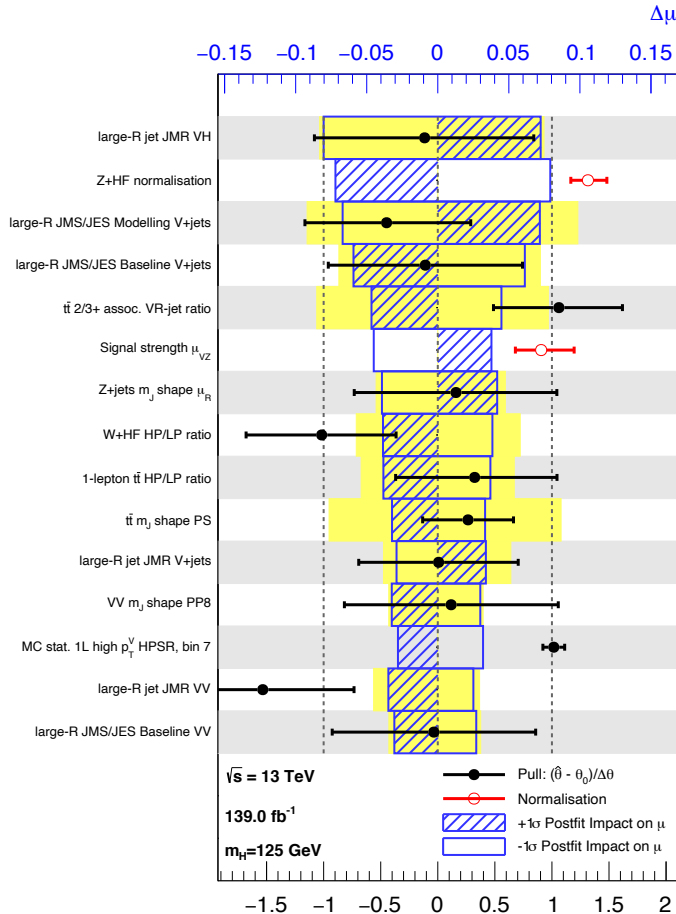


**Figure 7.10:** Impact of systematic uncertainties on the fitted  $VH$  signal-strength parameter  $\hat{\mu}_{VH}^{\text{bb}}$  sorted in decreasing order. The boxes show the variations of  $\hat{\mu}$ , referring to the top  $x$ -axis, when fixing the corresponding individual nuisance parameter to its post-fit value modified upwards or downwards by its post-fit uncertainty, i.e.  $\hat{\theta} \pm \sigma_{\hat{\theta}}$ , and repeating the fit. The impact of up- and down-variations can be distinguished via the dashed and plane box fillings. The yellow boxes show the pre-fit impact (top  $x$ -axis) by varying each nuisance parameter by  $\pm 1$ . The filled circles show the deviation of the fitted value for each nuisance parameter,  $\hat{\theta}$ , from their nominal input value  $\theta_0$  expressed in standard deviations with respect to their nominal uncertainties  $\Delta\theta$  (bottom  $x$ -axis). The error bars show the post-fit uncertainties on  $\hat{\theta}$  with respect to their nominal uncertainties. The open circles show the fitted values and uncertainties of the normalization parameters that are freely floating in the fit. Pre-fit, these parameters have a value of one [177].

Source of uncertainty	Signed impact	Avg. impact
Total	+0.388 / -0.356	0.372
Statistical	+0.286 / -0.280	0.283
↔ Data stat only	+0.251 / -0.245	0.248
↔ Floating normalisations	+0.096 / -0.092	0.094
Systematic	+0.261 / -0.219	0.240
<hr/>		
Experimental uncertainties		
small-R jets	+0.041 / -0.034	0.038
large-R jets	+0.161 / -0.105	0.133
$E_T^{\text{miss}}$	+0.008 / -0.007	0.007
Leptons	+0.013 / -0.007	0.010
<i>b</i> -tagging	<i>b</i> -jets	+0.028 / -0.004
	<i>c</i> -jets	+0.012 / -0.011
	light-flavour jets	+0.009 / -0.007
	extrapolation	+0.004 / -0.005
Pile-up	+0.001 / -0.002	0.001
Luminosity	+0.019 / -0.007	0.013
<hr/>		
Theoretical and modelling uncertainties		
Signal	+0.073 / -0.026	0.050
Backgrounds	+0.106 / -0.095	0.100
↔ $Z + \text{jets}$	+0.049 / -0.047	0.048
↔ $W + \text{jets}$	+0.059 / -0.056	0.058
↔ $t\bar{t}$	+0.037 / -0.032	0.035
↔ Single top quark	+0.031 / -0.023	0.027
↔ Diboson	+0.034 / -0.029	0.032
↔ Multijet	+0.009 / -0.009	0.009
↔ MC statistical	+0.091 / -0.092	0.092

**Table 7.16:** Breakdown of the absolute contributions to the uncertainty on the signal strength  $\mu_{VH}^{bb}$  obtained from the (1+1)-POI fit. The average impact represents the average between the positive and negative uncertainties on  $\mu_{VH}^{bb}$ . The sum in quadrature of the systematic uncertainties attached to the categories differs from the total systematic uncertainty due to correlations [177].

### 2692 7.4.5 STXS Interpretation

2693 The Simplified Template Cross Sections (STXS) framework provides a common  
2694 categorisation of candidate Higgs boson events according to certain truth-level  
2695 properties of the production mode under study [26, 185]. The STXS framework is  
2696 designed to be independent of the decay mode of the Higgs boson, and is therefore  
2697 well suited to the combination of measurements between different decay channels  
2698 and experiments.

2699 The STXS cross sections are independently measured for the  $ZH$  and  $WH$  production  
2700 modes following the approach described in [180]. For each production mode, two  
2701 bins in the truth vector boson transverse momentum  $p_T^{V,t}$  are considered,  $250 \text{ GeV} <$   
2702  $p_T^{V,t} < 400 \text{ GeV}$  and  $p_T^{V,t} \geq 400 \text{ GeV}$ , leading to four independent analysis regions.  
2703 Events from the simulated signal samples are categorised into the regions and used  
2704 to estimate the expected cross section times branching ratio  $\sigma \times B$  in each region,  
2705 where

$$B = B(H \rightarrow b\bar{b}) \times B(V \rightarrow \text{leptons}), \quad (7.10)$$

2706 A simultaneous fit of the four cross section times branching ratios is performed.  
2707 The uncertainties described in Section 7.2 are reused for the STXS fit, with the  
2708 exception of the theoretical uncertainties on the signal cross section and branching  
2709 ratios. The result from the fit is shown in Section 7.4.5 and compared with the  
2710 expected prediction from the SM. The expected and observed results agree within  
2711 the given uncertainties.

## 2712 7.5 Conclusion

2713 The analysis of the associated production of vector bosons with boosted Higgs bosons  
2714 decaying to a pair of  $b$ -quarks using large- $R$  jets is presented. The Higgs candidate is  
2715 reconstructed as a large- $R$  jet in order to improve sensitivity in the boosted regime  
2716 in which the Higgs decay products are significantly collimated. The analysis is  
2717 performed using  $139 \text{ fb}^{-1}$  of proton–proton collision data at  $\sqrt{s} = 13 \text{ TeV}$  collected  
2718 throughout the duration of Run 2 of the LHC.

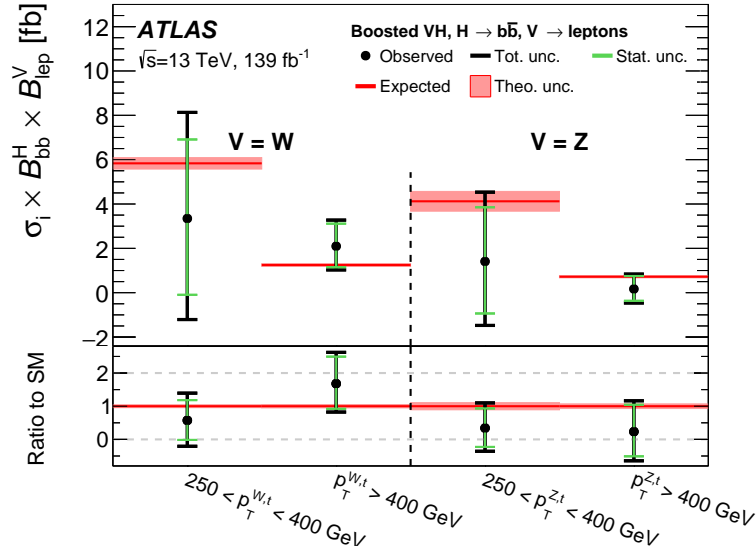


**Figure 7.11:** Measured  $VH$  simplified template cross sections times the  $H \rightarrow b\bar{b}$  and  $V \rightarrow \text{leptons}$  branching fractions in the medium and high  $p_T^{V,t}$  bins [131].

2719 In comparison with the null hypothesis, the Standard Model (SM)  $VH$ ,  $H \rightarrow b\bar{b}$   
 2720 process is found to have an observed significance of 2.1 standard deviations, whereas  
 2721 the corresponding expected significance is 2.7 standard deviations. The  $VH$ ,  $H \rightarrow b\bar{b}$   
 2722 process is measured simultaneously with the diboson  $VZ$ ,  $Z \rightarrow b\bar{b}$  process, which  
 2723 provide a cross-check for the main analysis. The observed (expected) significance for  
 2724 the diboson process is 5.4 (5.7).

2725 The statistical and systematic sources of uncertainty contribute a similar amount  
 2726 to the overall uncertainty on the result. This analysis would therefore likely benefit  
 2727 greatly from the improved  $b$ -tagging efficiency at high- $p_T$  enabled by GN1 as discussed  
 2728 in Chapter 6, due to the associated reduction in statistical uncertainty provided by  
 2729 the increased number of events used in the analysis.

2730 The large- $R$  jet mass resolution is found to be the dominant source of systematic  
 2731 uncertainty on the  $\mu_{VH}^{bb}$  measurement. An improved method of reconstructing the  
 2732 large- $R$  jet mass, for example by using a machine learning based regression approach,  
 2733 possibly as an additional auxiliary task to GN1 (see Chapter 6), would therefore be  
 2734 expected to reduce the systematic uncertainty on the  $\mu_{VH}^{bb}$  measurement.

# 2735 Chapter 8

## 2736 Conclusion

### 2737 8.1 Summary

2738 The current understanding of particle physics contains many unanswered questions,  
2739 and improving our understanding of the Standard Model is a promising way to  
2740 attempt to answer some of them. One of the key objects which may enhance this  
2741 understanding is the Higgs Boson, which was first observed only a decade ago and  
2742 remains under intense scrutiny at the LHC. Given it's propensity to decay to heavy  
2743 flavour  $b$ -quarks, reconstructing and identifying  $b$ -jets is of crucial importance to  
2744 improving our understanding in this area. As discussed in Chapter 4, this task  
2745 becomes increasingly difficult at high transverse momenta.

2746 One of the effects that hampered tracking and  $b$ -tagging performance at high- $p_T$  was  
2747 identified to be the increased rate of fake tracks. To address this issue, a tools was  
2748 developed which was able to successfully identify fake tracks within jets 45% of the  
2749 time, with a minimal loss of signal tracks of 1.2%. Removal of such tracks was found  
2750 to improve the light-jet mistagging rate of the SV1 and JetFitter algorithms by up  
2751 to 20% at high transverse momentum.

2752 A novel approach to  $b$ -tagging, GN1 was also developed using a Graph Neural Network  
2753 (GNN) architecture. The model is encouraged to learn the topology of the jet through  
2754 vertexing and track classification auxiliary tasks. As a single end-to-end trained  
2755 model, GN1 simplifies the complexity of the flavour tagging pipeline and is able to  
2756 achieve superior performance to the current state-of-the-art algorithms, which rely  
2757 on a two-tiered approach. Compared with DL1r, GN1 improves the light-jet rejection

2758 by a factor of  $\sim 1.8$  for jets in the  $t\bar{t}$  sample with  $20 < p_T < 250$  GeV at the 70%  
2759  $b$ -jet WP and by a factor of  $\sim 6$  for jets in the  $Z'$  sample with  $250 < p_T < 5000$  GeV  
2760 for a corresponding  $b$ -jet efficiency of 30%. GN1 also demonstrates a significant  
2761 improvement in the discrimination between  $b$ - and  $c$ -jets.

2762 The work in this thesis demonstrates that even with suboptimal track reconstruction  
2763 in this regime, it is possible to make algorithmic advancements to the flavour tagging  
2764 pipeline to improve the identification of  $b$ -jets. This work has impacts for any analysis  
2765 which relies on the identification of  $b$ -jets, including those which are sensitive to the  
2766 Higgs Boson.

2767 Analysis of  $VH$ ,  $H \rightarrow b\bar{b}$  events was also carried out with  $139\text{ fb}^{-1}$  of Run 2  
2768 ATLAS at  $\sqrt{s} = 13$  TeV. Various background modelling uncertainties were derived  
2769 and investigations into the fit model were carried out. The analysis observed a  
2770 signal strength of  $\mu_{VH}^{bb} = 0.72_{-0.36}^{+0.39} = 0.72_{-0.28}^{+0.29}(\text{stat.})_{-0.22}^{+0.26}(\text{syst.})$  corresponding to an  
2771 observed (expected) significance of  $2.1\sigma$  ( $2.7\sigma$ ). The result was validated using a  
2772 simultaneous fit to the  $VZ$ ,  $Z \rightarrow b\bar{b}$  process, which acts as a cross check to validate  
2773 the primary analysis. The results of the analysis are the most precise measurements  
2774 available in the high- $p_T$  for the  $VH$ ,  $H \rightarrow b\bar{b}$  process. The high- $p_T$  region is of  
2775 particular interest as it is a region of phase space with good sensitivity to new physics.

## 2776 8.2 Future Work

2777 Additional algorithmic improvements are likely to yield further improved flavour  
2778 tagging performance. Aside from these, large improvements to the flavour tagging  
2779 performance will likely be possible if improvements are made to the  $b$ -hadron decay  
2780 track reconstruction efficiency and accuracy.

2781 At the moment only the tracks from the Inner Detector and kinematic information  
2782 about the jet are provided as inputs to the tagging algorithms. In Chapter 6 it  
2783 was shown that the addition of a simple track-level variable corresponding to the  
2784 ID of the reconstruction lepton to the model improved the performance. However  
2785 there is still untapped potential in the form of additional information from the full  
2786 parameters of the reconstructed leptons (making full use of the Calorimeters and  
2787 Muon Spectrometer), the calorimeter clusters, and even the low level hits. Providing

2788 such additional inputs to the model is likely to complement the information provided  
2789 by the tracks and further aid in the improvement of performance.

2790 On the output side, additional auxiliary training objectives may yield improved  
2791 performance and also help to add to the explainability of the model. Regression of  
2792 jet-level quantities such as the transverse momentum and mass, in addition to the  
2793 truth  $b$ -hadron decay length are promising regression targets.

2794 The GN1 architecture can also be readily optimised for new use cases and topologies,  
2795 as demonstrated by the studies described in Section 6.6. For example, a model  
2796 with only hit-level information provided as inputs could be used for a fast trigger  
2797 preselection on jets without the need to run the computationally expensive tracking  
2798 algorithms. The model could also be repurposed for primary vertexing, or a pile-up  
2799 jet tagger. Finally, training a version of GN1 to identify large- $R$  jets would benefit  
2800 those analysis investigating such boosted topologies. Ultimately the improved jet  
2801 tagging performance enabled by the new algorithm will have a large impact across a  
2802 broad spectrum of the ATLAS physics programme.

2803    

# Bibliography

- 2804 [1] A. Buckley, *A class for typesetting academic theses*, (2010). [http://ctan.tug.org/  
2805 tex-archive/macros/latex/contrib/heptesis/heptesis.pdf](http://ctan.tug.org/tex-archive/macros/latex/contrib/heptesis/heptesis.pdf).
- 2806 [2] J. Shlomi, S. Ganguly, E. Gross, K. Cranmer, Y. Lipman, H. Serviansky et al.,  
2807 *Secondary vertex finding in jets with neural networks*, *The European Physical Journal C* **81** (2021) .  
2808
- 2809 [3] ATLAS Collaboration, *Graph Neural Network Jet Flavour Tagging with the ATLAS  
2810 Detector*, **ATL-PHYS-PUB-2022-027** (2022).
- 2811 [4] L. Morel, Z. Yao, P. Cladé and S. Guellati-Khélifa, *Determination of the  
2812 fine-structure constant with an accuracy of 81 parts per trillion*, *Nature* **588** (2020)  
2813 pp. 61–65.
- 2814 [5] T. Sailer, V. Debierre, Z. Harman, F. Heiße, C. König, J. Morgner et al.,  
2815 *Measurement of the bound-electron g-factor difference in coupled ions*, *Nature* **606**  
2816 (2022) pp. 479–483.
- 2817 [6] CDF collaboration, *Observation of top quark production in  $\bar{p}p$  collisions*, *Phys. Rev.  
2818 Lett.* **74** (1995) pp. 2626–2631 [[hep-ex/9503002](#)].
- 2819 [7] D0 collaboration, *Observation of the top quark*, *Phys. Rev. Lett.* **74** (1995)  
2820 pp. 2632–2637 [[hep-ex/9503003](#)].
- 2821 [8] S. W. Herb et al., *Observation of a Dimuon Resonance at 9.5-GeV in 400-GeV  
2822 Proton-Nucleus Collisions*, *Phys. Rev. Lett.* **39** (1977) pp. 252–255.
- 2823 [9] UA1 collaboration, *Experimental Observation of Isolated Large Transverse Energy  
2824 Electrons with Associated Missing Energy at  $\sqrt{s} = 540$  GeV*, *Phys. Lett. B* **122**  
2825 (1983) pp. 103–116.
- 2826 [10] DONUT collaboration, *Observation of tau neutrino interactions*, *Phys. Lett. B* **504**  
2827 (2001) pp. 218–224 [[hep-ex/0012035](#)].

- 2828 [11] F. Englert and R. Brout, *Broken Symmetry and the Mass of Gauge Vector Mesons*,  
2829 *Phys. Rev. Lett.* **13** (1964) pp. 321–323.
- 2830 [12] P. W. Higgs, *Broken Symmetries and the Masses of Gauge Bosons*, *Phys. Rev. Lett.*  
2831 **13** (1964) pp. 508–509.
- 2832 [13] G. S. Guralnik, C. R. Hagen and T. W. B. Kibble, *Global Conservation Laws and*  
2833 *Massless Particles*, *Phys. Rev. Lett.* **13** (1964) pp. 585–587.
- 2834 [14] ATLAS Collaboration, *Observation of a new particle in the search for the Standard*  
2835 *Model Higgs boson with the ATLAS detector at the LHC*, *Phys. Lett. B* **716** (2012)  
2836 p. 1 [[1207.7214](#)].
- 2837 [15] CMS Collaboration, *Observation of a new boson at a mass of 125 GeV with the CMS*  
2838 *experiment at the LHC*, *Phys. Lett. B* **716** (2012) p. 30 [[1207.7235](#)].
- 2839 [16] Particle Data Group collaboration, *Review of Particle Physics*, *PTEP* **2022** (2022)  
2840 p. 083C01.
- 2841 [17] C. N. Yang and R. L. Mills, *Conservation of isotopic spin and isotopic gauge*  
2842 *invariance*, *Phys. Rev.* **96** (1954) pp. 191–195.
- 2843 [18] S. L. Glashow, *Partial Symmetries of Weak Interactions*, *Nucl. Phys.* **22** (1961)  
2844 pp. 579–588.
- 2845 [19] S. Weinberg, *A Model of Leptons*, *Phys. Rev. Lett.* **19** (1967) pp. 1264–1266.
- 2846 [20] A. Salam, *Weak and Electromagnetic Interactions*, *Proceedings of the 8th Nobel*  
2847 *symposium*, Ed. N. Svartholm, Almqvist & Wiksell, 1968, **Conf. Proc. C680519**  
2848 (1968) pp. 367–377.
- 2849 [21] T. D. Lee and C. N. Yang, *Question of parity conservation in weak interactions*,  
2850 *Phys. Rev.* **104** (1956) pp. 254–258.
- 2851 [22] C. S. Wu, E. Ambler, R. W. Hayward, D. D. Hopper and R. P. Hudson, *Experimental*  
2852 *test of parity conservation in beta decay*, *Phys. Rev.* **105** (1957) pp. 1413–1415.
- 2853 [23] R. L. Garwin, L. M. Lederman and M. Weinrich, *Observations of the failure of*  
2854 *conservation of parity and charge conjugation in meson decays: the magnetic moment*  
2855 *of the free muon*, *Phys. Rev.* **105** (1957) pp. 1415–1417.
- 2856 [24] Y. Nambu, *Quasi-particles and gauge invariance in the theory of superconductivity*,  
2857 *Phys. Rev.* **117** (1960) pp. 648–663.

- 2858 [25] J. Goldstone, *Field theories with « superconductor » solutions*, *Il Nuovo Cimento*  
2859 (1955-1965) **19** (1961) pp. 154–164.
- 2860 [26] LHC Higgs Cross Section Working Group collaboration, *Handbook of LHC Higgs*  
2861 *Cross Sections: 4. Deciphering the Nature of the Higgs Sector*, [1610.07922](https://arxiv.org/abs/1610.07922).
- 2862 [27] ATLAS Collaboration, *Observation of  $H \rightarrow b\bar{b}$  decays and VH production with the*  
2863 *ATLAS detector*, [ATLAS-CONF-2018-036](https://cds.cern.ch/record/2620000) (2018).
- 2864 [28] CMS Collaboration, *Observation of Higgs Boson Decay to Bottom Quarks*, *Phys.*  
2865 *Rev. Lett.* **121** (2018) p. 121801 [[1808.08242](https://arxiv.org/abs/1808.08242)].
- 2866 [29] L. Evans and P. Bryant, *LHC Machine*, *JINST* **3** (2008) p. S08001.
- 2867 [30] The ALICE Collaboration, *The ALICE experiment at the CERN LHC*, *Journal of*  
2868 *Instrumentation* **3** (2008) pp. S08002–S08002.
- 2869 [31] CMS Collaboration, *The CMS experiment at the CERN LHC*, *JINST* **3** (2008)  
2870 p. S08004.
- 2871 [32] The LHCb Collaboration, *The LHCb detector at the LHC*, *Journal of*  
2872 *Instrumentation* **3** (2008) pp. S08005–S08005.
- 2873 [33] ATLAS Collaboration, *The ATLAS Experiment at the CERN Large Hadron Collider*,  
2874 *JINST* **3** (2008) p. S08003.
- 2875 [34] ATLAS Collaboration, *Integrated luminosity summary plots for 2011-2012 data*  
2876 *taking*, (2022). <https://twiki.cern.ch/twiki/bin/view/AtlasPublic/LuminosityPublicResults>.
- 2877 [35] ATLAS Collaboration, *Public ATLAS Luminosity Results for Run-2 of the LHC*,  
2878 (2022). <https://twiki.cern.ch/twiki/bin/view/AtlasPublic/LuminosityPublicResultsRun2>.
- 2881 [36] CERN, “The accelerator complex.” (2012).
- 2882 [37] G. C. Strong, *On the impact of selected modern deep-learning techniques to the*  
2883 *performance and celerity of classification models in an experimental high-energy*  
2884 *physics use case*, [2002.01427](https://arxiv.org/abs/2002.01427).
- 2885 [38] ATLAS Collaboration, *Atlas track reconstruction – general overview*, (2022).  
2886 <https://atlassoftwaredocs.web.cern.ch/trackingTutorial/idoverview/>.
- 2887 [39] ATLAS Collaboration, *Performance of b-jet identification in the ATLAS experiment*,

- 2888        *JINST* **11** (2016) p. P04008 [[1512.01094](#)].
- 2889 [40] ATLAS Collaboration, *Luminosity determination in pp collisions at  $\sqrt{s} = 13 \text{ TeV}$  using the ATLAS detector at the LHC*, **ATLAS-CONF-2019-021** (2019).
- 2891 [41] ATLAS Collaboration, *ATLAS Detector and Physics Performance: Technical Design Report, Volume 1*, .
- 2893 [42] for the ATLAS Collaboration collaboration, *Status of the ATLAS Experiment*, Tech. Rep., Geneva (2010). 10.3204/DESY-PROC-2010-04/1.
- 2895 [43] ATLAS Collaboration, *ATLAS Inner Tracker Pixel Detector: Technical Design Report*, ATLAS-TDR-030; CERN-LHCC-2017-021 (2017).
- 2897 [44] ATLAS Collaboration, *ATLAS Inner Tracker Strip Detector: Technical Design Report*, ATLAS-TDR-025; CERN-LHCC-2017-005 (2017).
- 2899 [45] ATLAS Collaboration, *The inner detector*, (2022).  
<https://atlas.cern/Discover/Detector/Inner-Detector>.
- 2901 [46] ATLAS Collaboration, *ATLAS Insertable B-Layer: Technical Design Report*, ATLAS-TDR-19; CERN-LHCC-2010-013 (2010).
- 2903 [47] B. Abbott et al., *Production and integration of the ATLAS Insertable B-Layer*, *JINST* **13** (2018) p. T05008 [[1803.00844](#)].
- 2905 [48] ATLAS Collaboration, *Operation and performance of the ATLAS semiconductor tracker*, *JINST* **9** (2014) p. P08009 [[1404.7473](#)].
- 2907 [49] ATLAS Collaboration, *Calorimeter*, (2022).  
<https://atlas.cern/Discover/Detector/Calorimeter>.
- 2909 [50] ATLAS Collaboration, *ATLAS Tile Calorimeter: Technical Design Report*, .
- 2910 [51] G. Artoni, *Muon momentum scale and resolution in pp collisions at  $\sqrt{s} = 8 \text{ TeV}$  in ATLAS*, Tech. Rep., Geneva (2016). 10.1016/j.nuclphysbps.2015.09.453.
- 2912 [52] ATLAS Collaboration, *Muon spectrometer*, (2022).  
<https://atlas.cern/Discover/Detector/Muon-Spectrometer>.
- 2914 [53] ATLAS Collaboration, *Performance of the ATLAS trigger system in 2015*, *Eur. Phys. J. C* **77** (2017) p. 317 [[1611.09661](#)].
- 2916 [54] ATLAS Collaboration, *The ATLAS Collaboration Software and Firmware*, **ATL-SOFT-PUB-2021-001** (2021).

- 2918 [55] T. Cornelissen, M. Elsing, S. Fleischmann, W. Liebig and E. Moyse, *Concepts,  
2919 Design and Implementation of the ATLAS New Tracking (NEWT)*, .
- 2920 [56] ATLAS Collaboration, *The Optimization of ATLAS Track Reconstruction in Dense  
2921 Environments*, ATL-PHYS-PUB-2015-006 (2015).
- 2922 [57] ATLAS Collaboration, *Performance of the ATLAS track reconstruction algorithms in  
2923 dense environments in LHC Run 2*, *Eur. Phys. J. C* **77** (2017) p. 673 [[1704.07983](#)].
- 2924 [58] ATLAS Collaboration, *A neural network clustering algorithm for the ATLAS silicon  
2925 pixel detector*, *JINST* **9** (2014) p. P09009 [[1406.7690](#)].
- 2926 [59] R. Jansky, *Truth Seeded Reconstruction for Fast Simulation in the ATLAS  
2927 Experiment*, .
- 2928 [60] ATLAS Collaboration, *Reconstruction of primary vertices at the ATLAS experiment  
2929 in Run 1 proton–proton collisions at the LHC*, *Eur. Phys. J. C* **77** (2017) p. 332  
2930 [[1611.10235](#)].
- 2931 [61] ATLAS Collaboration, *ATLAS b-jet identification performance and efficiency  
2932 measurement with  $t\bar{t}$  events in  $pp$  collisions at  $\sqrt{s} = 13$  TeV*, *Eur. Phys. J. C* **79**  
2933 (2019) p. 970 [[1907.05120](#)].
- 2934 [62] ATLAS Collaboration, *Secondary vertex finding for jet flavour identification with the  
2935 ATLAS detector*, ATL-PHYS-PUB-2017-011 (2017).
- 2936 [63] M. Cacciari, G. P. Salam and G. Soyez, *The anti- $k_t$  jet clustering algorithm*, *JHEP*  
2937 **04** (2008) p. 063 [[0802.1189](#)].
- 2938 [64] M. Cacciari, G. P. Salam and G. Soyez, *Fastjet user manual*, *Eur. Phys. J. C* **72** (2012)  
2939 p. 1896 [[1111.6097](#)].
- 2940 [65] M. Cacciari, G. P. Salam and G. Soyez, *The Catchment Area of Jets*, *JHEP* **04**  
2941 (2008) p. 005 [[0802.1188](#)].
- 2942 [66] ATLAS Collaboration, *Topological cell clustering in the ATLAS calorimeters and its  
2943 performance in LHC Run 1*, *Eur. Phys. J. C* **77** (2017) p. 490 [[1603.02934](#)].
- 2944 [67] ATLAS Collaboration, *Jet reconstruction and performance using particle flow with  
2945 the ATLAS Detector*, *Eur. Phys. J. C* **77** (2017) p. 466 [[1703.10485](#)].
- 2946 [68] ATLAS Collaboration, *Jet energy scale measurements and their systematic  
2947 uncertainties in proton–proton collisions at  $\sqrt{s} = 13$  TeV with the ATLAS detector*,  
2948 *Phys. Rev. D* **96** (2017) p. 072002 [[1703.09665](#)].

- 2949 [69] J. M. Butterworth, A. R. Davison, M. Rubin and G. P. Salam, *Jet Substructure as a*  
2950 *New Higgs Search Channel at the Large Hadron Collider*, *Phys. Rev. Lett.* **100** (2008)  
2951 p. 242001 [[0802.2470](#)].
- 2952 [70] ATLAS collaboration, *Measurement of the associated production of a Higgs boson*  
2953 *decaying into b-quarks with a vector boson at high transverse momentum in pp*  
2954 *collisions at  $\sqrt{s} = 13$  TeV with the ATLAS detector*, *Phys. Lett. B* **816** (2021)  
2955 p. 136204 [[2008.02508](#)].
- 2956 [71] ATLAS collaboration, *Performance of jet substructure techniques for large-R jets in*  
2957 *proton-proton collisions at  $\sqrt{s} = 7$  TeV using the ATLAS detector*, *JHEP* **09** (2013)  
2958 p. 076 [[1306.4945](#)].
- 2959 [72] ATLAS Collaboration, *In situ calibration of large-radius jet energy and mass in*  
2960 *13 TeV proton–proton collisions with the ATLAS detector*, *Eur. Phys. J. C* **79** (2019)  
2961 p. 135 [[1807.09477](#)].
- 2962 [73] D. Krohn, J. Thaler and L.-T. Wang, *Jets with Variable R*, *JHEP* **06** (2009) p. 059  
2963 [[0903.0392](#)].
- 2964 [74] ATLAS Collaboration, *Variable Radius, Exclusive- $k_T$ , and Center-of-Mass Subjet*  
2965 *Reconstruction for  $H \rightarrow b\bar{b}$  Tagging in ATLAS*, ATL-PHYS-PUB-2017-010  
2966 (2017).
- 2967 [75] ATLAS Collaboration, *Improved electron reconstruction in ATLAS using the*  
2968 *Gaussian Sum Filter-based model for bremsstrahlung*, ATLAS-CONF-2012-047 (2012).
- 2969 [76] ATLAS Collaboration, *Electron efficiency measurements with the ATLAS detector*  
2970 *using the 2015 LHC proton–proton collision data*, ATLAS-CONF-2016-024 (2016).
- 2971 [77] ATLAS Collaboration, *Muon reconstruction performance of the ATLAS detector in*  
2972 *proton–proton collision data at  $\sqrt{s} = 13$  TeV*, *Eur. Phys. J. C* **76** (2016) p. 292  
2973 [[1603.05598](#)].
- 2974 [78] ATLAS Collaboration, *Performance of missing transverse momentum reconstruction*  
2975 *with the ATLAS detector using proton–proton collisions at  $\sqrt{s} = 13$  TeV*, *Eur. Phys.*  
2976 *J. C* **78** (2018) p. 903 [[1802.08168](#)].
- 2977 [79] ATLAS Collaboration, *Observation of  $H \rightarrow b\bar{b}$  decays and VH production with the*  
2978 *ATLAS detector*, *Phys. Lett. B* **786** (2018) p. 59 [[1808.08238](#)].
- 2979 [80] ATLAS Collaboration, *Observation of Higgs boson production in association with a*  
2980 *top quark pair at the LHC with the ATLAS detector*, *Phys. Lett. B* **784** (2018) p. 173

- 2981 [1806.00425].
- 2982 [81] ATLAS Collaboration, *Search for new resonances in mass distributions of jet pairs*  
2983 *using  $139\text{fb}^{-1}$  of  $pp$  collisions at  $\sqrt{s} = 13\text{ TeV}$  with the ATLAS detector*, *JHEP* **03**  
2984 (2020) p. 145 [1910.08447].
- 2985 [82] P. Nason, *A new method for combining nlo qcd with shower monte carlo algorithms*,  
2986 *Journal of High Energy Physics* **2004** (2004) p. 040–040.
- 2987 [83] S. Frixione, G. Ridolfi and P. Nason, *A positive-weight next-to-leading-order monte*  
2988 *carlo for heavy flavour hadroproduction*, *Journal of High Energy Physics* **2007** (2007)  
2989 p. 126–126.
- 2990 [84] S. Frixione, P. Nason and C. Oleari, *Matching nlo qcd computations with parton*  
2991 *shower simulations: the powheg method*, *Journal of High Energy Physics* **2007** (2007)  
2992 p. 070–070.
- 2993 [85] S. Alioli, P. Nason, C. Oleari and E. Re, *A general framework for implementing nlo*  
2994 *calculations in shower monte carlo programs: the powheg box*, *Journal of High Energy*  
2995 *Physics* **2010** (2010) .
- 2996 [86] NNPDF collaboration, *Parton distributions for the LHC run II*, *JHEP* **04** (2015)  
2997 p. 040 [1410.8849].
- 2998 [87] ATLAS Collaboration, *Studies on top-quark Monte Carlo modelling for Top2016*,  
2999 *ATL-PHYS-PUB-2016-020* (2016).
- 3000 [88] T. Sjöstrand, S. Ask, J. R. Christiansen, R. Corke, N. Desai, P. Ilten et al., *An*  
3001 *introduction to PYTHIA 8.2*, *Comput. Phys. Commun.* **191** (2015) p. 159  
3002 [1410.3012].
- 3003 [89] ATLAS Collaboration, *ATLAS Pythia 8 tunes to 7 TeV data*,  
3004 *ATL-PHYS-PUB-2014-021* (2014).
- 3005 [90] R. D. Ball et al., *Parton distributions with LHC data*, *Nucl. Phys. B* **867** (2013)  
3006 p. 244 [1207.1303].
- 3007 [91] D. J. Lange, *The EvtGen particle decay simulation package*, *Nucl. Instrum. Meth. A*  
3008 **462** (2001) p. 152.
- 3009 [92] ATLAS Collaboration, *The ATLAS Simulation Infrastructure*, *Eur. Phys. J. C* **70**  
3010 (2010) p. 823 [1005.4568].
- 3011 [93] GEANT4 Collaboration, S. Agostinelli et al., *GEANT4 – a simulation toolkit*, *Nucl.*

- 3012        *Instrum. Meth. A* **506** (2003) p. 250.
- 3013 [94] ATLAS Collaboration, *Tagging and suppression of pileup jets with the ATLAS*  
3014        *detector*, [ATLAS-CONF-2014-018](#) (2014).
- 3015 [95] ATLAS Collaboration, *Identification of Jets Containing b-Hadrons with Recurrent*  
3016        *Neural Networks at the ATLAS Experiment*, [ATL-PHYS-PUB-2017-003](#) (2017).
- 3017 [96] ATLAS Collaboration, *Deep Sets based Neural Networks for Impact Parameter*  
3018        *Flavour Tagging in ATLAS*, [ATL-PHYS-PUB-2020-014](#) (2020).
- 3019 [97] ATLAS Collaboration, *Expected performance of the ATLAS b-tagging algorithms in*  
3020        *Run-2*, [ATL-PHYS-PUB-2015-022](#) (2015).
- 3021 [98] ATLAS Collaboration, *Optimisation and performance studies of the ATLAS*  
3022        *b-tagging algorithms for the 2017-18 LHC run*, [ATL-PHYS-PUB-2017-013](#) (2017).
- 3023 [99] ATLAS collaboration, *ATLAS flavour-tagging algorithms for the LHC Run 2 pp*  
3024        *collision dataset*, [2211.16345](#).
- 3025 [100] B. R. Webber, *Fragmentation and hadronization*, *Int. J. Mod. Phys. A* **15S1** (2000)  
3026        pp. 577–606 [[hep-ph/9912292](#)].
- 3027 [101] Particle Data Group collaboration, *Review of particle physics*, *Phys. Rev. D* **98**  
3028        (2018) p. 030001.
- 3029 [102] ATLAS Collaboration, *Comparison of Monte Carlo generator predictions for bottom*  
3030        *and charm hadrons in the decays of top quarks and the fragmentation of high  $p_T$  jets*,  
3031        [ATL-PHYS-PUB-2014-008](#) (2014).
- 3032 [103] Nazar Bartosik, *Diagram showing the common principle of identification of jets*  
3033        *initiated by b-hadron decays*, (2022).  
3034        [https://en.m.wikipedia.org/wiki/File:B-tagging\\_diagram.png](https://en.m.wikipedia.org/wiki/File:B-tagging_diagram.png).
- 3035 [104] ATLAS Collaboration, *Tracking efficiency studies in dense environments*, (2022).  
3036        <https://atlas.web.cern.ch/Atlas/GROUPS/PHYSICS/PLOTS/IDTR-2022-03/>.
- 3037 [105] S. Adorni Braccesi Chiassi, *Vector Boson Tagging in the Context of the Search for*  
3038        *New Physics in the Fully Hadronic Final State*, Ph.D. thesis, Geneva U., 2021.  
3039        10.13097/archive-ouverte/unige:158558.
- 3040 [106] E. Boos, M. Dobbs, W. Giele, I. Hinchliffe, J. Huston, V. Ilyin et al., *Generic User*  
3041        *Process Interface for Event Generators*, *ArXiv High Energy Physics - Phenomenology*  
3042        *e-prints* (2001) .

- 3043 [107] J. Alwall, A. Ballestrero, P. Bartalini, S. Belov, E. Boos, A. Buckley et al., *A  
3044 standard format for Les Houches Event Files*, *Computer Physics Communications*  
3045 **176** (2007) pp. 300–304.
- 3046 [108] K. Hornik, M. Stinchcombe and H. White, *Multilayer feedforward networks are  
3047 universal approximators*, *Neural Networks* **2** (1989) pp. 359–366.
- 3048 [109] D. E. Rumelhart, G. E. Hinton and R. J. Williams, *Learning representations by  
3049 back-propagating errors*, *nature* **323** (1986) pp. 533–536.
- 3050 [110] W. McCulloch and W. Pitts, *A logical calculus of the ideas immanent in nervous  
3051 activity*, *The bulletin of mathematical biophysics* **5** (1943) pp. 115–133.
- 3052 [111] J. Hopfield, *Neural networks and physical systems with emergent collective  
3053 computational abilities*, in *Spin Glass Theory and Beyond: An Introduction to the  
3054 Replica Method and Its Applications*, pp. 411–415, World Scientific, (1987).
- 3055 [112] A. F. Agarap, *Deep Learning using Rectified Linear Units (ReLU)*, *arXiv e-prints*  
3056 (2018) p. arXiv:1803.08375 [[1803.08375](#)].
- 3057 [113] S. Elfwing, E. Uchibe and K. Doya, *Sigmoid-Weighted Linear Units for Neural  
3058 Network Function Approximation in Reinforcement Learning*, *arXiv e-prints* (2017)  
3059 p. arXiv:1702.03118 [[1702.03118](#)].
- 3060 [114] Y. A. LeCun, L. Bottou, G. B. Orr and K.-R. Müller, *Efficient backprop*, in *Neural  
3061 networks: Tricks of the trade*, pp. 9–48, Springer, (2012).
- 3062 [115] D. P. Kingma and J. Ba, *Adam: A Method for Stochastic Optimization*, *arXiv  
3063 e-prints* (2014) p. arXiv:1412.6980 [[1412.6980](#)].
- 3064 [116] H. Serviansky, N. Segol, J. Shlomi, K. Cranmer, E. Gross, H. Maron et al.,  
3065 *Set2Graph: Learning Graphs From Sets*, *arXiv e-prints* (2020) p. arXiv:2002.08772  
3066 [[2002.08772](#)].
- 3067 [117] P. W. Battaglia, J. B. Hamrick, V. Bapst, A. Sanchez-Gonzalez, V. Zambaldi,  
3068 M. Malinowski et al., *Relational inductive biases, deep learning, and graph networks*,  
3069 *arXiv e-prints* (2018) p. arXiv:1806.01261 [[1806.01261](#)].
- 3070 [118] M. Zaheer, S. Kottur, S. Ravanbakhsh, B. Poczos, R. Salakhutdinov and A. Smola,  
3071 *Deep Sets*, *arXiv e-prints* (2017) p. arXiv:1703.06114 [[1703.06114](#)].
- 3072 [119] ATLAS Collaboration, *Muon reconstruction performance in early  $\sqrt{s} = 13$  TeV data*,  
3073 **ATL-PHYS-PUB-2015-037** (2015).

- 3074 [120] ATLAS Collaboration, *Electron reconstruction and identification in the ATLAS*  
3075       *experiment using the 2015 and 2016 LHC proton–proton collision data at*  
3076        $\sqrt{s} = 13\text{ TeV}$ , *Eur. Phys. J. C* **79** (2019) p. 639 [[1902.04655](#)].
- 3077 [121] D. Hwang, J. Park, S. Kwon, K.-M. Kim, J.-W. Ha and H. J. Kim, *Self-supervised*  
3078       *Auxiliary Learning with Meta-paths for Heterogeneous Graphs*, arXiv e-prints (2020)  
3079       p. arXiv:2007.08294 [[2007.08294](#)].
- 3080 [122] S. Brody, U. Alon and E. Yahav, *How Attentive are Graph Attention Networks?*,  
3081       arXiv e-prints (2021) p. arXiv:2105.14491 [[2105.14491](#)].
- 3082 [123] A. Vaswani, N. Shazeer, N. Parmar, J. Uszkoreit, L. Jones, A. N. Gomez et al.,  
3083       *Attention Is All You Need*, arXiv e-prints (2017) p. arXiv:1706.03762 [[1706.03762](#)].
- 3084 [124] D. P. Kingma and J. Ba, *Adam: A Method for Stochastic Optimization*, arXiv  
3085       e-prints (2014) p. arXiv:1412.6980 [[1412.6980](#)].
- 3086 [125] J. Bai, F. Lu, K. Zhang et al., *ONNX: Open neural network exchange*, (2019).  
3087       <https://github.com/onnx/onnx>.
- 3088 [126] ATLAS Collaboration, *Performance of Run 3 HLT b-tagging with fast tracking,*  
3089       *Public b-Jet Trigger Plots for Collision Data*, (2022).  
3090       [https://twiki.cern.ch/twiki/bin/view/AtlasPublic/  
3091       BJetTriggerPublicResults#Performance\\_of\\_Run\\_3\\_HLT\\_b\\_taggi](https://twiki.cern.ch/twiki/bin/view/AtlasPublic/BJetTriggerPublicResults#Performance_of_Run_3_HLT_b_taggi).
- 3092 [127] ATLAS Collaboration, *Neural Network Jet Flavour Tagging with the Upgraded*  
3093       *ATLAS Inner Tracker Detector at the High-Luminosity LHC*,  
3094       **ATL-PHYS-PUB-2022-047** (2022).
- 3095 [128] ATLAS Collaboration, *Jet flavour tagging with gn1 and dl1d. generator dependence,*  
3096       *run 2 and run 3 data agreement studies*, (2023).  
3097       <https://atlas.web.cern.ch/Atlas/GROUPS/PHYSICS/PLLOTS/FTAG-2023-01/>.
- 3098 [129] R. Lafaye, T. Plehn, M. Rauch, D. Zerwas and M. Duhrssen, *Measuring the Higgs*  
3099       *Sector*, *JHEP* **08** (2009) p. 009 [[0904.3866](#)].
- 3100 [130] ATLAS Collaboration, *Measurements of WH and ZH production in the  $H \rightarrow b\bar{b}$*   
3101       *decay channel in pp collisions at 13 TeV with the ATLAS detector*, *Eur. Phys. J. C*  
3102       **81** (2021) p. 178 [[2007.02873](#)].
- 3103 [131] ATLAS Collaboration, *Measurement of the associated production of a Higgs boson*  
3104       *decaying into b-quarks with a vector boson at high transverse momentum in pp*  
3105       *collisions at  $\sqrt{s} = 13\text{ TeV}$  with the ATLAS detector*, *Phys. Lett. B* **816** (2021)

- 3106 p. 136204 [[2008.02508](#)].
- 3107 [132] K. Mimasu, V. Sanz and C. Williams, *Higher order QCD predictions for associated*  
3108 *Higgs production with anomalous couplings to gauge bosons*, *JHEP* **08** (2016) p. 039  
3109 [[1512.02572](#)].
- 3110 [133] ATLAS Collaboration, *Performance of jet substructure techniques for large- $R$  jets in*  
3111 *proton–proton collisions at  $\sqrt{s} = 7$  TeV using the ATLAS detector*, *JHEP* **09** (2013)  
3112 p. 076 [[1306.4945](#)].
- 3113 [134] S. Alioli, P. Nason, C. Oleari and E. Re, *A general framework for implementing NLO*  
3114 *calculations in shower Monte Carlo programs: the POWHEG BOX*, *JHEP* **06** (2010)  
3115 p. 043 [[1002.2581](#)].
- 3116 [135] ATLAS collaboration, *Measurement of the  $Z/\gamma^*$  boson transverse momentum*  
3117 *distribution in  $pp$  collisions at  $\sqrt{s} = 7$  TeV with the ATLAS detector*, *JHEP* **09**  
3118 (2014) p. 145 [[1406.3660](#)].
- 3119 [136] G. Cullen, N. Greiner, G. Heinrich, G. Luisoni, P. Mastrolia, G. Ossola et al.,  
3120 *Automated one-loop calculations with GoSam*, *Eur. Phys. J. C* **72** (2012) p. 1889  
3121 [[1111.2034](#)].
- 3122 [137] K. Hamilton, P. Nason and G. Zanderighi, *MINLO: multi-scale improved NLO*,  
3123 *JHEP* **10** (2012) p. 155 [[1206.3572](#)].
- 3124 [138] G. Luisoni, P. Nason, C. Oleari and F. Tramontano,  *$HW^\pm/HZ + 0$  and 1 jet at*  
3125 *NLO with the POWHEG BOX interfaced to GoSam and their merging within*  
3126 *MiNLO*, *JHEP* **10** (2013) p. 083 [[1306.2542](#)].
- 3127 [139] M. L. Ciccolini, S. Dittmaier and M. Krämer, *Electroweak radiative corrections to*  
3128 *associated  $WH$  and  $ZH$  production at hadron colliders*, *Phys. Rev. D* **68** (2003)  
3129 p. 073003 [[hep-ph/0306234](#)].
- 3130 [140] O. Brein, A. Djouadi and R. Harlander, *NNLO QCD corrections to the*  
3131 *Higgs-strahlung processes at hadron colliders*, *Phys. Lett. B* **579** (2004) pp. 149–156  
3132 [[hep-ph/0307206](#)].
- 3133 [141] G. Ferrera, M. Grazzini and F. Tramontano, *Associated Higgs-W-Boson Production*  
3134 *at Hadron Colliders: a Fully Exclusive QCD Calculation at NNLO*, *Phys. Rev. Lett.*  
3135 **107** (2011) p. 152003 [[1107.1164](#)].
- 3136 [142] O. Brein, R. V. Harlander, M. Wiesemann and T. Zirke, *Top-quark mediated effects*  
3137 *in hadronic Higgs-Strahlung*, *Eur. Phys. J. C* **72** (2012) p. 1868 [[1111.0761](#)].

- 3138 [143] G. Ferrera, M. Grazzini and F. Tramontano, *Higher-order QCD effects for associated*  
3139 *WH production and decay at the LHC*, *JHEP* **04** (2014) p. 039 [[1312.1669](#)].
- 3140 [144] G. Ferrera, M. Grazzini and F. Tramontano, *Associated ZH production at hadron*  
3141 *colliders: The fully differential NNLO QCD calculation*, *Phys. Lett. B* **740** (2015)  
3142 pp. 51–55 [[1407.4747](#)].
- 3143 [145] J. M. Campbell, R. K. Ellis and C. Williams, *Associated production of a Higgs boson*  
3144 *at NNLO*, *JHEP* **06** (2016) p. 179 [[1601.00658](#)].
- 3145 [146] L. Altenkamp, S. Dittmaier, R. V. Harlander, H. Rzehak and T. J. E. Zirke,  
3146 *Gluon-induced Higgs-strahlung at next-to-leading order QCD*, *JHEP* **02** (2013) p. 078  
3147 [[1211.5015](#)].
- 3148 [147] B. Hespel, F. Maltoni and E. Vryonidou, *Higgs and Z boson associated production via*  
3149 *gluon fusion in the SM and the 2HDM*, *JHEP* **06** (2015) p. 065 [[1503.01656](#)].
- 3150 [148] R. V. Harlander, A. Kulesza, V. Theeuwes and T. Zirke, *Soft gluon resummation for*  
3151 *gluon-induced Higgs Strahlung*, *JHEP* **11** (2014) p. 082 [[1410.0217](#)].
- 3152 [149] R. V. Harlander, S. Liebler and T. Zirke, *Higgs Strahlung at the Large Hadron*  
3153 *Collider in the 2-Higgs-doublet model*, *JHEP* **02** (2014) p. 023 [[1307.8122](#)].
- 3154 [150] O. Brein, R. V. Harlander and T. J. E. Zirke, *vh@nnlo – Higgs Strahlung at hadron*  
3155 *colliders*, *Comput. Phys. Commun.* **184** (2013) pp. 998–1003 [[1210.5347](#)].
- 3156 [151] S. Frixione, G. Ridolfi and P. Nason, *A positive-weight next-to-leading-order Monte*  
3157 *Carlo for heavy flavour hadroproduction*, *JHEP* **09** (2007) p. 126 [[0707.3088](#)].
- 3158 [152] M. Czakon and A. Mitov, *Top++: A program for the calculation of the top-pair*  
3159 *cross-section at hadron colliders*, *Comput. Phys. Commun.* **185** (2014) p. 2930  
3160 [[1112.5675](#)].
- 3161 [153] S. Alioli, P. Nason, C. Oleari and E. Re, *NLO single-top production matched with*  
3162 *shower in POWHEG: s- and t-channel contributions*, *JHEP* **09** (2009) p. 111  
3163 [[0907.4076](#)].
- 3164 [154] N. Kidonakis, *Next-to-next-to-leading logarithm resummation for s-channel single top*  
3165 *quark production*, *Phys. Rev. D* **81** (2010) p. 054028 [[1001.5034](#)].
- 3166 [155] N. Kidonakis, *Next-to-next-to-leading-order collinear and soft gluon corrections for*  
3167 *t-channel single top quark production*, *Phys. Rev. D* **83** (2011) p. 091503 [[1103.2792](#)].
- 3168 [156] E. Re, *Single-top Wt-channel production matched with parton showers using the*

- 3169        *POWHEG method*, *Eur. Phys. J. C* **71** (2011) p. 1547 [[1009.2450](#)].
- 3170 [157] N. Kidonakis, *Two-loop soft anomalous dimensions for single top quark associated*  
3171 *production with a  $W^-$  or  $H^-$* , *Phys. Rev. D* **82** (2010) p. 054018 [[1005.4451](#)].
- 3172 [158] T. Gleisberg, S. Höche, F. Krauss, M. Schönherr, S. Schumann, F. Siegert et al.,  
3173 *Event generation with SHERPA 1.1*, *JHEP* **02** (2009) p. 007 [[0811.4622](#)].
- 3174 [159] E. Bothmann et al., *Event generation with Sherpa 2.2*, *SciPost Phys.* **7** (2019) p. 034  
3175 [[1905.09127](#)].
- 3176 [160] F. Cascioli, P. Maierhöfer and S. Pozzorini, *Scattering Amplitudes with Open Loops*,  
3177 *Phys. Rev. Lett.* **108** (2012) p. 111601 [[1111.5206](#)].
- 3178 [161] T. Gleisberg and S. Höche, *Comix, a new matrix element generator*, *JHEP* **12** (2008)  
3179 p. 039 [[0808.3674](#)].
- 3180 [162] S. Schumann and F. Krauss, *A parton shower algorithm based on Catani–Seymour*  
3181 *dipole factorisation*, *JHEP* **03** (2008) p. 038 [[0709.1027](#)].
- 3182 [163] S. Höche, F. Krauss, M. Schönherr and F. Siegert, *QCD matrix elements + parton*  
3183 *showers. The NLO case*, *JHEP* **04** (2013) p. 027 [[1207.5030](#)].
- 3184 [164] S. Catani, L. Cieri, G. Ferrera, D. de Florian and M. Grazzini, *Vector Boson*  
3185 *Production at Hadron Colliders: a Fully Exclusive QCD Calculation at NNLO*, *Phys.*  
3186 *Rev. Lett.* **103** (2009) p. 082001 [[0903.2120](#)].
- 3187 [165] J. Butterworth et al., *PDF4LHC recommendations for LHC Run II*, *J. Phys. G* **43**  
3188 (2016) p. 023001 [[1510.03865](#)].
- 3189 [166] A. Denner, S. Dittmaier, S. Kallweit and A. Mück, *Electroweak corrections to*  
3190 *Higgs-strahlung off  $W/Z$  bosons at the Tevatron and the LHC with Hawk*, *JHEP* **03**  
3191 (2012) p. 075 [[1112.5142](#)].
- 3192 [167] A. Denner, S. Dittmaier, S. Kallweit and A. Mück, *HAWK 2.0: A Monte Carlo*  
3193 *program for Higgs production in vector-boson fusion and Higgs strahlung at hadron*  
3194 *colliders*, *Comput. Phys. Commun.* **195** (2015) pp. 161–171 [[1412.5390](#)].
- 3195 [168] ATLAS Collaboration, *Measurements of  $b$ -jet tagging efficiency with the ATLAS*  
3196 *detector using  $t\bar{t}$  events at  $\sqrt{s} = 13$  TeV*, *JHEP* **08** (2018) p. 089 [[1805.01845](#)].
- 3197 [169] ATLAS Collaboration, *Calibration of light-flavour  $b$ -jet mistagging rates using*  
3198 *ATLAS proton–proton collision data at  $\sqrt{s} = 13$  TeV*, *ATLAS-CONF-2018-006*  
3199 (2018).

- 3200 [170] ATLAS Collaboration, *Measurement of  $b$ -tagging efficiency of  $c$ -jets in  $t\bar{t}$  events using*
- 3201 a likelihood approach with the ATLAS detector, **ATLAS-CONF-2018-001** (2018).
- 3202 [171] ATLAS Collaboration, *Flavor Tagging with Track-Jets in Boosted Topologies with the*
- 3203 *ATLAS Detector*, **ATL-PHYS-PUB-2014-013** (2014).
- 3204 [172] ATLAS Collaboration, *Identification of boosted Higgs bosons decaying into  $b$ -quark*
- 3205 *pairs with the ATLAS detector at 13 TeV*, **Eur. Phys. J. C** **79** (2019) p. 836
- 3206 [[1906.11005](#)].
- 3207 [173] J. K. Anders and M. D'Onofrio, *V+Jets theoretical uncertainties estimation via a*
- 3208 *parameterisation method*, Tech. Rep. ATL-COM-PHYS-2016-044, Geneva (2016).
- 3209 [174] L. A. Harland-Lang, A. D. Martin, P. Motylinski and R. S. Thorne, *Parton*
- 3210 *distributions in the LHC era: MMHT 2014 PDFs*, **Eur. Phys. J. C** **75** (2015) p. 204
- 3211 [[1412.3989](#)].
- 3212 [175] S. Dulat, T.-J. Hou, J. Gao, M. Guzzi, J. Huston, P. Nadolsky et al., *New parton*
- 3213 *distribution functions from a global analysis of quantum chromodynamics*, **Phys. Rev.**
- 3214 **D93** (2016) p. 033006 [[1506.07443](#)].
- 3215 [176] ATLAS Collaboration, *Measurement of the Inelastic Proton–Proton Cross Section at*
- 3216  *$\sqrt{s} = 13$  TeV with the ATLAS Detector at the LHC*, **Phys. Rev. Lett.** **117** (2016)
- 3217 p. 182002 [[1606.02625](#)].
- 3218 [177] ATLAS Collaboration, *Search for the Standard Model Higgs boson produced in*
- 3219 *association with a vector boson and decaying to a pair of  $b$ -quarks using large- $R$  jets*,
- 3220 **ATL-COM-PHYS-2019-1125** (2019).
- 3221 [178] J. Pumplin et al., *New generation of parton distributions with uncertainties from*
- 3222 *global qcd analysis*, **JHEP** **07** (2002) p. 012 [[0201195](#)].
- 3223 [179] S. Frixione, E. Laenen, P. Motylinski, C. White and B. R. Webber, *Single-top*
- 3224 *hadroproduction in association with a  $W$  boson*, **JHEP** **07** (2008) p. 029 [[0805.3067](#)].
- 3225 [180] ATLAS Collaboration, *Measurement of  $VH$ ,  $H \rightarrow b\bar{b}$  production as a function of the*
- 3226 *vector-boson transverse momentum in 13 TeV pp collisions with the ATLAS detector*,
- 3227 **JHEP** **05** (2019) p. 141 [[1903.04618](#)].
- 3228 [181] ATLAS Collaboration, *Evidence for the  $H \rightarrow b\bar{b}$  decay with the ATLAS detector*,
- 3229 **JHEP** **12** (2017) p. 024 [[1708.03299](#)].
- 3230 [182] LHC Higgs Cross Section Working Group, S. Dittmaier, C. Mariotti, G. Passarino

- 3231        and R. Tanaka (Eds.), *Handbook of LHC Higgs Cross Sections: 2. Differential*  
3232        *Distributions*, [CERN-2012-002](#) (2012) [[1201.3084](#)].
- 3233 [183] LHC Higgs Cross Section Working Group, *Handbook of LHC Higgs Cross Sections: 3.*  
3234        *Higgs Properties*, [CERN-2013-004](#) (2013) [[1307.1347](#)].
- 3235 [184] L. Moneta, K. Belasco, K. Cranmer, S. Kreiss, A. Lazzaro, D. Piparo et al., *The*  
3236        *roostats project*, *arXiv preprint arXiv:1009.1003* (2010) .
- 3237 [185] J. R. Andersen et al., *Les Houches 2015: Physics at TeV Colliders Standard Model*  
3238        *Working Group Report*, in *9th Les Houches Workshop on Physics at TeV Colliders*  
3239        (*PhysTeV 2015*) *Les Houches, France, June 1-19, 2015*, 2016, [1605.04692](#).

## 3240 List of figures

<small>3241</small>	2.1 The Higgs potential $V(\phi)$ of the complex scalar field singlet $\phi = \phi_1 + i\phi_2$ , with a choice of $\mu^2 < 0$ leading to a continuous degeneracy in the true vacuum states. A false vacuum is present at the origin. . . . .	21
<small>3242</small>		
<small>3243</small>		
<small>3244</small>	2.2 Higgs boson production cross sections as a function of Higgs mass ( $m_H$ ) at $\sqrt{s} = 13$ TeV [26]. Uncertainties are shown in the shaded bands. At $m_H = 125$ GeV, Higgs boson production is dominated by gluon-gluon fussion, vector boson fusion, associated production with vector bosons, and top quark fusion. . . . .	26
<small>3245</small>		
<small>3246</small>		
<small>3247</small>		
<small>3248</small>		
<small>3249</small>	2.3 Diagrams for the four main Higgs boson production modes at the LHC for a Higgs mass $m_H = 125$ GeV at a centre of mass energy $\sqrt{s} = 13$ TeV. . . . .	26
<small>3250</small>		
<small>3251</small>	2.4 Higgs boson branching ratios as a function of Higgs mass ( $m_H$ ) at $\sqrt{s} = 13$ TeV [26]. Uncertainties are shown in the shaded bands. At $m_H = 125$ GeV, the Higgs predominantly decays to a pair of $b$ -quarks, around 58% of the time. The leading subdominant decay mode is to a pair of $W$ bosons. . . . .	27
<small>3252</small>		
<small>3253</small>		
<small>3254</small>		
<small>3255</small>	3.1 An overview of the CERN accelerator complex [36]. The LHC is fed by a series of accelerators starting with Linac2 (or Linac4 from 2020). Next are the Proton Synchrotron Booster, the Proton Synchrotron, and finally the Super Proton Synchrotron which injects protons into the LHC. . . . .	30
<small>3256</small>		
<small>3257</small>		
<small>3258</small>		
<small>3259</small>	3.2 The coordinate system used at the ATLAS detector, showing the locations of the four main experiments located at various points around the LHC. The 3-vector momentum $\mathbf{p} = (p_x, p_y, p_z)$ is shown by the red arrow. Reproduced from Ref. [37]. . . . .	31
<small>3260</small>		
<small>3261</small>		
<small>3262</small>		

3263	3.3 The track parameterisation used at the ATLAS detector. Five coordinates $(d_0, z_0, \phi, \theta, q/p)$ are specified, defined at the track's point of closest approach to the nominal interaction point at the origin of the coordinate system. The figure shows the three-momentum $\mathbf{p}$ and the transverse momentum $p_T$ (defined in Eq. (3.2)). The basis vectors $e_x$ , $e_y$ and $e_z$ are also shown. Reproduced from Ref. [38]. . . . .	33
3269	3.4 Delivered, recorded, and usable integrated luminosity as a function of time over the course of Run 2 [35]. A total of $139\text{ fb}^{-1}$ of collision data is labelled as good for physics, meaning all sub-detector systems were operating nominally. . . . .	35
3273	3.5 Average pile-up profiles measured by ATLAS during Run 2 [35]. . . . .	35
3274	3.6 A 3D model of the entire ATLAS detector [42]. Cutouts to the centre of the detector reveal the different subdetectors which are arranged in concentric layers around the nominal interaction point. . . . .	36
3277	3.7 A 3D model of the ATLAS ID showing the pixel, SCT and TRT subdetectors [45]. . . . .	37
3279	3.8 A cross-sectional view of the ATLAS ID, with the radii of the different barrel layers shown [38]. . . . .	38
3281	3.9 A schematic cross-sectional view of the ATLAS IBL [46]. . . . .	39
3282	3.10 The ATLAS calorimeters [49]. The ECal uses LAr-based detectors, while the HCal uses mainly scintillating tile detectors. In the forward region the HCal also includes the LAr hadronic endcaps. . . . .	41
3285	3.11 The ATLAS muon spectrometer [52]. . . . .	43
3286	3.12 Particles (left) which have enough separation will leave charge depositions which are resolved into separate clusters. Sufficiently close particles (right) can lead to merged clusters. Their combined energy deposits are recon- structed as a single merged cluster [57]. . . . .	47
3290	3.13 A sketch of electron reconstruction using the ATLAS detector [76]. Electron reconstruction makes use of the entire ID and the calorimeters. . . . .	52

3292	4.1 An overview of different high and low level taggers used in ATLAS.	
3293	The low level taggers are IPxD, SV1 and JetFitter, and RNNIP and DIPS	
3294	[61, 62, 95, 96]. The outputs of these taggers are fed into the high-level	
3295	taggers DL1, DL1r and DL1d [98, 99]. . . . .	57
3296	4.2 The truth $b$ -hadron decay radius $L_{xy}$ as a function of truth transverse	
3297	momentum $p_T$ for reconstructed $b$ -jets in $Z'$ events. Error bars show the	
3298	standard deviation. The pixel layers are shown in dashed horizontal lines. . . . .	59
3299	4.3 Diagram of a typical $b$ -jet (blue) which has been produced in an event	
3300	alongside two light jets (grey) [103]. The $b$ -hadron has travelled a significant	
3301	distance (pink dashed line) from the primary interaction point (pink dot)	
3302	before its decay. The large transverse impact parameter $d_0$ is a characteristic	
3303	property of the trajectories of $b$ -hadron decay products. . . . .	60
3304	4.4 At lower $p_T$ (left) the decay length of the $b$ -hadron is on average reduced, and	
3305	the decay tracks are less collimated. At higher $p_T$ (right) the $b$ -hadron decay	
3306	length increases and the resulting decay tracks are more collimated and have	
3307	less distance over which to diverge before reaching detector elements. As a	
3308	result, the ID may be unable to resolve charged depositions from different	
3309	particles, resulting merged clusters. . . . .	61
3310	4.5 $b$ -hadron decay track reconstruction efficiency as a function of truth $b$ -hadron	
3311	$p_T$ [104]. Nominal track reconstruction is shown in black, while the track	
3312	reconstruction efficiency for track candidates (i.e. the pre-ambiguity solver	
3313	efficiency) is shown in green. For high- $p_T$ $b$ -hadrons, the ambiguity solver	
3314	is overly aggressive in its removal of $b$ -hadron decay tracks. Suggestions for	
3315	the improvement of the track reconstruction efficiency in this regime by the	
3316	loosening of cuts in the ambiguity solver are shown in blue and red. . . . .	62
3317	4.6 Hit multiplicities on the IBL (left) and the pixel layers (right) as a function	
3318	of the $p_T$ of the reconstructed track for tracks in jets in a $Z'$ sample at	
3319	$\sqrt{s} = 13$ TeV. Tracks from the weak decay of the $b$ -hadron are shown in red,	
3320	while fragmentation tracks (which are prompt) are in blue. Baseline tracks	
3321	are those produced in the standard reconstruction described in Section 3.4.1,	
3322	while pseudotrack represent the ideal performance of the ATLAS detector	
3323	and are described in Section 3.4.1. . . . .	63

---

3324	4.7 The fraction of IBL (left) and B-layer (right) hits which are shared on 3325 <i>b</i> -hadron decay tracks as a function of the production radius of the <i>b</i> -hadron 3326      decay product for tracks in jets in a $Z'$ sample at $\sqrt{s} = 13$ TeV. Pseudotrack 3327      represent the ideal performance given the ATLAS detector, see Section 3.4.1.	65
3328	4.8 The average number of good (left) and wrong (right) IBL hits as a function 3329      of <i>b</i> -hadron $p_T$ for tracks using baseline tracking (black) and the modified 3330      version of the outlier removal procedure (red). . . . .	67
3331	4.9 (left) <i>b</i> -hadron decay track $d_0$ pulls ( $d_0/s(d_0)$ ) for baseline and modified 3332      GX2F tracks. (right) The absolute value of the $d_0$ pull as a function of the 3333      truth <i>b</i> -hadron transverse momentum. . . . .	67
3334	5.1 A diagram displaying the logical flow of a single neuron with three inputs 3335 $x_i^j$ . Each input is multiplied by a weight $\theta_j$ , and the resulting values are 3336      summed. A bias term $\theta_0$ is added, and the result $z$ is passed to an activation 3337      function. Each neuron can be thought of as a logistic regression model. . . . .	71
3338	5.2 The output of several common choices for the activation function $g(z)$ of 3339      an artificial neuron. The input $z$ is the output of the dot product between 3340      the activation and the weights, plus a bias term. . . . .	72
3341	5.3 Rate of fake tracks as a function of jet transverse momentum (left) and 3342 $\Delta R(\text{track}, \text{jet})$ (right) for jets in the $Z'$ sample. The rate of fake tracks 3343      increases significantly as a function of $p_T$ , and also increases as the distance 3344      to the jet axis decreases. . . . .	75
3345	5.4 The light-jet efficiency of the low level tagger SV1 for jets in the $Z'$ sample 3346      with $250 < p_T < 5000$ GeV, as a function of <i>b</i> -jet efficiency. The nominal 3347      tracking setup (black) is shown alongside the case where fake tracks which 3348      are not from the decay of a <i>b</i> -hadron are removed. The light-jet efficiency 3349      is decreased, demonstrating that the presence of fake tracks is detrimental 3350      to the algorithm performance. . . . .	76

3351	5.5 (left) Normalised histograms of the fake track classification model output 3352 separated for signal and fake tracks, and further separated by those tracks 3353 which are from the decay of a $b$ -hadron. (right) The ROC curve for all 3354 tracks (solid line) and tracks from the decay of a $b$ -hadron (dashed line). 3355 The plots show tracks in the combined $t\bar{t}$ and $Z'$ testing sample. The model 3356 is able to successfully discriminate between signal and fake tracks, and 3357 shows a very similar performance when looking specifically at tracks from 3358 the decay of a $b$ -hadron. . . . .	79
3359	5.6 (left) Normalised histogram of the $b$ -hadron track identification model 3360 output separated for tracks from the decay of a $b$ -hadron and tracks from 3361 other sources. The two groups are further separated into those tracks which 3362 are fake. (right) The ROC curve for all tracks (solid line). The plots show 3363 tracks in the combined $t\bar{t}$ and $Z'$ testing sample. . . . .	81
3364	5.7 The effect of applying the fake track identification algorithm together with 3365 the $b$ -hadron decay track identification on the jet tagging performance of 3366 SV1 for jets in the $Z'$ sample with $250 \text{ GeV} < p_T < 400 \text{ GeV}$ (left) and 3367 $400 \text{ GeV} < p_T < 1 \text{ TeV}$ (right). The nominal SV1 light-jet rejection (black) 3368 is compared to two working points of fake track removal, labelled “A” (red) 3369 and “B” (orange), which represent two different 2D working points of the 3370 track classification tools. Removal of fake tracks based on truth information 3371 is shown by the green curves. . . . .	82
3372	6.1 Comparison of the existing flavour tagging scheme (left) and GN1 (right). 3373 The existing approach utilises low-level algorithms (shown in blue), the 3374 outputs of which are fed into a high-level algorithm (DL1r). Instead 3375 of being used to guide the design of the manually optimised algorithms, 3376 additional truth information from the simulation is now being used as 3377 auxiliary training targets for GN1. The solid lines represent reconstructed 3378 information, whereas the dashed lines represent truth information [3]. . .	85
3379	6.2 The flow of information through a graph neural network layer for (left) a full 3380 implementation of the layer and (right) a deep sets model [118]. Reproduced 3381 from Ref. [117]. . . . .	88

---

3382	6.3 The inputs to GN1 are the two jet features ( $n_{\text{jf}} = 2$ ), and an array of 3383 $n_{\text{tracks}}$ , where each track is described by 21 track features ( $n_{\text{tf}} = 21$ ). The 3384 jet features are copied for each of the tracks, and the combined jet-track 3385 vectors of length 23 form the inputs of GN1 [3]. . . . .	93
3386	6.4 The network architecture of GN1. Inputs are fed into a per-track initialisation 3387 network, which outputs an initial latent representation of each track. 3388 These representations are then used to populate the node features of a 3389 fully connected graph network. After the graph network, the resulting node 3390 representations are used to predict the jet flavour, the track origins, and 3391 the track-pair vertex compatibility [3]. . . . .	93
3392	6.5 Comparison between the DL1r and GN1 $b$ -tagging discriminant $D_b$ for jets 3393 in the $t\bar{t}$ sample. The 85% WP and the 60% WP are marked by the solid 3394 (dashed) lines for GN1 (DL1r), representing respectively the loosest and 3395 tightest WPs typically used by analyses. A value of $f_c = 0.018$ is used in the 3396 calculation of $D_b$ for DL1r and $f_c = 0.05$ is used for GN1. The distributions 3397 of the different jet flavours have been normalised to unity area [3]. . . . .	98
3398	6.6 The $c$ -jet (left) and light-jet (right) rejections as a function of the $b$ -jet 3399 tagging efficiency for jets in the $t\bar{t}$ sample with $20 < p_{\text{T}} < 250 \text{ GeV}$ . The 3400 ratio with respect to the performance of the DL1r algorithm is shown in 3401 the bottom panels. A value of $f_c = 0.018$ is used in the calculation of $D_b$ 3402 for DL1r and $f_c = 0.05$ is used for GN1 and GN1Lep. Binomial error bands 3403 are denoted by the shaded regions. The $x$ -axis range is chosen to display 3404 the $b$ -jet tagging efficiencies usually probed in these regions of phase space [3].	101
3405	6.7 The $c$ -jet (left) and light-jet (right) rejections as a function of the $b$ -jet 3406 tagging efficiency for jets in the $Z'$ sample with $250 < p_{\text{T}} < 5000 \text{ GeV}$ . The 3407 ratio with respect to the performance of the DL1r algorithm is shown in 3408 the bottom panels. A value of $f_c = 0.018$ is used in the calculation of $D_b$ 3409 for DL1r and $f_c = 0.05$ is used for GN1 and GN1Lep. Binomial error bands 3410 are denoted by the shaded regions. The $x$ -axis range is chosen to display 3411 the $b$ -jet tagging efficiencies usually probed in these regions of phase space [3].	101

3412	6.8 The $b$ -jet tagging efficiency for jets in the $t\bar{t}$ sample (left) and jets in the $Z'$ sample (right) as a function of jet $p_T$ with a fixed light-jet rejection of 100 in each bin. A value of $f_c = 0.018$ is used in the calculation of $D_b$ for DL1r and $f_c = 0.05$ is used for GN1 and GN1Lep. GN1 demonstrates improved performance with respect to DL1r across the $p_T$ range shown. Binomial error bands are denoted by the shaded regions [3]. . . . .	102
3413		
3414		
3415		
3416		
3417		
3418	6.9 The $b$ -jet (left) and light-jet (right) rejections as a function of the $c$ -jet tagging efficiency for $t\bar{t}$ jets with $20 < p_T < 250$ GeV. The ratio to the performance of the DL1r algorithm is shown in the bottom panels. Binomial error bands are denoted by the shaded regions. The $x$ -axis range is chosen to display the $c$ -jet tagging efficiencies usually probed in these regions of phase space [3]. . . . .	104
3419		
3420		
3421		
3422		
3423		
3424	6.10 The $b$ -jet (left) and light-jet (right) rejections as a function of the $c$ -jet tagging efficiency for $Z'$ jets with $250 < p_T < 5000$ GeV. The ratio to the performance of the DL1r algorithm is shown in the bottom panels. Binomial error bands are denoted by the shaded regions. The $x$ -axis range is chosen to display the $c$ -jet tagging efficiencies usually probed in these regions of phase space [3]. . . . .	104
3425		
3426		
3427		
3428		
3429		
3430	6.11 The $c$ -jet (left) and light-jet (right) rejections as a function of the $b$ -jet tagging efficiency for $t\bar{t}$ jets with $20 < p_T < 250$ GeV, for the nominal GN1, in addition to configurations where no (GN1 No Aux), only the track classification (GN1 TC) or only the vertexing (GN1 Vert) auxiliary objectives are deployed. The ratio to the performance of the DL1r algorithm is shown in the bottom panels. A value of $f_c = 0.018$ is used in the calculation of $D_b$ for DL1r and $f_c = 0.05$ is used for GN1 [3]. . . . .	106
3431		
3432		
3433		
3434		
3435		
3436		
3437	6.12 The $c$ -jet (left) and light-jet (right) rejections as a function of the $b$ -jet tagging efficiency for $Z'$ jets with $250 < p_T < 5000$ GeV, for the nominal GN1, in addition to configurations where no (GN1 No Aux), only the track classification (GN1 TC) or only the vertexing (GN1 Vert) auxiliary objectives are deployed. The ratio to the performance of the DL1r algorithm is shown in the bottom panels. A value of $f_c = 0.018$ is used in the calculation of $D_b$ for DL1r and $f_c = 0.05$ is used for GN1 [3]. . . . .	106
3438		
3439		
3440		
3441		
3442		
3443		

3444	6.13 A schematic showing the truth track origin and vertex information (left) compared with the predictions from GN1 (right). The diagrams show the truth (left) and predicted (right) structure of a $b$ -jet. The true and predicted origins of the tracks is shown by the coloured circles along the diagonal. The shaded black boxes show the groupings of tracks into different vertices. Vertices reconstructed by SV1 and JetFitter are also marked. Class probabilities $p_b$ , $p_c$ and $p_u$ are rounded to three significant figures. GN1 improves over SV1 and JetFitter by successfully determining the origins and vertex compatibility of all the tracks in the jet with the exception of the truth OtherSecondary track, which is misidentified as pile-up. . . . .	108
3445		
3446		
3447		
3448		
3449		
3450		
3451		
3452		
3453		
3454	6.14 A schematic showing the truth track origin and vertex information (left) compared with the predictions from GN1 (right). The diagrams show the truth (left) and predicted (right) structure of a $b$ -jet. The true and predicted origins of the tracks is shown by the coloured circles along the diagonal. The shaded black boxes show the groupings of tracks into different vertices. Vertices reconstructed by SV1 and JetFitter are also marked. Class probabilities $p_b$ , $p_c$ and $p_u$ are rounded to three significant figures. GN1 improves over SV1 and JetFitter by successfully determining the origins and vertex compatibility of all but one tracks in the jet. . . . .	108
3455		
3456		
3457		
3458		
3459		
3460		
3461		
3462		
3463	6.15 Heavy flavour vertex finding efficiency as a function of jet $p_T$ for $b$ -jets in the $t\bar{t}$ sample using the exclusive (left) and inclusive (right) vertex finding approaches. The exclusive vertexing approach includes single track vertices while the inclusive approach requires vertices to contain at least two tracks. Efficient vertex finding requires the recall of at least 65% of the tracks in the truth vertex, and allows no more than 50% of the tracks to be included incorrectly. Binomial error bands are denoted by the shaded regions. . .	111
3464		
3465		
3466		
3467		
3468		
3469		
3470	6.16 Heavy flavour vertex finding efficiency as a function of jet $p_T$ for $b$ -jets in the $Z'$ sample using the exclusive (left) and inclusive (right) vertex finding approaches. The exclusive vertexing approach includes single track vertices while the inclusive approach requires vertices to contain at least two tracks. Efficient vertex finding requires the recall of at least 65% of the tracks in the truth vertex, and allows no more than 50% of the tracks to be included incorrectly. Binomial error bands are denoted by the shaded regions. . .	111
3471		
3472		
3473		
3474		
3475		
3476		

---

3477	6.17 Vertex finding efficiency for other secondary decays as a function of jet $p_T$	112
3478	for light-jets in the $t\bar{t}$ sample using the exclusive (left) and inclusive (right)	
3479	vertex finding approaches. The exclusive vertexing approach includes single	
3480	track vertices while the inclusive approach requires vertices to contain at	
3481	least two tracks. Efficient vertex finding requires the recall of at least 65%	
3482	of the tracks in the truth vertex, and allows no more than 50% of the tracks	
3483	to be included incorrectly. Binomial error bands are denoted by the shaded	
3484	regions. . . . .	
3485	6.18 Vertex finding efficiency as a function of jet $p_T$ for light-jets in the $Z'$ sample	112
3486	using the exclusive (left) and inclusive (right) vertex finding approaches.	
3487	The exclusive vertexing approach includes single track vertices while the	
3488	inclusive approach requires vertices to contain at least two tracks. Efficient	
3489	vertex finding requires the recall of at least 65% of the tracks in the truth	
3490	vertex, and allows no more than 50% of the tracks to be included incorrectly.	
3491	Binomial error bands are denoted by the shaded regions. . . . .	
3492	6.19 ROC curves for the different groups of truth origin labels defined in Table 5.1	115
3493	for jets in the $t\bar{t}$ sample (left) and jets in the $Z'$ sample (right). The	
3494	FromB, FromBC and FromC labels have been combined, weighted by their	
3495	relative abundance, into the Heavy Flavour category, and the Primary and	
3496	OtherSecondary labels have similarly been combined into a single category.	
3497	The mean weighted area under the ROC curves (AUC) is similar for both	
3498	samples [3]. . . . .	
3499	6.20 The $c$ -jet (left) and light-jet (right) rejections as a function of the $b$ -jet	117
3500	tagging efficiency for $t\bar{t}$ jets with $20 < p_T < 250$ GeV, for the looser track	
3501	selection trainings of GN1. The ratio to the performance of the baseline	
3502	GN1 model is shown in the bottom panels. A value of $f_c = 0.05$ is used for	
3503	all models. Binomial error bands are denoted by the shaded regions. . .	
3504	6.21 The $c$ -jet (left) and light-jet (right) rejections as a function of the $b$ -jet	
3505	tagging efficiency for $Z'$ jets with $250 < p_T < 5000$ GeV, for the looser track	
3506	selection trainings of GN1. The ratio to the performance of the baseline	
3507	GN1 model is shown in the bottom panels. A value of $f_c = 0.05$ is used for	
3508	all models. Binomial error bands are denoted by the shaded regions. . .	

3509	6.22 The HLT light-jet rejection as a function of the $b$ -jet efficiency jets in the $t\bar{t}$ sample with $20 < p_T < 250$ GeV for events with a centre of mass energy $\sqrt{s} = 13.6$ TeV [126]. The ratio to the performance of the DL1d algorithm [99] is shown in the bottom panels. Binomial error bands are denoted by the shaded regions. The purple vertical dashed lines represent the most common working points used for b-tagging. . . . .	118
3510		
3511		
3512		
3513		
3514		
3515	6.23 The $c$ -jet rejection (left) and light-jet rejection (right) for the upgraded HL-LHC ATLAS detector with $\langle \mu \rangle = 200$ as a function of the $b$ -jet efficiency for jets in the $t\bar{t}$ sample with $20 < p_T < 250$ GeV for events with a centre of mass energy $\sqrt{s} = 14$ TeV [127]. The ratio to the performance of the DL1d algorithm is shown in the bottom panels. Binomial error bands are denoted by the shaded regions. The purple vertical dashed lines represent the most common working points used for b-tagging. . . . .	120
3516		
3517		
3518		
3519		
3520		
3521		
3522	6.24 The $c$ -jet rejection (left) and light-jet rejection (right) for the upgraded HL-LHC ATLAS detector with $\langle \mu \rangle = 200$ as a function of the $b$ -jet efficiency for jets in the $Z'$ sample with $250 < p_T < 5000$ GeV for events with a centre of mass energy $\sqrt{s} = 14$ TeV [127]. The ratio to the performance of the DL1d algorithm is shown in the bottom panels. Binomial error bands are denoted by the shaded regions. . . . .	120
3523		
3524		
3525		
3526		
3527		
3528	7.1 Diagrams of the signal process (top) and $t\bar{t}$ background (bottom). Object to the right of centre are reconstructed within the large- $R$ jet. For the $t\bar{t}$ background, the large- $R$ jet contains a mis-tagged $c$ -jet or (less often) a mis-tagged light-jet. The contribution in the 0-lepton channel results from hadronically decaying $\tau$ lepton, or a electron or muon which is out of the analysis acceptance. . . . .	131
3529		
3530		
3531		
3532		
3533		
3534	7.2 Leading large- $R$ jet mass for the $Z$ and $W+hf$ processes in the HP SR of the 0-lepton channel [177]. The renormalisation scale $\mu_r$ has been varied by a factor of 0.5 (1DOWN) and 2 (1UP). An exponential function is fitted to the ratio between the nominal and alternate samples. . . . .	142
3535		
3536		
3537		
3538	7.3 Leading large- $R$ jet $m_J$ inclusive in $p_T^V$ for the $V+hf$ process modelled using both the SHERPA (blue) and MADGRAPH (red) samples [177]. The Kolmogorov-Smirnov test and $\chi^2/ndf$ are shown on the plots. . . . .	143
3539		
3540		

3541	7.4 Leading large- $R$ jet mass distribution for the $WZ$ and $ZZ$ processes, inclusive across all signal regions and lepton channels [177]. The renormalisation scale $\mu_R$ has been varied by a factor of 2 (1up) and 0.5 (1down). The red line shape shows the fitting results of the hyperbolic tangent function. . . . .	145
3542		
3543		
3544		
3545	7.5 The comparison of the shapes of the large- $R$ jet mass $m_J$ between SHERPA (black) and POWHEG+PYTHIA8 (red) samples from $WZ$ and $ZZ$ process in high and low purity signal regions, integrated over $p_T^V$ regions and the 0- and 1-lepton channels [177]. The dashed green line shows the fitted third order polynomial function and the blue lines show the function after a protection is added in the high mass region. . . . .	146
3546		
3547		
3548		
3549		
3550		
3551	7.6 The $m_J$ post-fit distributions in (top) the 0-, (middle) 1- and (bottom) 2-lepton SRs for (left) $250 \text{ GeV} < p_T^V < 400 \text{ GeV}$ and (right) $p_T^V \geq 400 \text{ GeV}$ . The LP and HP regions are merged for the 0-lepton and 1-lepton channels. The fitted background contributions are shown as filled histograms. The Higgs boson signal ( $m_H = 125 \text{ GeV}$ ) is shown as a filled histogram and is normalised to the signal yield extracted from data ( $\mu_{VH}^{bb} = 0.72$ ), and as an unstacked unfilled histogram, scaled by the SM prediction times a factor of two. The size of the combined on the sum of the fitted signal and background is shown in the hatched band. The highest bin contains the overflow [131]. . . . .	154
3552		
3553		
3554		
3555		
3556		
3557		
3558		
3559		
3560		
3561	7.7 The $m_J$ post-fit distributions in the $t\bar{t}$ control region for (top) the 0-lepton channel and the 1-lepton channel for $250 \text{ GeV} < p_T^V < 400 \text{ GeV}$ and (bottom) the 0-lepton channel and the 1-lepton channel for $p_T^V > 400 \text{ GeV}$ . The background contributions after the likelihood fit are shown as filled histograms. The Higgs boson signal ( $m_h = 125 \text{ GeV}$ ) is shown as a filled histogram on top of the fitted backgrounds normalised to the signal yield extracted from data ( $\mu_{VH}^{bb} = 0.72$ ), and unstacked as an unfilled histogram, scaled by the SM prediction times a factor of 2. The size of the combined statistical and systematic uncertainty for the sum of the fitted signal and background is indicated by the hatched band. The highest bin in the distributions contains the overflow [131]. . . . .	155
3562		
3563		
3564		
3565		
3566		
3567		
3568		
3569		
3570		
3571		

3572 7.8  $m_J$  distribution in data after subtraction of all backgrounds except for the  
 3573  $WZ$  and  $ZZ$  diboson processes. The contributions from all lepton channels  
 3574 and signal regions are summed and weighted by their respective values of  
 3575 the ratio of fitted Higgs boson signal and background yields. The expected  
 3576 contribution of the associated  $WH$  and  $ZH$  production of a SM Higgs  
 3577 boson with  $m_H = 125$  GeV is shown scaled by the measured combined  
 3578 signal strength ( $\mu_{VH}^{bb} = 0.72$ ). The diboson contribution is normalised to  
 3579 its best-fit value of  $\mu_{VZ}^{bb} = 0.91$ . The size of the combined statistical and  
 3580 systematic uncertainty is indicated by the hatched band. This error band is  
 3581 computed from a full signal-plus-background fit including all the systematic  
 3582 uncertainties defined in Section 7.2, except for the  $VH/VZ$  experimental  
 3583 and theory uncertainties [131]. . . . .

3584 7.9 Signal strength compatibility test between the (3+1)-POI fit (with the three  
 3585 lepton channels splitted) and the default (1+1)-POI fit. The compatibility  
 3586 of the three channels is evaluated via a  $\chi^2$  difference test and results in a  
 3587 p-value of 49% [131]. . . . . 159

3588 7.10 Impact of systematic uncertainties on the fitted  $VH$  signal-strength pa-  
 3589 rameter  $\mu_{VH}^{bb}$  sorted in decreasing order. The boxes show the variations  
 3590 of  $\hat{\mu}$ , referring to the top  $x$ -axis, when fixing the corresponding individual  
 3591 nuisance parameter to its post-fit value modified upwards or downwards by  
 3592 its post-fit uncertainty, i.e.  $\hat{\theta} \pm \sigma_{\hat{\theta}}$ , and repeating the fit. The impact of  
 3593 up- and down-variations can be distinguished via the dashed and plane box  
 3594 fillings. The yellow boxes show the pre-fit impact (top  $x$ -axis) by varying  
 3595 each nuisance parameter by  $\pm 1$ . The filled circles show the deviation of the  
 3596 fitted value for each nuisance parameter,  $\hat{\theta}$ , from their nominal input value  
 3597  $\theta_0$  expressed in standard deviations with respect to their nominal uncer-  
 3598 tainties  $\Delta\theta$  (bottom  $x$ -axis). The error bars show the post-fit uncertainties  
 3599 on  $\hat{\theta}$  with respect to their nominal uncertainties. The open circles show  
 3600 the fitted values and uncertainties of the normalization parameters that are  
 3601 freely floating in the fit. Pre-fit, these parameters have a value of one [177]. 161

3602 7.11 Measured  $VH$  simplified template cross sections times the  $H \rightarrow b\bar{b}$  and  
 3603  $V \rightarrow$  leptons branching fractions in the medium and high  $p_T^{V,t}$  bins [131]. 164

# 3604 List of tables

<small>3605</small>	2.1 The fermions of the SM [16]. Three generations of particles are present. <small>3606</small> Also present (unlisted) are the antiparticles, which are identical to the <small>3607</small> particles up to a reversed charge sign. . . . .	15
<small>3608</small>	2.2 The bosons of the SM [16]. The photon, weak bosons and gluons are gauge <small>3609</small> bosons arising from gauge symmetries, and carry the four fundamental forces <small>3610</small> of the SM. The recently discovered Higgs boson is the only fundamental <small>3611</small> scalar particle in the SM. . . . .	16
<small>3612</small>	3.1 Overview of the different LHC runs [34, 35]. The average number of interactions per bunch-crossing is denoted as $\langle \mu \rangle$ (see Section 3.2.3), and is here averaged over the entire run. The luminosity is the peak instantaneous luminosity. Numbers for Run 3 are preliminary and are only provided to give an indication of expected performance. . . . .	29
<small>3617</small>	3.2 Quality selections applied to tracks, where $d_0$ is the transverse IP of the track, $z_0$ is the longitudinal IP with respect to the PV and $\theta$ is the track polar angle (see Section 3.2.2 for the IP definitions). Silicon hits are hits on the pixel and SCT layers. Shared hits are hits used on multiple tracks which have not been classified as split by the cluster-splitting neural networks [57]. A hole is a missing hit, where one is expected, on a layer between two other hits on a track. . . . .	46

3624	5.1	Truth origins which are used to categorise the physical process that led to the production of a track. Tracks are matched to charged particles using the truth-matching probability [57]. A truth-matching probability of less than 0.75 indicates that reconstructed track parameters are likely to be mismeasured and may not correspond to the trajectory of a single charged particle. The “OtherSecondary” origin includes tracks from photon conversions, $K_S^0$ and $\Lambda^0$ decays, and hadronic interactions.	75
3631	5.2	Input features to the fake track classification NN. Basic jet kinematics, along with information about the reconstructed track parameters and constituent hits are used. Shared hits, are hits used on multiple tracks which have not been classified as split by the cluster-splitting neural networks [57], while split hits are hits used by multiple tracks which have been identified as merged, and therefore split.	77
3637	5.3	Hyperparameter for the track classification model	78
3638	5.4	Good and fake track selection efficiencies for the combined $t\bar{t}$ and $Z'$ samples. Two working points are defined, cutting on the NN output at 0.06 and 0.12.	80
3640	5.5	Cut values for the fake and $b$ -hadron decay track MVAs for the two defined working points. Working point “B” cuts more aggressively on the MVA outputs than WP “A”, removing more fake tracks but resulting in an increased loss of signal tracks (which here are all $b$ -hadron decay tracks).	81
3644	6.1	Input features to the GN1 model. Basic jet kinematics, along with information about the reconstructed track parameters and constituent hits are used. Shared hits, are hits used on multiple tracks which have not been classified as split by the cluster-splitting neural networks [57], while split hits are hits used on multiple tracks which have been identified as merged. A hole is a missing hit, where one is expected, on a layer between two other hits on a track. The track leptonID is an additional input to the GN1Lep model [3].	90
3651	6.2	A summary of GN1’s different classification networks used for the various training objectives, adapted from Ref. [3]. The hidden layers column contains a list specifying the number of neurons in each layer. ReLU activation is used through the network [112].	95

3655 6.3 The area under the ROC curves (AUC) for the track classification from  
3656 GN1, compared to a standard multilayer perceptron (MLP) trained on a  
3657 per-track basis. The unweighted mean AUC over the origin classes and  
3658 weighted mean AUC (using as a weight the fraction of tracks from the  
3659 given origin) is provided. GN1, which uses an architecture that allows track  
3660 origins to be classified in a conditional manner as discussed in Section 6.4.3,  
3661 outperforms the MLP model for both  $t\bar{t}$  and  $Z'$  jets. . . . . 114

3662 7.1 Summary of the definitions of the different analysis regions . Signal enriched  
3663 regions are marked with the label SR. There are regions with relatively  
3664 large signal purity (HP SR) and with low purity (LP SR). Background  
3665 enriched regions are marked with the label CR. The shorthand “add” stands  
3666 for additional small- $R$  jets, i.e. number of small- $R$  jets not matched to the  
3667 Higgs-jet candidate. The medium and high  $p_T^V$  regions are referred to as  
3668  $Mp_T^V$  and  $Hp_T^V$ , respectively [131]. . . . . 125

3669 7.2 Signal and background processes with the corresponding generators used for the  
3670 nominal samples [131]. If not specified, the order of the cross-section calculation  
3671 refers to the expansion in the strong coupling constant ( $\alpha_s$ ). (★) The events  
3672 were generated using the first PDF in the NNPDF3.0NLO set and subsequently  
3673 reweighted to the PDF4LHC15NLO set [165] using the internal algorithm in  
3674 PowHEG-Box v2. (†) The NNLO(QCD)+NLO(EW) cross-section calculation for  
3675 the  $pp \rightarrow ZH$  process already includes the  $gg \rightarrow ZH$  contribution. The  $qq \rightarrow ZH$   
3676 process is normalised using the cross-section for the  $pp \rightarrow ZH$  process, after  
3677 subtracting the  $gg \rightarrow ZH$  contribution. An additional scale factor is applied to  
3678 the  $qq \rightarrow VH$  processes as a function of the transverse momentum of the vector  
3679 boson, to account for electroweak (EW) corrections at NLO. This makes use of  
3680 the  $VH$  differential cross-section computed with HAWK [166, 167]. . . . . 127

3681 7.3 Selections applied to baseline and signal electrons and muons. . . . . 128

3682	7.4 Event selection requirements for the boosted $VH$ , $H \rightarrow b\bar{b}$ analysis channels and sub-channels [131]. Various channel dependent selections are used to maximise the signal efficiency and reduce the number of background events in each analysis region. The $\min[\Delta\phi(\mathbf{E}_T^{\text{miss}}, \text{small-}R \text{ jets})]$ selection is used to remove jets when the missing transverse momentum $\mathbf{E}_T^{\text{miss}}$ is pointing in the direction of the Higgs candidate, and the $\Delta\phi(\mathbf{E}_T^{\text{miss}}, \mathbf{E}_{T, \text{trk}})$ is used to reject events where the calorimeter missing transverse momentum $\mathbf{E}_T^{\text{miss}}$ is not pointing in the direction of the track-based missing transverse momentum $\mathbf{E}_{T, \text{trk}}^{\text{miss}}$ . The $\Delta y(V, H_{\text{cand}})$ quantifies the rapidity difference between the reconstructed vector boson and Higgs candidate. . . . .	130
3692	7.5 Different sources of uncertainty (i.e. variations in the model) considered for the $V + \text{jets}$ background, and the corresponding implementation. For each uncertainty, acceptance and shape uncertainties are derived. . . . .	134
3695	7.6 0-lepton $W + \text{jets}$ nominal sample flavour composition and total event yield [177]. $Mp_T^V$ refers to the medium $p_T^V$ region, and $Hp_T^V$ refers to the high $p_T^V$ region (see Table 7.1). . . . .	138
3699	7.7 1-lepton $W + \text{jets}$ nominal sample flavour composition and total event yield [177]. $Mp_T^V$ refers to the medium $p_T^V$ region, and $Hp_T^V$ refers to the high $p_T^V$ region (see Table 7.1). . . . .	138
3701	7.8 0-lepton $Z + \text{jets}$ nominal sample flavour composition and total event yield [177]. $Mp_T^V$ refers to the medium $p_T^V$ region, and $Hp_T^V$ refers to the high $p_T^V$ region (see Table 7.1). . . . .	139
3704	7.9 2-lepton $Z + \text{jets}$ nominal sample flavour composition and total event yield [177]. $Mp_T^V$ refers to the medium $p_T^V$ region, and $Hp_T^V$ refers to the high $p_T^V$ region (see Table 7.1). . . . .	139
3707	7.10 $V + \text{jets}$ acceptance uncertainties [177]. $W + \text{jets}$ SR and CR uncertainties marked with a superscript † are correlated. The 1L $W + \text{jets}$ H/M uncertainty marked by * is applied as independent and uncorrelated NPs in both HP and LP signal regions. . . . .	140
3711	7.11 Diboson acceptance uncertainties [177]. All uncertainties except channel extrapolation uncertainties are fully correlated between $ZZ$ and $WZ$ processes and channels. . . . .	145

3714	7.12 Factors applied to the nominal normalisations of the $t\bar{t}$ , $W+\text{hf}$ , and $Z+\text{hf}$ backgrounds, as obtained from the likelihood fit [131]. The errors represent the combined statistical and systematic uncertainties. . . . .	153
3715		
3716		
3717	7.13 Post-fit yields in the 0-lepton channel. Combined statistical and systematic uncertainties are shown [177]. . . . .	156
3718		
3719	7.14 Post-fit yields in the 1-lepton channel. Combined statistical and systematic uncertainties are shown [177]. . . . .	156
3720		
3721	7.15 Post-fit yields in the 2-lepton channel. Combined statistical and systematic uncertainties are shown [177]. . . . .	157
3722		
3723	7.16 Breakdown of the absolute contributions to the uncertainty on the signal strength $\mu_{VH}^{bb}$ obtained from the (1+1)-POI fit. The average impact represents the average between the positive and negative uncertainties on $\mu_{VH}^{bb}$ . The sum in quadrature of the systematic uncertainties attached to the categories differs from the total systematic uncertainty due to correlations [177]. . . . .	162
3724		
3725		
3726		
3727		
3728		